INVESTIGATION OF THE THERMAL TREATMENT OF HIGHER ACTIVITY WASTE

Luke Boast

University of Sheffield

Immobilisation Science Laboratory

Department of Materials Science and Engineering

University of Sheffield

This dissertation is submitted for the degree of Doctor of Philosophy

September 2018

ABSTRACT

Considering the high overall costs of radioactive waste disposal and the growing requirements for improved quality of the final waste form, the benefits offered by thermal processing become very significant. Key drivers for the application of thermal treatment processes include the reduced volume, improved passive safety, and superior long term stability of the vitrified wasteform products. Currently, a fundamental lack of scientific knowledge and understanding significantly hinders the uptake of thermal treatment processes for the immobilisation and disposal of plutonium contaminated material waste. The project will contribute to accelerating the acquisition of knowledge and experience required to support the Nuclear Decommissioning Authority (NDA) in deploying thermal technologies as a national asset for intermediate level waste (ILW) treatment.

Plutonium contaminated materials (PCM) waste is a sub category of ILW. The current treatment method for PCM is supercompaction and cement encapsulation, however, there are significant concerns regarding the reliability of the treatment method to consistently deliver a waste form suitable for long term performance. This project follows on from previous work which provided proof of concept studies for thermally treating PCM waste. This work uses a soda lime silica (SLS) glass cullet as the glass forming additive to aid vitrification, providing substantial benefits in terms of costs saving compared to previous work. The thermal treatment experiments showed no violent reactions between the waste simulant and the glass additives. The Ce (acting as a Pu surrogate) was effectively partitioned within the slag fractions of the waste form, with crystalline regions present in certain formulations. The Ce was found as trivalent species providing confidence that the slag component of the wasteforms developed here could incorporate Pu at the concentrations expected from treatment of PCM wastes. The materials produced here are broadly comparable, in terms of durability, to other simulant UK ILW glass products considered potentially suitable for geological disposal.

The project also investigates the potential to use the glass forming oxides found within the ILW itself to aid vitrification. Using suitable ternary phase diagrams, it is possible to use the waste and any additional additives to create a formulation to ensure a glass is successfully formed at a reasonable operating temperature whilst always maintaining compatibility with currently available technology platforms. This method was utilised to vitrify representative pond scabbling waste. The simulant waste contained high levels of SiO_2 which, in combination with glass forming oxides, were successfully vitrified.

Characterisation studies were performed to understand the relationship between Na_2O and B_2O_3 and the effect this had on the microstructure of the resultant structure of the glass. Glass dissolution experiments were also performed to test the performance of the glass in conditions expected within a geological disposal facility (GDF). The thesis also includes the results of samples acquired from a three month student placement working with Kurion's geomelt facility at the Workington site (UK).

Contained within this PhD are experiments which aim to provide significant information into the mechanism that drive glass alteration. However this data has only been applicable to short-term alteration. The research presented in Chapter 7 aims to understand the long term mechanism of the vitrified PCM waste by using 250 year old slag samples as a glass alteration analogue. The results presented provide evidence for the long term durability of the vitrified PCM waste samples.

ACKNOWLEDGEMENTS

Thanks to everyone who I have met during my time in Sheffield, from all the friendships made within the ISL, to everyone who I have played tennis/ cricket/ football/ shared a beer with, you have certainly helped with the inevitable stresses of completing a PhD.

My final and biggest thanks is to my family. The love, humour and support you provide is the bedrock to my successes in life, including the completion of this PhD. To my parents Julie and Keith Boast, thanks for everything you have done for me, I dedicate this thesis to you.

CONTENTS

LIST OF TABLES

LIST OF FIGURES

LIST OF ABBREVIATIONS AND ACRONYMS

ASTM – American society for testing and materials

BSE – Back scattered electrons

CASH - Calcium aluminosilicate hydrate

CS – Centre shift

CSH – Calcium silicate hydrate

CSSF – Calcined solids storage facility

DILWEP – Decommissioning intermediate level waste encapsulation plant

DOE – Department of energy

DTA – Differential thermal analysis

EA – Environmental assessment

EDS – Energy dispersive spectroscopy

ESRF – European synchrotron radiation facility

GDF – geological disposal facility

GGBS – Ground granulated blast furnace slag

HIP – Hot isostatic pressing

HLW – High level waste

IAEA – International atomic agency

ICDD – International centre for diffraction data

ICP – Idaho cleanup project

ICP-OES – Inductively coupled plasma optical emission spectroscopy

ICV – Incontainer vitrification

INL – Idaho national laboratory

INTEC – Idaho national technology and engineering centre

IS – Isomer shift

ILW - Intermediate level waste

LLW – Low level waste

MCC – Materials characterisation centre

MS – Mössbauer spectroscopy

NDA – Nuclear decommissioning authority

NNL – National nuclear laboratory

NMR – Nuclear magnetic resonance

NSLS – National synchrotron light source

PC – Portland cement

PCM – Plutoniuam contaminated materials

PCT-B – Product consistency test

PES – Polyetheslphane

PNNL – Pacfic northwest national laboratory

PVC – polyvinyl chloride

QS – Quadropole splitting

SA/V – Suface area to volume ratio

SC – Silicon carbide

SEM – Scanning electron microscopy

SLC – site licence company

SLS – Soda lime silica

UKAEA – United Kingdom atomic energy agency

TRL – Technology readiness level

VLLW – Very low level waste

WAC – Waste acceptance criteria

XANES – X-ray near edge spectroscopy

XRF – X-ray fluorescence

XRD – X-ray diffraction

LIST OF APPENDICES

1 INTRODUCTION

The decommissioning of nuclear power stations and their related facilities, as well as the clean-up of sites contaminated by radionuclides from accidents and nuclear weapons programs, are international issues, with varying levels of progress. Without a clear path towards long term disposal, with high profile cases such as Yucca Mountain as a geological repository in the USA failing to deliver substantial progress, a solution to this problem remains a considerably vexing technical and political challenge.

The central issues for nuclear waste management include the storage, transportation and disposal of radioactive waste generated at the back-end of the nuclear fuel cycle. Intergenerational responsibility means inaction is not an option. Governments cannot reap the benefits of nuclear power without taking responsibility for the legacy waste this produces. This includes managing suitable disposal methods for used fuel, high-level waste and contaminated sites.

The Nuclear Decommissioning Authority (NDA) is responsible for managing the effective and efficient clean-up of the UK's nuclear legacy waste. The Energy Act (2004) states the NDA is required to carry out R&D in support of decommissioning and clean up. As part of this programme the NDA funds a number of PhD projects through a bursary scheme, including this one. The PhD Bursary Scheme and wider support for University R&D play an important role in securing the future skill base for nuclear decommissioning. The project reported in this thesis will support the NDA's commitment to "generate credible and preferred strategic options for the estate-wide use of thermal technologies", by developing the necessary skills, capability, fundamental knowledge and understanding, required to support timely insertion of thermal treatment technologies and develop national expertise in this subject.

This thesis focuses on the application of thermal treatment to process two particular sub categories of ILW streams including; plutonium contaminated materials (PCM) waste (Chapter 4) and masonry waste in the form of pond scabblings (Chapter 5). The thesis aims to develop an understanding of the waste and matrix reactions during thermal

treatment of PCM and masonry waste which are prominent at a number of NDA sites. The specific objectives are to understand;

- The sequence of reactions leading to waste digestion in thermal treatment;
- Control of radionuclides partitioning between off gas and the waste form using inactive surrogates;
- Selection of glass forming additives to optimise waste digestion and waste form quality.

More broadly the project will underpin the fundamental scientific knowledge to support the need for a baseline strategy towards a major investment in thermal treatment of ILW.

A recent development within the thermal treatment industry, is the commissioning of the GeoMelt in-container vitrification (ICV) plant at NNL's flagship central laboratory on the Sellafield site. The author undertook a three month secondment, with Kurion Inc, to support the commissioning of the system. The fundamental scientific knowledge obtained by the author through laboratory scale thermal treatment processes, enabled the author to contribute to the project and use the work to form part of this thesis. Chapter 6 describes the student involvement within the project whilst also using the facilities at Sheffield to analyse samples produced during the secondment period.

Due to the nature of long lived radionuclides, the long term behaviour of the waste form needs to be considered. The project will develop an understanding of product stability with respect to generic ILW disposal concepts, through accelerated dissolution experiments. A number of studies have used archaeological glass samples to predict and study the long term behaviour of glass samples including radioactive waste glasses. This method will be utilised within this thesis to evaluate the long term performance of the vitrified PCM waste products synthesised in Chapter 4. Chapter 7 describes the methods used to study archaeological samples found within the town of Hayle, situated in west Cornwall.

The overall aims of the investigation is to underpin the scientific processes of thermally treating PCM and masonry waste, using laboratory scale waste simulants. The fundamental knowledge and processes used in this thesis would be applicable to a number of ILW streams. The project aims to gain a complete understanding of the vitrified products through characterisation methods, product performance and long term behaviour.

2 LITERATURE REVIEW

2.1 Radioactive Waste

Radioactive wastes are classified into different categories by different countries, some subdivide waste streams into long and short-lived wastes, or by radioactivity levels. The civil nuclear industry is the main source for radioactive waste in the UK, however hospitals, universities and weapons decommissioning also contribute.

There are four classifications for radioactive nuclear waste in the UK (Ojovan 2005) (DEFRA 2004)

Very low level waste (VLLW): 0.1 m^3 of VLLW contains less than 400 kBq of total activity or single items contain less than 40 kBq of total activity. Waste of this type can include contaminated gloves, paper etc,. from sources such as universities and hospital waste. VLLW, due to its low activity, can be incinerated and then placed in a landfill site.

Low level waste (LLW): Containing radioactive materials other than those suitable for disposal with ordinary refuse, but not exceeding 4 GBq per tonne of alpha or 12 GBq per tonne of beta/gamma activity. The current treamtment method is to send the waste to the LLW Repository in Cumbria.

Intermediate level waste (ILW): Waste with radioactivity exceeding the upper limits of LLW, but without the need to consider heat generating capacity in the design of storage or disposal facility. Waste includes fuel cladding, reactor components, and sludge from the treatment of radioactive effluents. ILW streams are usually made into cementations waste forms.

High Level Waste (HLW): HLW can be described as heat-generating radioactive waste, as a result of the radioactive decay. The management of the heat generated needs to be addressed when selecting suitable storage and disposal options. HLW is mainly fission products originating from the reprocessing of spent nuclear fuels. Current treatment for high level liquid waste is incorporation into borosilicate glass, using a process called vitrification.

International agreement is that a deep geological disposal facility is the best options for long term storage of radioactive waste. The NDA is responsible for planning and implementing geological disposal in the UK. To implement geological disposal the NDA has set up the Radioactive Waste Management (RWM). RWM will eventually be developed into a Site Licence Company (SLC) responsible for the construction and operation of a geological disposal facility. RWM has developed a Generic Disposal System Specification (NDA/RWM 2010) which describes the requirements of the disposal system.

To identify potential sites where a GDF could be located, the UK government favours a voluntarist approach, working with communities that are willing to participate in the siting process. A number of different geological disposal (GDF) concepts have been developed around the world for different geological environments and disposal inventories. Each concept will utilise a 'multi barrier' approach. This approach involves engineered and natural barriers working together to prevent radioactivity being released to the surface in amounts that could cause harm to life and the environment. These barriers are, from the waste outwards:

Conditioned waste in the container - provide a stable, low-solubility matrix that limits the rate of release of the majority of radionuclides by dissolution in groundwater that comes into contact with the waste form.

Over pack - prevent groundwater from reaching the waste form.

Buffer - condition the chemical characteristics of groundwater and pore water in contact with the container and the waste form so as to reduce corrosion rate and/or solubility of radionuclides.

Host rock - isolate waste from people and the surface environment by providing a large radiation shield.

A geological disposal facility shall only accept wastes that comply with the Waste Acceptance Criteria (WAC). WAC specify the characteristics that waste packages will have to satisfy before being accepted for disposal. Such WAC are produced and issued by the facility operator following appropriate regulatory scrutiny.

One of the major driving forces for thermally treating nuclear waste is the potentially large volume reduction. This becomes very important when considering final disposal

within a GDF. A larger volume reduction will equate to lower costs to the UK tax payer when constructing a GDF. Other drivers for thermal treatment include increased passive safety and improved long term performance within a GDF.

2.1.1 Plutonium Contaminated Materials (PCM) Waste.

PCM waste is a subcategory of intermediate level waste, which is generated as a result of the handling of plutonium during nuclear fuel processing and other related activities. PCM waste accounts for 7 % of the UK ILW inventory (NDA 2011). The amount of PCM waste in the UK is estimated to be over 31,000m³, with 70% of PCM waste stored at the Sellafield site (NDA 2013). PCM waste, similar to that held at Sellafield, is also stored at other public sector civil nuclear sites including Dounreay (4%) and Harwell (4%), which are all operated by the United Kingdom Atomic Energy Authority (UKAEA), as shown in Table 2.1.

Site	Existing Volume (m³)	Total (including future arising m³)
Sellafield	7975	22000
Dounreay	840	1250
Harwell	1230	1390
Aldermaston	3400	6500
Total Derived	13445	31140

Table 2.1 Total PCM waste UK inventory – (NDA 2013)

The PCM waste, which can incorporate masonry, metal, organic items, are double bagged in heat sealed PVC linings before being stored in 200L mild steel drums, as shown in Figure 2.1. The heterogeneous nature of the waste material presents a considerable materials science and engineering challenge for PCM waste immobilisation.

Figure 2.1 PCM waste stored in 200L mild steel drums.

The radioactive content and waste composition are generally well understood within an acceptable degree of accuracy to underpin management controls for ensuring safe storage in the short term. However, longer-term control depends on managing the hazards that the waste present due to the presence of long-lived Pu isotopes which are radiotoxic and mobile in the subsurface. This requires that the PCM waste is converted into a passive, safe waste form suitable for long term storage.

A process is already in place at the Sellafield site for the treatment of some categories of PCM waste, centred on the Waste Treatment Centre (WTC). The general method of the WTC is compression of the 200L drums containing the PCM waste, and the resulting crushed drums are grouted in cement, as shown in Figure 2.2, and stored within 500L steel storage containers (NuSAC 2005).

However, there are concerns regarding the reliability of the supercompaction and subsequent grouting process to deliver a consistent waste form suitable for long-term storage and eventual disposal. Recognised issues associated with the reliability of the treatment process include:

Non-compactable waste – prevent the drums from being crushed into pucks smaller than the maximum height of 500 mm

Wood rubber and PVC components – which may reassert their shape following supercompaction causing deformation.

Liquid content of the waste – causes downtime of the facility, as well as additional costs of disposing of liquid waste.

Figure 2.2 Compacted and cemented PCM waste drums

Operating experience with the WTC demonstrates that significant challenges still remain in order to process existing stocks of PCM at Sellafield rapidly enough to satisfy current regulatory requirements for dealing with the legacy of past operations at the site. The work contained in this thesis demonstrates the applicability of thermal treatment methods as an alternative treatment method for PCM waste.

2.1.2 Pu and the use of possible surrogates

Pu is created in a nuclear reactor when uranium atoms absorb neutrons, Pu can then be extracted and recycled as fuel or for defence purposes (Ewing 2005). Nirex (2004) provides a comprehensive review of international literature on immobilisation matrices

for separated stocks of Pu. The radiotoxicity of Pu and the associated hazard this presents, makes it vital that the Pu contained within the PCM waste is safely immobilised. PCM waste originates from a ranges of processes, including fuel reprocessing and fast reactor fuel fabrication (Egan 2008). The main areas of concern within this study, when designing waste forms to immobilise Pu, are criticality issues and the segregation / partitioning of Pu. The ability to safely simulate the behaviour of Pu using a suitable surrogate, will be very important for this study.

In order to alleviate concerns regarding the environmental damage that could ensue from a potential critical mass assembly within a nuclear waste form or from a waste repository, there have been a number of studies which analyse the bounding estimates for criticality risks (Rechard et al. 1996; Forsberg 1997). The amount of Pu required to form a critical mass is dependent on several factors resulting in values ranging from several hundred grams to infinity (Kienzler et al. 2003). However, the levels of Pu within the PCM waste under consideration in this study are expected to be much lower than the calculated amount of Pu required to reach critical mass, as shown from previous works by Cerefice (1996). Previous studies have shown PuO_2 solubility in glass to be 10-11 wt% in silicate glass waste forms (Vienna et al. 1996; Fox et al. 2008). A homogenous distribution of Pu within the waste form would further lower the risk of criticality issues; designing a glass waste form to permit this will be critical to determining the success of the project. A significant disadvantage with the current treatment method of super- compaction and cement encapsulation is the potential for "hotspots" of Pu within the cemented waste product. As discussed, the risk of criticality is not considered likely within the PCM wastes or waste forms, but the ability to determine the partitioning of the Pu within the waste form is still important. If Pu preferentially resides in a minority phase within the waste form, the ability to immobilise the Pu from the environment relies on the properties of that one phase. If this phase is water soluble then this will obviously be a major concern. Previous laboratory scale studies of PCM waste conducted by Hyatt et al. (2014) produced multi phased glass waste forms. The experiments in this study are expected to produce similar compositions given the heterogeneous nature of the PCM waste.

On the ground of safety and expenditure, surrogates were used to simulate the behaviour of Pu. In many cases the chemical behaviour of a radioactive element can be safely simulated using one of its inactive isotopes. This method is utilised in Chapter 5, with the chemical and physical effects of ^{90}Sr, ^{137}Cs and ^{60}Co simulated using their naturally

occurring isotopes. In the case of Pu, however, inactive isotopes of the same element do not exist. Therefore a surrogate element that mimics aspects of the chemical and physical properties of Pu must be used. Bingham et al. (2008) identified a number of chemical and physical properties of Pu which must be closely considered when selecting a surrogate element. Based upon this, and to maintain consistency with previous studies (Hyatt et al. 2014), CeO_2 was used as a Pu surrogate within this body of work. Ce has a similar ionic radius and electronic configuration, which are known to determine structural, chemical and solubility behaviour of Pu in the final waste form (Lopez et al. 2003). Ce is also a useful surrogate for elements, such as Pu, that exhibit both 3+ (trivalent) and 4+ (tetravalent) valence states (Reid et al. 2012). A number of studies have determined that trivalent species such as Pu^{3+} and Ce^{3+} are much more soluble in borosilicate systems (Lopez et al. 2003) (Deschanels et al. 2007), with Cachia et al. (2006) showing that Pu solubility was effectively doubled by modifying its oxidation state, from 2 wt.% for Pu(IV) to 4 wt. % for Pu(III). This information is important for this study as the melting conditions will be designed to maximise waste loading within the vitrified product. A degree of caution should be exercised however, as it is reported that redox potential of Ce is dissimilar to that of Pu, as shown below, (Caravaca et al. 2008; Trinidad et al. 2008) meaning the Ce^{3+} / Ce^{4+} ratio would not be representative of the Pu^{3+} / Pu^{4+} ratio in the resulting glasses.

$$Ce^{4+} + e^- \rightleftharpoons Ce^{3+} \qquad (E^0/V = 1.72)$$

$$Pu^{4+} + e^- \rightleftharpoons Pu^{3+} \qquad (E^0/V = 1.006)$$

2.2 Additional waste streams vitrified within the project

The main focus of the project was to gain a greater understanding of the thermal treatment of PCM waste. The principles of thermally treating nuclear waste can be applied to a number of ILW streams within the nuclear waste industry. With a large investment in thermal treatment technologies planned at sites such as Sellafield, it is important for research engineers to be able to identify potential waste streams which would benefit from thermal treatment and to underpin the science behind these processes to aid with increasing the TRL for thermal treatment technologies. The following section describes the origin and technical information regarding a number of different waste streams studied within this thesis.

2.2.1 Masonry waste in the form of decommissioned silo pond scabblings

The project will also look at vitrifying contaminated masonry waste (Chapter 5). This waste stream originates from the removal of masonry waste from decommissioned silo fuel ponds in the form of scabblings.

The concrete walls have been in contact with fuel pond water and with the items held in the pond. The waste stream data sheet in Table 2.2, contains the activity of the listed alpha or beta/gamma emitting radionuclides.

The radionuclides from Table 2.2 originate from the spent nuclear fuel within the ponds and are classified as fission products. Most reactors in the world are fuelled with uranium, with ^{235}U being the most common isotope associated with the fission events induced by low-energy neutrons, so-called thermal neutrons (Wilson 1997). During the nuclear fuel cycle, fuel within the reactor needs to be replaced due to depleted amounts of ^{235}U.

The spent fuel requires cooling and storage to allow the short half-life fission products to decay. ^{137}Cs and ^{90}Sr have half-lives of approximately 30 years. During this time in the silo ponds, similar to the one investigated within the project, the ^{137}Cs and ^{90}Sr undergo β decay. The decay of fission products within the silo ponds leads to the contamination of the concrete walls as shown in Table 2.2.

The total waste volume of contaminated masonry waste is 248.7 m^3. The current treatment method is to place the contaminated masonry waste in 3 m^3 boxes with further processing occurring at the decommissioning ILW encapsulation plant (DILWEP) involving cement encapsulation. The major disadvantage with this treatment method is the large increase in waste volume. Chapter 5 investigates the possibility of using the glass forming additives found within the masonry waste to aid vitrification. This would produce a monolithic, stable and highly durable waste form whilst providing substantial volume reductions.

Nuclide	Mean radioactivity, TBq/m³
^{90}Sr	7.62E-04
^{60}Co	2.31E-07
^{137}Cs	2.87E-03
^{238}Pu	7.87E-06
^{241}Pu	1.82E-04
^{241}Am	1.61E-06
Total α	2.95E-05
Total β/γ	3.82E-03

Table 2.2 Best estimate of the derived activity of the main radionuclides contained within the contaminated masonry waste. The totals shown are the sums of the listed alpha or beta.gamma emitting radionuclides (adapted from NDA waste inventory 2016)

2.2.2 Contaminated soils from the Sellafield site

Chapter 6 focuses on a three-month industrial placement undertaken by the student working with the GeoMelt system, which is a Joule Heated Ceramic Melter (JHCM). Using the facilities within the ISL, analytical studies were performed on a number of glass samples from various projects. One such project was looking at the viability of vitrifying contaminated soils from the Sellafield site (section 6.4).

A large amount of the contaminated soils contained within the UK radioactive waste inventory is classified as VLLW/LLW (670,000 tonnes, (NDA 2011)), which can be directly disposed of in a landfill site or LLW repository sites such as Drigg. There is a significant amount of contaminated soil classified as ILW (2,600 tonnes) which will not be suitable for direct disposal and will need further processing to immobilise the waste stream from the environment. There is considerable interest in thermally treating this waste stream to produce a stable, durable waste form with any volume reduction achieved, resulting in large savings in disposal costs. If the vitrified soils produce a high performing waste form, it provides the opportunity to use the LLW soil as the glass forming additive, bringing substantial savings by avoiding disposal costs through the LLW repository. The

thesis will determine the effectiveness of vitrifying contaminated soils using the GeoMelt process through analytical studies.

2.3 Glass and its Relationship to Vitrification

The properties of glass make vitrification of radionuclides an attractive proposition. Ojovan (2011), Donald (2010), Caurant et al. (2009) provides an overview of the glass wasteforms currently used for HLW as well as for low and intermediate level ratioactive waste (LILW) immobilization. The properties give vitrification its high-quality product and flexibility in incorporating radionuclides within the glass matrix (Bingham et al. 2012). Because an understanding of the properties of glass is fundamental to understanding the advantages of vitrification as a waste treatment process, this section of the literature review will concentrate on providing a brief overview of glass structure and discusses how this structure relates to the durability of vitrified glass containing hazardous waste.

2.3.1 Glass Structure

Glass is a rigid, non $-$ crystalline material defined by the absence of long $-$ range ordering within the system. Glass materials generally have low porosity, often composed of primarily silica, alumina, and oxides of alkali and alkaline earth elements. There are a varying number of glass types including phosphate, oxynitride and sulphate glasses, however most glasses used in waste immobilisation are silicate glasses, therefore this literature review will focus mainly on borosilicate glass systems. There have been many theories of glass structure over the years, the difficulty can be drawn from the unique and complex cooling and nucleation behaviour exhibited by glass structures.
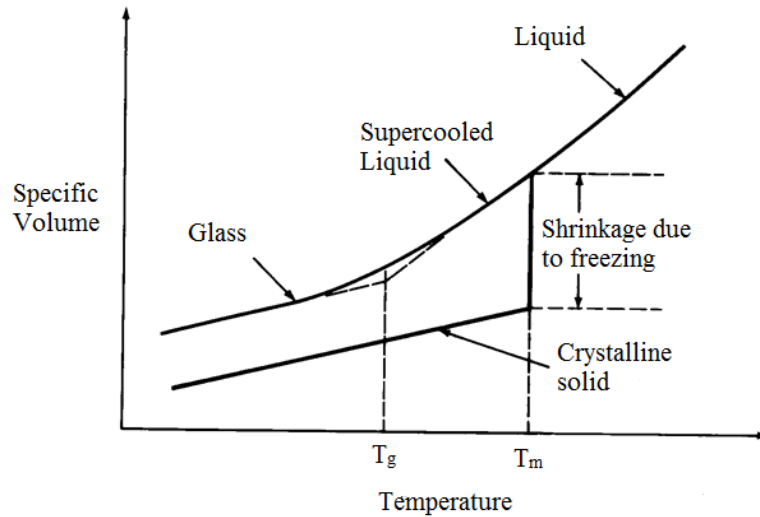
Figure 2.3 Glass melting behaviour- graph adapted from (Warren 1941)

When a molten material is cooled from its liquid state, a point is usually reached (freezing point) where spontaneous nucleation and growth of crystals occurs and the material rapidly solidifies in a crystalline state. The nucleation event can occur homogenously or heterogeneously. However this spontaneous nucleation and growth model can be delayed under certain conditions and the material may remain in a liquid state at a temperature well below its normal freezing point. As the temperature further reduces, the viscosity of this supercooled liquid increases rapidly to a point where it is so high that the supercooled liquid is, for practicable purposes, a solid. This is known as a glass. It is generally accepted that this unique solidification behaviour produces a three dimensional random network model when describing glass structure (Zachariasen 1932). The model shows the glass composed of polyhedral structures, same as conventional crystal lattice, however with sufficient distortion of the bond angles to permit structural units to arrange in a non-periodic manner giving rise to a random network.

Silicate glasses are composed of three dimensional topographically disordered interconnected structural blocks of network forming silicon-oxygen tetrahedra (SiO_4). Some of the oxygen atoms from the tetrahedra can be shared to form organised three-dimensional silica networks. This model assumes that silicate glasses are built up of SiO_4 tetrahedra joined at their corners with variable Si-O-Si bond angles, unlike in crystals where bond angles and lengths are essentially constant. This leads to a fairly random and open network structure.

Warren (1941) used an extension to this model to describe the structure of alkali silicates. In this model, oxides can be divided into three main categories. There are those that can form continuous three-dimensional random networks by themselves (network formers), and there are oxides for which the cation can enter the network interstitially (network modifiers) (Shelby 2005). This arrangement of oxides is shown in Figure 2.4. The third category are classed as intermediate network formers. These oxides can form part of the glass network structure, but as either the network former or modifier. Al_2O_3 is a well-known examples of an intermediate oxide network former. The tetrahedron AlO_4^- negative charge is compensated for by a network modifying cation. In the absence of sufficient charge compensation however, Al can also behave as a network modifier.
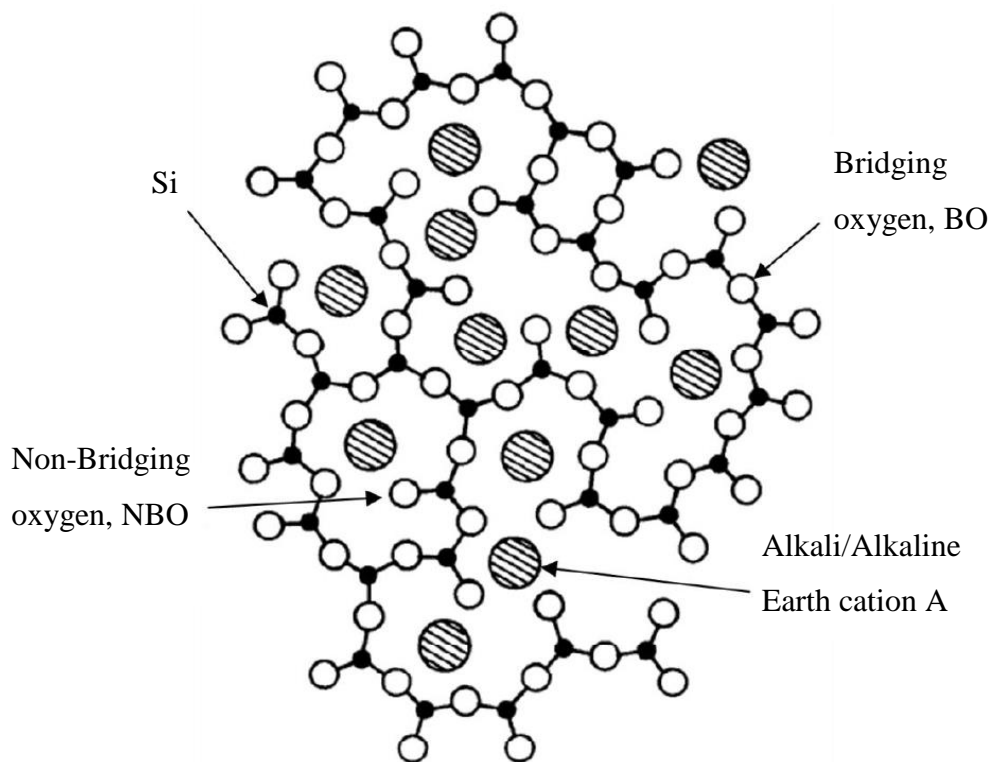
Figure 2.4 Structure of an alkali silicate (2D), as described by the Zachariasen-Warren model. Adapted from (Warren 1941).

Appreciable amounts of most inorganic oxides can be incorporated in silicate glasses. Elements replace silicon within the glass to become network formers. By replacing silicon in the network, inorganic species such as metals found in the middle part of the periodic table (e.g. Fe, Cr) can be incorporated within the glass structure. Most monovalent and

divalent cations including Na and Ca do not enter the network but form ionic bonds assuming the role of network modifiers within the glass.

2.3.2 Glass theory and the relationship with ILW vitrification

The mechanism of how certain elements are incorporated and immobilised within the glass network is very important for this project. The reason for this is that few legacy waste and intermediate level waste are as closely controlled in their chemistry and physical composition as HLW, this includes PCM waste. Vitrification of ILW is made possible by the unique nature of glass formation allowing the glass waste form to be highly versatile and allowing the majority of elements to be safely incorporated within the glass structure.

Vitrification of ILW offers many advantages over cementitious waste treatment, including greater volume reduction and superior long term performance. Legacy and intermediate waste streams suitable for vitrification contain a large number of different materials, these include;

- Sand, concrete and cement
- Sludges arising from magnox storage ponds
- Spent organic exchange material
- Zeolites and ceramics

Given the varying degree of composition between the different waste streams, glass compositions developed for vitrification will need to incorporate substantial quantities of the key organic materials. These materials include SiO_2, Fe_2O_3 and Al_2O_3. This presents a considerable opportunity for maximising waste loading. Many of the waste streams listed contain the glass forming oxides Therefore, unlike HLW vitrification, where all the silica required for glass making originates from the addition of glass frit, the silica in the vitrified product could originate from the ILW itself. The idea of using the glass forming oxides originating from the waste itself to aid vitrification will be utilised within this project.

2.3.3 Glass durability

The durability of a nuclear waste form is critically important due to the long lived nature of radionuclides. The dissolution behaviour of glass has typically involved subjecting the

glass to an attacking solution for commercially or scientifically important glasses. There are two generally accepted ways of measuring the durability of glass, static or dynamic testing. The glasses produced in this project were subjected to static testing involving PCT-B and MMC-1 testing . These test are similar in the sense that the glass is placed inside a container with the testing solution remaining sealed for the duration of the test. The major difference between in the two testing methods is that PCT-B uses powdered glass whilst MCC-1 uses a glass monolith.

The main parameters that determine the rate of dissolution of a glass in aqueous solution is the composition of the glass (Gin et al. 2012), the attacking solution (Leemann et al. 2011), pH (Vienna et al. 2013) and temperature. There have a number of studies performed determining the influence of each parameter on glass durability (Grambow 2011; Knauss et al.1989). The waste forms produced in this project are mainly silicate and borosilicate systems therefore this section will mainly focus on issues affecting these types of glass waste forms. Figure 2.5 shows the generally accepted mechanism of nuclear waste glass dissolution within the literature. The following briefly describes each stage (Frugier et al. 2008).
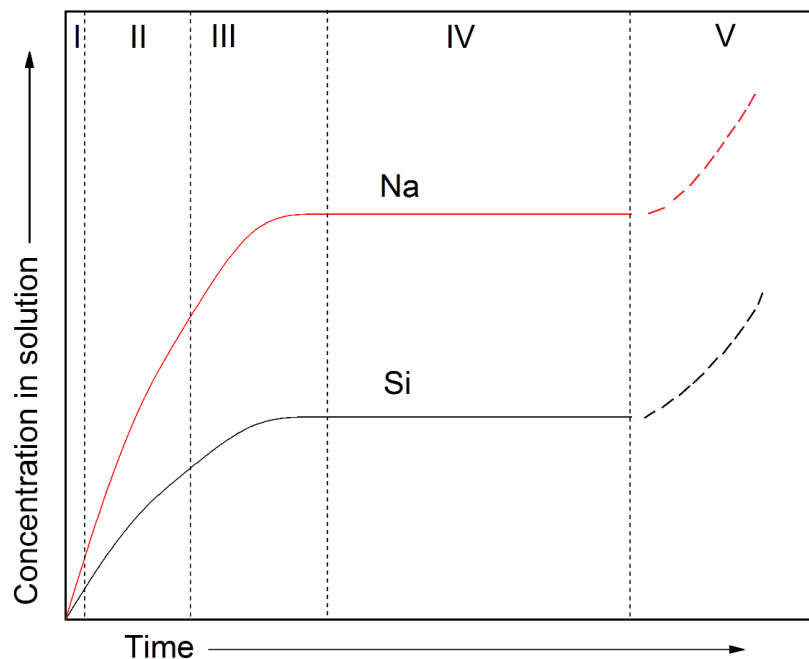
Figure 2.5 Schematic of the five stages (I – V) which describe the mechanism of nuclear waste glass durability (adapted from frugier et al. (2008)).

Stage I: **Ion exchange** (interdiffusion) of alkali ions – Referred to as the initial rate regime. Alkali ions exchange with positively-charged species from aqueous solution (H^+ and H_3O^+) leading to leaching of the alkali ions from the glass (Doremus 1975).

Si-O-R + H_2O → Si – OH + R^+ + OH^- (R = an alkali ion)
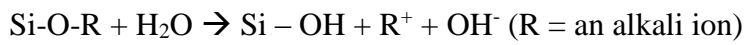
Stage II: **Hydrolysis of the silicate network** – Interdiffusion results in hydrolysis of the silica network = Si – O^- + H_2O → Si – OH + OH^-

The OH^- ions are formed to charge-balance the alkali ions released into solution, which leads to an increase in the pH of the solution in a closed system (Cailleteau et al. 2008).

Stage III: **The rate drop** is associated with:

- The development of a hydrated glass layer acting as a kinetic barrier to further ion exchange (Delage et al. 1992).
- Dissolution rate will drop as silica concentration in solution increases, as it approaches silica saturation (Helgeson et al. 1984).
- Increase in the aqueous concentration of elements from the glass (Arab et al. 2006)
- Passivation of the glass surface (Delage et al. 1992), as shown in Figure 2.6.
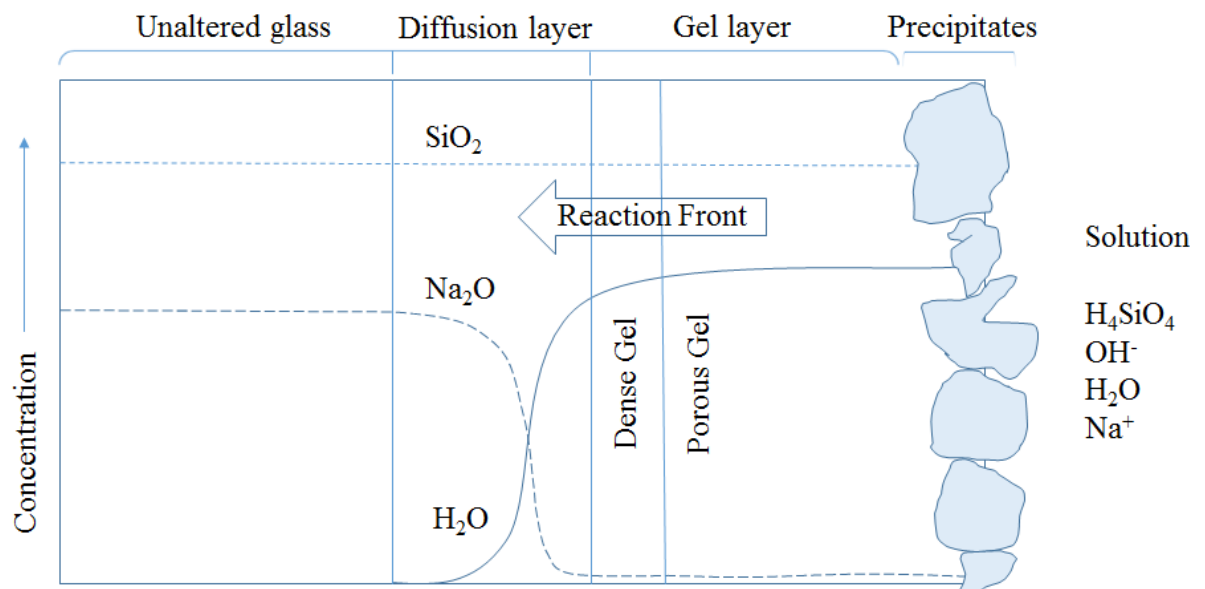
Figure 2.6 Schematic of the alteration products which form on the surface of silicate glasses during aqueous dissolution. The concentration gradients of key species are included. (adapted from Frugier et al. (2008))

It is now accepted that the rate drop is likely to be a result of a combination of both the increase of silica levels in solution and the alteration layer formation, as shown from studies of solution saturation effects (Snellings 2013), study of the gel layer properties and alteration products. Once the dense gel layer has formed glass dissolution proceeds according to regime IV.

Stage IV: **The residual rate (saturation)**

During the residual stage of alteration, in closed systems such as the static PCT experiments performed in this project, the glass maintains low levels of dissolution. Elements within the glass will continue to be leached into solution despite the formation of the dense protective gel layer, shown in Figure 2.6. This is because glass is inherently thermodynamically unstable and as such the glass will continue to undergo some form of reaction (Grambow 1992).

Stage V: **Precipitation of alteration products and possibly resumption of dissolution**.

This stage is not seen in all compositions of glass or under all test scenarios. This resumption occurs due to the precipitation of crystalline phases which damages the passivating layer (Cailleteau et al. 2008). This results in the concentration of dissolved species in the surrounding solution being reduced leading to resumption of dissolution destroying the diffusion barrier. Previous studies have shown this mechanism is due to a precipitation of zeolites at a given pH or solution concentration level (Ribet 2004).

2.4 Previous studies of thermal treatment of PCM waste.

There have been a number of proof of concept studies demonstrating the compatibility of thermally treating PCM waste (Witwer et al. 2010; Schumacher et al. 1995; Soelberg et al. 1995) however, a fundamental understanding of waste incorporation reactions and the impact of waste inventory on product quality remains to be established. The experimental methods demonstrated within this project follow previous work performed by the University of Sheffield (Hyatt et al. 2014),which aimed to underpin the scientific understanding behind the thermal treatment process of PCM waste, using ground granulated blast furnace slag (GGBS) as the glass forming additive. The study used the following process considerations:

- Due to the high metal fraction contained within the waste, the aim was to oxidise the metal fraction to produce a mix slag / metal waste form.

- Partitioning of the Ce, acting as Pu surrogate, was expected to occur within the slag phase of the waste form, based upon previous studies (Schlienger et al. 1997). If sufficient decontamination of the metal fraction can be achieved, then it may be possible to dispose the metal fraction as LLW resulting in significant savings in terms of disposal.

- To achieve this high partitioning ratio, all of the components need to be molten, including the metal fraction, therefore a melting temperature of 1560 ℃ was aimed for. One of the aims of this project will be to lower this operating temperature, which is advantageous in terms of avoiding volatilisation of radionuclides and can increase the lifetime of various thermal treatment technology platforms.

The study produced considerable success, with the glass waste forms developed physically and chemically immobilising the PuO_2 (CeO_2 surrogate), with analysis indicating, as expected, that Ce was incorporated within the oxide fraction. Substantial volume reductions of between 65 – 95 % against a baseline treatment method was also achieved. Despite this success, due to the economic difficulties faced by the steel industry coupled with the wide range of applications for GGBS, renders the material a poor choice as a glass forming additive. The aims of this project follow on from Hyatt et al. (2014) study, but with the use of soda-lime-silica (SLS) glass as the glass forming additive, which given its unlimited supply, provides much greater economic benefits to the thermal treatment operator.

The work presented within this body of work addresses a number of identified gaps in scientific understanding needed to further the development of thermal treatment technology for processing PCM and other ILW streams. The work presented in this thesis contributes new results adding to the body of knowledge developed by Hyatt et al. (2014) and other studies, in a number of areas including;

- Analysis of iron redox ratio, Fe^{2+} / Σ Fe, in vitrified products of PCM waste simulants will be performed to provide insight into the oxygen partial pressure during processing. This will be achieved through using ^{57}Fe Mössbauer spectroscopy. This is much better than trying to measure absolute oxygen fugacity over the melt.

- Long term, detailed leaching experiments will be performed to understand the long term behaviour of the vitrified products within a hyper alkaline environment similar to that with which would be expected within a GDF.

- Optimisation of the process will be attempted by establishing redox conditions necessary to produce a fully vitreous waste form and to also lower the melting temperature to decrease volatilisation.

2.4.1 Pu segregation via metal decontamination

A number of PCM waste streams contain high levels of contaminated metal waste. Because of this, the waste form design will incorporate a mixed slag / metal waste form with the idea that the Pu (Ce surrogate) will partition into the slag fraction essentially decontaminating the metal fraction of the waste form. There have been a large number of publications that include information on decontamination of radioactive scrap materials (Ozturtc 1994). For the purpose of brevity, this section will focus on decontamination of steel. Worchester et al. (1993) provides a summary of previous experimental test results in the subject area, and the reader is referred to this for greater information. Reimann (1991) determined that the most efficient slag to decontaminate LLW metal waste at 1500 ℃ had a composition of approximately 40% SiO_2 – 40% CaO – 20% Al_2O_3, obtaining decontamination of the metal to 0.04 ppm U. This composition is similar to the GGBS used as the glass forming additive in N. C. Hyatt et al. (2014) study producing decontamination factor of 99% of Ce within the slag fraction. For economic reasons (Motz 2001) this fluxing material is unsuitable for this application. Seitz et al. (1979) investigates a number of slagging materials suitable for decontaminating Pu containing metal, including additives similar to the SLS glass used in this study. During this study Seitz et al. (1979) demonstrated Pu partitioning coefficients (ratio of plutonium in slag / plutonium in steel) exceeding 10^6, sufficient to decontaminate steel wastes below the classification threshold for LLW wastes, using a slag material with composition 81% SiO_2 – 13 % CaO – 4 % Na_2O. This composition is similar to the SLS glass used in this study, providing a degree of confidence that partitioning of the Ce will occur within the slag phase. Min et al. (2008) study also found slag formers containing high amounts of silica proved to be effective for melt decontamination of stainless steel wastes contaminated in depleted uranium. The increased B found in the SLS glass frit may also be beneficial. Durinck et al. (2008) study shows that the addition of B_2O_3 is sufficient to

stabilize steel slags at an industrial scale by depressing the migration of Ca^+ ions and rotations of the SiO_4^{-4} tetrahedrons which causes internal stresses within the slag.

2.4.2 Combustible materials

The PCM waste can essentially be categorised into combustible and non-combustible materials. The main combustible materials include PVC materials (originating from the double heat sealed bags containing the waste), rubber, gloves, paper towels and polythene. These materials present considerable problems for thermal treatment operators due to their low melting temperatures resulting in volatilisation occurring very early in the process, making it difficult to incorporate radioactive contaminates into the waste form without losses within the off-gas system. These material also contain a lot of carbon which can cause a highly reducing atmosphere during the thermal treatment process. Non-combustible materials include concrete, metals, glass and filters. The concrete and glass components tend to have a high melting point and are ideal glass formers. The thermal treatment process will aim to oxidise metal component into a slag waste form. A number of studies have been performed which investigates the effectiveness of burning combustible material whilst oxidising non combustibles materials into a virtuous slag material (Flinn et al. 1980; Freeman 1997; Applewhite-Ramsey et al. 1995). All of these studies produced separable glass and metallic phases for each of the various compositions vitrified. Promisingly none of the waste surrogates variations tested was found to have a singular impact on plutonium partitioning to the metal or off-gas solid phases. This shows despite the heterogeneous nature of the PCM waste, with a mixture of combustible and non-combustible material, consistently high partitioning of the Pu into the glass phase is to be expected.

The main organic material of concern in this study is PVC as it is present in all the simulated waste streams in this project, therefore an understanding of thermal behaviour is important. Mara (1977) examines the thermal decomposition mechanisms of PVC. Within this work Mara (1977) determines that by 600 ºC, 100 % of the PVC material is decomposed with carbon monoxide and carbon dioxide released in various quantities depending on melting conditions. At this temperature the non-combustible materials will not be molten and therefore it is unlikely that the combustible materials will affect the redox conditions necessary to oxidise the metal content (Siwadamrongpong et al. 2004).

2.4.3 Redox considerations

As discussed in this section, one of the major advantageous of thermally treating nuclear waste is the ability to oxidise metal components, therefore it is important to understand the redox conditions within the melt as this will define the composition and properties of the glass and metal components. For a more comprehensive and theoretical discussion on redox behaviour in glasses, the reader is referred to Paul (1990).

The glass oxidation state is most commonly observed by measuring the ferrous / ferric ratio of Fe. Won (1976) states that the Fe redox equilibria can be described by the following reaction:

$$Fe^{2+} + \tfrac{1}{4} O_2 + \tfrac{3}{2} O^{2-} = FeO_2^-$$
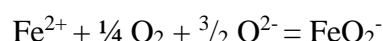
For this reaction, the Fe^{2+}/ Fe^{3+} ratio increases with increasing polymerisation of the silicate network which shows that the Fe^{2+} / Fe^{3+} ratio increases under more reducing conditions, at higher temperatures and with a lower alkali content in the glass (Goldman et al. 1985; Johnston 1964). Mössbauer spectroscopy will be used in this project to investigate the Fe^{2+} / Fe^{3+} ratio within the vitrified waste forms, which will show the effect that the processing conditions and glass composition have on this ratio. This ratio will also have an effect on the waste form performance in terms of chemical durability as Fe^{2+} tends to decrease chemical durability in borosilicate glasses (Volf 1984).

In terms of processing considerations, an understanding of redox chemistry in glass compositions is very important for potential technology platform operators. Potential processing problems that can be controlled by the redox chemistry in the glass include, foaming of the melt (Goldman et al. 1986), precipitation of metals (Bickford et al. 1988) and accelerated corrosion of the refractory lining (Plodinec 1986). Schreiber (1987) study concluded that to alleviate potential problems with foaming and precipitation of metals during processing of the nuclear waste in these glass melts, the Fe^{2+} / Fe^{3+} ratio of the melt should be between 0.1 and 0.5. This value will be determined in these studies via Mössbauer spectroscopy within this body of work.

2.5 Thermal treatment technology platforms

This section of the literature review with give a brief overview of the currently available thermal treatment technology platforms, for a more in-depth review of the application of thermal technologies for processing radioactive waste the author is referred to IAEA

(2006), Chapman et al. (1986) and Ojovan (2005). No single waste form or process is suitable to economically handle the total clean-up of the UK's nuclear legacy waste, with which the NDA faces. It is important to examine the key factors influencing the selection of thermal technologies as part of the NDA national waste management strategy. This section will concentrate on joule and plasma heating, as these two thermal treatment processes have been utilised in full scale thermal treatment plants processing radioactive waste.

2.5.1 Joule heating

Joule heating depends on the transfer of heat energy to a material from the resistance of an electric current flowing through that material. This dissipated power is predicted by Joules law:

$$P = I^2 R$$

P = Dissipated power (watt W), I = Current through the material (amps A), R = Resistance (ohms Ω)

This shows that if the current can be maintained then an increase in electrical resistance will result in additional power being dissipated in the form of thermal energy resulting in the material heating more rapidly. Importantly to the operator, unless the voltage is increased, an increase in resistance will also decrease current, as predicted by Ohm's Law:

$$R = V/I \text{ or } V = IR$$

$$V = \text{Voltage (volts V)}, I = \text{Current and } R = \text{Resistance}$$

Several properties of glass impact the joule heating process, with Jantzen (1995) providing a detailed account. Among these properties is glass has poor electrical conductivity (high resistivity) as a solid, however as temperatures pass the liquidus temperature the resistance falls. This is due to the breakup of the glass structure allowing ions in the silica framework to be much more mobile (Shelby 2005), increasing the ability to carry the electrical charge. In terms of processing parameters, melt viscosity is considered the most important. Viscosity controls processing rate, glass homogeneity and heat transfer within the molten glass by controlling the strength of convection currents within the melt (Orfeuil 1987). Viscosity is modified by changing the feed composition or process temperature. This is an important point for operators of melter technology such as the GeoMelt system, as an increase in temperature can increase the performance of the

vitrified product through increased homogeneity due to an increase in convection currents, however it is known that an increase in operating temperature can also volatilise radionuclides resulting in poor retention within the glass matrix. There are a number of variations to induction melters including cold crucible induction melting (CCIM) (Sugilal 2008).

2.5.2 Plasma Vitrification

Plasma vitrification uses extremely high temperatures in an oxygen starved environment to completely decompose waste material enabling plasma facilities to treat a large number of waste streams safely. Radioactive waste vitrification exploits the plasma's ability to rapidly initiate a variety of chemical reactions including decomposition and oxidation (Moustakas et al. 2005). The author is refereed to Gomez et al. (2009) for a comprehensive review of plasma treatment of waste. This section provides relevant operational experience of plasma treatment of PCM and LLW with particular attention to radionuclide partitioning and off gas considerations.

Tetronics have demonstrated the use of plasma vitrification to treat simulant PCM waste (Deegan 2004). Full oxidation of the PCM feed was attempted with an operating temperature was 1600 ℃, with the aims to volatilise the organic component whilst oxidising the metallic fraction. The Hyatt et al. (2006) study characterises the resultant vitrified product which had a glassy appearance with noticeable porosity. Porosity is a disadvantageous characteristic of a vitrified waste form as a porous structure increases the area from which chemical dissolution can occur, potentially increasing the rate at which radionuclides are released. The porosity and fraction of crystalline components was observed to increase with increased waste loading of PCM simulants. CeO_2 (as a Pu surrogate) was found to be incorporated in the slag phase at 90 % of the initial inventory. PCT experiments were used to determine the dissolution of the vitrified slag, with results showing no Ce detected in solution. Despite the relevant success of the vitrification trials in terms of incorporation of Ce and the apparent durability of the vitrified product, there were concerns relating to the off gas emission, expressed by Deegan (2007) study. These concerns arise from the high PVC content which, upon volatilisation, result in the possibility of enhanced cerium volatility through the formation of oxychlorides.

2.5.3 Hot isostatic pressing

A brief overview of hot isostatic pressing is presented here. HIP essentially applies high temperature and pressure simultaneously to densify and remove porosity from materials. Atkinson (2000) provides an overview of HIPing, which the reader is referred to for more information. Figure 2.7 shows that the HIP utilises a furnace (maximum temperature up to 2200 ℃) contained within a pressure vessel (maximum pressure 300 MPa). The HIP process densifies the material through sintering of the bulk material. The added pressure to the system improves densification further by forcing the particles together which promotes the formation of grain boundaries by providing an opposing force to the internal pressure of the porosity Kinger et al. (1976).
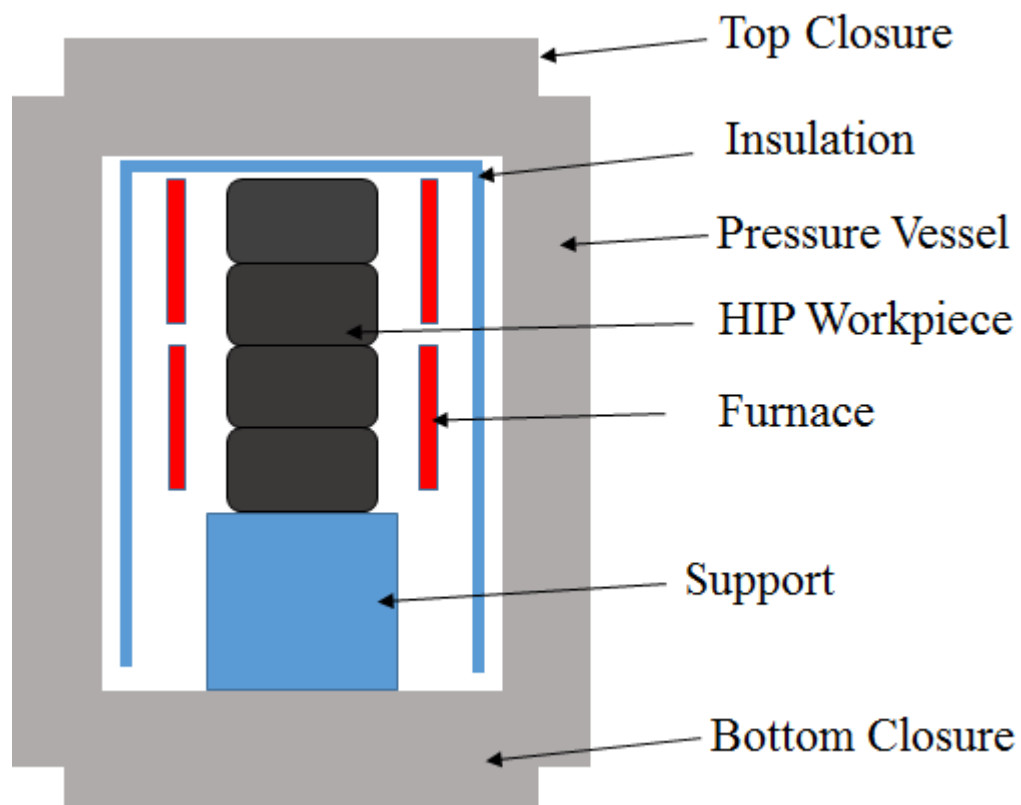
Figure 2.7 Schematic of HIP unit for nuclear application. Figure adapted from Maddrell (2013)

There are a number of distinct advantages to HIPing radioactive waste, these include (Maddrell 2013):

- HIP has a wide processing window allowing suitability for processing a number of waste streams generating minimal secondary waste
- Unlike JHCM, HIPing is insensitive to the physical, electrical and thermal properties of the waste form.
- The major benefit as opposed to other thermal treatment systems is that the process is consolidated meaning no volatile losses.

For these reason there are a number of active HIPing facilities currently under development for processing a number of waste streams including, ILW liquid waste resulting from [99]Mo production at ANSTO (Carstens et al. 2014).

2.6 Summary

This section has shown the clear advantages to vitrifying radioactive waste, including large volume reductions, long term durability and increased stability of the vitreous waste form. A large amount of fundamental research has been performed during the last 20 years in the area of glass science which is applicable to the thermal treatment of higher activity radioactive waste. The radioactive waste management industry is now recognising that a baseline waste treatment method of cementation is unsuitable for a large number of problematic waste streams. This has led to a large investment in a number of thermal treatment technology platforms, including the recent partnership between NNL and Kurion (Chapter 6). To support this level of investment, a fundamental understanding of waste incorporation during thermal treatment needs to be established. This project utilises the previous work performed, as covered in this chapter, to aid with glass formulations to vitrify a number of higher activity waste streams. The work performed will be compatible with currently available technology platforms, providing the scientific understanding to progress a number of thermal treatment processes further along the technology readiness level (TRL). The research will also gain an understanding of the long term performance of the vitrified waste form. This will provide a strong safety case, allowing disposal within the UK's planned GDF.

3 EXPERIMENTAL METHODS

3.1 PCM laboratory scale experiments

Four bounding waste streams were used in the project to represent the spectrum of PCM waste streams found at the Sellafield site, defined as masonry, organic, metal and mixed waste streams. Section 2.1.1 describes how PCM waste is stored, but to recap, the contaminated material is firstly double bagged in heat sealed PVC linings before being stored in 200 L mild steel drums. Each steel drum weighs 20 kg and is expected to be packed with 25-80 kg of PCM waste, depending on the nature of the waste, and is limited to a total overall safety limit of 100kg (Egan 2008).

Table 3.1 shows representative PCM waste simulants based on previous studies by Bingham (2010). Table 3.2 lists the individual PCM waste components.

Weight %	PVC	Metals	Masonry	Mixed
Mild Steel	44.44	20.00	30.00	30.00
PVC	55.56	10.00	10.00	10.00
Metal Items	0	70.00	0	15.00
Masonry Waste	0	0	60.00	40.00
Glass	0	0	0	5.00
Total	100.00	100.00	100	100

Table 3.1 Representative PCM simulant waste

PCM Waste Component	Constituent	Weight %
Metal items	316 Stainless Steel	96.5
	Aluminium	1.0
	Copper	0.5
	Lead	2.0
Masonry waste	Masonry, crushed	95.0
	Windows glass	5.0
PuO_2	CeO_2 surrogate	1.043

Table 3.2 List of individual PCM components

3.1.1 Plutonium (Cerium) Content

The projected PuO_2 contents of PCM wastes are expected to have an average value in the region of 33 g Pu per 200 L drum, making an average of 0.165 g/L (Hyatt et al. 2006). Criticality limits dictate that the upper PuO_2 content of the PCM waste is no greater than 230 g PuO_2, equivalent to 0.32 wt% PuO_2. CeO_2 was used as a PuO_2 surrogate, information regarding justification for this decision can be found in section 2.1.2.

The abundance of PuO_2 in PCM waste is inherently low (<1.0 wt. %). A key aim of the project is to accurately determine the partitioning of Ce between different phases within the final waste form, therefore over-doping of CeO_2 was carried out. This provided a conservative approach, effectively representing the highest conceivable PuO_2 content. This approach assisted the detection and quantification of CeO_2 by analytical methods (particularly XRF and SEM/EDS).

Assuming a molar equivalent of PuO_2 by CeO_2, the upper estimated limit of 230 g Pu per 80 kg drum equates to 0.207 wt% CeO_2. To meet the aims of the project, as stated above, five times the amount of CeO_2 was used. Therefore all melts were doped with 1.043 wt% CeO_2 as a PuO_2 surrogate.

3.1.2 Waste form and Process Formulation Criteria

An aim of this work is to develop a set of formulation criteria based on the physical and chemical properties of the raw waste and match these to generic waste form types. The formulation criteria were;

High Metal Content – Due to the high metal content of the PCM waste, as shown in Table 3.1, a mixed metal / oxide waste form was aimed for initially, but with optimisation studies performed to attempt full oxidation of the system following initial trials.

Pu Partitioning – Pu is largely insoluble in steel and is expected to transfer into the oxide (slag) fraction (Strachan 2001).

Thermal Processing – Metal components should be molten during processing in order to maximise volume reduction and assist the transfer of Pu and subsequent distribution throughout the oxide material. The Fe-Cr-C phase diagram shows that, depending on the carbon content of the steel, the liquidus temperature (T_{liq}) varies from approximately 1548°C for pure Fe to 1150°C at 4.3 wt.% carbon (eutectic point). If the raw waste components are to be molten a target temperature of at least 1500°C should be aimed for. One of the aims of the study is to lower this processing temperature to optimise the process.

3.1.3 Oxide Waste Fraction

In the absence of glass forming oxides within the waste itself, a glass forming additive must be added prior to, or during processing. In this study a ratio of 1g of additive to 1g of PCM waste (including the drum) was used.

Previous work (Hyatt et al. 2014), effectively used ground granulated blast furnace slag (GGBS) as a glass forming additive, vitrifying the waste at 1560°C.

This study used recycled commercial soda – lime – silica (SLS) as the glass forming additive sourced from Specialist Aggregates. Unlike GGBS, SLS is a low cost cullet and is widely available. This family of glasses is also used in the immobilisation of high level waste therefore the physically and chemical properties are very well understood. Table 3.3 shows the composition of the GGBS and SLS aggregate.

Component Wt %	GGBS	SLS
SiO_2	35.7	70.77
Al_2O_3	13.2	1.57
Na_2O	0.2	13.27
K_2O	0.4	0.62
MgO	8.8	1.5
CaO	39.7	10.16
Fe_2O_3	0.3	0.36
MnO	0.5	0.05
TiO_2	0.5	0.05
SO_3	0.8	-
Total	100.1	98.35

Table 3.3 Composition of GGBS and SLS additive

3.1.4 Product quality assessment criteria.

To ensure the quality of the waste form reaches the standards imposed by the criteria, the following assessment criteria were agreed upon.

1. PuO_2 (CeO_2 surrogate) from the PCM should be physically and chemically immobilised in the resulting materials
2. No residual waste remains following processing
3. No reactive products remain following processing (thermodynamically stable)
4. No adverse waste / matrix reaction occur during or following processing.
5. Resulting waste forms are sufficiently durable
6. Significant volume reduction is achieved

3.1.5 Prototype Waste form Development

The PCM wastes were simulated using the most appropriate materials. The same representative materials as used in previous studies (Hyatt et al. 2014) were used, as these

waste simulants closely represents the make-up of PCM waste. The waste containers, PVC bags and PCM simulants selected are shown in Table 3.4.

PCM Simulant Component	Source	Details
Mild steel can + lids	Fenton Packaging Ltd, Bridge street, Morley, LS27 0LE	Mild steel, unlined small paint can + lids
PVC Sheeting	Romar Workwear Ltd, Ivy Mill, Main Street, Hensingham, Whitehaven, Cumbria, CA28 8TP	PVC sheeting identical to that used on Sellafield site to bag PCM.
316 Stainless Steel	Avus Metals, Unit 7 Enterprise Park, Woodbourn Road, Sheffield S9 3JL	Commercial grade
Aluminium		
Copper		
Lead	Airgun Spares, Hillside, Shawbury Lane, Shustoke, Warwickshire B46 2RR	Lead shot pellets
Borosilicate lab glassware	Pyrex ® glass labware	Commercial grade
Crushed masonry + concrete	Core drilling from the Hadfield building	Mixed, crushed masonry waste using TEMA milling machine
Window glass	Hadfield building	Discarded window pane glass
CeO_2	Acros Organics	>99.9% purity

Table 3.4 PCM waste simulant components, suppliers and details

3.1.6 PCM simulant experimental setup

PCM simulants and additives were weighed out according to the calculated waste composition shown in Table 3.1. The actual composition of the PCM waste simulants are shown in Table 3.5. B_2O_3 was also added at 1wt% to act as a tracer element during later dissolution experiments.

Weight (g)	PVC	Metal	Masonry	Mixed
Mild steel	41.1	41.4	41.3	41.1
Metal items	0	144.0	0	20.5
Masonry waste	0	0	82.6	54.7
Glass (Pyrex®)	0	0	0	6.8
PVC sheeting	51.5	20.7	13.8	13.7
CeO_2	0.948	2.143	1.433	1.416
B_2O_3	0.916	2.081	1.385	1.373
Sub-total	91.6	208.1	138.5	137.2
Glass frit additive	91.9	208.1	138.8	137.3
Total weight	182.6	416.1	275.9	274.6
Crucible	610.0	1035.6	574.7	499.5
Total weight inc. crucible	792.6	1451.7	850.5	774.1

Table 3.5 Actual weights used for PCM simulants
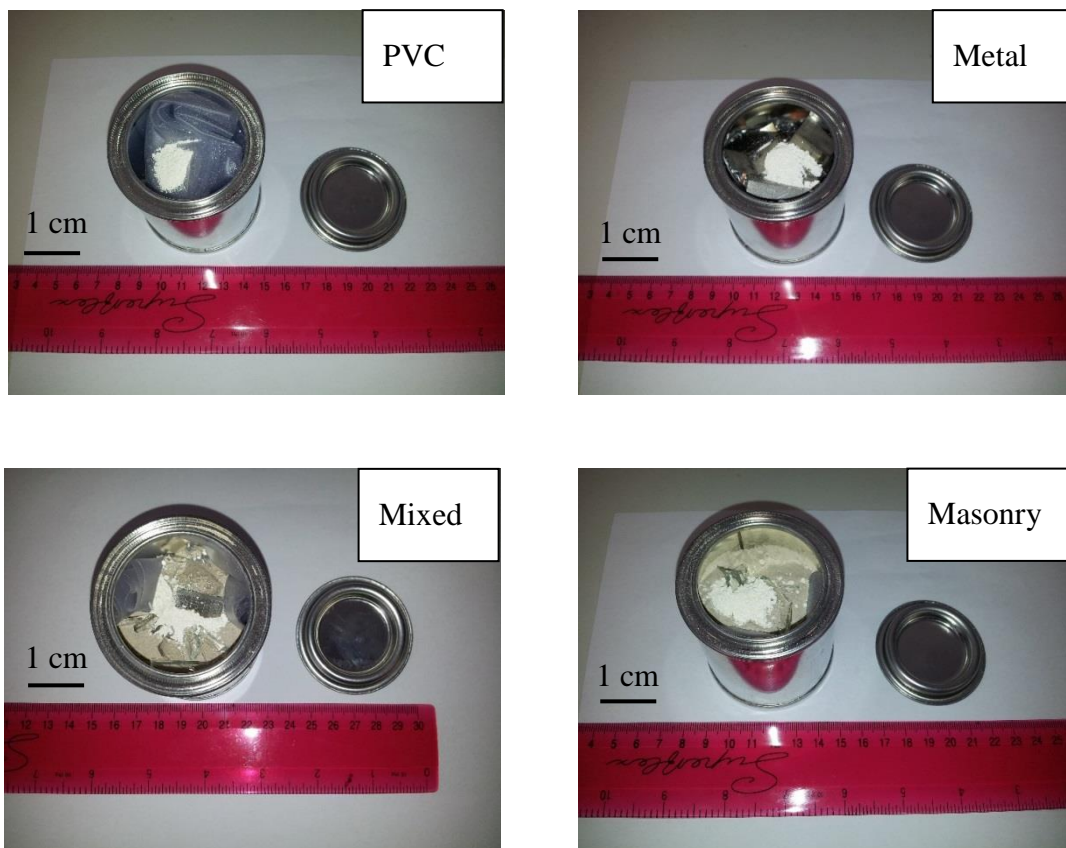
Figure 3.1 Representative PCM mock up drums with simulant waste (Top Left)
PVC, (Top Right) Metal, (Bottom Left) Mixed and (Bottom Right) Masonry.

Figure 3.2 PCM simulants plus SLS additive prior to thermal treatment. The black
crucible is a graphite/clay composite crucible.

Figure 3.1 shows the experimental set-up of the representative PCM waste prior to
thermal treatment. The paint tin cans were used to represent the 200 L drums found at

Sellafield. These were pierced to allow PVC combustion gas egress early in the thermal cycle and thereby avoid potentially dangerous explosive releases. The metal waste stream, was contained within a graphite / clay crucible called a Plumbago crucible, as shown in Figure 3.2. This was due to the high corrosive nature of the metal waste stream at high temperatures during the glass melt.

3.1.7 Thermal Treatment process

Crucibles containing the additive and waste, as shown in Figure 3.2, were placed in an electric muffle furnace and preheated overnight at 2°C per minute to 1100°C. The crucibles were held at this temperature for 8 hours until they were transferred to a gas fired furnace which had been preheated to 1100 ± 25°C. The gas fired furnace was ramped to 1560°C ± 25°C over a period of 90 minutes. The crucibles were held at 1560°C for 4 hours, this amount of time is necessary to ensure that the glass/ceramic fraction is homogenised and that the CeO_2 is fully incorporated and evenly distributed within the glass fraction of the waste form. The preheat step was to avoid thermal shock of the alumina crucibles. Temperature measurements were verified using an optical pyrometer throughout the melting procedure. Crucibles were removed from the furnace, as shown in Figure 3.3, and allowed to cool in air, as shown in Figure 3.4.

Figure 3.3 Crucibles removed at 1560ºC from gas fired furnace
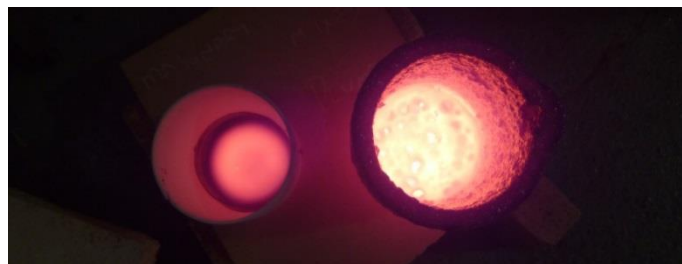
Figure 3.4 Crucibles allowed to cool in air once removed from the furnace

3.2 Product and Process optimisation

A key aim of the project is to evaluate waste forms against product quality criteria and to develop and implement a plan for process and product optimisation, based on the fundamental understanding of waste / additive interactions during thermal treatment. This was achieved with the help of various meetings with industrial stakeholders within the project including NDA and NNL. The main areas of optimisation that were explored were, lowering processing temperature and full oxidation of waste form.

3.2.1 Lowering processing temperature

Section 3.1.2 explains that due to the high content of metallic material, and the need for the raw material to be molten, a suitable processing temperature should be above 1500°C. From previous studies a reasonable starting temperature of 1560°C was agreed. Lowering this processing temperature provides a number of advantages including radionuclide retention and also lowers the risk of volatilisation issues. From an operators point of view a lowering operating temperature equates to greater longevity of the refractory material and other components.

3.2.2 Oxidation of metal components

Section 3.1.2 also states that due to the high metal content of the PCM waste, it is unlikely that a fully oxidised waste form could be achieved and that a mixed metal/oxide waste form would be suffice. There are a number of benefits to achieving a fully oxidised waste product. A completely oxidised waste form provides a homogenous, monolithic waste form as opposed to a mixed slag / metal system. The long term performance of the homogenous waste package can be confidently modelled and predicted enabling a strong safety case to be built for disposal. However, the long term behaviour of a mixed system would be difficult to predict and model, with the interactions of the corrosion products of the metal and the slag material needing careful consideration. Fully oxidising the high metallic waste streams also avoids any further processing to separate the slag and metal phase, which has not yet been demonstrated in an active context. After consultation with industrial stakeholders it was decided that iron oxide in the form of Fe_2O_3 would be used as an additional additive to act as an oxidising agent for the metal content within the PCM waste.

The amount of Fe_2O_3 to be added should be kept to a minimum to achieve maximum volume reduction. It was agreed that enough Fe_2O_3 should be added to target the metal fraction post processing.

Fe_2O_3 was added at a 1:1 molar ratio with the expected metallic fraction obtained in the previous melt, plus 10wt% of that amount as a margin of conservatism to permit complete oxidation.

Based upon previous studies (Hyatt et al. 2014), it is expected that certain waste streams with a relatively low metallic content will produce a fully vitreous product. If this is the case and no metallic fraction is produced, a 1:1 molar ratio of Fe_2O_3 to the metallic drum will be added to ensure a common process for all waste streams, regardless of the metal content.

3.2.3 Small Scale PCM melts experimental setup

For proof of concept studies it was decided to perform the experiments on a smaller scale using 200ml crucibles. The exact same composition was used as previous melts just scaled down to 200ml crucible size (28.57% of original weight of components). The following materials were used to represent the PCM waste at a smaller scale as shown in Table 2.1. The first sets of melts were performed without the addition of Fe_2O_3 to determine the expected metallic fraction. The composition for both sets of experiment (with/without Fe_2O_3) is shown in Table 3.6.

Due to the size of the crucibles, coupled with the thermal processing temperature agreed at 1450°C, an electric muffle furnace was suitable for this set of experiments. The crucibles were heated to 1450°C at 3°C per minute. The crucibles were held at 1450°C for 4 hours before being removed and left to cool in air. 200ml Plumbago crucibles were used for the high metal content in the first melt trials. Since the aim of the experiment was to oxidise the metal content for optimisation purposes, alumina crucibles were used following initial proof of concept trials. The reason for this is the graphite clay composition of the plumbago crucible induces a reducing atmosphere which would be undesirable when attempting to oxidise the metallic content.

Weight (g)	PVC No Fe_2O_3	PVC with Fe_2O_3	Metal No Fe_2O_3	Metal with Fe_2O_3	Masonry No Fe_2O_3	Masonry with Fe_2O_3	Mixed No Fe_2O_3	Mixed with Fe_2O_3
Stainless steel	11.57	11.57	11.74	11.74	11.57	11.57	11.74	11.74
Metal items	0	0	41.29	41.29	0	0	5.78	5.78
Masonry waste	0	0	0	0	22.00	22.00	14.86	14.86
Glass	0	0	0	0	1.17	1.17	0.83	0.83
PVC sheeting	14.45	14.45	5.91	5.91	3.85	3.85	3.91	3.91
CeO_2	0.27	0.27	0.67	0.67	0.40	0.40	0.40	0.40
B_2O_3	0.26	0.27	0.64	0.64	0.39	0.39	0.39	0.39
Sub-total	26.29	26.29	60.10	60.10	38.59	38.59	39.85	39.85
Glass frit	26.29	26.29	60.10	60.10	38.59	38.59	39.85	39.85
Fe_2O_3 [*]	-	9.11	-	97.96	-	32.85	-	11.19
Total weight	52.58	61.69	120.20	218.16	77.59	110.44	79.70	90.89
Crucible	157.63	153.7	166.90	163.5	133.96	163.60	173.56	160.87
Sub total	210.20	215.39	287.90	381.66	210.65	274.14	222.67	250.80

Table 3.6 PCM waste simulants at 200ml scale with addition of Iron Oxide

* Fe_2O_3 was calculated from amount of metallic content from the melt with no Fe_2O_3. A 1:1 molar ratio of Fe_2O_3 to the metallic content was added to the batch. If the melt resulted in no metallic fraction then Fe_2O_3 was added at a 1:1 molar ratio with the PCM waste drum (masonry waste).

3.3 Overview of PCM mock up vitrification trials

Table 3.7 gives a general overview of the PCM vitrification trials as described in 3.1.5. The difference between the three melts are the type of crucible used and the operating temperature.

Melt Number	Crucible type	Operating temperature	Samples
Melt 1	Alumina classic	1560°C	Melt 1 – PVC
	Alumina classic	1560°C	Melt 1 – Masonry
	Plumbago	1560°C	Melt 1 – Metal
	Alumina classic	1560°C	Melt 1 – Mixed
Melt 2	Alumina tapered edge	1560°C	Melt 2 – PVC
	Alumina tapered edge	1560°C	Melt 2 – Masonry
	Plumbago	1560°C	Melt 2 – Metal
	Alumina tapered edge	1560°C	Melt 2 – Mixed
Melt 3	Alumina tapered edge	1450°C	Melt 3 – PVC
	Alumina tapered edge	1450°C	Melt 3 – Masonry
	Plumbago	1450°C	Melt 3 – Metal
	Alumina tapered edge	1450°C	Melt 3 – Mixed

Table 3.7 General overview of PCM vitrification trials as described in section 3.1.5)

Table 3.8 gives a general overview of the PCM vitrification trials as described in 3.2.3. PC = plumbago crucible and AC= alumina crucible.

Melt	Crucible type	Details of Work package	Samples
Melt 1 (small scale)	Alumina 200 ml	1450°C operating temperature. 1:1 wt. % glass frit additive to waste components. Waste components small particle size fraction (>1mm)	SSM1 – PVC
	Alumina 200 ml		SSM1 – Masonry
	Alumina 200 ml		SSM1 – Mixed
	Plumbago 200 ml		SSM1P- Metal (PC)
	Alumina 200 ml		SSM1A- Metal (AC)
Melt 2 (small scale)	Alumina 200 ml	1450°C operating temperature. 1:1 wt. % glass frit additive to waste components. Waste components small particle size fraction (>1mm) Fe_2O_3 added at 1:1 molar ratio with metallic fraction of SSM1.	SSM2 – PVC
	Alumina 200 ml		SSM2 – Masonry
	Alumina 200 ml		SSM2 – Mixed
	Plumbago 200 ml		SSM2 – Metal

Table 3.8 General overview of PCM vitrification trials as described in section 3.2.3

3.4 Glass formulations to effectively condition and immobilise UK ILW – Contaminated Masonry Waste

Section 3.1.3 explains the use of additives to act as oxidising agents within the melt, however, a large number of ILW streams already contain large amounts of SiO_2 within the waste itself, which could potentially be used as a glass forming oxide to aid with vitrification. Therefore some, or possibly all, of the SiO_2 in the vitrified product could originate from the ILW itself. Section 2.3 describes the properties of glass, which makes it an excellent medium for waste immobilisation. The ability to incorporate a large number of elements into the glass structure is particularly important for this project as few legacy and intermediate level wastes are as closely controlled in their chemical and physical makeup as HLW. This section of the project evaluates whether contaminated

masonry waste from decommissioned silo ponds, in the form of concrete scabblings, contains enough SiO_2 to aid vitrification and produce a durable, passive glass waste form.

3.4.1 Materials

To represent contaminated concrete in the form of pond scabblings from decommissioned silo ponds, core drillings were sourced from the recent buildings work taking place on the Sir Robert Hadfield Building, Mappin St, Sheffield, South Yorkshire, S1 3JD, as shown in Figure 3.5.

Figure 3.5 Core drilling from Hadfield building works to represent concrete waste

Using a TEMA mill, the core drillings were reduced to a fine powder as shown in Figure 3.6.

Figure 3.6 Concrete waste from Hadfield building milled to small particle sized powder

The powdered concrete as shown in Figure 3.6 was sent for XRF analysis to determine the composition of the material, in particular the amount of SiO_2 within the masonry waste. Due to the vast amount of research performed, it was decided that a sodium borosilicate system would be aimed for when vitrifying the masonry waste, using additions of boric acid and sodium carbonate. Donald (2010) and Ojovan (2005) provide

an excellent overview of vitrifying radioactive waste using a borosilicate system. When considering glass formulations to vitrify masonry waste it is important to consider the following parameters:

Minimise amount of additive – It is desirable to vitrify as much masonry waste as possible to increase waste loading. Therefore a system with as high a content of SiO_2 as possible should be aimed for with minimal use of other glass forming additives.

Minimise melting Temperature – To avoid volatilisation of radionuclides, temperatures above 1100°C should be avoided.

Viscosity – To assist with the thermal treatment process, it is important to maintain low melt viscosity.

Based on the requirements above, five varying compositions from the sodium borosilicate system were selected as shown by the numbered points (C1-C5) in Figure 3.7.
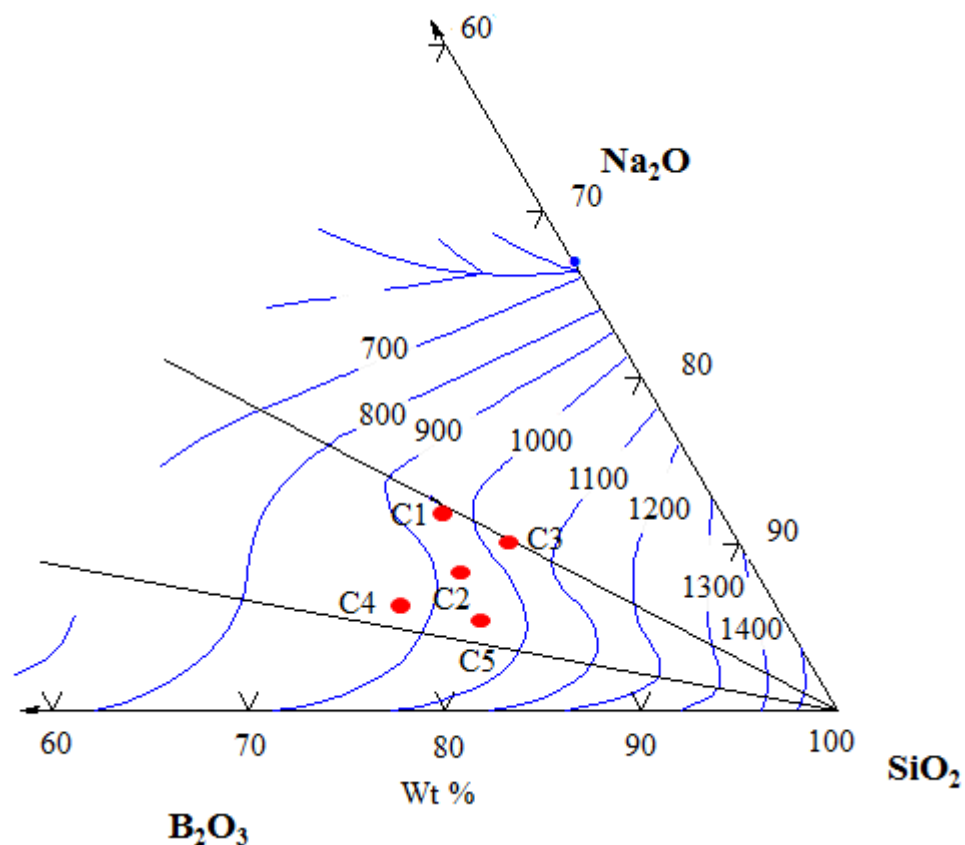
Figure 3.7 Modified version of the sodium borosilicate ternary system generated from thermos-calc phase diagram software, used to formulate glass composition. Numbers show selected compositions in Table 3.10.

Composition	SiO$_2$ (wt. %)	B$_2$O$_3$ (wt. %)	Na$_2$O (wt. %)
C1	68.0	18.0	14.0
C2	69.4	18.7	12.6
C3	72.0	15.0	13.0
C4	68.0	22.0	10.0
C5	72.0	19.0	9.0

Table 3.9 Composition selected and tested.

The masonry waste used in this project is assumed to be representative of contaminated masonry waste removed from decommissioned silo ponds in the form of scabbled concrete. The exact composition of the scabbled concrete from the silo ponds found at Sellafield is not yet available. However, it is likely to be a conventional Portland matrix. The main source of radionuclides is from the decay of spent fuel stored in the silo ponds, classified as fission products, this contaminates the concrete lining of the silo ponds. When considering suitable simulants to provide realistic behaviour of a radioactive element, an inactive isotope of that element can be considered. Senior (2013) states that ^{137}Cs is contained within the first 5 mm depth of the surface. The chemical and physical effects of ^{90}Sr, ^{137}Co and ^{137}Cs can be safely simulated using their naturally occurring stable isotopes. It is known from the NDA waste inventory that these radionuclides are present within the contaminated masonry waste as shown in Table 2.2. Although not listed as a contaminant within the scabbling waste (Table 2.2), UO$_3$ was used to provide a realistic representation of radionuclide behaviour in the glass, these would allow representation of the effect of sample irradiation due to radioactive decay (McGann et al. 2012). In order to maintain a conservative approach the masonry was doped with one part simulants/ actinides to 100 parts masonry waste. The simulant radionuclides and UO$_3$ were milled together and mixed with 8.64g of masonry waste. This gave a 3:1 ratio of masonry waste to simulant and UO$_3$. Masonry waste was used to dilute the contaminated masonry waste to provide a ratio of 1 part simulants to 100 parts masonry waste. Composition 1 and 2 were doped with the contaminated masonry waste to give samples CM1 (Contaminated Masonry waste 1) and CM2 (Contaminated Masonry waste 2).

Using the composition of the masonry waste, and with the glass forming oxides used, the expected compositions of the glass samples are shown in Table 3.10.

	Component	Oxide	C1	C2	C3	C4	C5	CM1	CM2
Base Glass	H_3BO_3	B_2O_3	18	18.7	15	22	19	18	18.7
	Na_2CO_3	Na_2O	14.1	12.68	13.1	10.1	9.1	14.1	12.68
Simulant		SiO_2	52.39	53.53	55.48	52.39	55.48	52.29	53.53
Waste		CaO	5.81	5.93	6.15	5.81	6.15	5.79	5.93
		Al_2O_3	2.35	2.4	2.49	2.35	2.49	2.34	2.4
		Fe_2O_3	0.83	0.85	0.88	0.83	0.88	0.83	0.85
		UO_3	0	0	0	0	0	0.05	0.05
		SrO	0	0	0	0	0	0.02	0.02
		Co_3O_4	0	0	0	0	0	0.05	0.05
		Cs_2O	0	0	0	0	0	0.06	0.06
		Other	5.79	5.16	6.12	5.79	5.67	5.74	4.98
Total			100	100	100	100	100	100	100

Table 3.10 Elemental compositions of seven vitrified masonry waste glass compositions (wt. %), including base glass, simulant waste components and total wt. % of waste loading.

3.4.2 Methods

The raw materials shown in Table 3.12 were mixed together in a plastic bag before 20ml crucibles were filled to below 1cm of the crucible with the composition shown in Table 3.10. The crucibles were heated at 4°C a minute to 300°C then held at this temperature for 30 minutes. The furnace was then ramped to 1100°C at 4°C a minute then held at 1100°C for 4 hours. The pre heat treatment at 300°C was required to avoid thermal shock of the crucibles. The molten glass was then poured into a cylindrical mould (6cm in diameter) to produce cylindrical glass samples. The glass was then allowed to anneal at 500°C for 1 hour before ramping down to room temperature at 1°C a minute.

3.5 Chemical Durability

3.5.1 Introduction

An accelerated static chemical durability test was used to assess the long term aqueous durability of a selection of the glasses reported in this thesis, based on the American Society for Testing and Materials (ASTM C1285-02 2002). The glass was prepared by crushing in a TEMA mill. The crushed glass was then sieved to 150-75 µm particle size fraction. Details for cleaning glass powder and vessels prior to dissolution experiments can be found in Appendix 1.

Monolithic samples were sectioned using a Buehler IsoMet ® low speed saw with a Buehler Series 15 LC wafering blade, lubricated with Buehler IsoCut ® fluid. The monoliths were cut to the required size of 10 x 10 x 5 mm. The sectioned glass samples were then ground using silicon carbide abrasive paper, to a surface roughness of P1200 (European P-Grade). The polished samples were then cleaned ultrasonically for 5 minutes in UHQ water. The samples were then cleaned ultrasonically in isopropanol for 5 minutes. After cleaning, the powdered glass and monolith glass were stored in desiccator until they were required.

3.5.2 Product Consistency Test B (PCT-B)

The product consistency test (PCT) is an international standard static leaching test designed to assess the durability of nuclear waste glasses and multiphase ceramics. The test uses powdered samples and is governed by ASTM International standards. There are

two variations of the PCT experiment, A and B. PCT-B allows for a range of temperatures, durations, particle size distribution, leachate compositions and test vessel materials. For the purpose of this investigation PCT-B was deemed most suitable and was used to assess the durability of the samples produced in all of the results chapters in this thesis.

To simulate the hyperalkaline conditions of a UK cementitious Geological Disposal Facility (GDF), saturated calcium hydroxide solution was used (Snellings 2013). To avoid carbonation of the test, the experiments were run under a nitrogen atmosphere. To achieve this without the use of an expensive environmental oven, a stainless steel airtight container was designed and fabricated to house the samples whilst dry nitrogen was passed through the container. It was decided that each stainless steel container would be big enough to house eight 1L HDPE vessel which equates to two separate glass dissolution experiments (three triplicate samples and one blank).

The following dimensions for the stainless steel container, Figure 3.8, were agreed upon to ensure eight 1L bottles would fit inside allowing two sets of dissolution experiments to be carried out per stainless steel container.
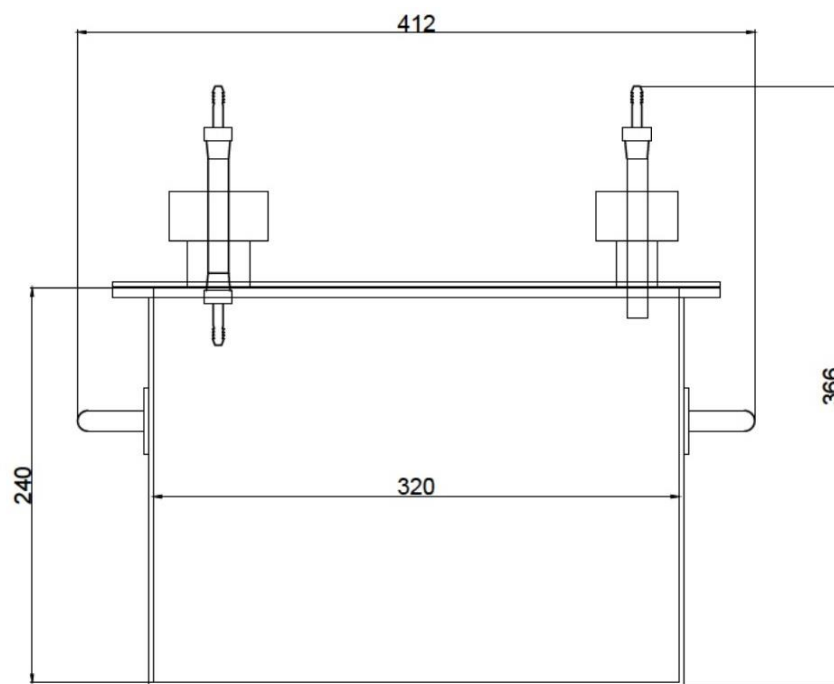
Figure 3.8 Dimensions of fabricated stainless steel drum to house eight 1L HDPE vessels, all measurements shown are in mm. Steel vessel has diameter of 320mm. Dimensions of eight 1L HDPE vessels shown with room for inlet tubing (filled circle).

The dimensions were such that it could fit within a 100L general purpose oven. Six stainless steel containers fabricated by CS Press Tools to the authors design, and six general purpose ovens were brought from Gen Lab. The fabricated steel vessels are shown in Figure 3.9, which also shows the eight 1L HDPE vessels housed within the container.
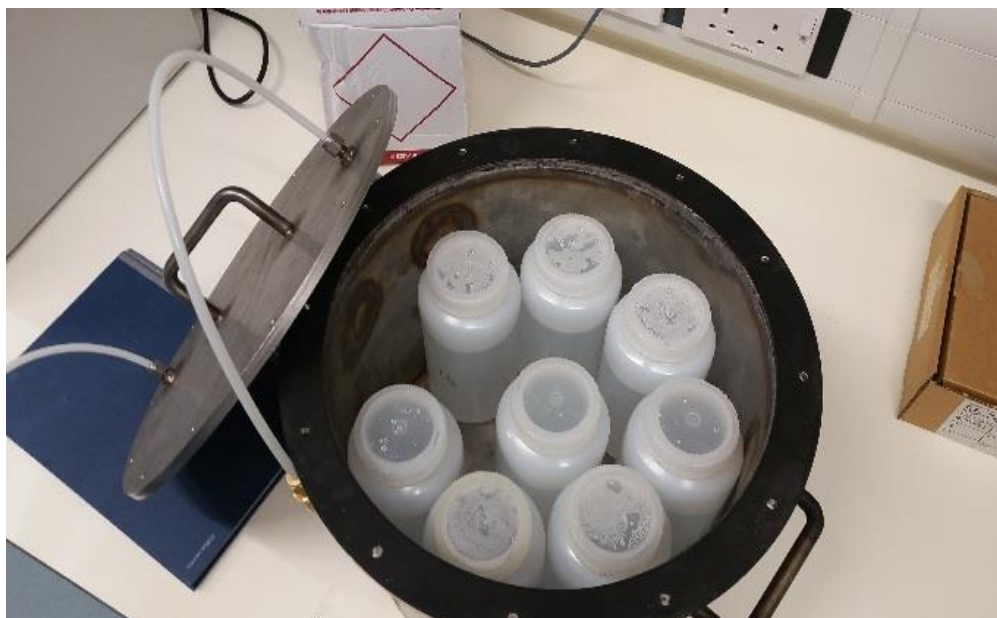
Figure 3.9 Fabricated stainless steel drum which houses eight 1L vessels for two sets of dissolution experiments

A six splitter manifold was fabricated to the authors design to carry nitrogen gas from the cylinder to the six general purpose ovens as shown in Figure 3.10. Inlet and outlet tubing were passed through the top of the general purpose oven and were connected to the stainless steel drums via a quick release valve. Nitrogen gas was then passed through a bubbler into the air tight stainless steel container and out through another bubbler. The lid was bolted shut with a rubber gasket between the fitting to ensure the system was airtight, this ensured the experimental conditions were under a nitrogen atmosphere. The experimental set up is shown below in Figure 3.10.

Figure 3.10 Experimental set up shown for glass dissolution experiment

Each test was carried out at 50°C with varying amounts of leachant depending on the amount of time points for solution to be taken. ASTM standards requires no more than 10% of the starting solution to be sampled. Each sample point uses 4ml of solution, so as

an example, for a 28 day PCT experiment which uses five time points, a starting solution of 200ml would be needed to ensure only 10% of the solution (20ml) was removed during the experiment. The amount of powder used for each study varied, depending on the density of the glass, to ensure a glass-surface area-to-leachant-volume ratio (SA/V) of $1200m^{-1}$.

$Ca(OH)_2$ leachant was produced by adding excess $Ca(OH)_2$ powder to UHQ water in a HDPE vessel. The vessels were then shaken vigorously in order to achieve full dissolution of the $Ca(OH)_2$ before being filtered to remove excess $Ca(OH)_2$ from solution. To ensure the solution maintained a high pH the test vessels contained an Advantec USY-1 ultrafilter unit, filled with a slurry of $Ca(OH)_2$ powder. The experimental setup for the HDPE vessels are shown in Figure 3.11. The vessels were placed inside the airtight stainless steel containers (Figure 3.9) under a nitrogen atmosphere, in an oven at 50°C.
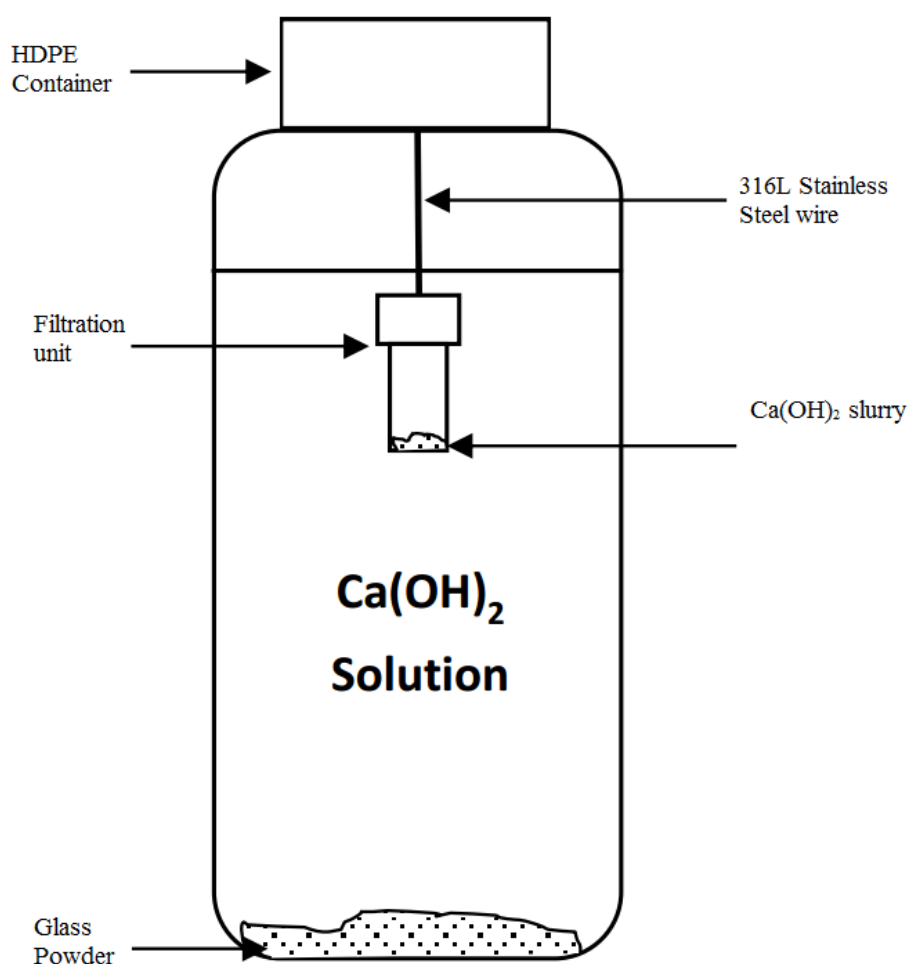
Figure 3.11 experimental setup of HDPE vessels used in PCT experiments using Ca(OH)₂ leachants. Image modified from Backhouse (2016).

For analysis, 4 ml aliquots of solution were taken at designated intervals using a FinnPipette F1 variable-volume pipettora and then filtered using a 0.22 μm polyethersulphone (PES) syringe filter. The time-points for sampling varied between the experiments, information regarding time points and duration of experiments can be found in the associated results chapter for the various samples. Before and after the removal of each aliquot, the vessels were weighed to account for any mass loss that might occur during the experiment. The filtered solution was acidified with 1 vol. % 69 % ultra-pure nitric acid, and analysed by Inductively-Coupled Plasma Optical Emission Spectroscopy (ICP-OES. The emission of characteristic photons associated with electron excitation is used to quantify elemental concentration in ICP-OES. Each element has a characteristic photon emission wavelength, the photons produced are then separated using a diffraction grating prior to detection using a photomultiplier The final signal count obtained is proportional to solution concentration and is quantified via calibration with standards of known composition. This measured the release rates of elements from the glass into solution.

Normalised mass losses and loss rates were calculated as follows. Firstly the sample concentrations were corrected for removal of liquid during sampling and testing. Mass loss in g of element i at the given time interval t (in days), m_{it}, was calculated using:

$$m_{it} = (C_{it} - B_{it})V_t$$

Where C_{it} is the concentration of element i in the aliquot in g L^{-1}; B_{it} is the concentration of element i in the blank in g L^{-1} and V_t is the solution volume, at time of aliquot removal in L. The normalised mass loss of element i, NLi, in g m^{-2} at a given time interval t (in days) is given by:

$$NL_i = \frac{m_{it}}{f_i . SA_i}$$

Where f_i is the mass fraction of element i in the glass before leaching. SA is the surface area of the initial glass in m^{2}g^{-1}. The values obtained on the triplicate samples were averaged to give NL$_i$, For convenience, the dissolution results contained within this thesis, when NL$_i$ values are given they are the mean values, NL$_i$. The normalised release rate of element i, NR_i, in g m^{-2} d^{-1}, is given by:

$$NR_i = \frac{dNL_i}{dt}$$

There are a number of error sources during analysis of dissolution rates a glass. These can include; Weighing/ volume error, error in standard concentration and instrument error. Therefore to a standard error range of ±10.25% was used for all normalised mass loss for all of the PCT data contained within this thesis.

The glass powder was analysed, post dissolution, using x-ray diffraction (XRD), to identify any secondary precipitates. SEM-EDS was also used to look at the morphology and composition of the precipitates.

3.5.3 Materials Characterisation Centre Test 1 (MCC-1)

Chapter 4 uses the MCC-1 test as part of the durability test. MCC-1 is a static leaching test designed for the assessment of the durability of monolithic waste forms for disposal of radioactive waste. It is defined by ASTM International. The test in Chapter 4 was carried out at 50°C, with a $Ca(OH)_2$ leachant. The surface area of the monolith was 400 ± mm^2 and a leachant volume of 40ml ensured the required SA/V ratio of 10 ± $0.5m^{-1}$. The vessels used for the MCC experiments were Savillex 60 ml perfluoralkoxy (PFA) Teflon standard jars. Figure 3.7 shows a schematic diagram of the experimental setup.
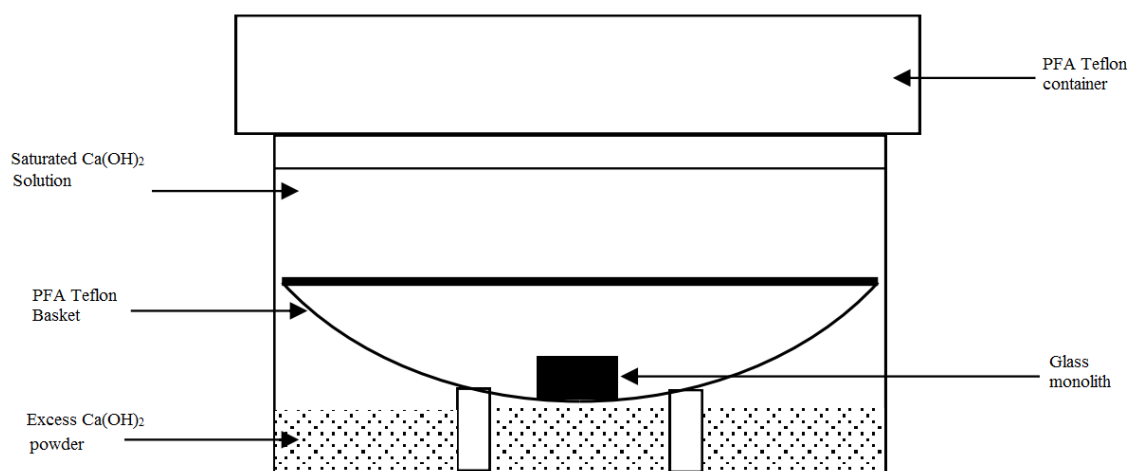
Figure 3.12 Experimental setup for MCC-1 dissolution tests. Image adapted from Backhouse (2016)

Each monolith was placed onto a PFA Teflon basket in a vessel, with 40 ml of $Ca(OH)_2$. The vessels were placed in the airtight stainless steel containers (Figure 3.9) in an oven at 50°C for 112 days. No sampling of the solution was performed as the intended purpose of the experiment was to identify any alteration products which had formed on the surface of the glass. To achieve this, the samples were gently rinsed with UHQ water, in order to

remove any remaining $Ca(OH)_2$ without washing off precipitates. The samples were then mounted in resin and ground to a P1200 grit finish before polishing to 1µm finish using diamond paste.

3.6 SEM – Scanning Electron Microscopy

White light has wavelength from 400-700 nanometers (nm), scanning electron microscopy was developed when this wavelength became the limiting factor in light microscopy. Observations of microstructure are limited in scale by the wavelength of the measuring medium. Smaller wavelength can be used to resolve smaller features. Electrons have much shorter wavelengths, enabling much better resolution.

Scanning electron microscopes (SEM) use a beam of electrons, produced at the top of the column, which are accelerated down across large voltages. Through a combination of lenses and apertures, a focused beam of electrons is directed at the sample which results in energetic electrons being released from the surface of the sample. This interaction yields information on the size, shape, texture and composition of the sample (Figure 3.13).
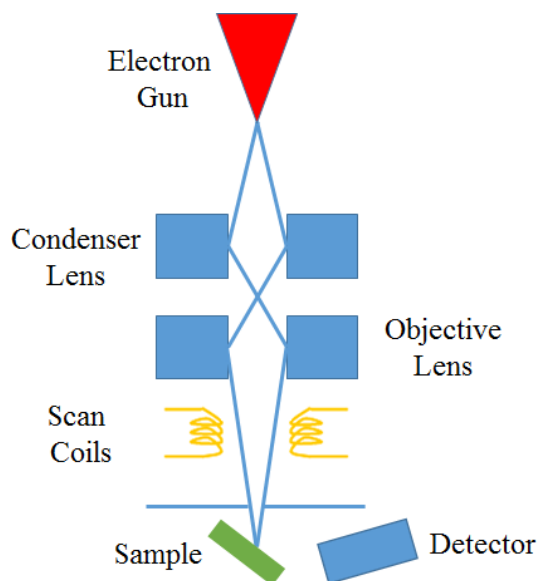
Figure 3.13 SEM schematic

When an electron of specific wavelength hits an atom:

- An electron from the inner shell (1s) is ejected.
- To stabilize the atom, an electron from an outer shell (2p) drops down to fill the vacant inner shell positon (1s).

- The electrons in the outer shell have relatively high energy compared to the inner shells, the difference in energy between the 1s electron and 2p electron is emitted as an x-ray. This X-ray has a characteristic energy related to the atom being ionised.

Therefore the characteristic X-ray can be analysed and the element of origin identified by energy dispersive X-ray spectroscopy (EDS).

SEM imaging was performed on a bench top Hitachi TM3030, which has magnification capability of x30000 with an accelerating voltage of 5-15kV. An Oxford instruments Quantax 70 EDX detector was used for microanalysis and element mapping of glass samples.

Glass monolith samples were cut using a slow saw to enable the sample to be mounted in epoxy resin. Powered samples were mixed in epoxy resin and carefully poured into 5 cylindrical moulds (3mm) within a standard epoxy mould and left to set. The remaining epoxy was carefully poured into the mould, as shown in Figure 3.14. The glass samples were sequentially polished with Silicon-carbide papers to 45µm before water based diamond pastes polished the sample to a 1µm finish.

Figure 3.14 Monolith samples mounted in epoxy resin, right: powered samples mixed with resin placed in inner cylindrical moulds before epoxy resin is carefully added.

Samples were carbon coated prior to analysis, to produce a conductive layer which inhibits charging and improves the secondary electron signal.

Three semi- quantitative EDX measurements were made throughout the crucible, near the top, in the middle, and towards the bottom of the cross sectioned vitrified waste within

the crucible. This enabled any microstructural and chemical inhomogeneity within the glass samples to be identified with respect to their location.

Metal fractions were cross sectioned, mounted and polished in the same way as the glass samples, with the obvious exclusion of carbon coating. Particular attention was made to cross section through the glass and metal interface.

3.7 X-ray diffraction

Vitrification consists of super-cooling a liquid with a high enough rate to avoid crystallisation. The detailed theoretical knowledge of nucleation, growth and crystallisation process in glass forming melts is a key issue for a number of industrial applications. Crystallisation needs to be well understood in nuclear waste vitrification for a number of reasons, one being that crystallisation can cause blockages during pouring of vitrified HLW.

In general if a molten glass is held at a temperature for a sufficient time, or cooled slower than the critical cooling rate, crystals will form in the melt. XRD is a very useful tool for detecting and identifying crystal phases within the glass samples.

X-rays are electromagnetic radiation of wavelength about 1Å (10^{-10}m), which is about the same size as an atom. When the X-rays are directed on a sample, diffraction of the X-rays occur at each crystal plane. This results in the atoms on the crystal plane acting as a scattering centre, emitting a secondary wave. All of these secondary waves interfere with each other to produce the diffracted beam. This interaction of the radiation and the crystal structure can be described by Braggs law, described below;

$\lambda = 2d_{hkl}\sin 2\theta$

Where λ is the wavelength, d_{hkl} is the interplanar spacing (distances between planes defined by the same set of miller indices) and θ is the diffraction angle.
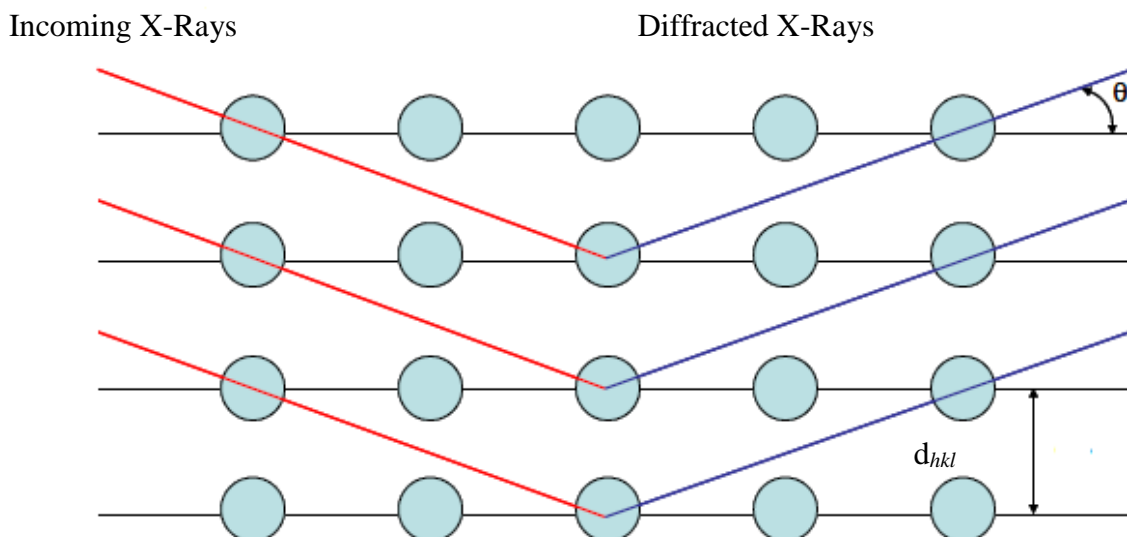
Figure 3.15 Schematic of incoming x-rays diffracting off a regular crystal lattice, demonstrating the principles of X-ray diffractometry.

If the wavelength is fixed, atoms on any particular plane will cause X-rays to be diffracted at such an angle which will correspond to a particular inplanar spacing. The wavelength can be fixed by using a characteristic radiation source such as Cu kα (1.5418Å).

Glass samples were prepared for XRD by grinding in a puck mill or grinding in a percussion mortar, based on the amount of material available. The resultant powder was sieved to a size fraction of <75µm. X-ray diffraction was performed on the powdered glass, using Bruker D2 Phaser instrument operating at 40kV and 30mA with Cu Kα radiation source (1.5418Å). The samples were scanned over the range 10-65 °2θ with a step size of 0.02 at a speed of 0.4 °2θ min^{-1}.

Analyses of the resulting diffraction patterns were performed using the Bruker Diffrac.suite EVA software package. The software is able to identify crystalline phases present (~>1 wt.%) in the X-ray diffraction patterns by comparing them against X-ray diffraction patterns in the international centre for diffraction data (ICDD) database.

3.8 X-Ray Fluorescence (XRF)

XRF was utilised regularly throughout the course of this project to identify and quantify the composition of solid samples. XRF works using the same principles as those described in Section 3.6 with the ionising radiation taking the form of an X-ray beam. The ionisation of the sample results in the emission of characteristic photons. The photons are collected

as the signal which is proportional to the elemental composition and quantification can thus be obtained via calibration with known standards.

The XRF analyser used in this project was a Panalytical Zetium. The equipment used a 4kW rhodium X-ray tube for high count rate. An advantage to using the Panalytical Zetium is its ability to quantify the amount of B in the sample, particularly useful when studying borosilicate glasses such as those synthesised in Chapter 5. Detection of low atomic mass components such as B can be problematic due to attenuation of the X-Rays in air.

If not quoted within the table of results, the errors associated with XRF analyses can be found within Appendix 2.

3.9 Density Measurements

The density of the each glass sample was determined using He gas pycnometry on powdered materials ($<75\mu$m). An AccuPyc II 1340 Pycnometer was used with 200 purges of the chamber, 50 cycles, and an equilibration rate of 0.005 psi min^{-1} at 25 °C in a 1 cm^3 chamber and a fill pressure of 12.5 psi. The estimated precision was ±0.01 g cm^{-3}. The AvvuPyc measures the density by measuring the density of gas displaced by that sample.

1. A sample of known mass is loaded into a calibrated sample chamber of known volume.
2. Gas is introduced into the chamber, which fills the void volume of the chamber including the pores of the sample.
3. The difference between the void volume of the empty chamber and the new volume with the sample, is the volume of the solid sample phase.
4. This volume is divided into sample weight, determining the density (g/cm^3)
5. Pressure vented off to atmosphere – Valve C opens.

Gas pycnometry is non-destructive and is more accurate and reproducible than the traditional Archimedes water displacement method.

3.10 Differential Thermal Analysis (DTA)

Differential thermal analysis is often used to measure the temperature difference (ΔT) between the samples under study with some reference material placed at the same

temperature and pressure conditions. DTA is used to measure endothermic and exothermic transitions as a function of temperature. Exothermic reactions are observed when reactions occur taking the sample to a lower energy state such as the crystallisation of the glass T(c), due to the enthalpy of fusion being released from the sample. Endothermic reactions are observed when reactions occur taking the sample to a higher energy state such as the glass transition temperature T(g) in glass. The heating profile shown in Figure 3.16, displays exothermic and endothermic peaks associated with various thermal events as the temperature of the glass sample is increased.

The samples were ground to <75µm using a TEMA mill. For DTA measurements a Netzsch TG449 F3 Jupiter, calibrated with aluminium standard in air, was used. Approximately 25mg of the powered sample, and aluminium standard, was weighed out using Oertling electronic balance to ±0.0001g. The samples were placed into two platinum crucibles and heated in an alumina furnace from room temperature, at a rate of $10°C \ min^{-1}$, under high purity atmosphere to 1100°C (T_m for glass samples). Temperature and temperature difference between sample and standard were recorded every 0.1 seconds. Data analysis was performed using Perkin Elmer, Pyris Software.
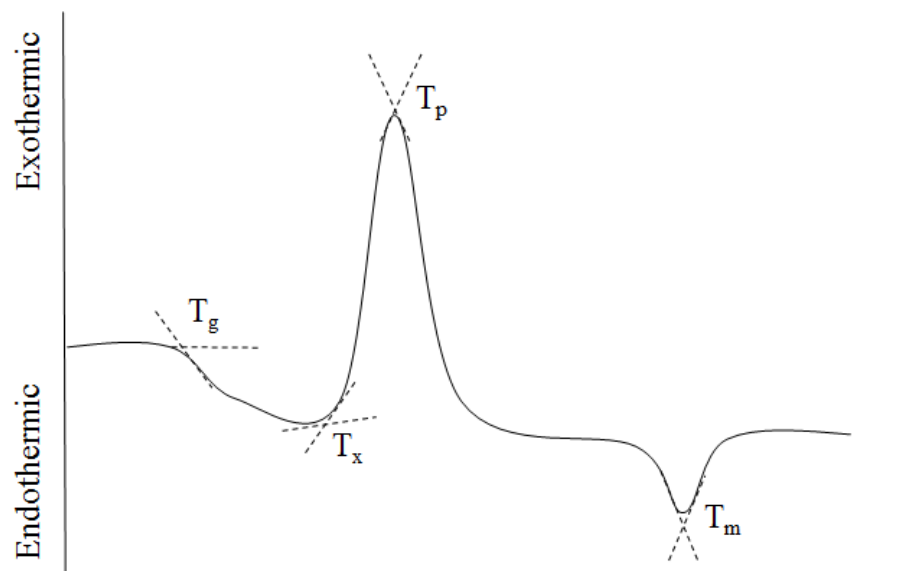
Figure 3.16 Typical DTA curve of a glass, Tg is the glass transition temperature (exotherm onset); Tx and Tp are the onset and peak of the crystallisation exotherm; respectively; and Tm is the melting endotherm.

77

3.11 Mossbauer Spectroscopy

The Fe^{2+} / Fe^{3+} ratio is a good internal standard of the redox conditions on the melt. The iron redox ratio is critical in terms of processing, with consideration needed to avoid issues such as foaming within the melter (Hrma et al. 1998). Due to the large amount of metal waste included within the PCM waste envelope, it is important to establish the redox conditions during vitrification of PCM waste, and what this effect has on the quality and performance of the final waste product.

Mössbauer spectroscopy (MS) is recognised as being the gold standard for determining the Fe^{2+} and Fe^{3+} ratio in solid materials, including nuclear waste vitrification with a number of studies using MS.

The Mössbauer effect is the recoil-free emission and resonant absorption of gamma (γ) rays by specific atomic nuclei in solids. This technique is a powerful probe of nuclear energy levels in solids, providing details of local electron configuration, including oxidation states.

^{57}Fe is the most commonly investigated Mössbauer active nucleus and is most useful for the current study. ^{57}Co is the source which decays to ^{57}Fe in an excited state as shown in Figure 3.17.
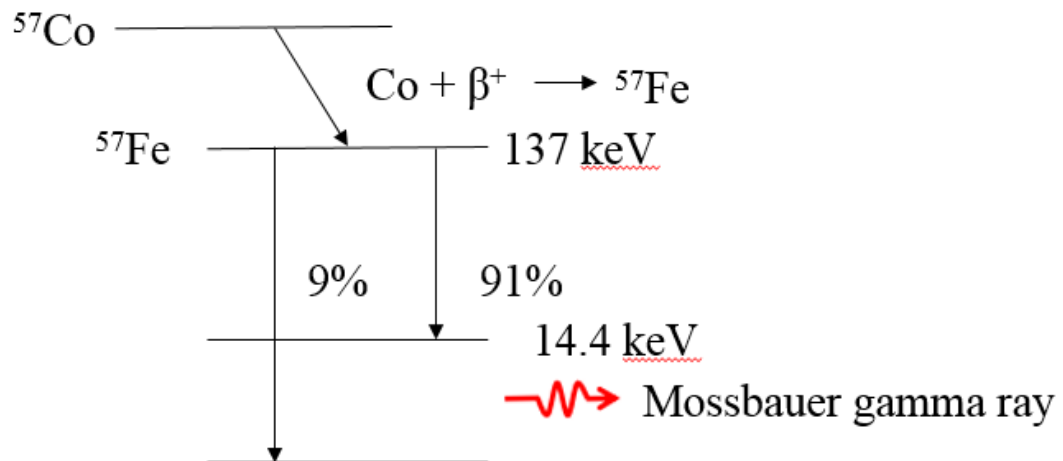
Figure 3.17 Energy level schematic for ^{57}Co to ^{57}Fe decay

^{57}Fe isotope has a large recoil free fraction which makes high quality Mössbauer measurements possible. The parent isotope used for measurements is ^{57}Co which has a 270-day half-life and decays primarily to the 137 KeV level of ^{57}Fe (Figure 3.17)

following capture of an atomic electron. From this ^{57}Fe can then decay to its 14.4 keV state resulting in the emission of a gamma ray. ^{57}Fe in a target sample, will resonantly absorb this gamma radiation and emit gamma radiation when it drops back to its ground state. The gamma emitting source is vibrated normal to the target in order to scan a range of frequencies.

To detect and analyse the local environment of the targeted nucleus, recoilless emission or absorption of a gamma ray is required. Resonant absorption occurs when the atoms in the emitting and absorbing matrices are in identical environments. In reality, it is more common for the emitting and absorbing materials to differ resulting in resonant absorption occurring at slightly different energies. The difference is referred to as the isomer shift. Figure 3.18 and Figure 3.19 shows the difference in Mössbauer spectrum between an emitter and an absorber in both identical and non-identical conditions. The isomer shift is sensitive to the oxidation state and can therefore be used to quantify the Fe^{2+}/Fe^{3+} ratio.
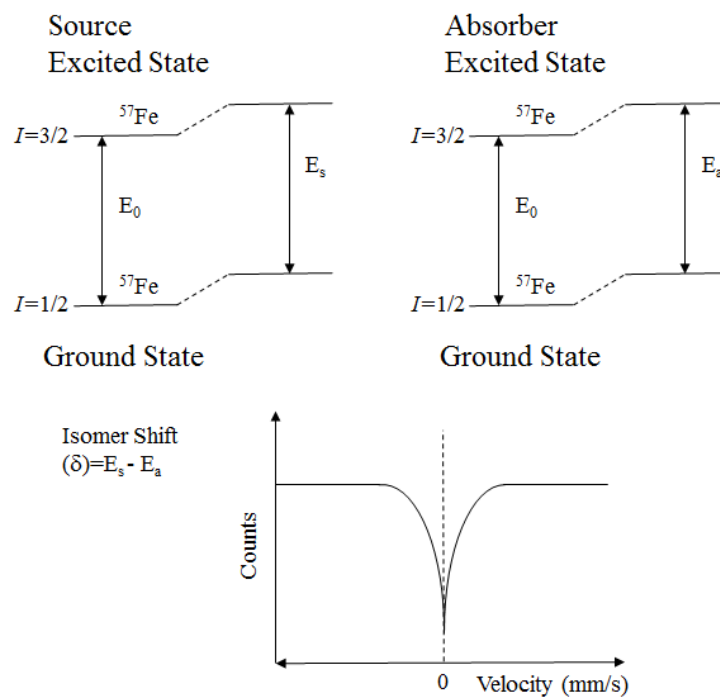
Figure 3.18 Mössbauer spectrum obtained from an emitter and an absorber in identical conditions
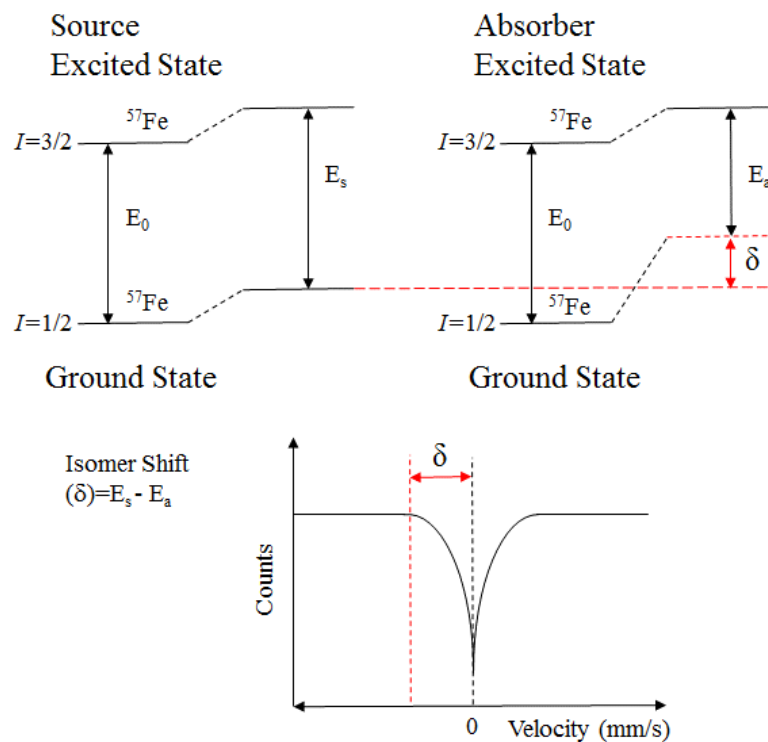
Figure 3.19 Mössbauer spectrum obtained from an emitter and an absorber in non-identical conditions

Hyper fine interactions are interactions between the nucleus and its surrounding electrons, leading to changes in the nuclear energy levels. These changes provide information that enables characterisation of the host material. These interactions result in complex spectra shown in Figure 3.20. A typical Mössbauer spectrum consists of doublets and sextet features as shown in Figure 3.20. The type of peak depends on a number of factors including the number of Fe electrons (Fe^0, Fe^{2+}, and Fe^{3+}). The spectra are also temperature dependent.

Interaction of the nuclear quadrupole moment with the electric field gradient leads to splitting of the nuclear energy levels, shown as the red spectra in Figure 3.20. For ^{57}Fe, this causes individual peaks in the transmission spectrum to split into doublets. The doublet features reflects the symmetry of the bonding environment and the local electronic structure.

Hyperfine splitting occurs due to the magnetic moment ^{57}Fe possess. If magnetically ordered materials are present, this will cause unsettling of the energy levels associated with ^{57}Fe causing hyperfine interactions resulting in the sextet feature shown in green in Figure 3.20.

The combination of IS and quadrupole splitting parameters (along with the hyper-fine field in the case of magnetically ordered phases) can be used to identify the valence state and site occupancy of Fe in a given site. There are number of studies present in the literature which determine the isomer shift versus quadrupole splitting data for common rock forming minerals, a discussion of which can be found in Burns (1990). From this information, it is shown that fairly distinctive ranges occur for each valence state and site occupancy of Fe, as shown in Figure 3.21. Figure 3.21 can be used to determine the valence state of Fe from a particular Mössbauer signal for amorphous materials allowing the Fe^{2+} / Fe^{3+} to be calculated for the glass samples produced in this project.

Figure 3.22 shows the typical experimental setup for the ^{57}Fe Mossbauer spectrometer. This was operated at room temperature utilising a ^{57}Co source, at a velocity of $\pm$ 6mms^{-1}. Samples were prepared using finely ground samples sieved to <75µm. For samples containing large amounts of Fe, the samples were mixed with graphite, which dilutes the samples, in order to keep the signal to noise ratio low.
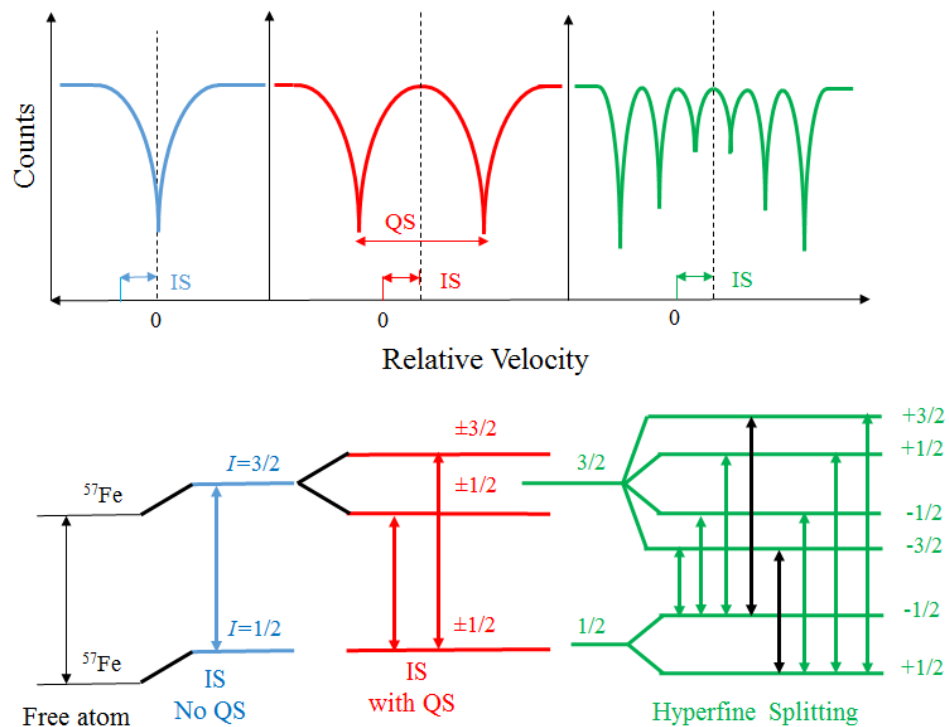
Figure 3.20 (blue) isomer shift (IS) the 1/2 and 3/2 labels represent the nuclear spin. (Red) Interaction of the nuclear quadrupole moment with the electric field gradient leads to splitting of the nuclear energy levels into doublets. (Green) When a magnetic field is present at the nucleus results in the formation of a sextet pattern. Simplest case, lines vary in the ratio 3:2:1:1:2:3. Figure modified from (Dyar et al. 2006)
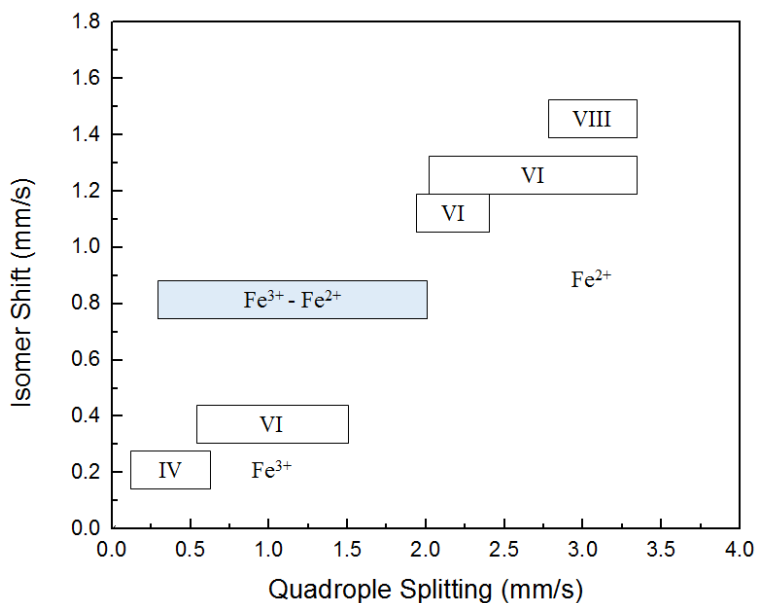
Figure 3.21 Room temperature, isomer shift versus quadrupole splitting data show fairly distinct ranges occur for each valance state and site occupancy of Fe.

The samples were loaded into a holder with a transparent Perspex window, normal to the gamma source vibration direction. The gamma waves passing from the sample were detected and fed into a channel analyser, where the counts are combined with the values for the gamma ray energy of the source. All Mössbauer spectra were deconvoluted using RECOIL software.
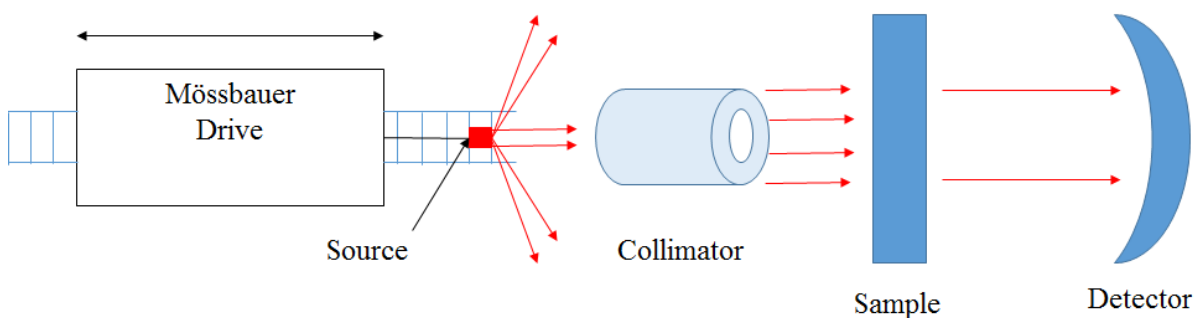
Figure 3.22 Typical experimental setup for a transmission Mössbauer experiment

3.12 Raman Spectroscopy

As discussed in previous chapters, glass is defined as an amorphous solid completely lacking in long-range, periodic atomic structure. This lack of long range order results in diffuse scattering when using X-ray diffraction techniques. This is due to the random distribution of atoms results in X-rays being scattered in many directions, leading to a

diffuse scattering over a wide 2Ө range instead of high intensity Bragg peaks. Raman spectroscopy is extremely useful for determining the atomic structure of amorphous materials especially in glass science.

Raman spectroscopy relies on the inelastic scattering of incident radiation through its interaction with vibrating molecules. This is achieved by using a monochromatic laser to illuminate the sample and detect the resultant scattered light. The majority of the scattered light is of the same frequency as the laser; known as Rayleigh or elastic scattering. A tiny fraction however is shifted in energy from the laser frequency due to interactions between the incident electromagnetic waves and the vibrational energy levels of the molecules in the sample. It is possible to plot the intensity of this "shifted" light against the frequency resulting in a Raman spectrum of the sample. In Raman spectra, the abscissa has arbitrary rather than absorption units because it is simply a measure of the number of scattered photons captured by the detector at any particular frequency (Yaday 2015).

3.13 XANES – X-Ray absorption near edge spectroscopy

X-ray absorption near edge spectroscopy (XANES) can be used to determine the valence state and coordination geometry of atoms. X-ray absorption spectroscopy probes the immediate environment of the selected element, within about 6 Ȧ, and its theory and interpretation does not rely on any assumption of symmetry or periodicity unlike XRD. For this reason XANES has been shown to be a powerful tool for the investigation of element speciation and local co-ordination in (boro) silicate glasses for radioactive waste immobilisation (McCloy et al. 2012; Short et al. 2005) and therefore will be used in this project.

Two synchrotron facilities were used over the course of this project, the National Synchrotron Light Source (NSLS) and the European Synchrotron Radiation Facility (ESRF). The use of these facilities enable X-ray absorption spectroscopy of glasses by bombarding thin powdered samples with high flux monochromatic X-rays. The principles used in XANES are based on the interactions of X-rays with matter. The X-ray absorption coefficient (μ) is the probability for an X-ray to be absorbed by a sample. X-ray absorption near edge spectroscopy involves measuring (μ) as a function of X-ray energy. The energy of the X-ray beam is slowly varied. As the energy is scanned through the energy space, the associated absorption of the X-ray beam is measured and may be plotted as shown in Figure 3.23. Each element has a specific set of absorption edges at the binding

energies of its electrons. Figure 3.23 shows the XANES part of the absorption spectrum near an absorption edge. The geometry and the oxidation state of the atom affect the XANES part of the absorption spectrum and can be used to determine the oxidation state of atoms, as used in this study. The XANES results throughout this thesis are analysed through the semi-quantitative approach (LCA). This approach utilises the fact that XANES features are a fingerprint of the valence state and local structure of the absorber. The XANES spectra can be analysed as a linear combination of reference compounds XANES. The author is grateful to Dr. Martin Stennett for data acquisition.
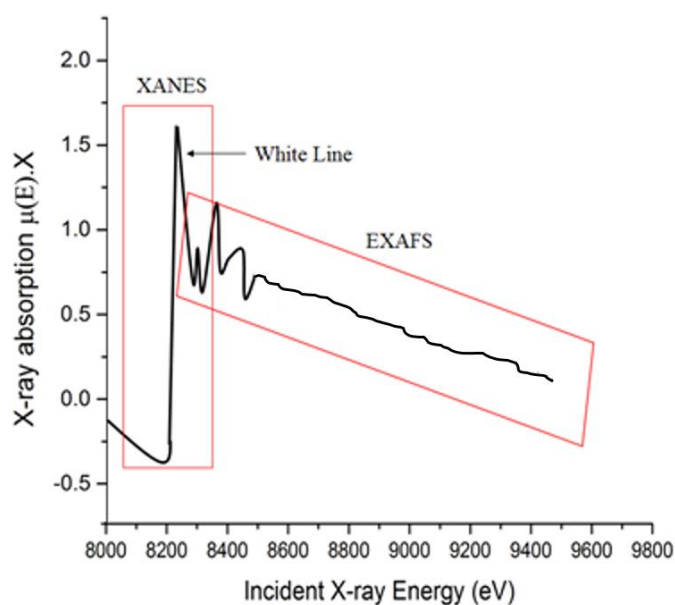
Figure 3.23 Typical XAS spectrum of the K-edge of a glass sample showing the XANES region including the pre-edge peak and the EXAFS region.

4 THERMAL TREATMENT OF PLUTONIUM CONTAMINATED MATERIALS (PCM) WASTE

4.1 Introduction

As outlined in Section 2.1.1, one possibility for treating plutonium contaminated material (PCM) waste, and which yields a large volume reduction, is via thermal treatment. Proof of concept studies have shown PCM waste compatibility with thermal treatment processes. However, to support the increased investment in thermal treatment technologies a fundamental understanding of the processes and the impact of waste inventory needs to be established. In this Chapter, laboratory scale experiments have been performed using SLS glass frit as a glass forming additive. A range of analytical techniques have been applied in order to understand the process and sequence of reactions that occur between the waste and glass matrix during vitrification.

To achieve the aims set out in this project, laboratory scale experiments using mock up PCM waste drums have been performed (Table 3.5) using the items described in Table 3.4. The mock-up PCM waste drums were thermally treated as described in section 3.1.7. Additional melts were performed in order to optimise the process, an overview of which can be found in Table 3.7. This Chapter is split into two parts. The first part discusses the results of the experiments described in Table 3.7, and the analysis of the vitrified waste forms. The second part of this chapter discusses the results of the experiments in Table 3.8 which aims to optimise the process by completely oxidising the waste form as described in section 3.2.

4.2 Melting behaviour

A summary of the samples generated are shown in Table 4.1 (A: W = additive: waste ratio)

	Waste description	Additives	Crucible	Details
Melt 1 1560°C	Can + PVC	SLS glass A:W = 1:1	Alumina classic	Failed
	Can + PVC + Metal	SLS glass A:W = 1:1	Plumbago	Successful
	Can + PVC + Masonry	SLS glass A:W = 1:1	Alumina classic	Failed
	Can + PVC + Mixed	SLS glass A:W = 1:1	Alumina classic	Failed
Melt 2 1560°C	Can + PVC	SLS glass A:W = 1:1	Alumina tapered	Successful
	Can + PVC + Metal	SLS glass A:W = 1:1	Plumbago	Successful
	Can + PVC + Masonry	SLS glass A:W = 1:1	Alumina tapered	Successful
	Can + PVC + Mixed	SLS glass A:W = 1:1	Alumina tapered	Successful
Melt 3 1450°C	Can + PVC	SLS glass A:W = 1:1	Alumina tapered	Successful
	Can + PVC + Metal	SLS glass A:W = 1:1	Plumbago	Successful
	Can + PVC + Masonry	SLS glass A:W = 1:1	Alumina tapered	Successful
	Can + PVC + Mixed	SLS glass A:W = 1:1	Alumina tapered	Failed

Table 4.1 Summary of the samples generated with SLS glass additive at a A:W 1:1 %wt. ratio.

Melt 1 was unsuccessful with all but the plumbago crucible failing. The alumina classic crucibles (Ø=96mm x I/D=90mm x 145mm high) used in melt 1 had a high failure rate. For the next set of melts (2) alumina crucibles with tapered edges (Ø=102mm x I/D=93mm x 145 mm high) were selected, providing immediate benefits, with all crucibles able to contain all of the vitrified material. The likely reason for this success is the increase thickness of the wall in the tapered edge crucible as shown by the dimensions. The classic crucible has approximately 3mm thick wall whilst the tapered edge crucible has approximately 4.5mm thick walls. This increase in the thickness of the crucible wall provided a slightly lower thermal gradient across the wall for the tapered edge crucible, thereby reducing the risk of cracks developing via thermal shock. Melt 3 used the same

tapered edge crucibles but unfortunately due to thermal shock of the crucible for the mixed waste, a large amount of material was lost. Melt 1 was discarded at this stage due to the failure of the crucibles. The following section concentrates on the melting behaviour and characterisation of Melt 2. The resulting vitrified products for Melt 2 are shown in Figure 4.1 to Figure 4.4.
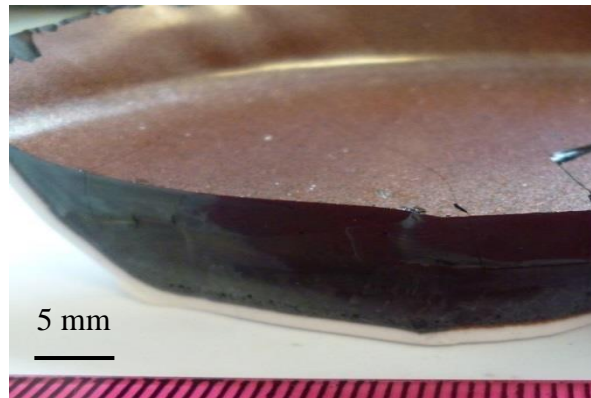
Figure 4.1 Vitrified can + PVC waste from Melt 2, 100% glass waste form
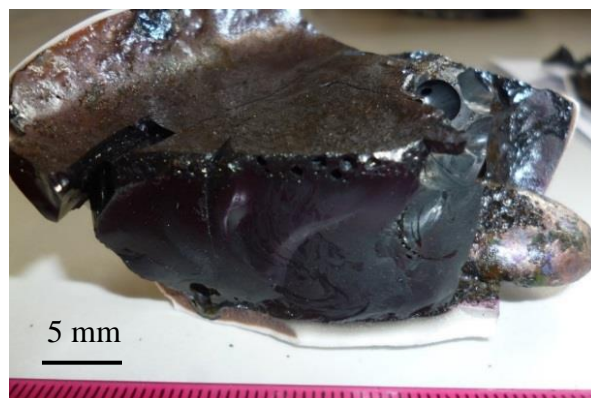
Figure 4.2 Vitrified Can + PVC + Mixed waste from melt 2, small metallic button located at the bottom of the crucible
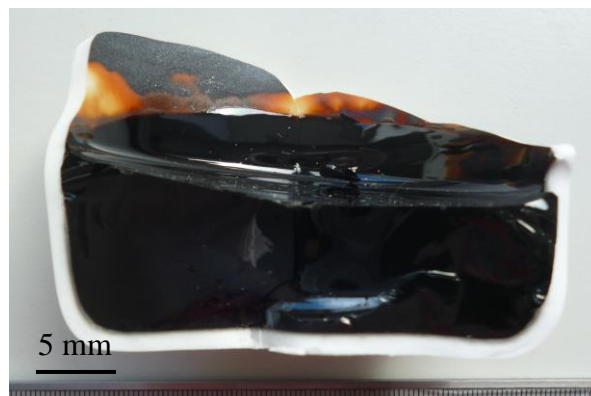
Figure 4.3 Vitrified Can + PVC + Masonry waste from melt 2, 100% glass waste form
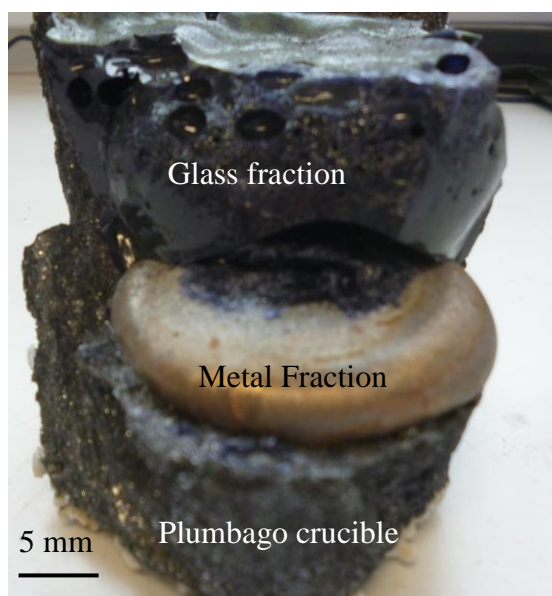
Figure 4.4 Vitrified Can + PVC + Metal waste from melt 2, glass waste form with metallic fraction at bottom of the crucible.

The melting behaviour showed no violent reactions between the waste simulant and glass additive. However, the alumina and graphite/clay crucibles suffered obvious corrosion during melting. In addition, the graphite/clay crucibles exhibited significant weight loss due to oxidation at high temperature. The observed melting behaviour generally showed that the last items to melt were, as expected, the steel components. A metallic fraction resulted for the vitrified metal waste (Figure 4.4) and the mixed waste (Figure 4.3). The waste forms derived from the PVC (Figure 4.1) and masonry waste types (Figure 4.2) were composed of 100% glass waste form. Glass in the masonry and metallic feed exhibited little crystallinity. Glass derived from the PVC and mixed waste streams were partially crystalline throughout. The composition of the four vitrified waste streams were determined by XRF, together with ICP-OES to determine the Ce content. Due to the absence of Cl within the XRF results, it was determined that the PVC was volatilised at high temperature. The results are shown in Table 4.2.

Due to the corrosive nature of the high metal waste feeds during vitrification, it was necessary to use a Plumbago graphite – clay crucible. This had a major effect on the content of the FeO within the glass due to the degree of oxidation available to the waste and additive mixture during thermal treatment.

Component (Wt%)	PVC	Masonry	Metal	Mixed	Glass frit
SiO_2	37.93 ±0.36	54.85 ±0.44	69.87 ±0.50	54.23 ±0.44	70.77 ±0.50
MgO	0.85 ±0.06	0.86 ±0.06	1.17 ±0.06	0.93 ±0.06	1.50 ±0.08
Al_2O_3	16.51 ±0.24	11.70 ±0.20	7.60 ±0.11	9.29 ±0.18	1.57 ±0.08
CaO	5.46 ±0.14	7.07 ±0.11	7.43 ±0.11	6.90 ±0.15	10.16 ±0.20
Na_2O	6.02 ±0.15	6.81 ±0.10	7.72 ±0.17	6.53 ±0.15	13.27 ±0.14
FeO	30.38 ±0.33	17.65 ±0.26	0.82 ±0.06	18.13 ±0.26	0.36 ±0.03
CeO_2	0.42 ± 0.05	0.33 ± 0.03	0.60 ± 0.05	0.43 ± 0.05	-
Sum	99.31 ±0.60	99.53 ±0.60	98.59 ±0.60	99.09 ±0.60	98.89 ±0.60

Table 4.2 XRF results show the composition of the 4 vitrified waste streams

The reducing environment, imposed upon by the graphite clay crucible, led to a combined slag and metal waste form; the slag component was thus strongly depleted in FeO. The higher FeO content in the slag fraction of the PVC waste, compared to the waste form derived from the masonry and mixed waste, is a consequence of the proportionally higher amount of mild steel in the PVC waste. Chemical analysis determined no measureable retention of Cl within the slag fraction of the waste form. It was therefore concluded that all the Cl present within the PVC was volatilised at high temperature.

Noticeable corrosion occurred for all the crucibles. This afforded higher levels of Al_2O_3 within the waste forms. PVC has the highest amount of Al_2O_3 in the glass because as much of the organic material will have volatilised, the corrosion of the Al_2O_3 will occupy a much greater proportion of the glass forming oxides within the glass as opposed to the other wasteforms. Table 4.3 reports the measured densities of the slag fractions of the PCM waste forms. The results were obtained through pycnometry as described in Section 3.9

Sample	Density (g cm^{-3})
PVC waste: slag fraction	3.08 ± 0.01
Metal waste: slag fraction	2.51 ± 0.01
Masonry waste: slag fraction	2.78 ± 0.01
Mixed waste: slag fraction	2.86 ± 0.01

Table 4.3 Pycnometry densities of PCM waste forms

4.3 Product waste form characterisation

4.3.1 PVC waste form (Melt 2)

Visual inspection (Figure 4.1) of the waste form showed a homogenous glassy material with no inclusions or un-melted components. The following characterisation methods, as described in Section 3, were used to determine the microstructure of the material.

Figure 4.5 shows the XRD pattern for the vitrified PVC waste stream. Identified reflections corresponding to Fe_3O_4 magnetite spinel phase are shown in the SEM images in Figure 4.5. Elemental X-ray maps shown in Figure 4.5 shows the composition of the phases identified within the XRD trace.

An aim of this work was to try and determine the partitioning of Ce between crystalline regions within the glass. This was not possible by the EDX scans shown in Figure 4.6, as there was little difference between the Ce signals for the two EDX spectra. Figure 4.6 does show where the expected Ce signal should be present at 4.84 KeV. A reason for this is because of volume interactions effects associated with the EDS measurements, which can lead to uncertainties with respect to the quantities analysed for different phases which are intimately associated in space. The EDX map does show that Ce is homogenously distributed throughout the sample. Cross sectional SEM images were taken from the top of the crucible down to the bottom of the crucible. There were no regional differences with the quantity of the spinel structures within the glass. However, there is a tendency for the crystals near the edge of the crucibles to have a common orientation into the glass, as shown in Figure 4.6.
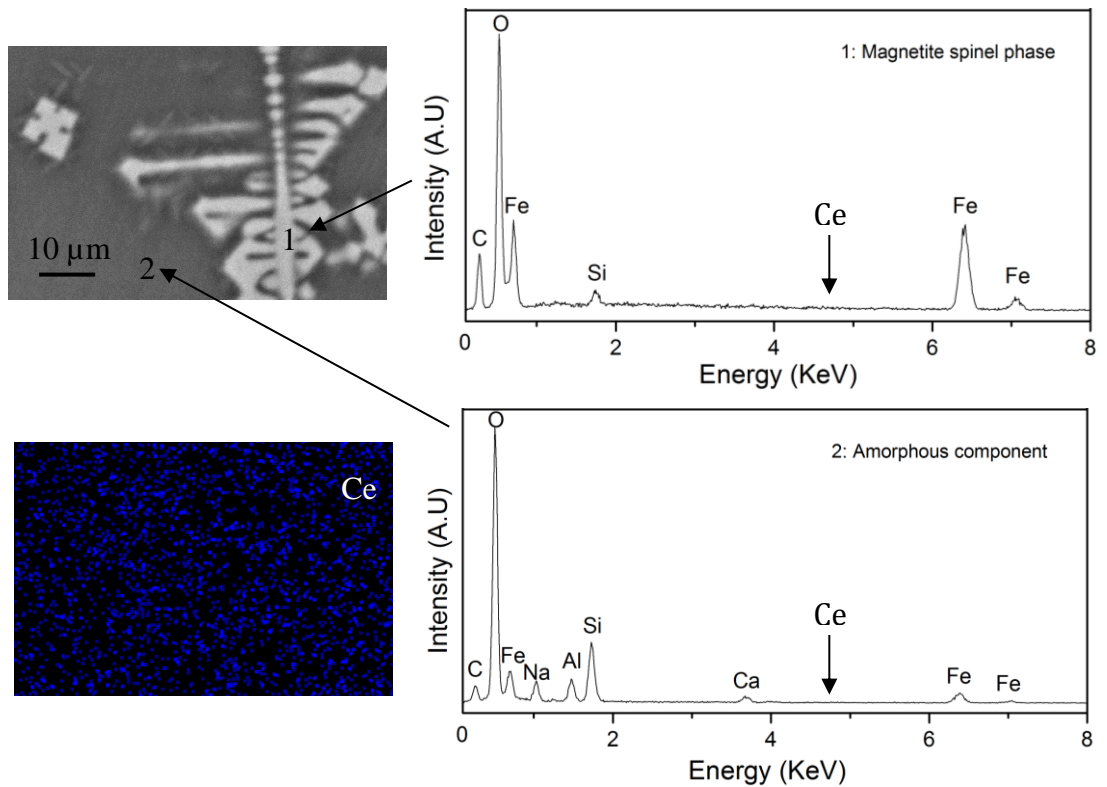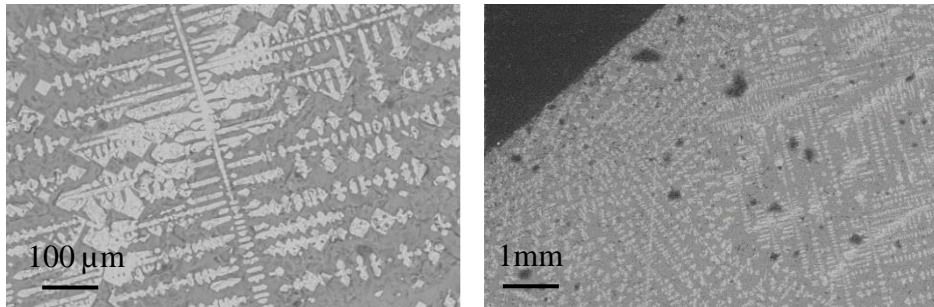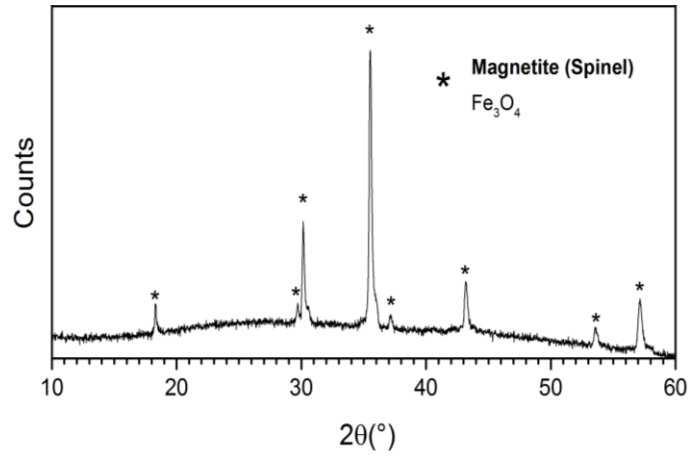
Figure 4.5 (Top) XRD pattern showing identified reflections corresponding to Fe₃O₄.

Figure 4.6 (Bottom) EDX scan showing distribution of elements within the structure.

This suggests that as the crucible is pulled out of the furnace, heterogeneous nucleation in the thermally supercooled region adjacent to the crucible wall is occurring. The grains grow rapidly, reject solute which lowers the liquidus and restricts their growth. This leads to further undercooling and additional nucleation. This theory is known as the "free chill crystals" (Hutt et al. 1999). According to this theory all the grains seen in the final material are nucleated immediately following supercooling.
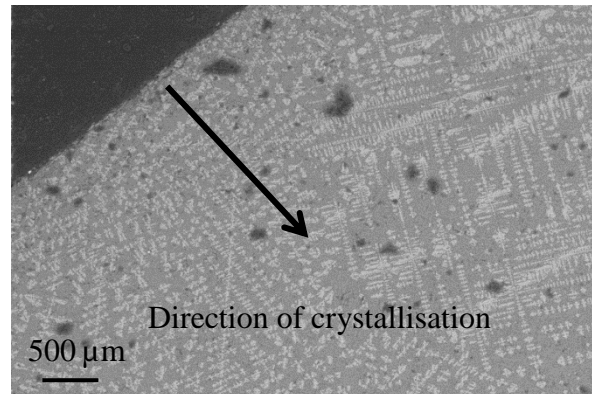
Figure 4.6 SEM Image showing crystal orientation directed towards the centre of the glass from the crucible wall

4.3.2 Metal Waste (Melt 2)

The high metal waste feed resulted in a mixed waste form with a metallic fraction located at the bottom of the crucible with a layer of slag on top, as shown in Figure 4.4. The graphite inclusions originate from the corrosion of the graphite clay crucible.

Due to the reducing conditions imposed upon the melt by the graphite clay crucible the Fe is reduced as it partitions to form metallic Fe at the bottom of the crucible. The SEM images show a number of metallic inclusions within the glass material. Ce was found to be overwhelmingly incorporated in the glass phase with 0.60 Wt% of Ce detected in the glass fraction. EDS analysis demonstrated Ce to be concentrated exclusively within the glass phase, within detection limits. This confirms that Ce is more thermodynamically favourable to partition into the slag fraction, as agreed with Millers (1993) study.
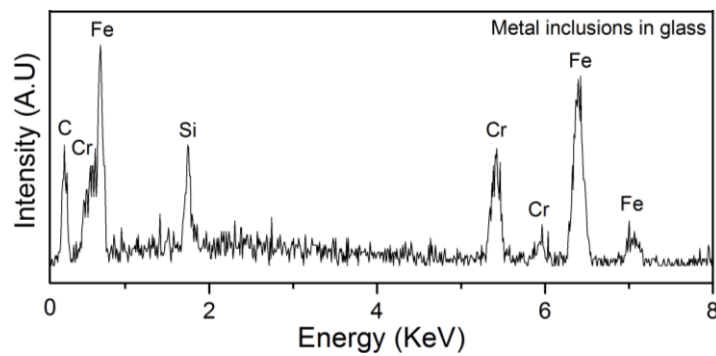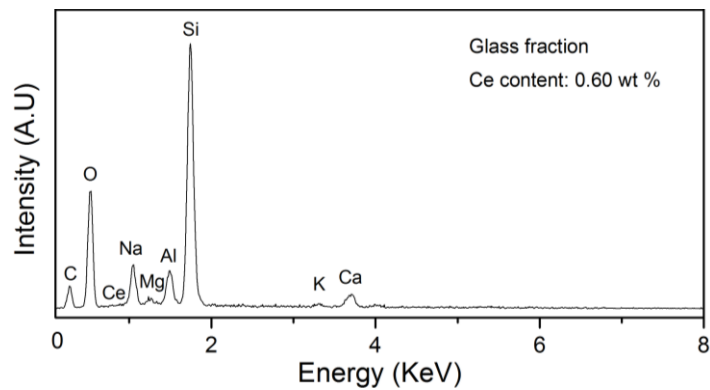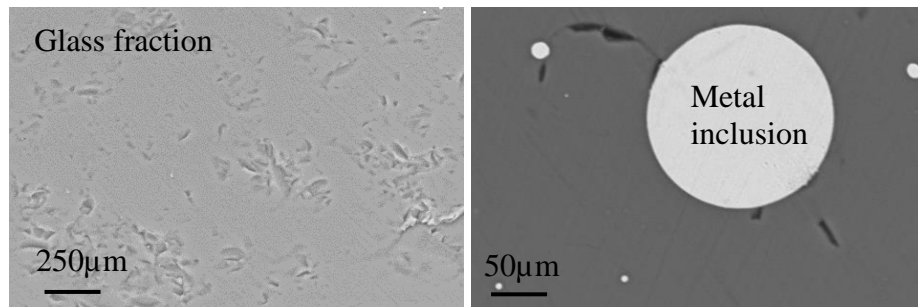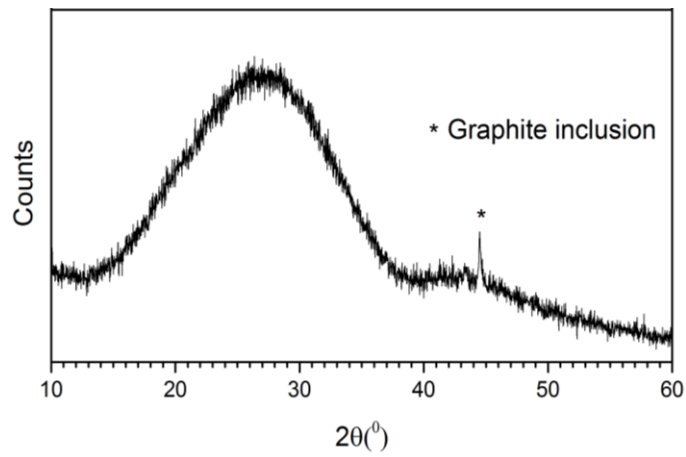
Figure 4.7 X-ray powder diffraction pattern showing diffuse scattering corresponding to amorphous structure in the form of CaO-Al₂O₃-SiO₂ glass with graphite inclusions. SEM images also show small metallic inclusions found within the glass matrix, as confirmed by the EDX scan.

It has been suggested that if clean separation of the slag and metallic fraction can be achieved it might be feasible to dispose the metal fraction as LLW, which would result in cost savings due to the decrease in waste volume classified as ILW. Figure 4.8 shows the metallic fraction from the melt. It is clear that a small amount of glass fraction remains in contact with the metal fraction, this is confirmed in the magnified image in Figure 4.10.
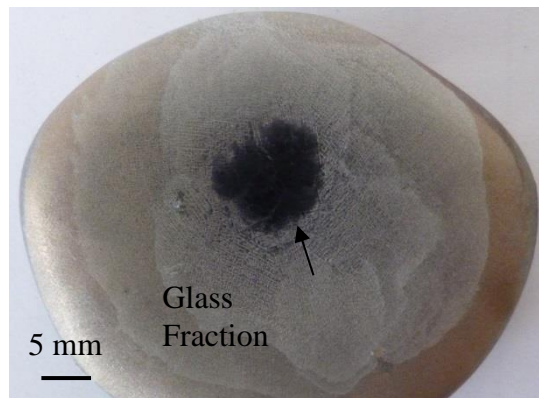
Figure 4.8 Metallic fraction from vitrified metal waste. Glass fraction remains on the surface showing complete separation has not occurred.
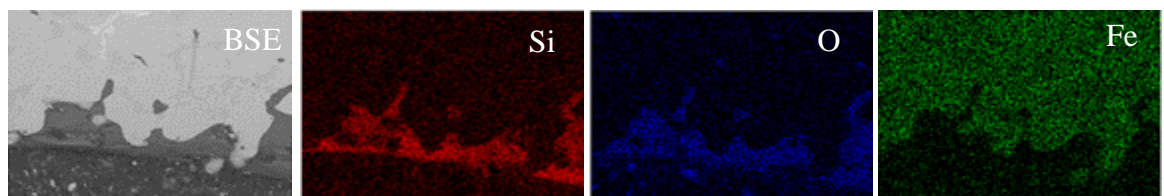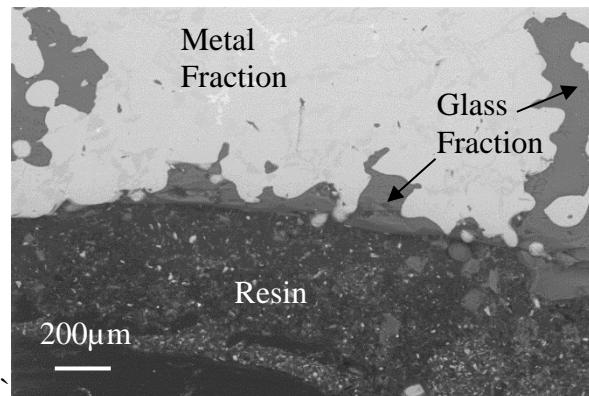
Figure 4.9 Magnified cross section of the metal and glass interface. EDX images show glass oxide fraction penetrating into the metal fraction.

Although small, the amount of Ce containing glass within the metal fraction is not negligible. Assuming Pu contaminated glass penetrated the metal fraction in a similar

way, then the partitioning achieved may not be sufficient to permit disposal of the metal fraction as LLW as it may exceed the upper limits of total Pu alpha activity of 0.1 GBq/t (Cummings 2014). It should be noted however, that clean separation between the two phases was not attempted in this work, and industrial practice in similar industries have shown good levels of separation between metallic and slag phases. Seitz et al. (1979) demonstrated Pu partitioning coefficients (i.e. ratio of plutonium in slag / plutonium in steel) exceeding 10^6, sufficient to decontaminate steel wastes below the classification of TRU wastes

Figure 4.11 shows the microstructure of the metal fraction. The elemental mapping shows a Fe-Si-Ni alloy with concentrated areas of Cr within the metal alloy. EDX spot mapping was performed on the metal fraction. The concentration of Ce in the metal fraction was below the detection limits. This provides strong evidence that the Ce is partitioning within the oxide fraction as expected.
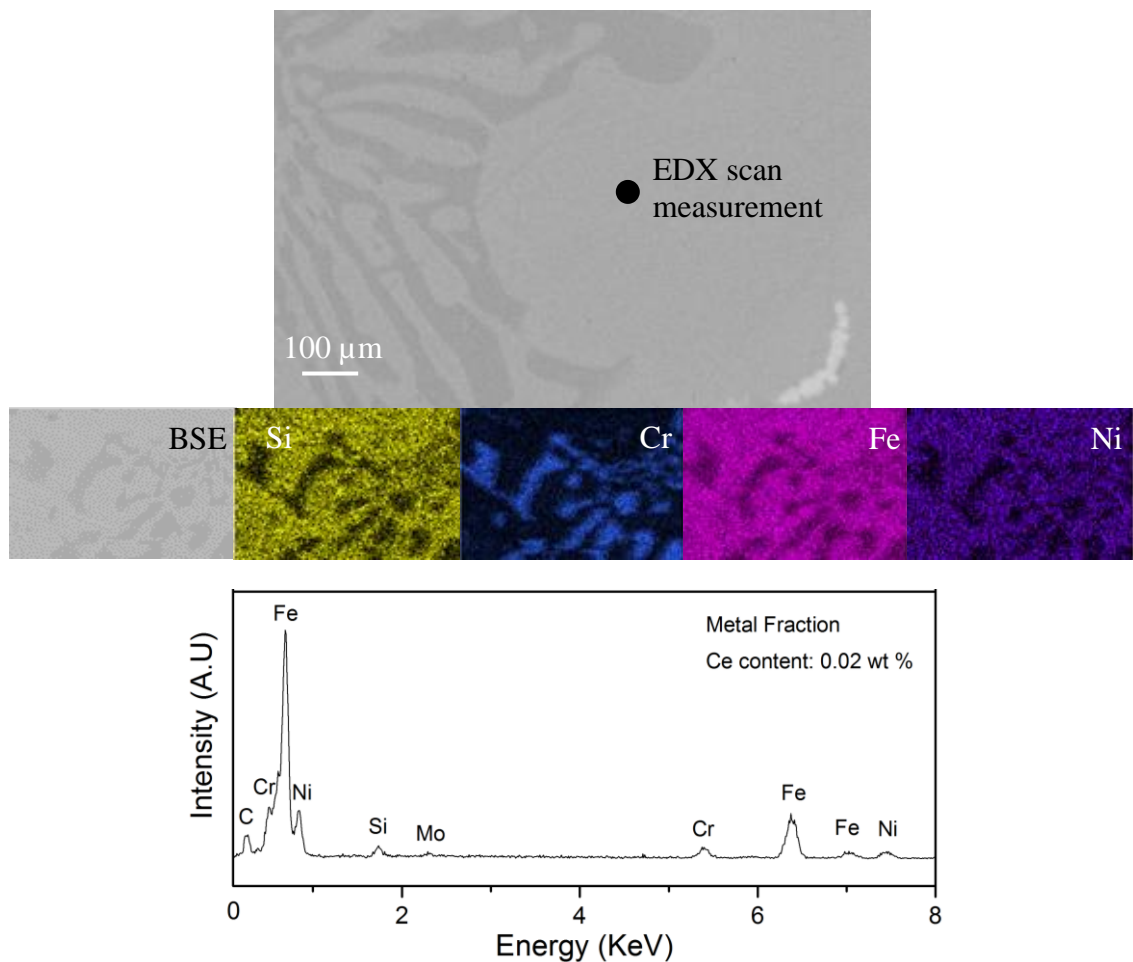
Figure 4.10 SEM image of metallic fraction from metallic waste stream with EDX mapping showing distribution of key elements within the metallic fraction

4.3.3 Mixed Waste (Melt 2)

The vitrified waste form resulted in a small metallic fraction at the bottom of the crucible as shown in Figure 4.2. XRD studies showed the slag fraction composed of an amorphous component related to $CaO–Fe_2O_3–Al_2O_3–SiO_2$ glass, and a number of crystalline phases within the glass matrix, labelled in Figure 4.12. EDX spot mapping (Figure 4.11) shows the relative concentrations of elements contained within the identified crystalline regions. The metallic fraction consisted of a Fe-Si-Ni alloy. EDX map shows that Ce is homogenously distributed throughout the wasteform.
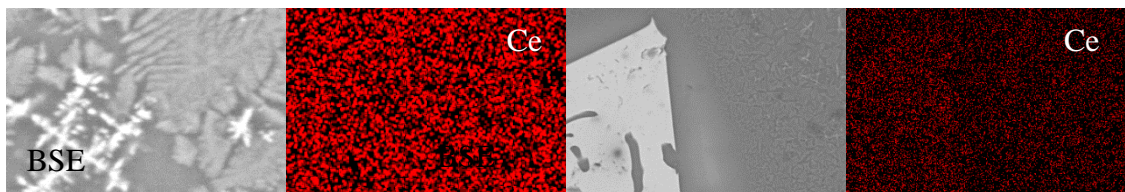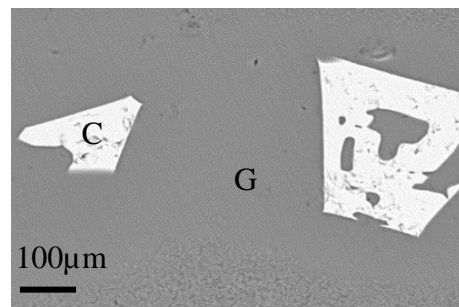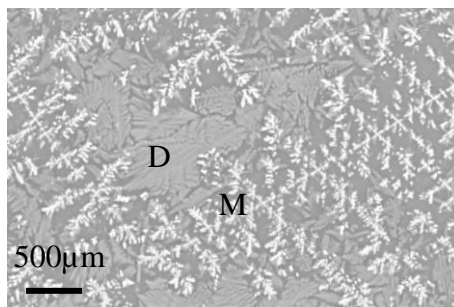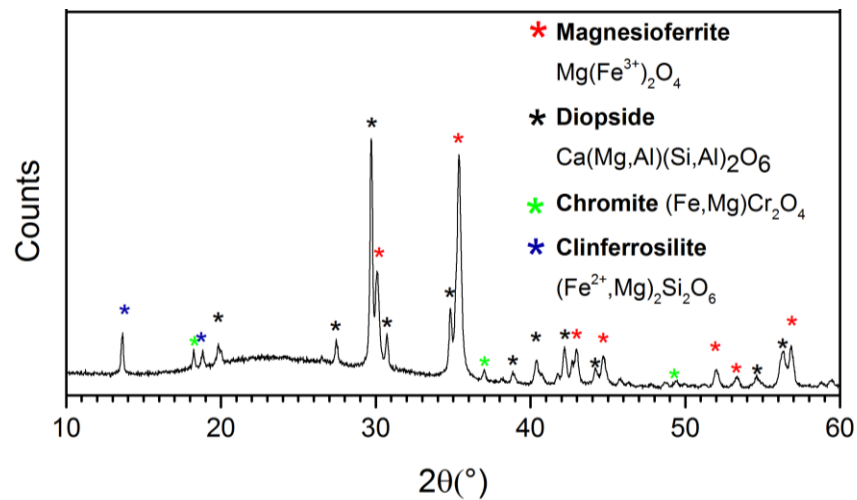
Figure 4.11 (Top) X- ray powder diffraction pattern showing identified reflections corresponding to identified crystal phases. (Bottom) SEM images show crystalline regions with associated EDX scan shown in Figure 4.12 (G=glass, D=diopside, M=magnetite and C=chromite).
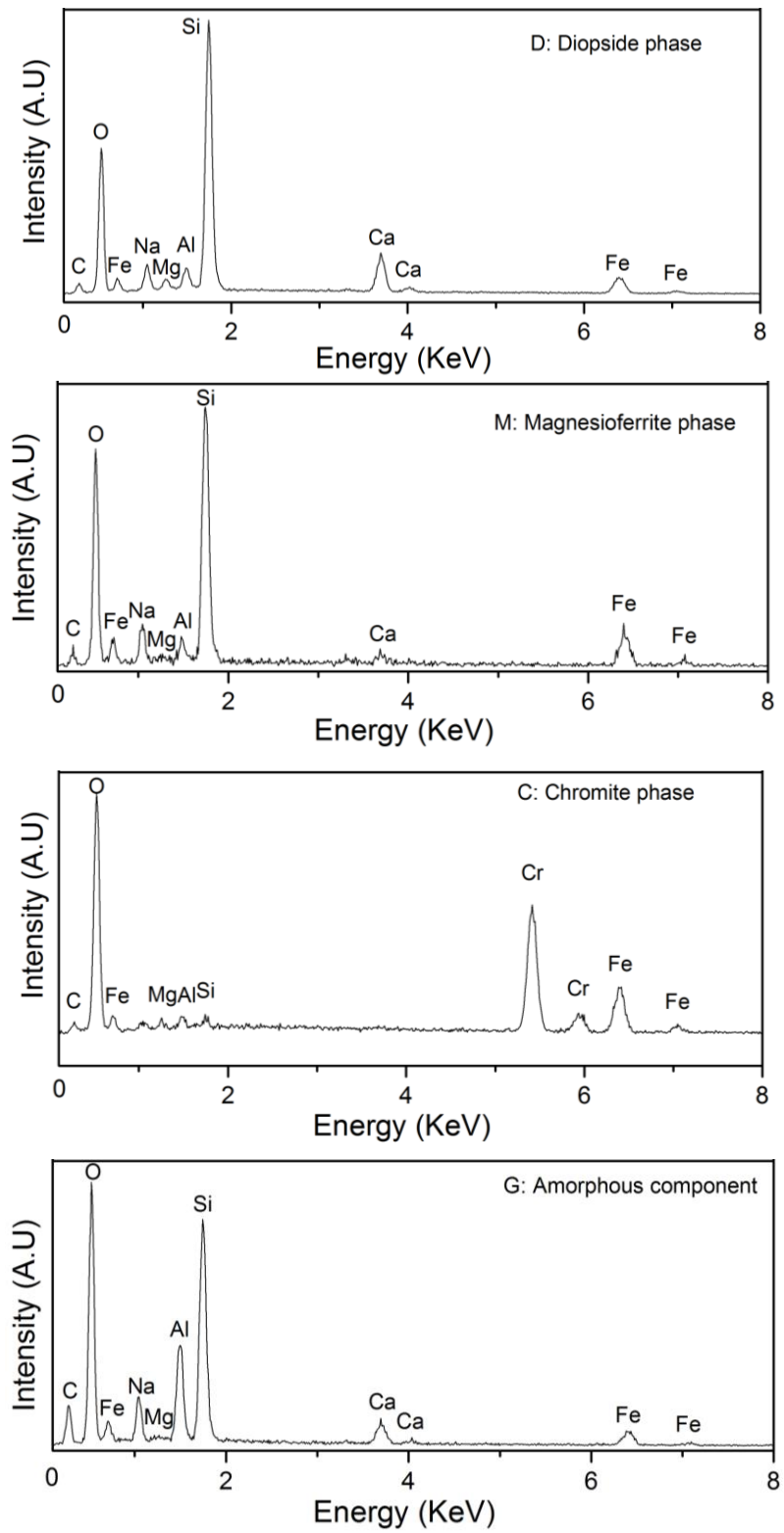
Figure 4.12 EDX scan of the phases identified in the XRD trace shown in Figure 4.11.

4.3.4 Masonry Waste (Melt 2)

The masonry waste formed a 100% glass waste form during vitrification, as shown in Figure 4.3. The XRD trace in Figure 4.13 shows a relatively amorphous structure with large amounts of background noise. It is likely that crystalline features are present within the XRD trace but are hard to distinguish from the background noise. TEM could be used to further probe the microstructure to determine any crystallite formation, however this is out of scope for this body of work. EDX spot mapping shows homogenous distribution of elements within the glass structure.
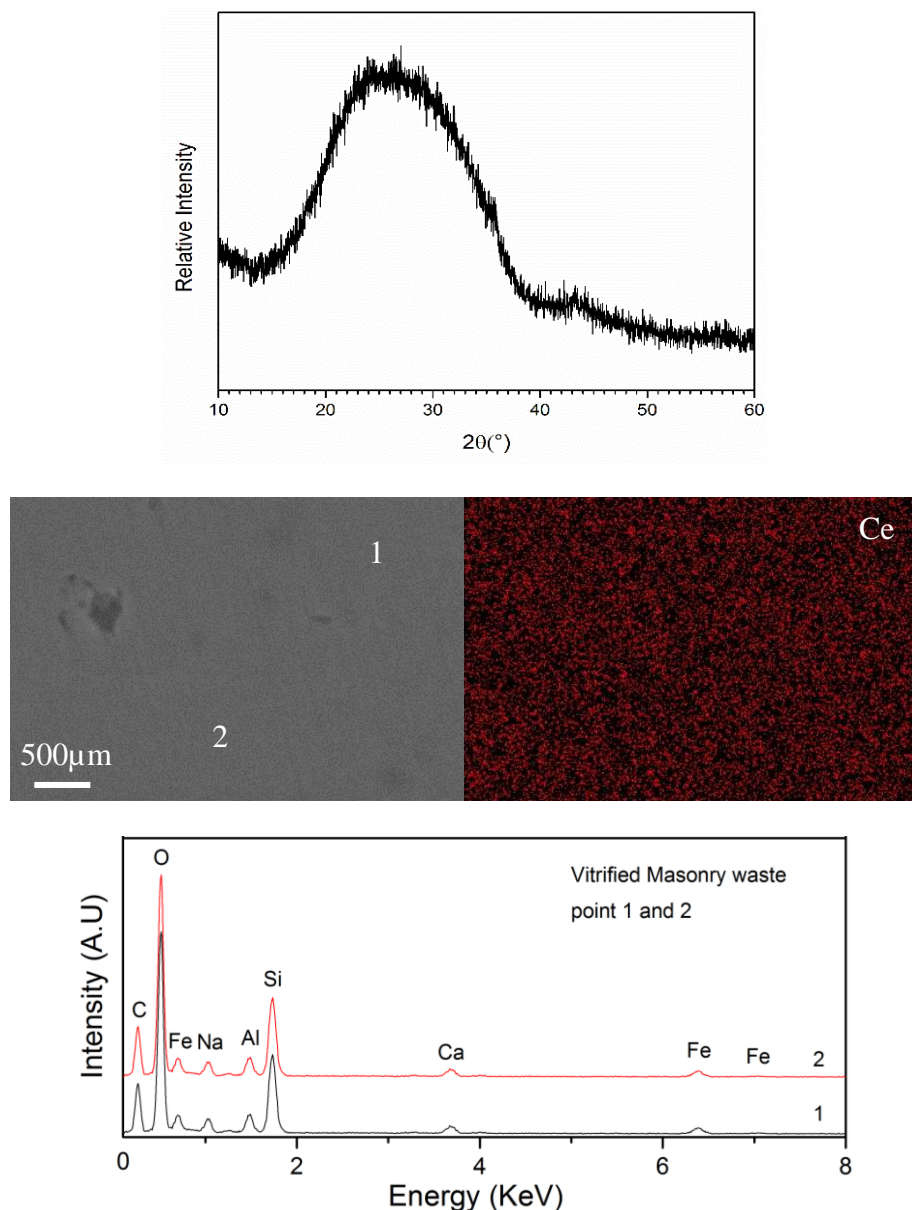
Figure 4.13 X-ray powder diffraction pattern showing diffuse scattering corresponding to amorphous structure in the form of CaO-Al$_2$O$_3$-SiO$_2$-Fe$_2$O$_3$ glass. EDX map shows homogenous distribution of Ce. EDX scan shows key elements within glass structure.

4.4 Determination of Ce oxidation state by Ce L$_3$ edge XAS

X-ray Absorption Spectroscopy has been shown to be a powerful tool for the investigation of elemental speciation and local co-ordination in (boro) silicate glasses for radioactive waste immobilisation (McCloy et al. 2012). Figure 4.14 shows the Ce L$_3$ edge X-ray Absorption Near Edge Structure (XANES) of the slag fractions, together with the data acquired for CeO$_2$ and CePO$_4$ (monazite) standards. The XANES spectra (Figure 4.14) permits straightforward fingerprinting of Ce oxidation state. From comparison of the spectra it is apparent that the XANES data of slag fraction closely resembles that of CePO$_4$, demonstrating that Ce^{3+} is the dominant species. Using the position of the pre – edge features for the four waste forms we can quantify the amount of Ce^{3+} within the glass. This is shown in Table 4.4. As stated in Section 2.1.2, A number of studies have determined that trivalent species such as Pu^{3+} and Ce^{3+} are much more soluble in borosilicate systems (Lopez et al. 2003) (Deschanels et al. 2007), with Cachia et al. (2006) showing that Pu solubility was effectively doubled by modifying its oxidation state, from 2 wt.% for Pu (IV) to 4 wt. % for Pu (III), Therefore it is reasonable to expect that the glass wasteforms developed in this study would be able to immobilise the Pu content expected from the PCM waste
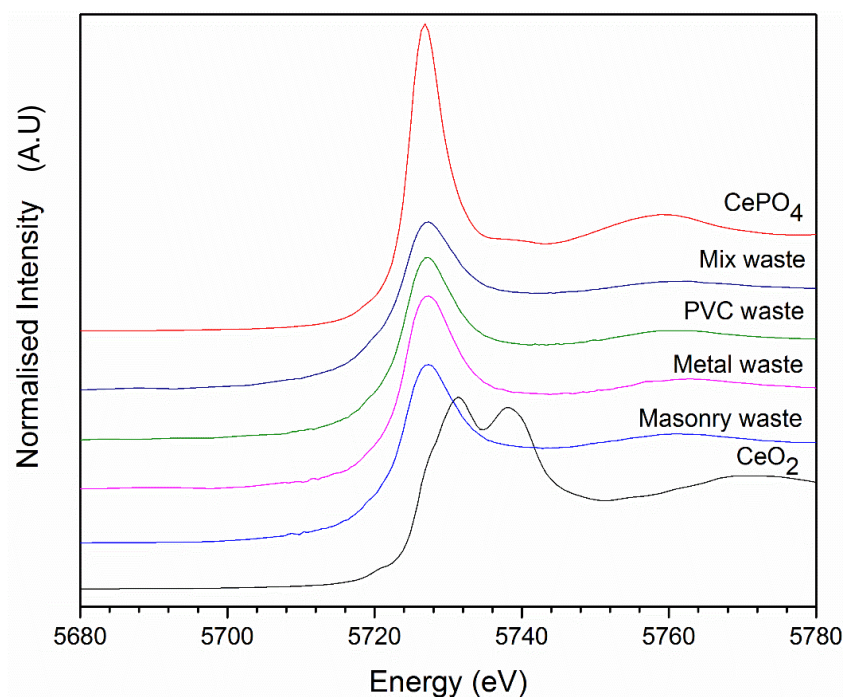
Figure 4.14 Ce L$_3$ edge XANES data from CeO$_2$ (Ce^{4+} standard), CePO$_4$ (Ce^{3+} standard with monazite structure) and slag fractions from vitrification of simulant PCM wastes.

Sample	E_0 (eV)	Oxidation state
(Ref) CeO_2	5731.41	+4
(Ref) $CePO_4$	5726.81	+3
Masonry	5727.47	+3 (86%)
Metal	5727.18	+3 (92%)
PVC	5727.11	+3 (93%)
Mix	5727.21	+3 (91%)

Table 4.4 Position of pre edge features for each of the samples determines the amount of Ce^{3+} in the glass. It is assumed that the position of the absorption edge (E_0) for mixed oxidation states is an interpretation of E_0 for the two reference materials.

4.5 Determination of redox conditions within the melt using Mössbauer spectroscopy

Mossbauer studies can be used to determine the redox conditions within the melt by calculating the iron ratio within the glass. The Fe^{2+}/Fe^{3+} ratio is a good internal standard of the redox conditions within the melt. The iron ratio provides important information in terms of processing and waste form considerations. For example, an Fe^{2+}/Fe^{3+} ratio value between 0.1 to 0.5 (as a measure of the redox state of the melt) should provide a sufficient level of safety against foaming or precipitation and should be the goal for processing nuclear waste glass (Goldman et al. 1985). The redox conditions can also induce gas solubility reactions that lead to the formation of a stable layer of glass foam. Depending on the melter design, reducing conditions may be disadvantageous, due to the risk of conductive phases forming within the melt. Within a glass, Fe can exist as either a network forming (tetrahedral) site or a network modifying (octahedral) site. It is known that the redox and coordination environment of Fe in glass can strongly influence the physical properties of that glass such as viscosity, liquidus temperature and density (Mysen 1985). For this reason, there have been a number of studies performed using

Mössbauer spectroscopy to determine and quantify the oxidation state of Fe in glass (DeGrave 1986). This section concentrates on the results of the Mössbauer studies performed on the PCM vitrified products and the resultant Fe^{2+}/Fe^{3+} ratio within the glass.

Figure 4.15 - Figure 4.18 show the Mössbauer spectrum for the four vitrified PCM waste streams. Using the various literature sources (Kuno et al. 2000; Dyar et al. 2006; De Grave 2003), enables each phase identified from the XRD traces (Figure 4.5 to Figure 4.12) to be assigned to a particular iron signal from the glass to give the relative area of each Fe species within the glass. For amorphous samples with no crystalline phases present (Figure 4.13 and Figure 4.7), the combination of the Isomer Shift (IS) and the Quadrupole Splitting parameters (QS) is sufficient to identify the valence state and site occupancy of Fe in a given site (Dyar et al. 2006). Table 4.5 gives the Mössbauer parameters in the glass, assigning each iron signal to a corresponding valence state to produce the Fe^{2+} / Fe^{3+} ratio within the vitrified product.
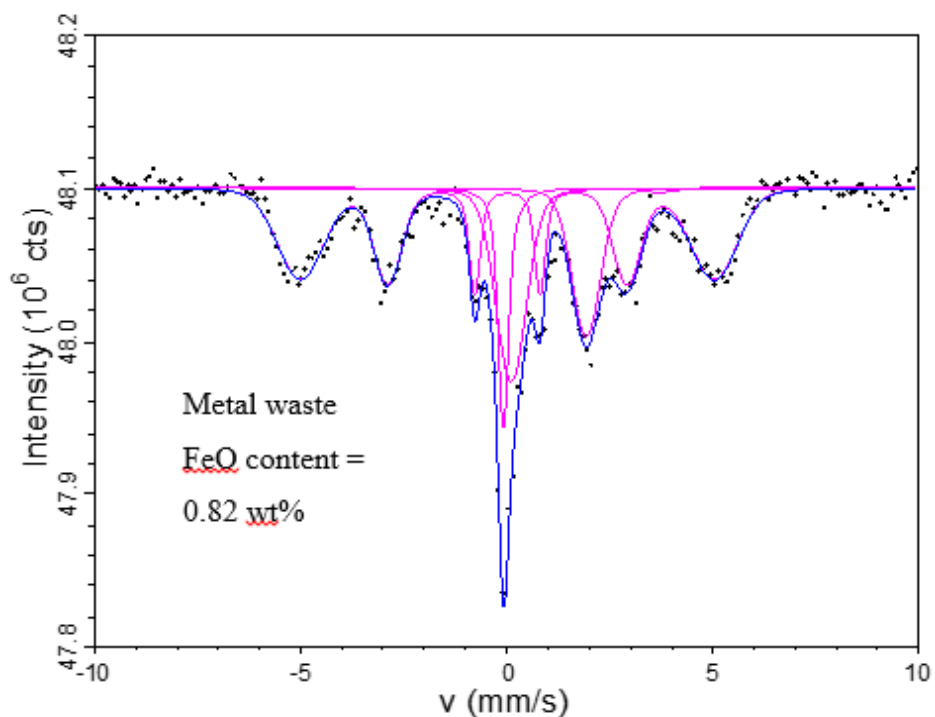
Figure 4.15 Mössbauer spectrum for the glass fraction of the vitrified metal waste with a FeO content of 0.82 wt%. X axis = velocity (mm/s)
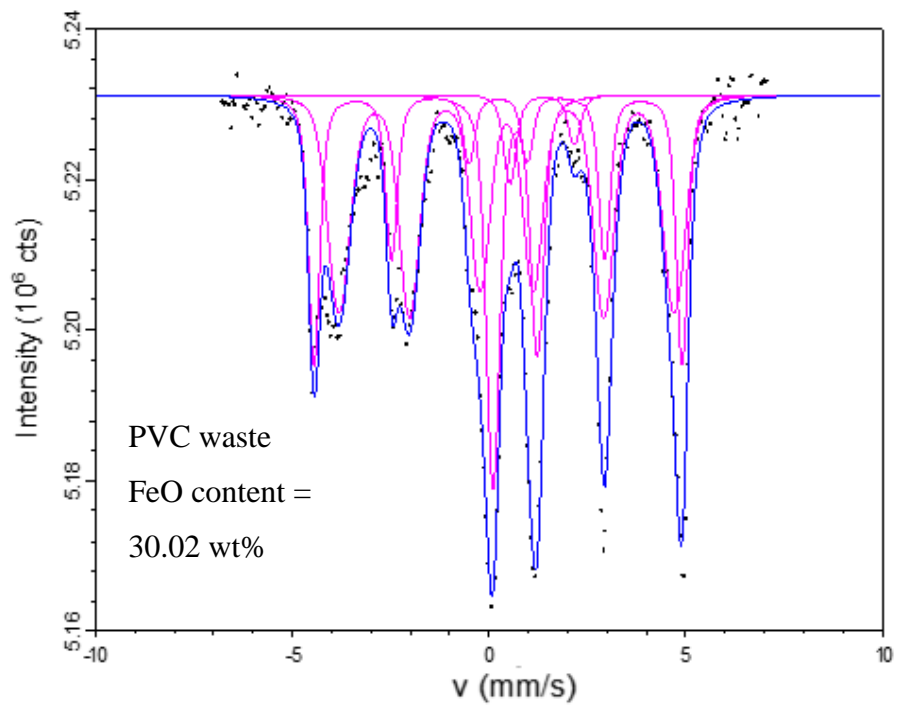
Figure 4.16 Mössbauer spectrum for vitrified PVC waste with a FeO content of 30.02 wt%. x axis = velocity (mm/s)
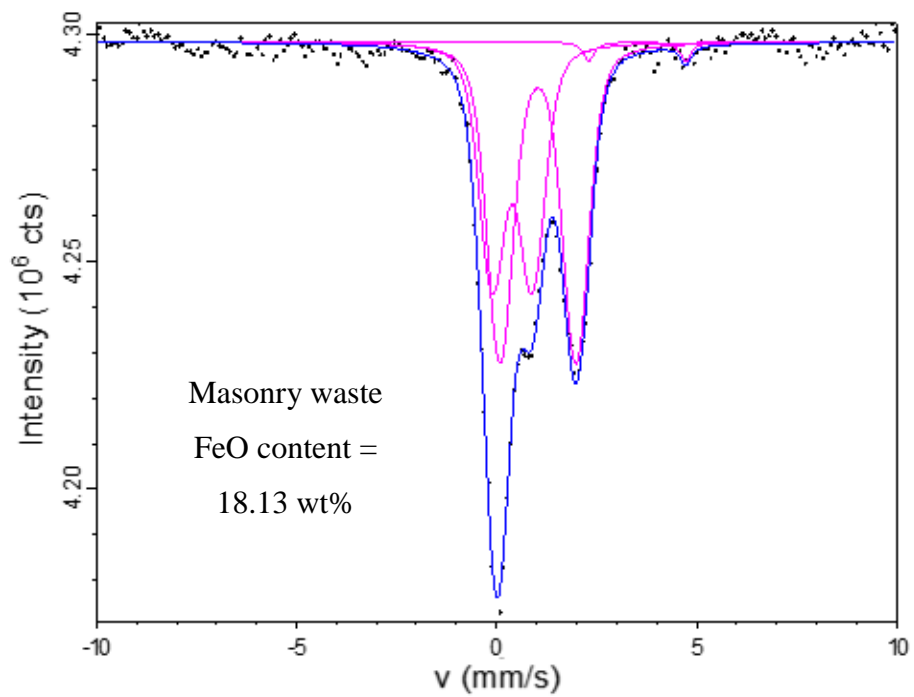
Figure 4.17 Mössbauer spectrum for vitrified Masonry waste with a FeO content of 18.13 wt%. x axis = velocity (mm/s)
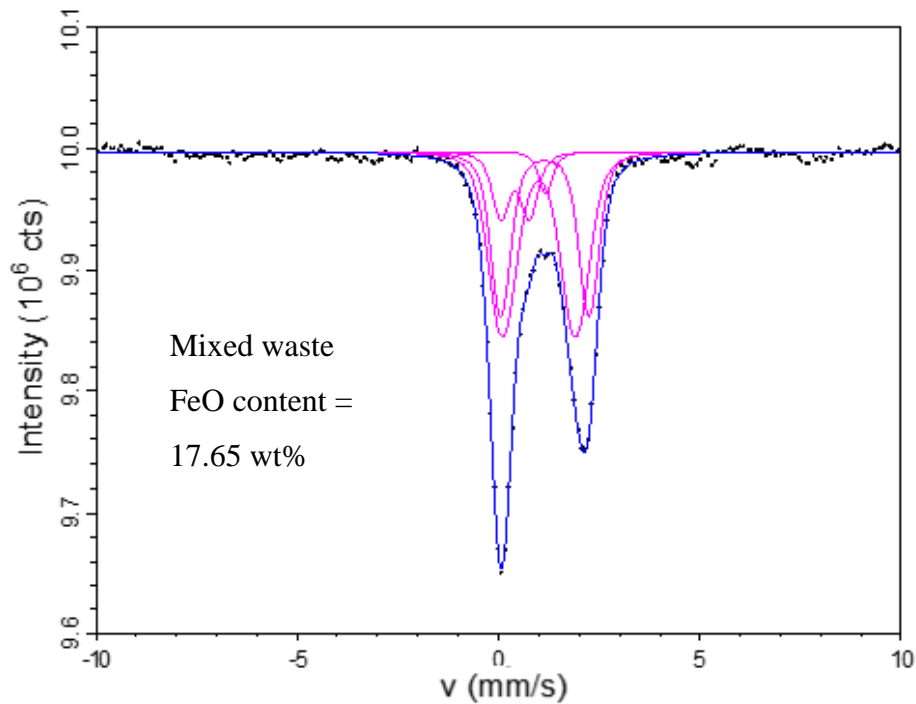
Figure 4.18 Mössbauer spectrum for vitrified Mixed waste with a FeO

content of 17.65 wt%. x axis = velocity (mm/s)

To calculate the Fe^{2+}/Fe^{3+} ratio within the glass the amorphous component has been used, as this will give a more accurate representation of the redox reactions within the glass melt. Table 4.5 provides a quantitative measure of the fraction of crystallisation within the glass. For example, using the IS and QS, the amount of magnetite in the PVC waste can be determined as 77.4 % ± 2%. It would be interesting to determine the consistency of this method of quantifying crystalline phases in materials with other methods such as Rietveld refinement (Kniess et al. 2005). Mössbauer spectroscopy could be used as a method of quantifying crystalline phases within glass provided the crystalline phases contained Fe. The following section begins by describing the Mössbauer spectra shown in Figures 4.15 to 4.18 before commenting on the effectiveness of using the Fe^{2+}/Fe^{3+} ratio within the amorphous component to predict redox conditions within the melt.

Sample	IS (mm/s)	QS (mm/s)	Assigned phase	Site	Area (±2%)	(Fe^{2+}/ΣFe)
Mixed waste	1.09	1.81	Magnesioferrite	Fe^{3+}	50.7	
	1.15	2.19	Glass	Fe^{2+}	34.1*	
	0.41	0.71	Glass	Fe^{3+}	11.1*	0.74*
	0.89	0.26	Chromite	Fe^{2+}	3.3	
Masonry waste	1.02	1.90	Glass	Fe^{2+}	59.0*	
	0.39	1.00	Glass	Fe^{3+}	41.1*	0.58*
Metallic waste	0.02	0.00	Metal (M)	Fe^{0}	54.9	
	0.14	0.43	Glass	Fe^{3+} (O)	8.4*	
	1.93	0.02	Glass	Fe^{3+} (T)	11.5*	0.55*
	1.90	3.59	Glass	Fe^{2+}	25.2*	
PVC waste	0.23	0.00	Magnetite (M)	^{T}Fe^{3+}	25.5	
	0.45	0.00	Magnetite (M)	^{O,T}Fe$^{2+,3+}$	51.9	
	0.67	1.13	Glass	Fe^{2+}	18.7*	0.83*
	1.35	1.64	Glass	Fe^{3+}	3.77*	

*Table 4.5 Assigned Mössbauer signal parameters (± 0.02 mm/s). Fe^{2+} / Fe^{3+} calculated using Is and Qs. (M) = magnetic site (sextet). O = octahedral site T = Tetrahedral site. * denotes the iron signal from the amorphous component which was used for the Fe^{2+}/Fe^{3+} ratio.*

Goldman et al (1985) states that operators should aim for a Fe^{2+}/Fe^{3+} ratio in terms of processing and wasteform consideration. From this information, it would suggest that the Mixed waste and PCV waste, were poor glasses based upon redox considerations. However from the characterisation and melting behaviour of both glasses, there was very little evidence of foaming or precipitation of the melt. This would suggest that the Fe^{2+}/Fe^{3+} can not be used in isolation to determine the processing capability of various glass wasteforms. It is clear from this study that the other factors are heavily influcing the processing conditions, this could be the large fraction of crystalline material or the hetergenous nature of the waste. Further study is needed to related the various factors to processability other than simply using the redox ratio, especially in complex glasses such as these with a number of multi-valent ions.

The Mössbauer spectrum shown in Figure 4.15 for the slag fraction of the vitrified metal waste shows a "sextet" feature which corresponds to magnetic ordering within the glass. The intensity of the peaks within the spectrum is very weak due to the small amounts of iron oxide within the slag fraction (0.82 wt. %). Figure 4.7 shows the slag fraction of the vitrified metal type has an amorphous structure. SEM images in Figure 4.7 show small metallic inclusions within the glass matrix which account for the sextet feature in the Mössbauer spectrum due to the magnetic properties of the metal inclusions. This accounts for 54.9 % of the iron signal from the spectrum. Excluding this, presents the Fe^{2+} / Fe^{3+} ratio of the slag fraction which is 0.55 ferrous ions within the glass structure.

The PVC waste has a complicated spectrum, as shown in Figure 4.16. Figure 4.5 shows that the crystalline phase within the glass is magnetite, and due to the wide range of uses of magnetite there have been a number of Mossbauer studies which determined the redox state of Fe within magnetite (Iyengar et al. (2014); Mada (1977); Gedikoǧlu (1983); Topsoe et al. (1974).

Magnetite is an inverse spinel because the tetrahedral sites (A) are occupied by Fe^{3+}, while the octahedral sites (B) are occupied by 50:50 mixture of Fe^{2+} and Fe^{3+}. This gives the structural formula for magnetite as $[Fe^{3+}]A [Fe^{3+}, Fe^{2+}]BO_4$. Magnetite is ferrimagnetic as a result of the crystal structure, this gives the slag waste form spontaneous magnetization properties. This was noticed when small shards of the slag waste from were attracted to the metallic tweezers.

Gorski (2010) states that magnetite can have a range of oxidation states dependent upon the amount of structural Fe^{2+}, which can be discussed quantitatively as the magnetite stoichiometry ($x = Fe^{2+}/Fe^{3+}$). Figure 4.5 states that the magnetite present within the PVC waste matched with PDF card 19-629, and contained 69.0% Fe^{3+} and 31.0% Fe^{2+}, confirming that the magnetite present within the glass waste form is stoichiometric magnetite (Fe_3O_4) giving an ideal Fe^{2+} content. The PVC waste Mössbauer spectrum shown in Figure 4.16 can be used to confirm this finding.

The PVC waste Mössbauer spectrum shown in Figure 4.16 is characterised by two sextet features. The left hand side of the spectrum has clearly defined sextet features, which then overlap on the right hand side of the spectrum. The Fe signal resulting in the sextet features are from the two magnetite sublattices, site A (tetragonal site $^{et}Fe^{3+}$) and site B (octahedral site $^{Oct}Fe^{2+, 3+}$). The sextet features can be assigned to each site by the position of the isomer shift (IS), as the IS is proportional to the electron density for Fe atoms. Lin et al. (2016) states that Fe^{2+} has a lower electron density than Fe^{3+} resulting in a IS value that is higher for Fe^{2+} atoms than that of Fe^{3+}. Therefore, it is observed that the IS value is greater in the combination of the Fe^{2+} and Fe^{3+} sextet than the $^{Tet}Fe^{3+}$ sextet, this approach is used to obtain the values shown in Table 4.5.

The stoichiometry of the relative areas of sites A and B within the magnetite structure can be obtained using the following formula (eq. 2) (Gorski 2010).

$$X_{MS} = \frac{Fe^{2+}}{Fe^{3+}} = \frac{\frac{1}{2}Fe_{Oct}^{2.5+}}{\frac{1}{2}Fe_{Oct}^{2.5+} + Fe_{Oct,Tet}^{3+}} \tag{2}$$

After inserting the values from Table 4.5 into the above formula the gives the following;

$$\frac{\frac{1}{2} \times 51.94}{\frac{1}{2} \times 51.94 + 25.59} = 0.50$$

This value corresponds to the most reduced form of magnetite (stoichmetric magnetite) and all of the available interstitial sites are occupied by ferrous and ferric ions. The results from the Mössbauer study shown in Table 4.5 agree with the XRD results shown in Figure

4.5 confirming the presence of stoichiometric magnetite, with an ideal Fe^{2+} content, within the glass.

Elemental mapping in Figure 4.5 shows the distribution of Fe is also present within the amorphous phase. Lorentzian doublets were fitted to account for the iron signal from the amorphous phase. Using the QS and IS values, the specific coordination environment of the relevant Fe^{+} ions can be obtained (Dyar et al. 2006) as shown in Table 4.5. The overall Fe^{2+} / Fe^{3+} ratio of the vitrified PVC waste form can be calculated, which gives a fraction of 0.83 ferrous ions within the amorphous component of the waste form.

Figure 4.13 shows that the vitrified masonry waste contains an amorphous structure. Therefore, using the approach of Dyar et al. (2006), the QS and IS values, from the Mossbauer spectrum shown in Figure 4.18, can be used to determine which $Fe^{2+/3+}$ coordination site is responsible for each signal in the spectrum. The masonry waste shows an iron ratio of 58.9% ferrous ions within the glass structure. Volf (1984) has shown that Fe^{2+} tends to decrease chemical durability of borosilicate glasses.

The Mössbauer spectrum for the mixed waste (Figure 4.18) was fitted with Lorentzian doublets, centre shift (IS) and quadrupole splitting (QS) parameters. Figure 4.12 identifies a number of crystalline phases within the glass, including $Mg(Fe^{3+})_2O_4$, magnesioferrite spinel phase and $(Fe,Mg)Cr_2O_4$ chromite phases. The EDX map in Figure 4.12 shows the distribution of Fe within the microstructure is contained to the magnesioferrite, chromite and the amorphous glass phase. The three fitted Lorentzian doublets for the mixed waste Mössbauer spectrum correspond to these three identified phases as shown in Table 4.5. From the available literature it is possible to assign each site, using the position of the QS and IS values, to a specific coordination environment of the relevant Fe ions. Using the iron signals from the amorphous component of the waste form, the Fe^{2+} / Fe^{3+} ratio can then be calculated. The mix waste shows a fraction of 0.74 ferrous ions within the glass structure.

When analysing Mössbauer results presented in this section, it is important to consider the redox reaction of ferrous and ferric iron. The redox reaction can be written in terms of the ionic species present in the system as (Eq.3) (Paul 1990):

$$4Fe^{2+} \text{ (glass)} + O_2 \text{ (glass)} \rightleftharpoons 4Fe^{3+} \text{ (glass)} + 2O^{-2} \text{ (glass)} \qquad (3)$$
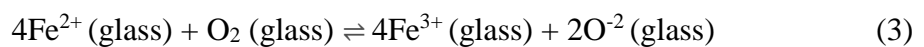
The reaction describes the way in which Fe ions are solvated by the medium in which they react. In this case the medium is the molten glass. Using this equation, the factors determining redox equilibrium in glass are;

- The activity of the oxygen in the melt
- The activity of the oxygen ion in the melt
- The equilibrium constant which is a function of the free energy change and temperature of the reaction
- The activity of the redox ions in the melt.

These factors will be used to analyse the results, in particular the effectiveness of using Mössbauer spectroscopy to determine the redox chemistry within the melt.

It has already been noted that the choice of crucible has a large influence on the redox chemistry of the glass. The plumbago crucible imposes a reducing atmosphere resulting in Fe metal forming at the base of the crucible. At equilibrium, the activity of oxygen in the furnace atmosphere and that in the glass melt are identical (Paul 1990). Baak (1961) studied what effect Pt and Al_2O_3 crucibles had on iron – oxygen equilibrium in glass. Baak (1961) was able to show that in an Al_2O_3 crucible the Fe^{2+} / Fe^{3+}ratio reached equilibrium after 3 hours of melting. The glass melts in this study were held at a temperature of 1560°C for 4 hours. Therefore it is likely that the activity of oxygen in the furnace atmosphere and that in the glass melts are identical for the waste streams vitrified within the Al_2O_3 crucibles. Using this approach enables a simple approach to discussing the FeO and Fe_2O_3 content of the glass in relation to the oxygen pressure (Eq. 4). This method avoids the unknown oxygen potential in the glass (O^{2-}).

$$2FeO + \frac{1}{2} O_2 = Fe_2O_3 \qquad\qquad (4)$$

Adding Fe to the system changes the oxygen potential. This factor has to be independently established by E.M.F measurements. This assumption can be justified by using the partial pressure phase diagram for the iron oxygen system Figure 4.19. It is known from characterising the vitrified PVC waste type (Figure 4.5), and through the Mössbauer analysis that the Fe_2O_3 present within the glass is stoichiometric magnetite. Therefore the ferrous and ferric iron associated with the magnetite exist within the glass as pure oxides in the form of spinel phases. The same method is used in the partial pressure phase diagram in Figure 4.19 and provides some estimation to the oxygen partial pressure of the system. Using the phase diagram for the vitrified PVC waste type, the formation of

stoichiometric magnetite upon cooling from 1560°C indicates a partial pressure value between -6 and 0 mbar. This is consistent to measurements taken within conventional glass making furnaces (Kemori et al. 1986).

The phase diagram in Figure 4.19 also indicates the oxygen partial pressure value for which Fe species forms. This indicates that the Plumbago crucible imposes a reducing atmosphere resulting in greater negative values for the partial pressure of the system of less than -12 mbar. This results indicates that for the melts performed within the Al_2O_3 crucibles, the activity of the oxygen inside the glass melt was at equilibrium with the activity of oxygen in the furnace.
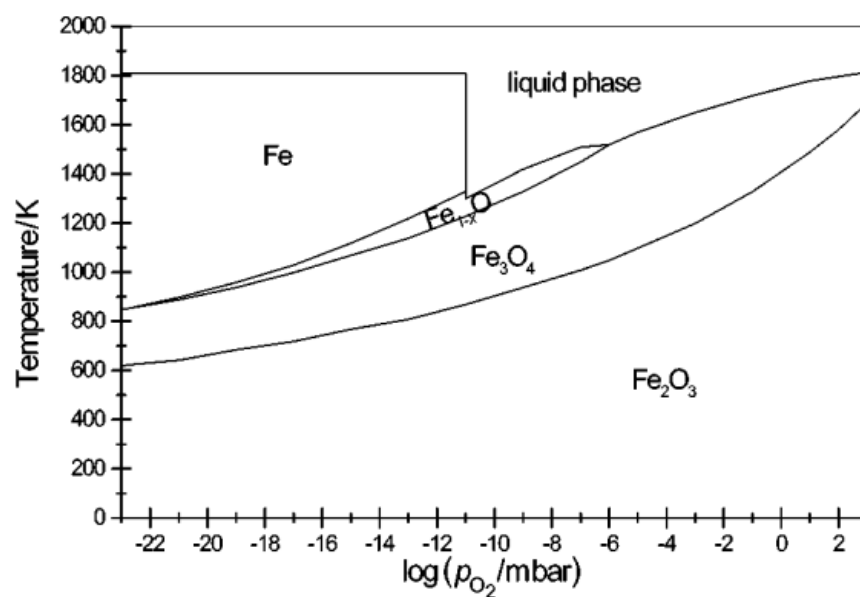
Figure 4.19 Calculated temperature pressure phase diagram for the iron oxygen system. Figure adapted from (Muan 1958).

A small metal fraction was present for the Mixed waste at the bottom of the crucible as shown in Figure 4.2. This disagrees with the partial pressure phase diagram in Figure 4.19, as it has been shown that the partial pressure within the alumina crucibles, for which the mixed waste was vitrified in, is above the value for which Fe metal forms. Therefore, this indicates other factors are influencing the redox chemistry of the glass, and the redox reaction in the glass melt is more complicated than simply a measure of the activity of oxygen inside the glass melt.

It is known that the glass composition can influence the thermodynamics of the Fe^{2+} / Fe^{3+} equilibrium and the iron diffusivity in silicate melts. Experimental studies in the

literature all show that the proportion of the redox ion in the higher oxidation state increases with the basicity of the glass (Duffy et al. 1976; Thiemsorn et al. 2008; Duffy et al. 2000). This generally translates as an increase in oxygen ion activity with increasing concentrations of the modifier oxide (Thiemsorn et al. 2008). This can be explained by considering the ability of the oxygen to donate negative charge, which is at a maximum when it exists as the O^{2-} ion uninfluenced by non-polarizing surrounding cations (Nanba 2011) (e.g Na^+, K^+ or Ca^{2+}). However, when oxygen is attached to Si, in the Si-O-Si units, the glass basicity is much less. This is due to the highly polarizing Si^{4+} ions. The polarization of O^{2-} results in negative charge being drawn off the ion therefore the oxygen atoms are less able to donate charge to a solute metal ion (Duffy 1976), resulting in a higher proportion of ferrous ions within the glass. Increased amounts of Na^+ in the glass also stabilize the FeO_4^- resulting in the Fe^{2+}/Fe^{3+} equilibrium adopting a more oxidised state (Rüssel 2004). The concentration of modifier oxides, including Na_2O and CaO, are similar for the vitrified PVC, Mixed and Masonry waste at approximately 6 and 5 wt% respectively, therefore it is unlikely this is influencing the redox chemistry for the various glass waste forms.

The Al_2O_3 content in the glass should not be discounted however. The increased amounts of Al_2O_3 in the glass originate from corrosion of the Al_2O_3 crucibles. Al is incorporated into the glass as AlO_4^-, which in a similar way to FeO_4^-, need cations for charge compensation. Therefore, increasing the Al_2O_3 concentration in the glass leads to decreasing alkali concentrations available to compensate the charge of FeO_4^- tetrahedra. Charge balanced AlO_4 tetrahedra can substitute for SiO_4 tetrahedron as a network former. As stated previously this reduces the ability for the oxygen atoms to donate charge to solute metal ions resulting in higher proportions of ferrous ions within the glass (Rüssel 2004). This may explain why the amorphous component within the PVC waste glass has higher proportion of ferrous ions within the glass network, as PVC has a higher proportion of Al_2O_3 within the glass structure as determined by XRF methods (Table 4.2).

This section has highlighted the complexity of the redox reactions for ferrous and ferric iron. The heterogeneous nature of the waste and the large amounts of elements within the glass including transition metals such as Cr and Fe which display a number of valence states within the glass further complicates the issue. This section has also shown that varying factors determining redox equilibrium in glass. Despite the fact that the partial pressure of oxygen within the system was shown to be similar for the glass melts

performed within the Al_2O_3 crucibles the varying ratio of Fe^{2+} / Fe^{3+} shows the large influence the glass composition plays with the redox chemistry. For this reason Mössbauer studies of laboratory scale melts within alumina crucibles are limited in the ability to predict redox conditions that might be present within an industrial scale melter. The metal fraction present within the Plumbago crucible for the high metal waste feed is a result of the reducing atmosphere. This is shown in the partial pressure phase diagram shown in Figure 4.19. The evidence shown in this section indicate that the resultant metal fraction seen in the mixed waste is influenced by the glass chemistry as opposed to the activity of oxygen inside the glass metal. The solubility of the FeO and Fe_2O_3 within the glass appears to be influencing the formation of the metal fraction in the mixed waste. It is known that an ordinary soda-lime-silica glass can dissolve some 30-40 wt% of iron at 1400°C (Paul 1990). Using the mass balance of the system before and after the melts, the solubility of the metal fraction can be determined for the various waste streams. The vitrified PVC waste successfully dissolved 44.7 wt% of the metal waste within the glass matrix. The Mixed waste however dissolved 30.3 wt % of the metal waste within the glass matrix. The reason for this difference comes from the presence of Cr from the stainless steel. The PVC waste vitrified only the mild steel which contains trace amounts of Cr. The mixed waste however had large amounts of stainless steel, containing substantial quantities of Cr. It is known that when more than one redox component is present in the same melt, the resulting oxidation-reduction equilibrium becomes more complicated due to interactions among the redox couples. Schreiber et al. (1987) experimental study of mutual interactions of redox couples for geochemical melt systems conclusively proved the following internal electron exchanges;

$$Cr_{(melt)}^{3+} + 3Fe_{(melt)}^{3+} \rightarrow Cr_{(melt)}^{6+} + 3Fe_{(melt)}^{2+}$$

$$2Cr_{(melt)}^{2+} + Fe_{(melt)}^{2+} \rightarrow 2Cr_{(melt)}^{3+} + Fe_{(metal)}^{0}$$
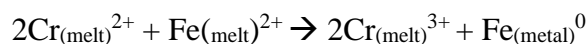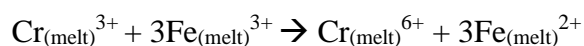
The bottom reaction clearly shows that the presence of Cr^{2+} in the melt causes the formation of Fe metal. This explains why the solubility of metal is lower in the mixed waste and why a metal fraction was present within the mixed waste. It would also explain the higher amounts of ferrous ions compared to ferric ions in the mixed waste glass. It should also be noted that internal electron exchanges will occur with other multivalent elements including Ce (acting as a Pu surrogate in this study). Schreiber (1980) was able to prove the following electron exchange reaction.

$$Ce_{(melt)}^{4+} + Fe_{(melt)}^{2+} \rightarrow Ce_{(melt)}^{3+} + Fe_{(melt)}^{3+}$$
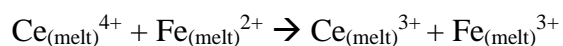
XANES analyses determined the Ce oxidation state to be predominately 3+. Therefore it is likely this reaction is leading to increased ferric ions within the glass samples. It would also explain why the masonry waste, with the higher proportion of Fe^{2+} within the glass, had the lowest amount of Ce^{3+} determined by the XANES analysis in Figure 4.15.

From a practical perspective, thermal treatment operators aiming to control the redox equilibrium of Fe^{2+}/Fe^{3+} ratio, may have more success by tailoring the glass chemistry to meet the objectives of the melt. For example Section 4.9 in this study investigates the potential for oxidising the metal fraction found within the vitrified waste by changing the glass chemistry. From the results seen in this section, this may be a more practical approach as opposed to controlling the activity of oxygen inside the melt.

4.6 Volume reduction calculations

As mentioned previously, one of the key advantages of thermally treating ILW is the potential volume reduction achieved, which can equate to large cost savings in terms of disposal within a GDF. With an estimated PCM waste volume of 30,000 m^3 (set to continually grow) volume reduction is a key requisite of PCM immobilisation. In terms of potential costs savings the greater the volume reduction the greater the savings will be in terms of storage. However, criticality issues also dictate the amount of host material available within the waste form, thereby requiring a minimum level of dilution to ensure safe dispersion of Pu within the host matrix. This provides an upper boundary for volume reduction which will need to be considered when analysing the waste forms produced in this project. This section uses the data generated to calculate potential levels of volume reduction, as demonstrated via thermal treatment, relative to untreated PCM drums.

Mass balance measurements before and after thermal treatment, are shown in Table 4.6, allowing quantification of the achieved volume reductions for each PCM waste stream as shown in Table 4.7. The results are given as volume reduction against a 200L untreated PCM waste drum. As expected the waste stream with the greatest volume reduction is the PVC waste (88.1% volume reduction), this is because the PVC glass additive was added at a 1:1 wt. % ratio, with the mass of PVC being considerably less than the other waste streams. Calculating the mass balance of the system for the metal waste stream was therefore challenging. This was due to the oxidation of the graphite clay crucible,

resulting in considerable mass loss from the crucible. Therefore it is difficult to differentiate between mass loss of the metal waste stream with that of the crucible. The volume reduction potential of the Mixed waste and Masonry waste was 55.5% and 64.9% respectively.

The results show that considerable volume reductions can be achieved when thermally treating PCM waste with volume reductions ranging from 88.1% - 55.4% against untreated 200L PCM waste drum. A potential risk with minimizing the host matrix is the increased criticality concerns as a result of concentrating the Pu within the waste form.

	PVC	Masonry	Metal	Mixed
Wt (empty crucible)/g	589.4	574.6	1035.6	499.4
Wt (can + PCM)/g	91.1	138.5	208.1	137.2
Wt (Additive)/g	91.1	138.5	208.1	137.3
Wt (Waste+Additive)/g	182.3	277.1	417.0	274.6
Wt (All) Before Melting/g	773.5	851.8	1451.7	774.1
Wt (All) After Melting / g	738.4	843.8	1298.4	766.6
Wt Mass loss/g	35.0	7.9	153.3	7.4
Wt (Waste Remaining)/g	148.9	269.1	262.8	267.2
Oxide Fraction/g	148.9	269.1	105.1	247.2
Metal Fraction/g	Na	Na	157.7	19.9
Oxide Fraction/Mass %	100%	100%	39.9%	92.5%
Metal Fraction/ Mass %	0%	0%	60.0%	7.4%
Final Mass %	163%	194%	126%	195%
Density (Oxide) / g/cm^3	3.0777	2.7752	2.5117	2.8579
Density (Metal) / g/cm^3	NA	NA	7.6910	7.8610

Table 4.6 Mass balance calculations of the vitrified PCM waste products

Hyatt et al. (2014) has calculated the lower boundaries for vitrified PCM volumes. This was done using the following information. Egan (2008) states that current PCM waste drums contain less than 230g Pu per 200L drum. Criticality concerns dictate the maximum allowable concentration of Pu is 60g / L, with the ideal value at a concentration of 6g / L. Therefore 38.3 litres of oxide material is needed to immobilise the Pu at a concentration of 6g / L.

This decreases to just 3.8 litres of oxide phase at the uppermost Pu concentration limit of 60g / L. The calculated oxide phase volumes from this study are 23.9 L for the vitrified PVC waste, 70.0 L for the Masonry waste and 89.1 L for the Mixed waste. The results for the metallic waste were excluded due to the uncertainty of the results from the mass loss of the graphite/clay crucible. The PVC oxide volume is higher than the preferred 6g / L, with Pu concentration of 9.61g / L achieved using the 1:1 wt % ratio of additive to waste. Section 4.3.1 has shown that the Ce is homogenously distributed which may provide confidence in terms of the safety case that the criticality risk, at concentrations of 9.61g / L is acceptable. The vitrified Masonry and Mixed wastes have large volumes providing dilution factors of 3.29 g / L and 2.58 g / L respectively, far below the acceptable value of 6 g / L. This provides the opportunity to potentially lower the amount of oxidizing agent providing greater volume reductions.

It is important to consider the waste volume potential against the current treatment method of super compaction with cement encapsulation. Figure 2.2 shows the cemented waste form containing the compacted 200 L steel drums. In this example there are six compacted drums encapsulated within cement, which will be contained within a 500 L container. From this we can calculate the volume reduction of a single PCM drum against an untreated 200 L PCM drum, which equates to 58.35 % volume reduction, via super compaction with cement encapsulation. It is known that not all PCM waste streams are suitable for super compaction and cement encapsulation, so it is likely that this figure is a best case scenario. Table 4.7 shows that the vitrified PCM waste has much greater volume reduction potentials compared to current treatment methods whilst producing a much more stable and durable waste form. In terms of criticality concerns, the vitrified waste product has much greater credentials compared to the cement encapsulated product. The work performed here has shown that the Ce (acting as a Pu surrogate) is homogenously distributed within the glass matrix. However, in the encapsulated cement wasteform there is no way of knowing confidently how the Pu is distributed within the

wastefrom giving rise to the risk of "hotspots" areas of highly concentrated Pu. This project has shown that in terms of volume reduction potential and avoidance of criticality issues the vitrified waste form are superior to the current treatment method.

	PVC	Masonry	Metal	Mixed
Uncompacted Volume / m^3	0.2	0.2	0.2	0.2
Untreated Mass / kg	45	100	100	100
Mass (additive)	45	100	100	100
Total Mass (Waste+Additive) / kg	90	200	200	200
Final Mass After Treatment / kg	73.56	194.28	126.32	194.60
Volume (Oxide) / m^3	0.0239	0.0700	0.0419	0.0865
Volume (Metal) / m^3	0	0	0.0205	0.0025
Total volume / m^3	0.0239	0.070	0.0624	0.0891
Total Volume / L	23.91	70.01	62.36	89.07
Volume as fraction of original volume	0.1195	0.3501	0.3118	0.4453
Volume Reduction / %	88.1%	64.9%	68.8%	55.4%
	±0.5%	±0.5%	±0.5%	±0.5%

Table 4.7 Calculated volume reduction potentials for the vitrified PCM waste drums based upon mass balance

Section 4.3.2 shows that Ce is more thermodynamically favourable to partition within the oxide fraction, this may allow the metal fraction to be disposed of as LLW. If this was achievable the potential cost savings can be estimated for the PCM waste inventory, using the volume reduction calculations in this section. LLW repository charges £3,077/m^3 to dispose LLW. A final disposal option for ILW is yet to be determined, therefore an estimation of the disposal of ILW will need to be taken. Miller et al. (2006) report provides the costing for the construction, operation and eventual closure of ILW repository, estimated to be £6.2 billion. In this same report the estimated ILW inventory is 220,000 m^3. Therefore a sensible estimate of £28,181/m^3 for disposal of ILW can be determined for the purpose of this study. Using the information from Table 4.7, the

estimated cost savings can be calculated per 0.2 m³ PCM waste drum containing a large fraction of metal waste. Table 4.7 shows each volume of PCM waste drum, once vitrified, is approximately 0.06 m³. Therefore, if no separation between the oxide and metallic fraction was attempted, then the entire volume of waste would be disposed as of ILW costing £1,758 per PCM waste drum. Table 4.7 states that approximately 0.04 m³ of the vitrified metal waste is oxide fraction and approximately 0.02 m³ is metal fraction. Table 4.8 demonstrates the potential cost savings from separating the metal and oxide fraction. Using the information from Table 4.7, the calculations shown in Table 4.8 show that ~30% cost savings can be achieved from disposing the metal fraction as LLW. This compares favourably to the cost of disposing of the supercompacted and cement encapsulated drums which, based upon 6 compacted drums per 0.96m³ of packaged waste, equates to £4508 per compacted drum. The calculations shown in Table 4.8 do not account for a number of other factors including packaging and transport of the waste form. However, considering the large volume of PCM waste drums containing large fractions of metal waste, the project has clearly shown large potential cost savings can be achieved if clean separation of the metal and oxide fraction can be achieved.

	No Separation	Separation	Cement Encapsulation
Volume of ILW (m³)	0.06	0.04	0.96 (6 compacted drums)
Volume of LLW (m³) separated metal fraction	0	0.02	0
Cost of ILW disposal (£)	0.06 m³ x 28181 = 1690	0.04m³ x 28181 = 1127	(0.96*28181)/6= 4508
Cost of LLW disposal (£)	0 m³ x 3,077 = 0	0.02m³ x 3,077 = 61	NA
Indicative cost of disposal of PCM waste drum (£)	1690	1188	4508

Table 4.8 Cost comparison of PCM waste containing high metal waste stream (as based upon Metal waste in this study) when oxide and metal fraction is separated. Volume information was taken from Table 4.7

4.7 Dissolution in simulated hyperalkaline conditions of a cementitious geological disposal facility (GDF)

Dissolution experiments utilising a modified version of the Product Consistency Test B (PCT-B) protocol were carried out on the simulated PCM waste streams. Section 3.5.2 describes the experimental set-up of the PCT-B test in greater detail. In summary, experiments were carried out for a period of 112 days in saturated $Ca(OH)_2$ solution, at a SA/V ratio of 1200 m^{-1}, at 50°C, and with sampling points at 1, 3, 7, 14, 28, 42, 56, 84 and 112 days. ICP-OES analysis was used to determine the concentrations of all elements in solution. The concentration data were used to calculate normalised mass losses and mass loss rates. Section 2.1 explains the concept of immobilising radioactive waste forms from the environment via a GDF. In the design of a GDF, the waste packages would be stored in underground vaults which would then be backfilled with a specially formulated cement-based material known as NRVB (Crossland 2001). NRVB is composed of a mixture of OPC, limestone flour, hydrated lime and water. This produces a high alkaline environment for which the radioactive waste forms would be stored. Previous work has shown that the pH of the repository will remain above 10.5 for about 10^6 years (Atkinson et al. 1989). The hyperalkaline conditions present within the cementitious GDF will minimise the solubility of long lived actinides (Atkins 1992). The slag samples in this experiment were leached in saturated $Ca(OH)_2$ solution, as this was taken to be a simplified representation of a solution that has come into contact with portland cement (PC) based mortar or concrete, which contain significant amounts of portlandite ($Ca(OH)_2$). It should be noted that Figure 4.20 through to Figure 4.22 use the following abbreviations within the graph legend. MET = metal waste stream, MAS = masonry waste stream, MIX = mixed waste stream and PVC = PVC waste stream.

Figure 4.20 shows the pH of the leachate for the vitrified PCM waste mock up drums for all of the waste streams. Generally, the leachate pH of the blanks remained consistent across the experiments at 11.5 to 12.7. The pH does show a noticeable drop at the beginning of the experiment, however this fall in the pH values are likely due to carbonation of the samples after removal from the anaerobic chamber rather than changes in the leachate chemistry. The pH consistency of the pH throughout the experiment indicate that dissolution of the glass does not significantly affect the pH of the system.

Figure 4.21 shows the concentration of Ca in the blank and slag containing solutions. The concentration of Ca remained relatively constant in the blank ($Ca(OH)_2$ solution at ~540

mg/L $\pm$ 60.7 mg/L. This is consistent with the exclusion of CO_2 under the anoxic conditions of the experiment, thereby avoiding carbonation and precipitation of $CaCO_3$. The $Ca(OH)_2$ solution containing the vitrified slag samples saw a rapid decrease of Ca concentration from 500 mg/L at the beginning of the experiment to Ca concentrations in the range of $60 - 200$ mg/L depending on the vitrified sample.
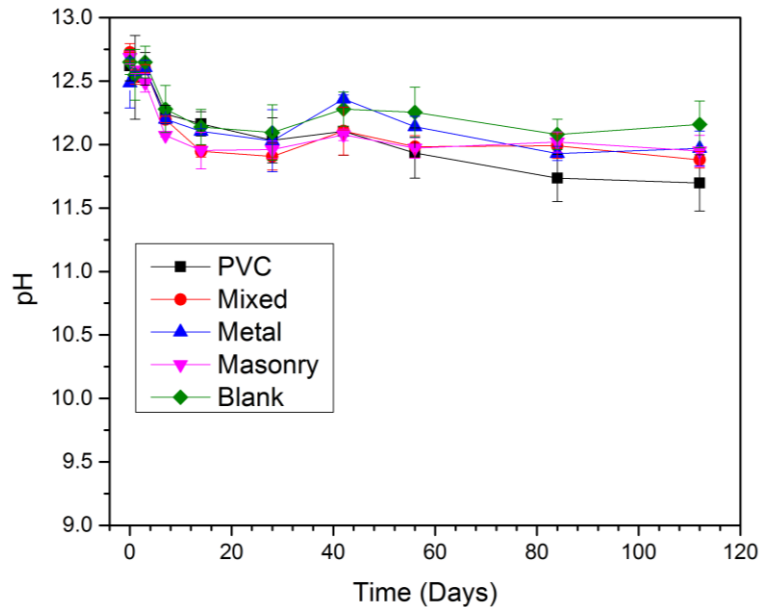
Figure 4.20 pH values for Ca(OH)₂ PCT-B experiments for the vitrified PCM waste mock up drums. MET = metal waste, MAS = Masonry waste, MIX = mixed waste and PVC = PVC waste.

The depletion of Ca from the glass sample solution, implies the consumption of Ca resulting in the precipitation of Ca bearing secondary phases at a rate which exceeds the diffusion of Ca into solution from the filter unit. This is consistent with previous work on other similar ILW glasses under similar conditions (Utton et al. 2013; Hyatt et al. 2014). Although calcium hydroxide was present, it appears that the rate of diffusion from the filter unit was insufficient to maintain a saturated concentration in solution. Despite this depletion of Ca from test solution, the hyper alkaline pH conditions, shown in Figure 4.20, were maintained throughout the experiment. Monolith samples were also run, with the experimental setup described in section 3.5.3, to analyse the formation of the secondary phases in the form of alteration layers. The results are presented in Section 4.8.
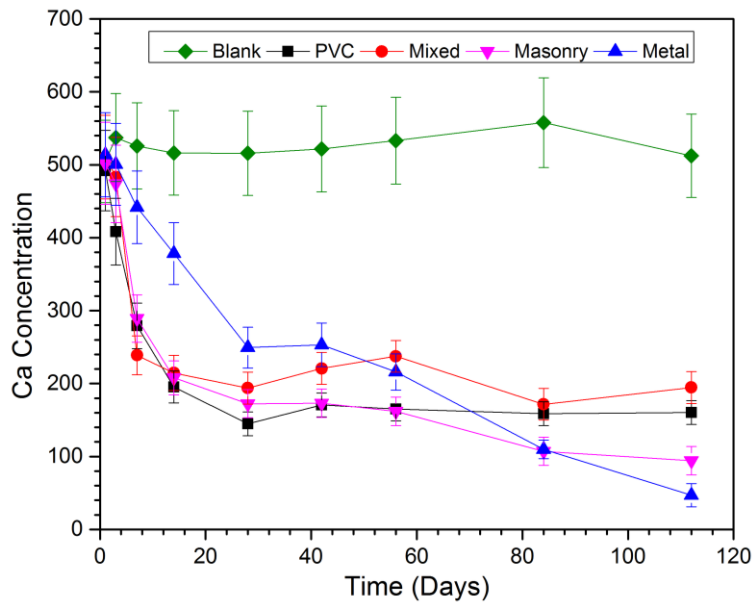
Figure 4.21 Solution concentration (mg/L) of dissolved Ca in blank (i.e. no glass) saturated Ca(OH)₂ solution and for the vitrified PCM waste mock up drums .

Figure 4.22 shows the normalised loss (NL) values of key elements within the glass, with Table 4.9 showing the NL values at day 7, 28 and 112 days. As stated in section 3.1.2, B was added to act as a soluble maker of glass dissolution since B is assumed to not participate with the formation of secondary alteration products. Therefore the NL_B can be a used to assess the durability of the slag products. The NL_{Na} can also be used as a marker for glass dissolution, with the NL_B and NL_{Na} showing similar behaviour for the four vitrified waste streams. The NL_B and NL_{Na} are observed to increase rapidly over the first 14 days of the experiment. After 28 days the rate begins to drop and the dissolution behaviour of the glass approaches the saturation/ residual rate regime. This is likely to be controlled by both saturation of the solution and formation of alteration layers.
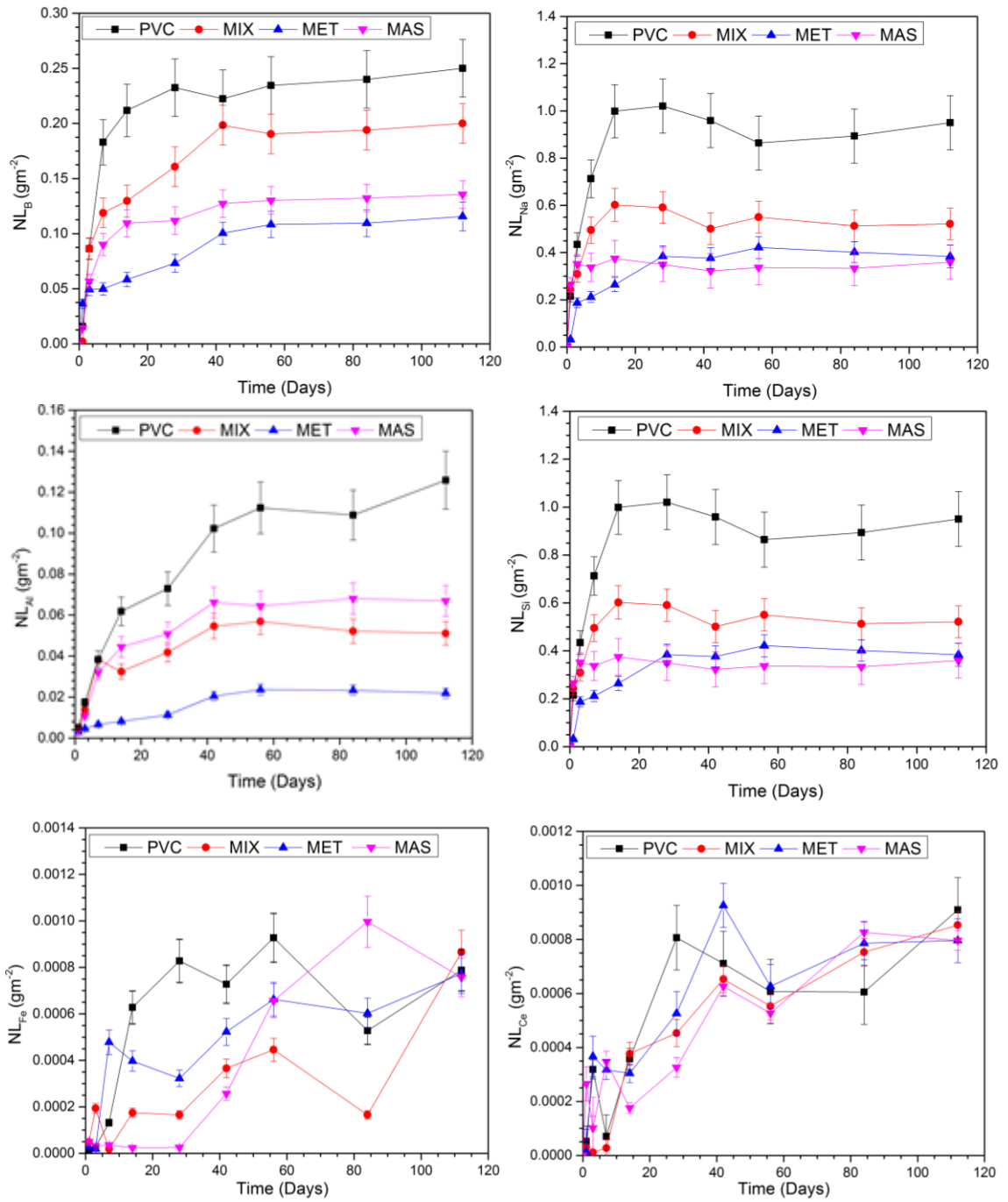
Figure 4.22 Normalized mass loss (gm^{-2}) of B, Na, Al, Si, Fe and Ce into solution from the four vitrified PCM waste streams during 112 day PCT in Ca(OH)$_2$

	NL$_{(Si)}$ (g/m^{-2})			NL$_{(B)}$ (g/m^{-2})			NL$_{(Na)}$ (g/m^{-2})			NL$_{(Ce)}$ (g/m^{-2})	
	7 days	28 days	112 days	7 days	28 days	112 days	7 days	28 days	112 days	7 days	112 days
PVC	(6.16±0.07) x 10^{-3}	(8.55±0.1) x 10^{-3}	(8.69±0.1) x 10^{-3}	0.18 ± 0.02	0.23 ± 0.03	0.25 ± 0.02	0.713 ± 0.10	1.02 ± 0.11	0.95 ± 0.11	(7.11±0.79) x 10^{-4}	(9.09±1.19) x 10^{-4}
MET	(2.69±0.03) x 10^{-3}	(6.17±0.07) x 10^{-3}	(7.91±0.09) x 10^{-3}	(4.97±0.56) x 10^{-2}	(7.30±0.82) x 10^{-2}	0.13 ± 0.01	0.21 ± 0.02	0.39 ± 0.04	0.38 ± 0.05	(3.47±0.38) x 10^{-4}	(4.96±0.36) x 10^{-4}
MIX	(2.41±0.02) x 10^{-3}	(3.91±0.03) x 10^{-3}	(6.38±0.08) x 10^{-3}	0.12 ± 0.01	0.16 ± 0.02	0.21 ± 0.02	0.50 ± 0.05	0.59 ± 0.06	0.52 ± 0.06	(2.73±0.32) x 10^{-4}	(8.53±0.51) x 10^{-4}
MAS	(2.39±0.02) x 10^{-3}	(4.78±0.05) x 10^{-3}	(4.91±0.05) x 10^{-3}	(9.01±1.01) x 10^{-2}	0.112 ± 0.013	0.136 ± 0.013	0.337 ± 0.06	0.34 ± 0.07	0.36 ± 0.07	(3.17±0.35) x 10^{-4}	(7.96±0.81) x 10^{-4}

Table 4.9 Normalized mass loss (g/m^{-2}) of B, Na, Ce and Si during the main phases of dissolution in the 112 days of testing (initial and residual phase) in saturated Ca(OH)$_2$ solution for composition all of the vitrified PCM waste products.

The NL_B and NL_{Na} for the PVC waste shown in Figure 4.22 are considerably greater than that of the other vitrified waste streams providing evidence that the PVC waste form is less durable. This is likely due to the lower amounts of SiO_2 within the glass composition of the PVC waste (37.93 wt %). The vitrified metal waste, deemed the most durable, has the highest SiO_2 content (69.87 wt%) but lowest NL_B. It is generally accepted that an increase in SiO_2 within the glass network increase the durability of the glass because of the increasing ratio of bridging to non-bridging oxygens, leading to an increase in glass network polymerization (Farges et al. 2007; Chick et al. 1981). This also reduces the interconnectivity of alkali channels resulting in lower rates of dissolution (Ellison et al. 1994; Doremus 1975).

The initial and residual dissolution rates based on the normalized release of Na were measured using the values shown in Table 4.9 over the first 7 days and the last 28 days of the experiment respectively. The initial rates were between $0.03 - 0.06$ $gm^{-2}d^{-1}$ and the residual rates were between $0.002 - 0.006$ $gm^{-2}d^{-1}$ for the waste forms derived from the Masonry, Mixed and Metal waste types. These dissolution rates are comparable to previous studies for simulant inactive UK ILW glasses, with initial and residual dissolution rates of $0.02 - 0.04$ $gm^{-2}d^{-1}$ and $0.003-0.005$ $gm^{-2}d^{-1}$, respectively. This was based upon NL_{Na} under similar conditions (Utton et al. 2013; Utton et al. 2012; Hyatt et al. 2014). This consistency in the durability results from this study and previous work is promising, as it shows that despite the heterogeneous nature of PCM waste and the varying composition of the resultant product, the chemical durability of the vitrified product consistently performs well. The initial dissolution rate of the slag derived from the PVC was considerably higher at 0.11 $gm^{-2}d^{-1}$. As discussed this is due to the lower amounts of SiO_2 within the glass. However the residual rate of 0.002 $gm^{-2}d^{-1}$ is comparable with that of the other vitrified products in this work and from the other studies mentioned.

The $NL_{(Na)}$ values are consistently higher than the $NL_{(B)}$ across the four vitrified waste streams. The reasons for this could be that Na ions are mainly ionically bonded to one oxygen within the glass network (Shelby 2005), whereas BO_3 and BO_4 units are covalently bonded to between $1 - 4$ other structural units which would indicate more resistance to leaching from the glass network. This was also seen in a number of glass samples analysed by Backhouse (2016).

4.8 Analysis of alteration product formation

Given that the main response of glass to PCT and MCC-1 tests are generally incongruent dissolution, it is important to study the phases that form on the surface of the glass in the form of alteration layers. The formation and structure of these products can have a large influence on the dissolution behaviour, and long term performance of the glass product. There have been a number of studies performed to better understand the formation of alteration layers on vitrified radioactive waste glasses (Gin et al. 2011; Cailleteau et al. 2008; Corkhill et al. 2013). This section will describe the alteration products formed on the surface of the vitrified PCM waste glass, as it is known that these layers can have a large influence on the chemical durability of the slag waste forms (Utton et al. 2013). Utton et al. (2013) analysed the formation of alteration products during the dissolution of vitrified model ILW in a high-pH Ca rich solution for 170 days. This will provide a useful comparison.

MCC-1 type durability tests were also carried out on the monolith samples to study the formation of alteration layers which had formed on the glass. The monolith samples were kept in $Ca(OH)_2$ solution for 112 days in anoxic conditions at 50°C. The samples were then mounted in resin before grinding and polishing down to a 1μm finish. SEM imaging was then performed, with EDX mapping to investigate the alteration products formed on the surface of the glass. The following section shows the alteration products formed.

EDX line scans perpendicular to the surface of the glass monoliths were used to examine the concentration of elements in different regions. The point at which the Na concentration drops was considered to be where the bulk glass ends (indicated by I in the figures used throughout this section). Normalised plots have been used for the EDX line scans to better show the overlap between elements.

4.8.1 PVC waste – alteration products

A BSE image and EDX line scan for the PVC wastefom altered for 112 days is shown in Figure 4.23. Measurments of the alteration layer consistently measure 8-10 µm along the surface of the glass.

It is clear from Figure 4.23 that the presence of Ca in the leachate is having a significant effect on the formation of alteration products. Previous studies by Utton et al. (2013) and Corkhill et al. (2013) have shown that the dissolution of radioactive waste glasses, in a

saturated Ca(OH)$_2$ leachant was lower than in deionised water. Figure 4.23 provides evidence to explain the lower rates of dissolution at a high pH in the presence of Ca(OH)$_2$ leachate. The EDX scans in Figure 4.24, show that an outer layer of the altered glass contains high concentrations of Ca, indicating the interaction of Ca from solution with the glass. Backhouse (2016) has shown that alteration layers formed on glass surface in Ca(OH)$_2$ are more passivating in nature than those formed in other leachate solutions, such as KOH. The EDX scans in Figure 4.24 show element signals relating to Si and Al on the outer surface of the altertion layer. This suggest the formation of a calcium-aluminosilicate-hydrate phase (CASH). This would explain the agglomeration of powders, as it is well known that CSH is the bounding phase in cement chemistry (Hewlett 1998). The mechanism of Ca-rich precipitates cementing particles together has been seen in other studies (Chave et al. 2011; Gin et al. 2012). These studies suggest that the diffusion of ions through a Ca rich layer, as seen in Figure 4.24, is up to four orders of magnitude lower than those through a Ca-free layer. Rajmohan et al. (2010) states that this is due to the ability of Ca to form strong complexes with H$_2$O molecules. Andriambololona (1992) assessed the dissolution of a simulant HLW borosilicate glass (R7T7) in contact with various cements, at high pH and 90 °C, and found the formation of a surface layer, most likely CSH gel, which appeared to slow the rate of dissolution of the glass.

Figure 4.24 shows cracks forming at the base of the spinel phase, this was consistantly seen throughout the microstructure. This suggests the spinel phase is more durable than the glass matix, The low vaules of NL$_{(Fe)}$ shown in Figure 4.23 confim that the Fe containing spinel phases are extremely durable. Fe was also shown to be retained within the Ca rich layer, likely a result of the low solubility of Fe as confirmed by the low values of NL$_{(Fe)}$ in Figure 4.23.

There is also evidence shown in Figure 4.25 that the durable spinel phase within the glass matrix causes mechanical fracture at the surface. This mechanism would result in fresh surfaces for dissolution to occur. The NL$_B$ for the PVC waste glass in Figure 4.23 shows that it takes longer for this glass to reach steady state, confirming this dissolution mechansim.

Due to the fact that Fe is a major component in most vitrified nuclear waste, there have been a number studies examining the role Fe plays in the dissolution process (Burger et al. 2013; Michelin et al. 2013; Stéphane Gin et al. 2013). Inagaki et al. (1997) observed

that the presence of magnetite casued an increase in the mass loss of soluble elements (B, Na). The higher B, Na release indicates that the presence of magnetite enhances glass dissolution. The NL_B from the PVC waste was highest compared with the other vitrified waste streams confirming this observation seen from Inagaki (1997). Ianagki (1997) proposed that amorphous silica was precipitating on the magnetite surfaces which was consistent with other studies. The high magnification image shown in Figure 4.25 shows the mechanical effect of the magnetite spinel phase. Unfortunately no other characterisation studies were performed in this region. This is certainly an area for future work, to determine what thermodynamic effects the spinel phase has in precipitating Si (and other elements) at the surface of the magnetitie crystal structure.

Three areas can be distinguished in Figure 4.24 including; bulk glass (grey), an altered glass layer (II) and surface precipitates (III). The dark layer (I) is where the alteration layer has pulled away from the bulk glass. This is likely a result of the sample preperation. The Ca peak is relatively wide compared with the width of the alteration layer. This is due to the analysis line crossing the CSH precipitates on the surface of the alteration layer (III). Outside of the bulk glass Figure 4.23 shows that Al, Fe and Mg maximum signal is contained within the Ca rich alteration layer (II). It is known that due to Fe low solubility, these ions will be less likely to enter solution. Therefore it appear the Fe ions accumulate within the alteration layer (II). Caution should be exercised when analysing the presence of Fe within the alteration layer, as Figure 4.24 shows that the Fe bearing spinel phases are extremely durable and are present within the alteration layer. This may influence the Fe signal within the alteration layer.

The EDX scan in Figure 4.24 demonstrates the complexity of the glass dissolution process. The rapid decrease in Na signal seen at the interface within the bulk glass and the alteration layer is inconsistent with a process controlled by diffusion. It is known that ion exchange is not the dominant process of glass dissolution at high pH (Cailleteau et al. 2008; Gin et al. 2011), instead congruent dissolution is more favourable. However, figure 4.24 also shows that Fe, Al and Mg are retained in the alteration layer, therefore the process shown in Figure 4.24 can not simply be described as congruent dissolution. Further studies determining the performance of glass in high pH conditions have been attempted with both calcium and other solutions (such as KOH), to understand what effect calcium and alkaline conditions have on the dissolution of glass (Backhouse 2016).
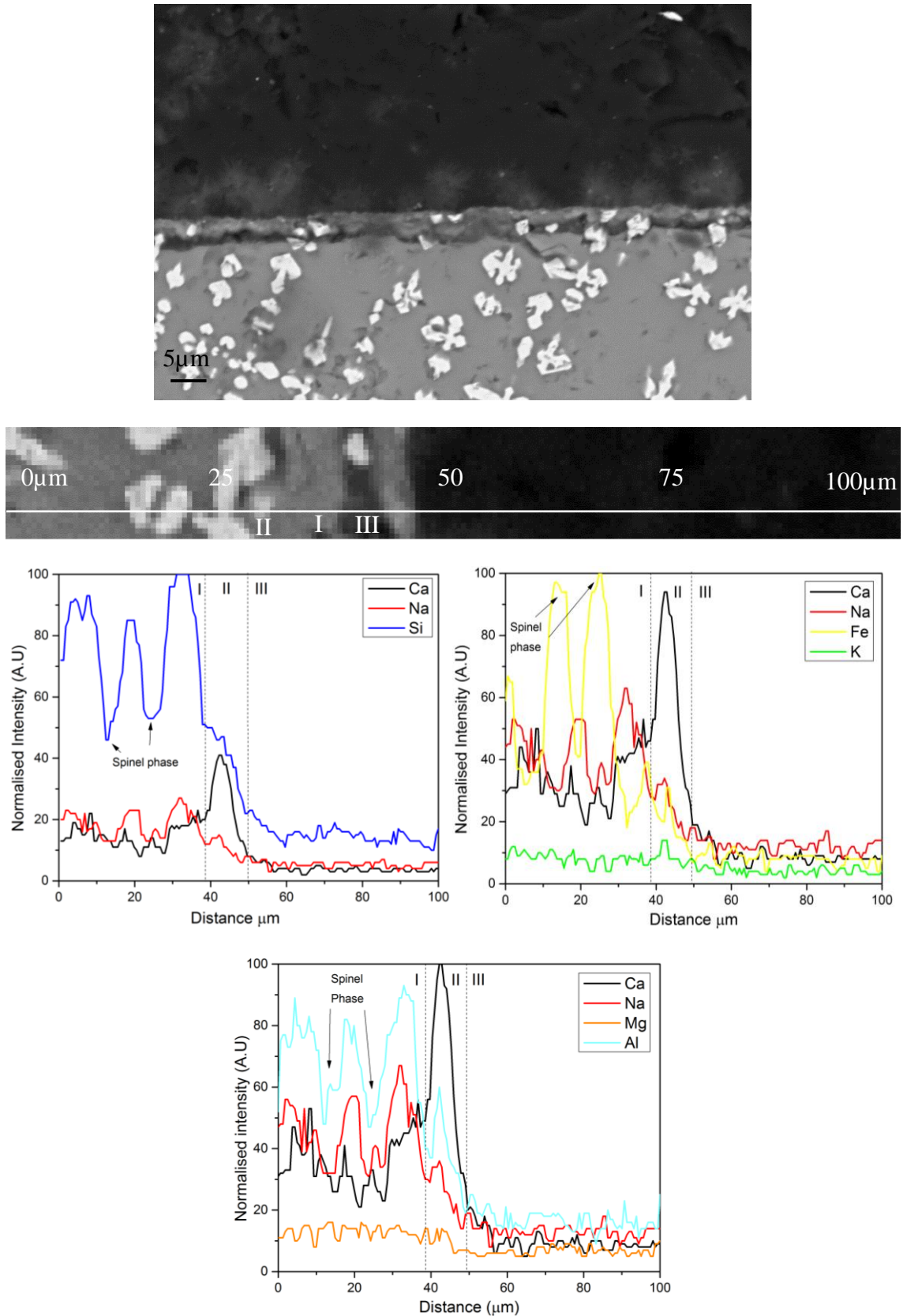
Figure 4.23 BSE micrographs and normalised EDX scan of the vitrified PVC waste from 112 day dissolution testing. Dotted line denote the thickness of the alteration layer. I = bulk glass II = altered glass layer III = surface precipitates
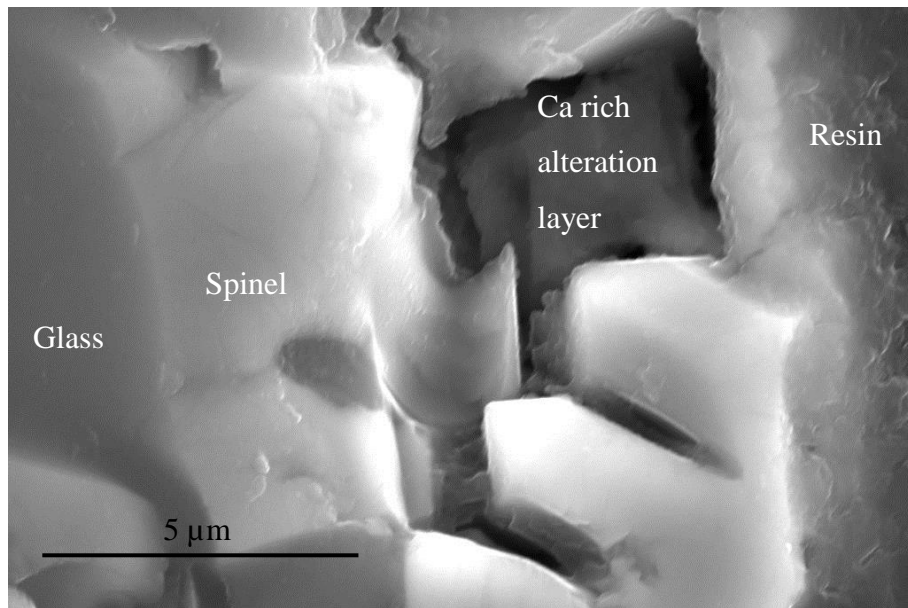
Figure 4.24 Corrosion layer of vitrified PVC waste. Interaction of crystalline phases within the alteration layer

4.8.2 Mixed Waste – Alteration products

Figure 4.26 shows the alteration layer formed on the surface of the mixed waste form 112 days after being submerged in saturated $Ca(OH)_2$ solution. EDX line scan was again taken perpendicular to the glass surface. There appears to be four distinct areas; bulk glass (I) alteration layer (II), precipitates on the surface of the glass (III) or separated from the surface of the glass (IV). The Si and Na line scan show a rapid drop off at (I). This is due to the alteration being pulled away from the bulk glass during sample preparation. It would be expected that this drop would not be present during glass dissolution. The Na signal drops linearly through the alteration layer (II) from the bulk glass. This indicates corrosion is occurring through a diffusion layer, this can be seen in Figure 4.26 with the gel layer having a different contrast to the pristine bulk glass (II). This mechanism is consistent with Frugier et al. (2008) explanation displayed in Figure 2.6. There is a large spike in Ca signal at the interface of the alteration layer and the attacking solution. This is likely to correspond to Ca rich precipitates as shown in Figure 4.26. The increased brightness at this area is associated to a reduction in porosity, suggesting the outer layer (II) is less porous than the inner layer (I). This is consistent with previous studies reporting porosity of alteration layer (Cailleteau et al. 2008).
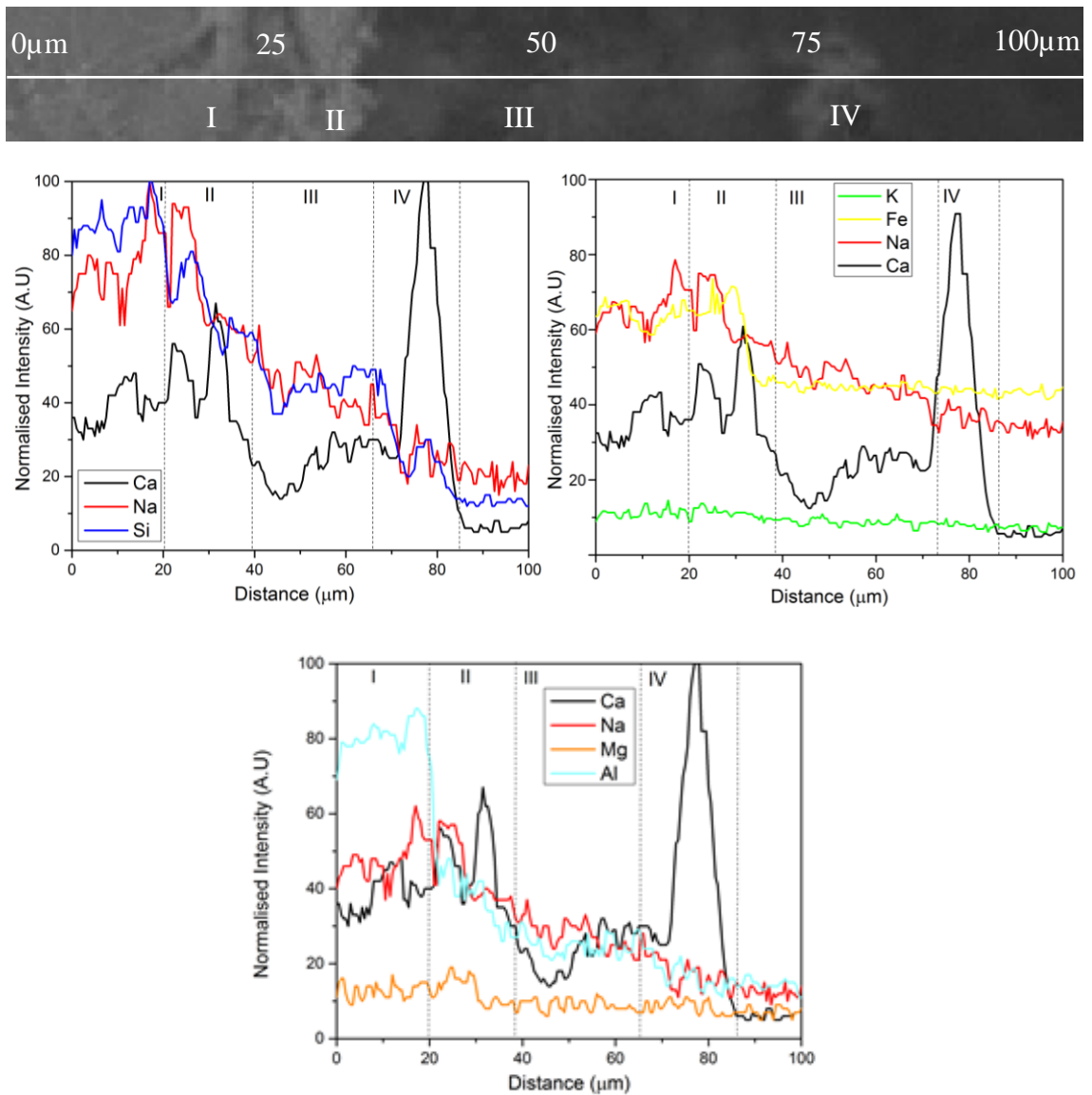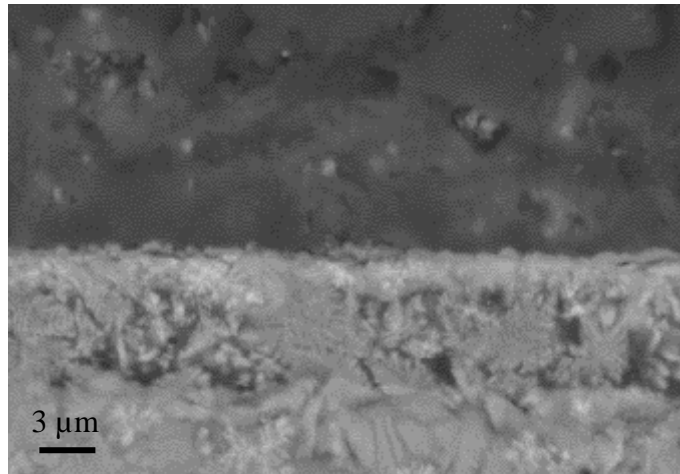
Figure 4.25 BSE micrograph and normalized EDX line scans of the vitrified Mixed waste glass monolith from the 112 day dissolution test. Dotted lines indicate distinct regions, I = bulk glass II =alteration layer III + IV = surface precipitates.
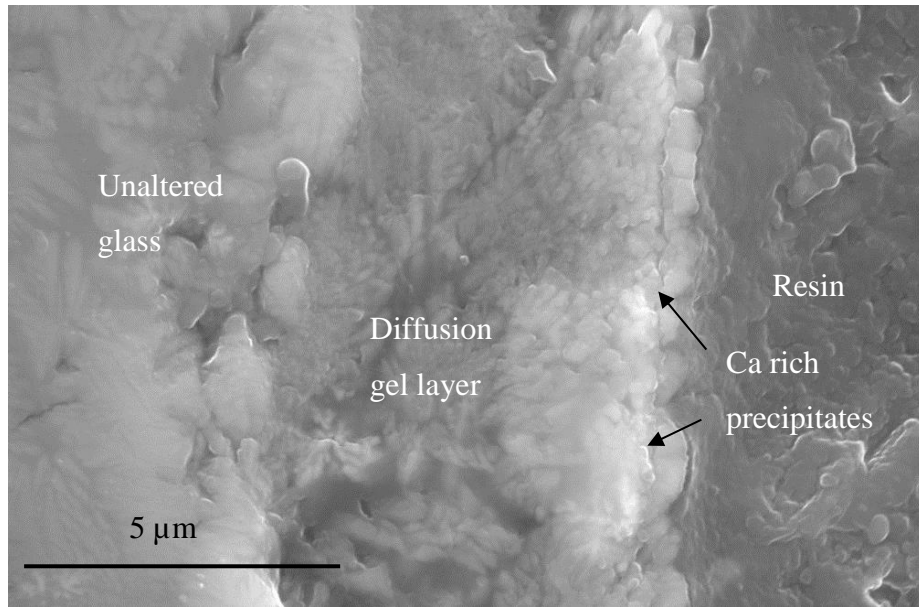
Figure 4.26 Corrosion layer of the vitrified mixed waste

4.8.3 Metallic Waste (Slag fraction) – Alteration products

Figure 4.27 shows that the surface of the glass has undergone significant corrosion with the surface of the glass showing a rough surface.
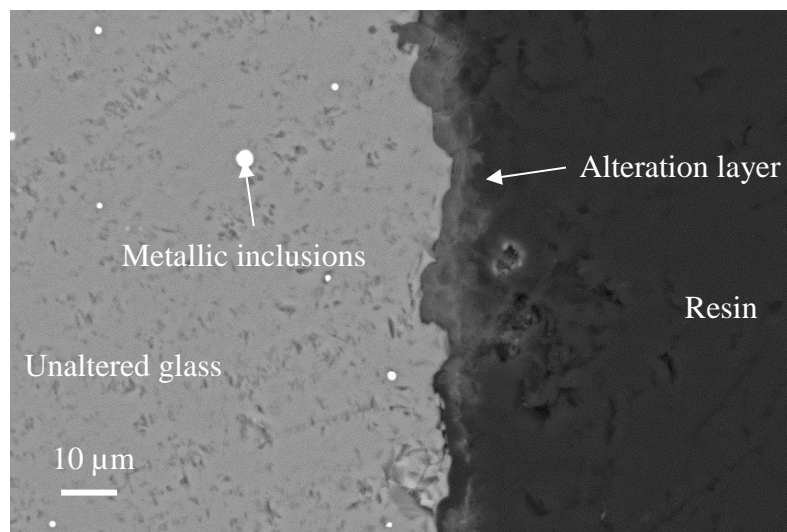
Figure 4.27 Surface of the Metal waste slag fraction. Obvious corrosion causing a rough finish to the corroded area

Figure 4.29 provides a higher magnification of the altered glass. A clear alteration layer has formed on the surface of the glass at roughly 6-7 µm thick, consisting mainly of Ca, Si and Al. Present on top of the alteration layer is a large amount of secondary phases in the form of precipitates up to 10µm thick in places.

The structure of the alteration layer shown in Figure 4.27 is very similar to that seen by Backhouse (2016), who carried out similar durability studies in hyper alkaline conditions on 25 wt% Magnox aluminosilicate glass. This study also found needle like crystals present within the alteration layer similar to that seen in Figure 4.27. Backhouse (2016) was able to characterise these needle like crystals using micro XRD, which were identified as the mineral meixnerite ($Mg_6Al_2(OH)_{18} \cdot 4(H_2O)$). Fournier et al. (2014) review of crystalline phases formed within the alteration layers of nuclear glass, does not mention meixnerite. The mechanism of the formation of the localised corroded areas in Figure 4.29, leading to the creation of divots and postulated by Backhouse (2016), is shown in Figure 4.30.

The surface of the corroded metal waste in Figure 4.28 would agree with Backhouse (2016) hypothesis concerning the formation of the needle like meixnerite crystals. Figure 4.28 clearly shows Ca rich particles away from the glass surface acting as nucleation sites for crystal growth. From this, the needle like crystals grow into the glass causing the divot formations seen in this body of work. The EDX line scan in Figure 4.28 also shows that Mg is clearly concentrated within the needle crystal features, providing further evidence that meixnerite is forming on the surface of the glass.

It is known from the normalised mass loss of elements into solution that the vitrified metal waste is the most durable wasteform. This is likely due to the higher concentration of Si and Al within the glass, as the presence of aluminium slows down the corrosion kinetics and decreases the silicon concentration in solution (Lediu 2005), as confirmed by the lowest NL_{Si} from the metal waste. Another reason the metal waste could be the most durable is due to the Al content driving enhanced formation of CASH precipitating on the surface of the glass as shown in Figure 4.29.

As a consequence of the precipitation of crystalline phases on the surface of the glass as shown in Figure 4.29, gel-forming elements are consumed in stable phases. Gin (2011) states that this would modify the gel composition, for example, zeolite precipitation is known to act as a Si and Al sink, leading to resumption of glass alteration. The formation of CASH phases precipitating on the surface of the glass, thereby increasing the content of Al and Si in the gel layer, could result in the resumption of glass alteration. Longer duration experiments would be needed to confirm this.
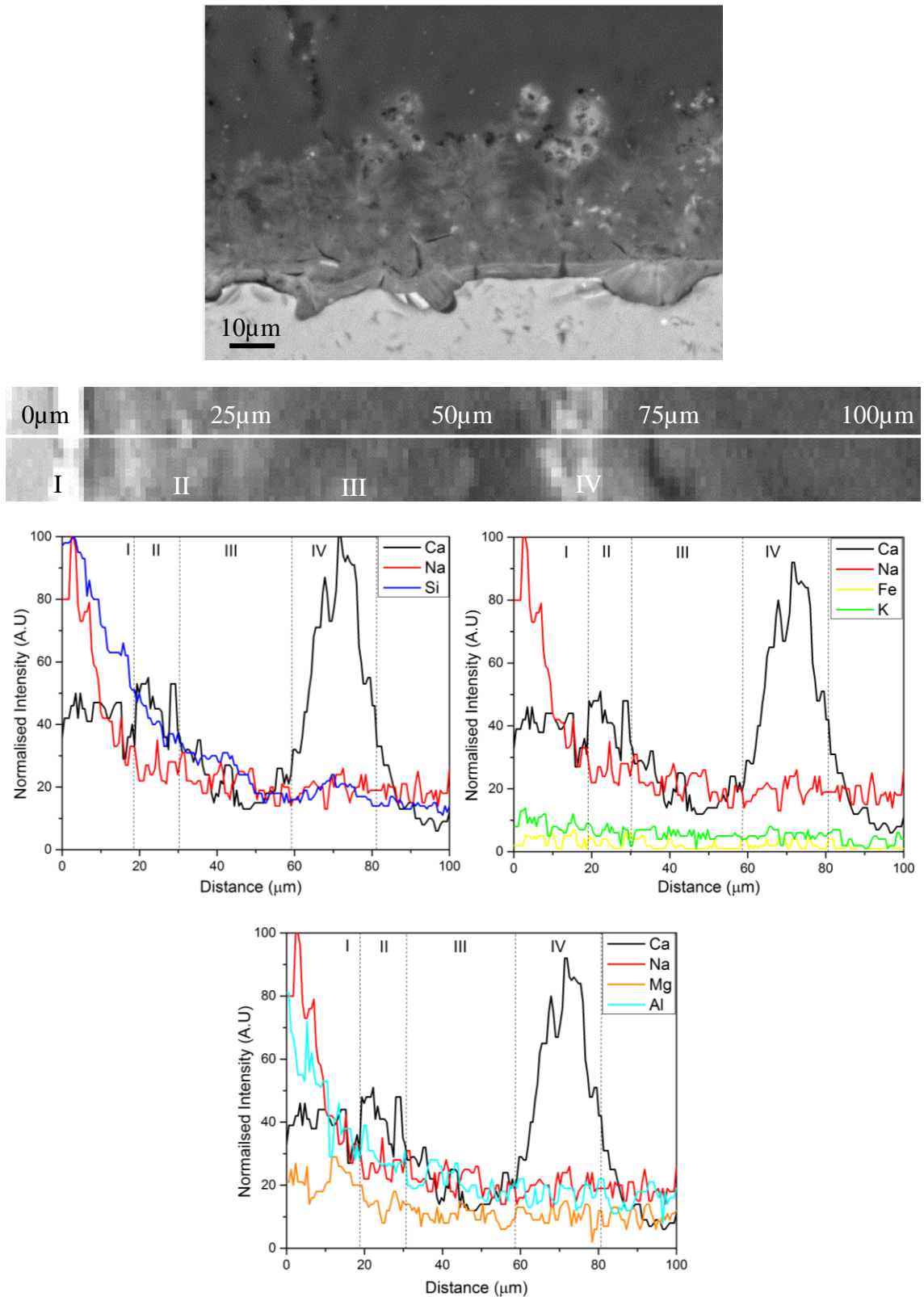
Figure 4.28 BSE micrograph and normalised EDX line scans of the vitrified metal waste (oxide fraction) after 112 days dissolution test. Dotted lines denote distinct areas within the alteration layer; Bulk glass (I), altered layer (II), surface precipitates (III) precipitates away from surface (IV).
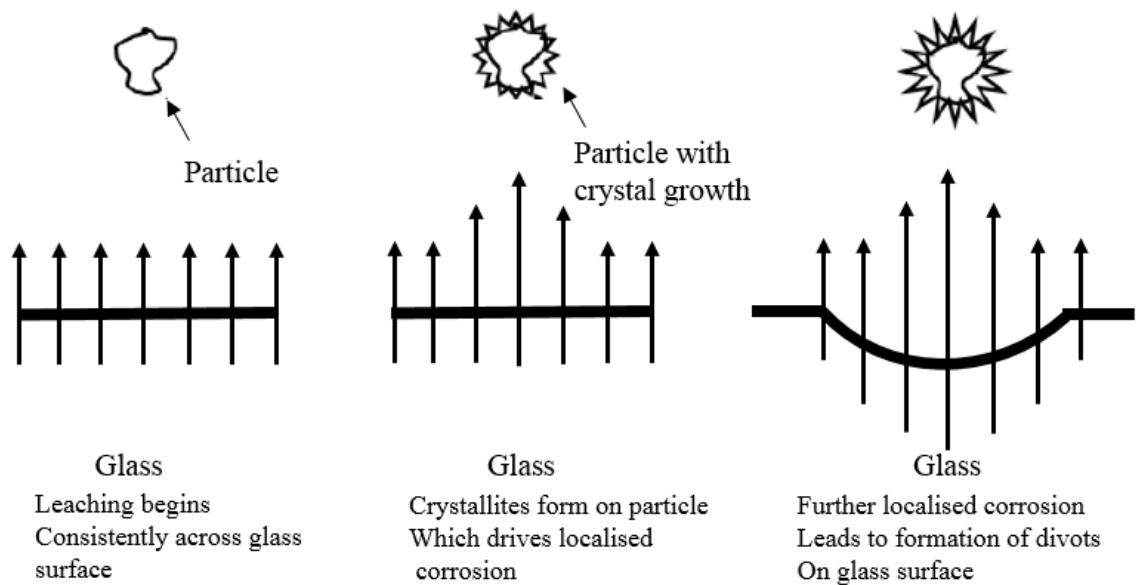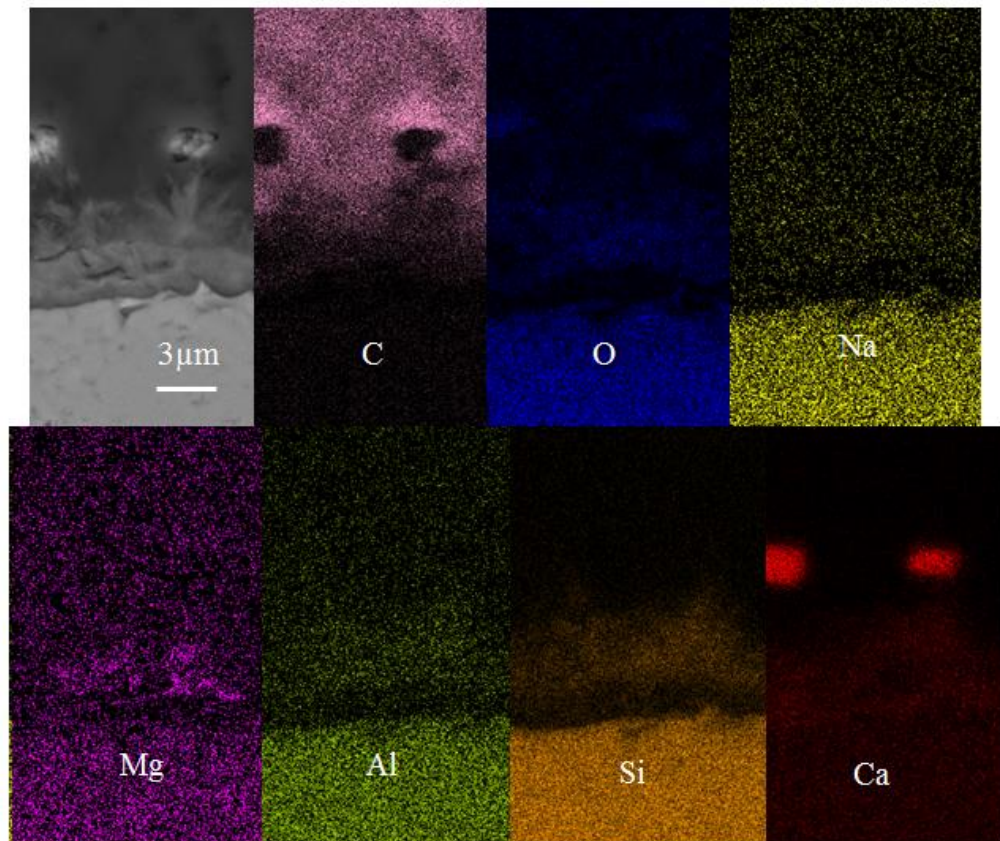
Figure 4.29(Top) EDX map clearly shows signal of Mg contained within the alteration layer. (Bottom) Schematic of mechanism of meixnerite crystal formulation through presence of particulate matter in solution. Image adapted from Backhouse (2016).

4.8.4 Masonry Waste – Alteration products

Figure 4.31 shows the surface of the vitrified masonry waste after being submerged in $Ca(OH)_2$ for 112 days. The alteration layer (II) has formed on the surface of the glass is approximately 5µm thick, which is considerably smaller than the alteration seen in the prvious examples. The NL_{Si} is the lowest in the Masonry sample, as shown in Figure 4.22, which corresponds to the smallest alteration layer.

Some general trends for all the alteration layers seen in this section are observed. Distinct CSH phases were present on the surface of the alteration layer. This accounted for the agglomeration of powders seen during the PCT experiment (Section 4.7). Using the rate data for elements in Seciton 4.7, it would appear that the formation of precipitates seen in this section (Section 4.8) are having an effect on the measured concentration of elements in solution as they are retained within the alteration layer. This would indicate that the dissolution beaviour is not congruent for all elements. The mechanism and size of the alteration layers present in this section are consistent with the work of Utton et al. (2013).
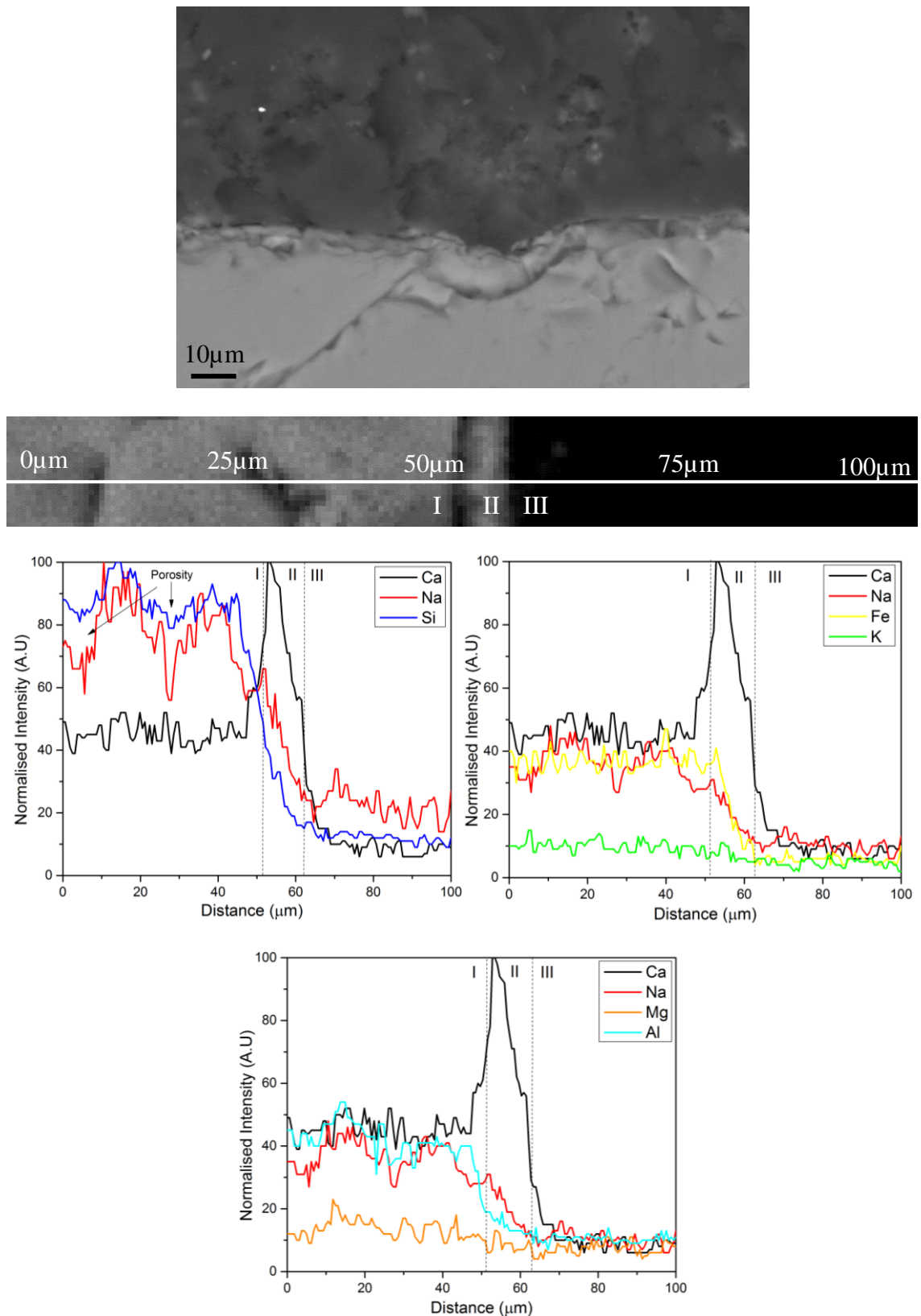
Figure 4.30 BSE micrograph and normalised EDX line scans of the vitrified masonry waste after 112 days dissolution test. Dotted lines denote distinct regions in the alteration layer including; bulk glass (I) alteration layer (II) surface precipitates (III).

4.9 Product and process optimisation

One of the aims of the investigation was to produce a full slag product with a single glass formulation, which could enable a more straightforward safety case to be considered for geological disposal facility. Section 3.2 provides the experimental information and reasoning behind this decision. This section will examine the results of the optimisation trials and determine the effectiveness of each mechanism.

Figure 4.4 shows that a mixed slag / metal waste form is produced when the waste stream contains large amounts of metal components. Section 3.2.2 discusses the potential benefits to completely oxidising the entire waste form to produce a 100% slag material. Table 3.6 gives batch calculations for the small scale melts performed. The following section analyses the resultant wasteforms.

Fe_2O_3 was calculated from amount of metallic content from the melt with no Fe_2O_3. A 1:1 molar ratio of Fe_2O_3 to the metallic content was added to the batch. If the melt resulted in no metallic fraction then Fe_2O_3 was added at a 1:1 molar ratio with the PCM waste drum (masonry waste).

4.9.1 Metal waste – Product optimisation

Figure 4.32 shows the phase assemblage and microstructure of the metal waste (small scale). The microstructure shows chromite spinel phase formed within the glass. Figure 4.32 shows that a small metallic fraction was also present within the waste weighing 31.81g. Table 3.6 states that 53.03g of stainless steel was originally added to the batch meaning that 40.02 % of the metallic fraction has oxidised due to the addition of 60.10g of glass frit which acts as an oxidising agent.

Figure 4.33 gives the microstructure of the vitrified metal samples with the addition of Fe_2O_3, which has completely oxidised the metal fraction resulting in no metallic fraction present, as shown in Figure 4.30.

Figure 4.31 shows an amorphous component within the microstructure with spinel crystallisation in the form of chromite occurring. With the addition of Fe_2O_3 the amount of amorphous phase is considerably smaller as seen from the reduction in the diffuse scattering the XRD trace.
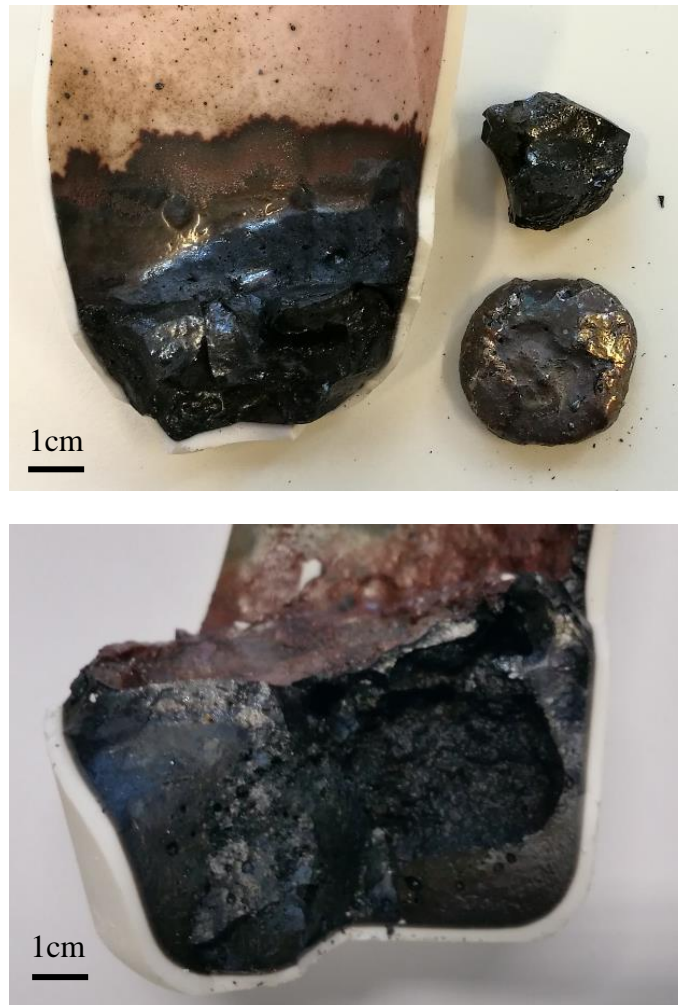
Figure 4.31 (Top) metal waste with no addition of Fe₂O₃, showing metallic fraction (Bottom) with the addition of Fe₂O₃ no metallic fraction is present.

The phase assemblage shown in the XRD trace in Figure 4.32 indicates that the metal fraction has been successfully oxidised through the following reactions.

$$3SiO_2 + 2Fe + 2Fe_2O_3 \rightarrow 3Fe_2SiO_4 \text{ (Fayalite)}$$

$$Fe + 4Fe_2O_3 \rightarrow Fe_3O_4 \text{ (Magnetite)}$$
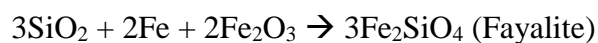
This is a promising step as it shows the effectiveness of treating the metal fraction with the addition of Fe₂O₃. There are a number of phases present in Figure 4.34 that are also present in the vitrified Mixed waste shown in Figure 4.2 including diopside and a number of spinel phases. The durability of the Mixed waste was comparable to the other vitrified PCM waste samples, and would be considered suitable for geological disposal. This shows that the completely oxidized system shown in Figure 4.32 would be suitable for

disposal, this should however be confirmed with similar dissolution experiments as described in Section 3.5.

There are a number of benefits to achieving a fully oxidised waste product. A completely oxidised waste form provides a homogenous, monolithic waste form as opposed to a mixed slag / metal system. The long term performance of the homogenous waste package can be confidently modelled and predicted enabling a strong safety case to be built for disposal. However, the long term behaviour of a mixed system would be difficult to predict and model, with the interactions of the corrosion products of the metal and the slag material needing careful consideration. Fully oxidising the high metallic waste streams also avoids any further processing to separate the slag and metal phase, which has not yet been demonstrated in an active context.

Figure 4.32 XRD pattern of the small scale metal waste with no Fe_2O_3 addition, with the associated microstructure showing crystal phases.
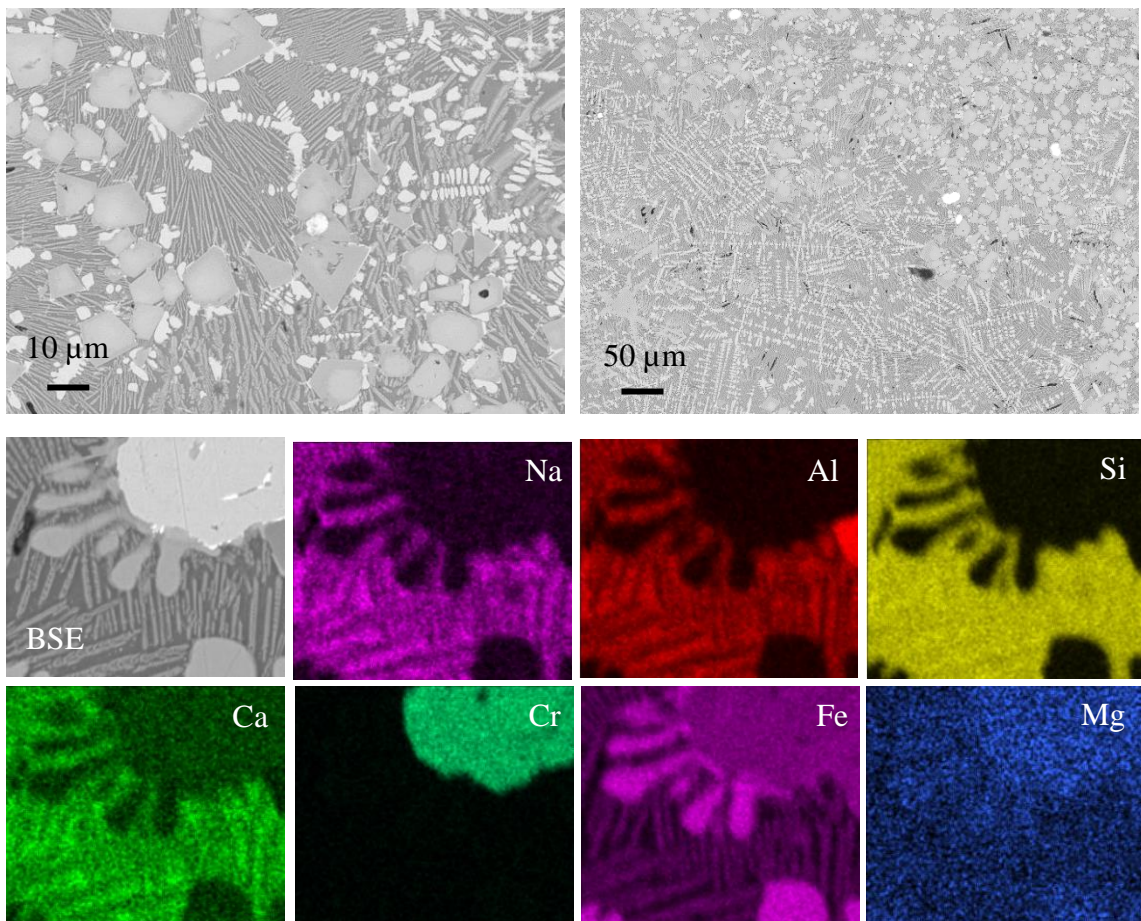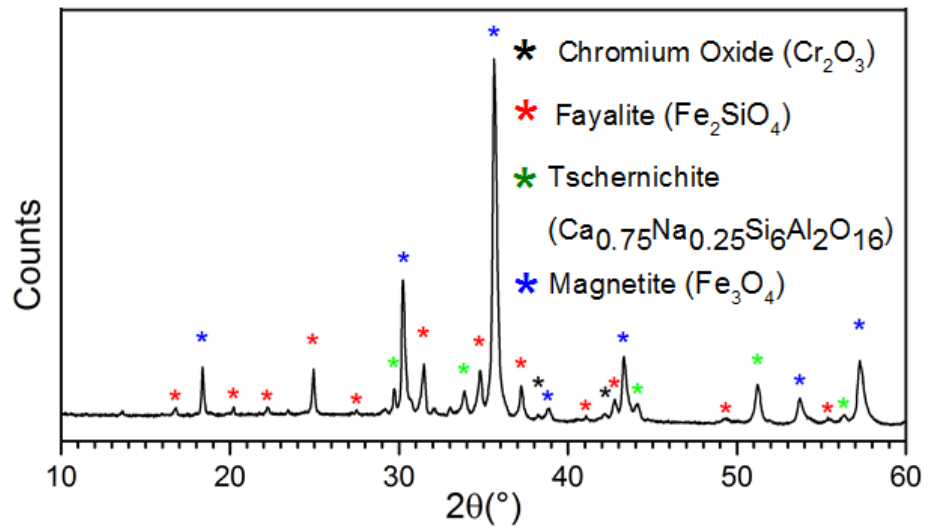
Figure 4.33 XRD pattern of the small scale metal waste with addition of the Fe₂O₃ with SEM/EDX images showing distribution of key elements within the microstructure.

4.9.2 Mixed waste – Product optimisation

Figure 4.33 shows the mixed waste without the addition of Fe_2O_3 contained a small metallic fraction at the bottom of the crucible.
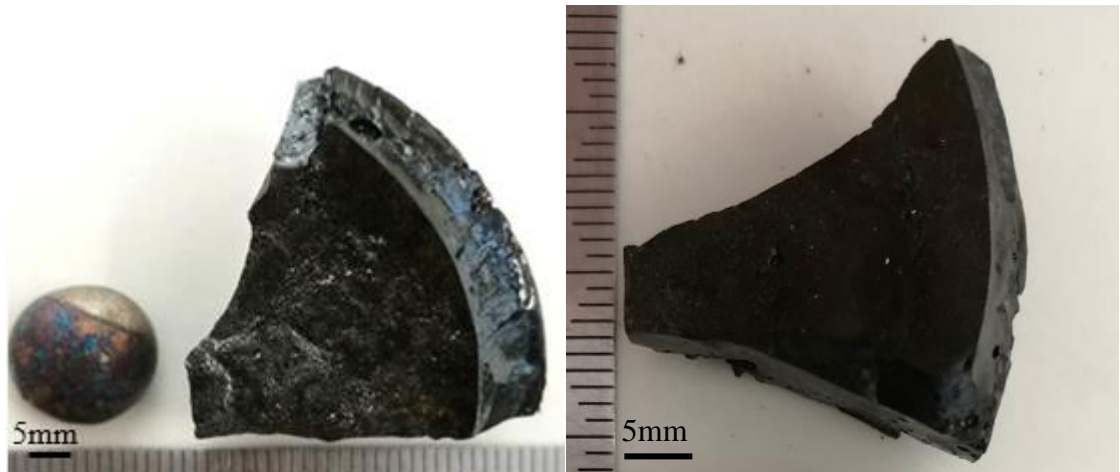
Figure 4.34 (Left) Mixed waste with no addition of Fe$_2$O$_3$, showing metallic fraction (Right) with the addition of Fe$_2$O$_3$ no metallic fraction is present.
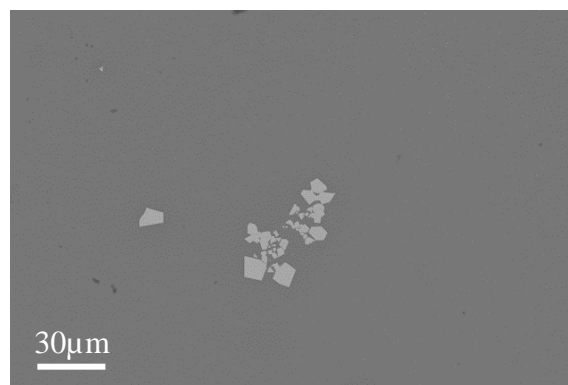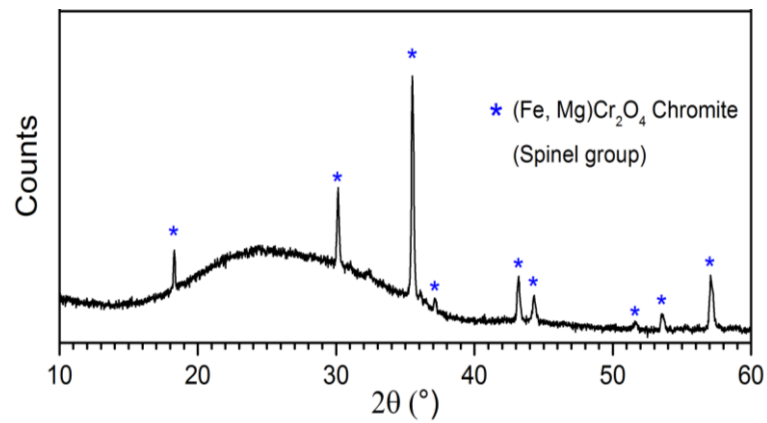
Figure 4.35 XRD pattern of the small scale Mixed waste with no Fe$_2$O$_3$ addition, with the associated microstructure showing crystal phases.
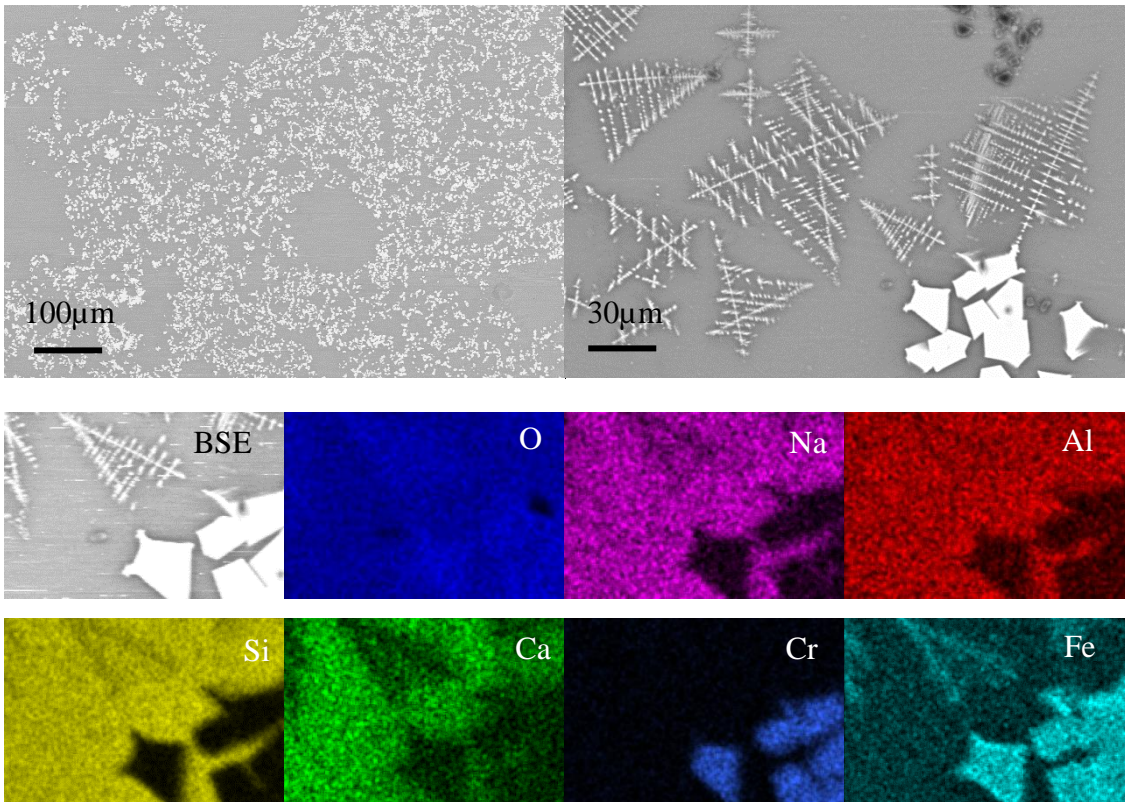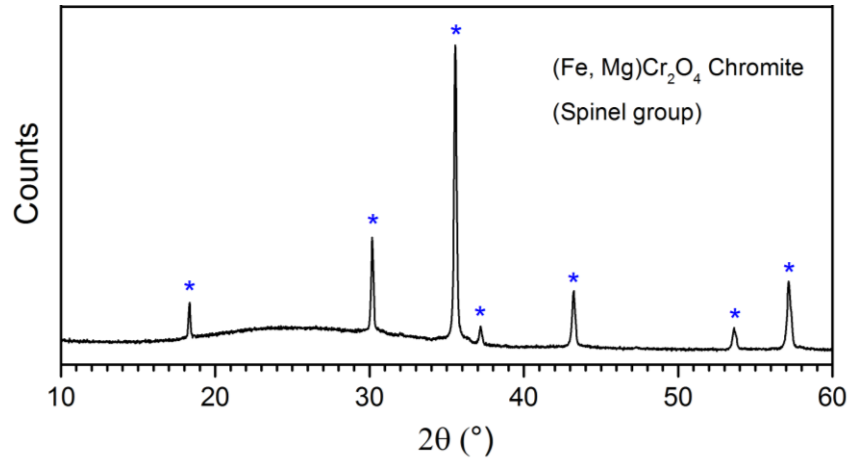
Figure 4.36 XRD pattern of the small scale Mixed waste with Fe$_2$O$_3$ addition, with the EDX mapping the distribution of key elements within the microstructure.

With the addition of Fe$_2$O$_3$ this small metallic fraction was oxidised to give a vitreous waste form with no metal fraction present, similar to that seen in Figure 4.32. Figure 4.36 shows that the microstructure of the vitrified Mixed waste with no Fe$_2$O$_3$ addition, contains chromite as identified by the corresponding XRD trace. Figure 4.37 shows the microstructure with the addition of Fe$_2$O$_3$. The XRD trace also shows chromite. Magnetite is also present within the microstructure, as shown by the EDX mapping in Figure 4.35. Magnetite and chromite share the same reflections within the XRD trace, therefore it is

difficult to distinguish between the two crystalline phases. The metal fraction has been oxidised through the following reaction.

$$Fe + 4Fe_2O_3 \rightarrow 3Fe_3O_4$$
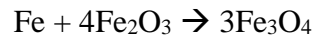
The results show that the addition of Fe_2O_3 has caused a greater degree of crystallisation within the glass structure.

4.9.3 Masonry Waste – Product optimisation

A major advantage of thermally treat PCM waste is that no pre-treatment or sorting needs to be performed before treatment. To ensure a consistent approach was maintained throughout the optimisation process, Fe_2O_3 was added to both the Masonry waste and the PVC waste despite the fact that there was not a metallic fraction waste present post processing during vitrification (Figure 4.37 (left)). Fe_2O_3 was added at a 1:1 molar ratio with the metal content of the metallic drum the masonry waste would be stored in. Full details of the batch calculations can be found in Section 3.2.
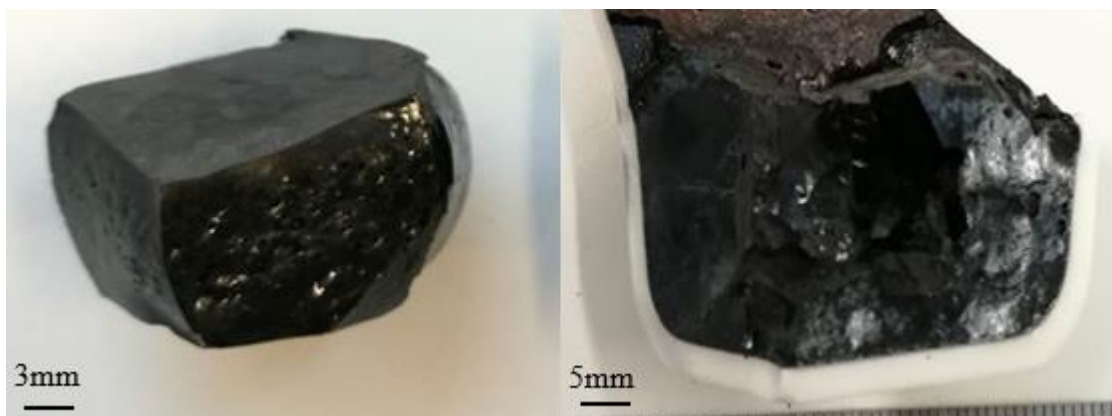
Figure 4.38 (Left) Masonry waste with no addition of Fe2O3 (Right) with the addition of Fe2O3.

Figure 4.38 shows the vitrified masonry waste with no additional Fe_2O_3, compared with the addition of Fe_2O_3. From visual inspection, it is clear that with the addition of Fe_2O_3, a greater degree of crystallisation has occurred. This is confirmed from the XRD trace shown in Figure 4.38, confirming a much greater signal from the chromite spinel phase within the glass waste form. The corresponding SEM images shows both the number and size of the chromite spinel phase is greater with the addition of Fe_2O_3. It should also be noted that the metal component, representing the metal drum, was stainless steel powder.

In reality the 200L drums which store the PCM waste is mild steel therefore the amount of Cr will be considerably less than the stainless steel powder used in these experiments. Section 4.3.4 confirms that that the chromite spinel would not be present in the case of the 200L drums. Section 4.3.4 uses the same batch composition for the masonry waste but with the use of mild steel to represent the 200L mild steel drum. In this case the vitrified product was completely amorphous with no crystalline phases present (Figure 4.3).
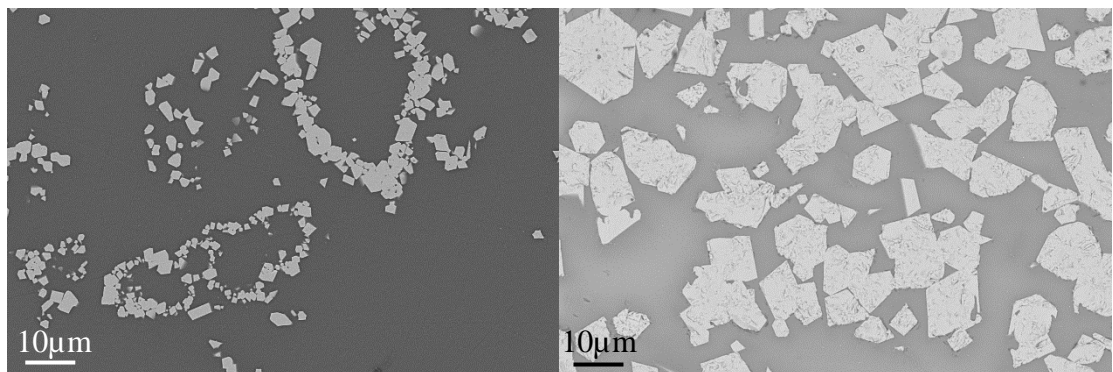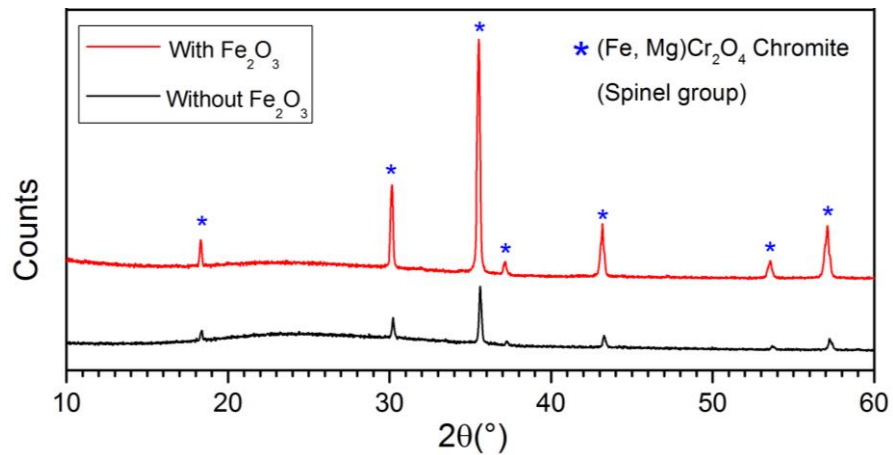
Figure 4.37 (Top) XRD pattern of the small scale Masonry waste with the addition of Fe₂O₃ addition and without, (Bottom left) Microstructure without the addition of Fe₂O₃. (Bottom Right) Microstructure with the addition of Fe₂O₃.

4.9.4 PVC Waste – Product optimisation

Figure 4.39 shows the PVC waste without the addition of Fe_2O_3 (left) compared with the vitrified PVC waste stream with the addition of Fe_2O_3 (right). Upon visual inspection the vitrified PVC waste with the Fe_2O_3 addition (right) was a poor waste form with substantial porosity and a number of cracks causing the vitrified product to disintegrate with little force. This is undesirable in a waste form as the increase in surface area, due to the

increased porosity and cracks, increases the sites which would be in contact with ground water within a GDF, accelerating corrosion of the vitrified waste form. Aboutaleb (2015) studied the effect of adding Fe_2O_3 to soda-borate glasses and found that the glass structure weakened significantly with the addition of Fe_2O_3. Aboutaleb (2015) concluded that the Fe_2O_3 had contributed to the creation of non-bridging oxygen sites within the glass structure. It is likely the same mechanism has contributed to the poor waste form seen in the right image of Figure 4.38.
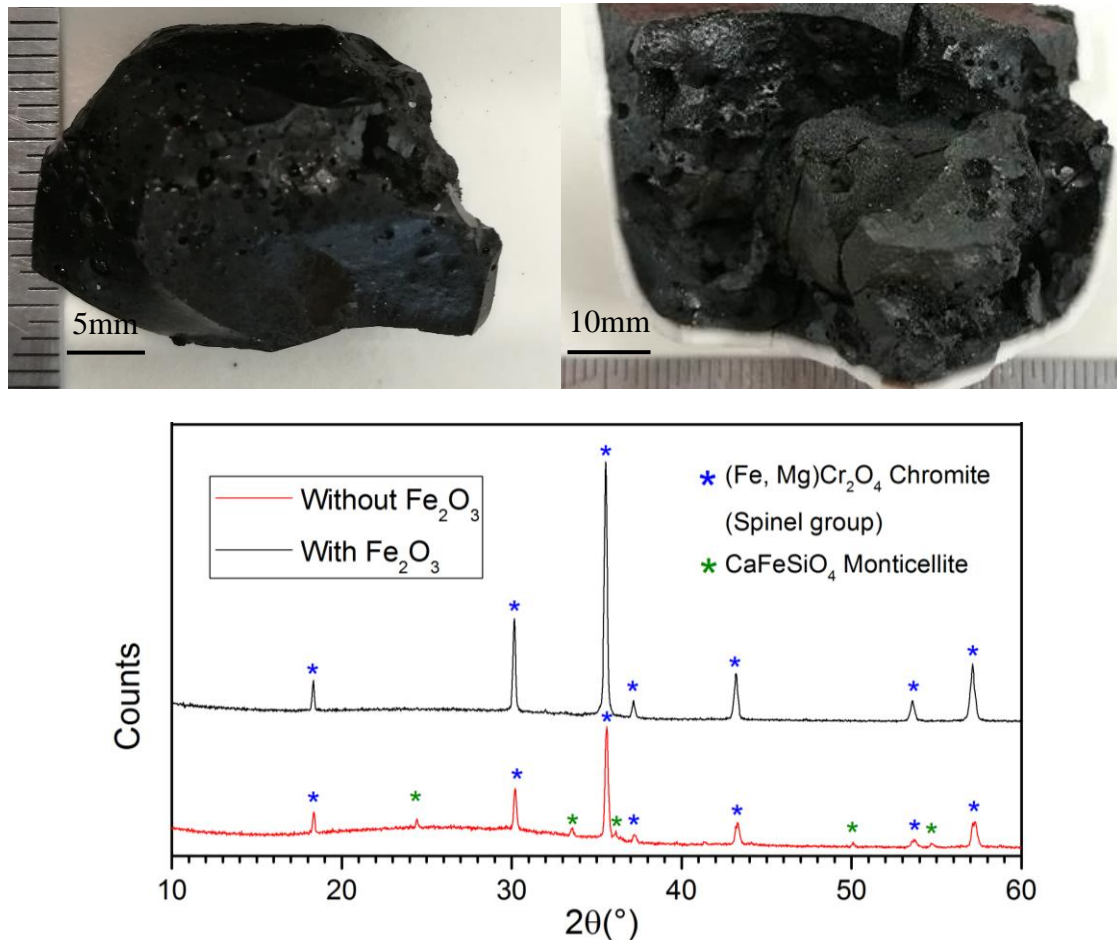
Figure 4.38 (Top Left) PVC waste with no addition of Fe_2O_3 (Top Right) with the addition of Fe_2O_3, with the corresponding XRD trace (Bottom)

The addition of Fe_2O_3 has essentially depolymerised the network, breaking up the random network and leaving nonbridging oxygen resulting in a poorly formed glass. From the XRD trace shown in Figure 4.39 and the microstructure in Figure 4.40, the vitrified PVC waste with the addition of Fe_2O_3 shows a relatively crystalline structure containing chromite spinel phase. The XRD traces shows a much greater amorphous content within the vitrified PVC waste without the addition of Fe_2O_3. Surprisingly there are no dendritic

crystalline features present within the vitrified product compared to the large scale PVC melts which saw a large degree of dendritic magnetite (Fe_2O_3) spinel phase present throughout the microstructure. The difference stems from the use of stainless steel powder to represent the 200L drum which houses the PVC waste. The stainless steel contains much greater concentration of Cr than the mild steel, which has resulted in the formation of Chromite spinel phase (Figure 4.41).
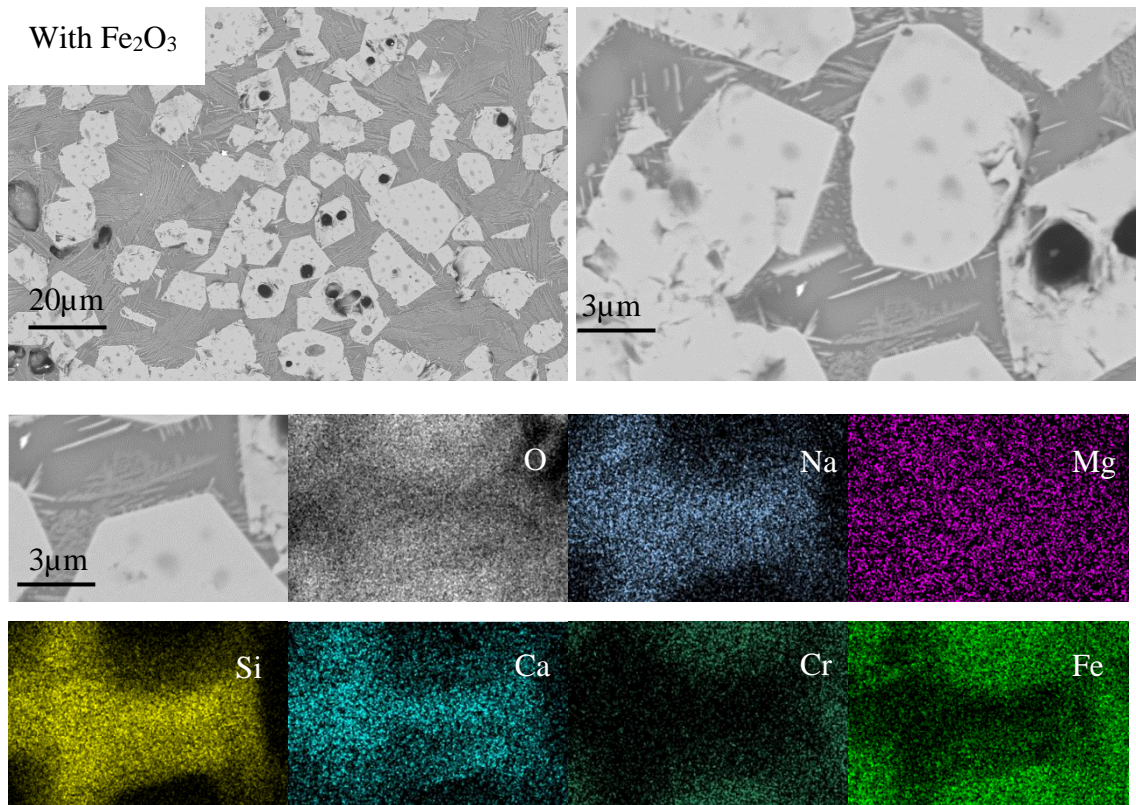
Figure 4.39 PVC waste with the addition of Fe₂O₃ with EDX mapping showing distribution of key elements within the glass.
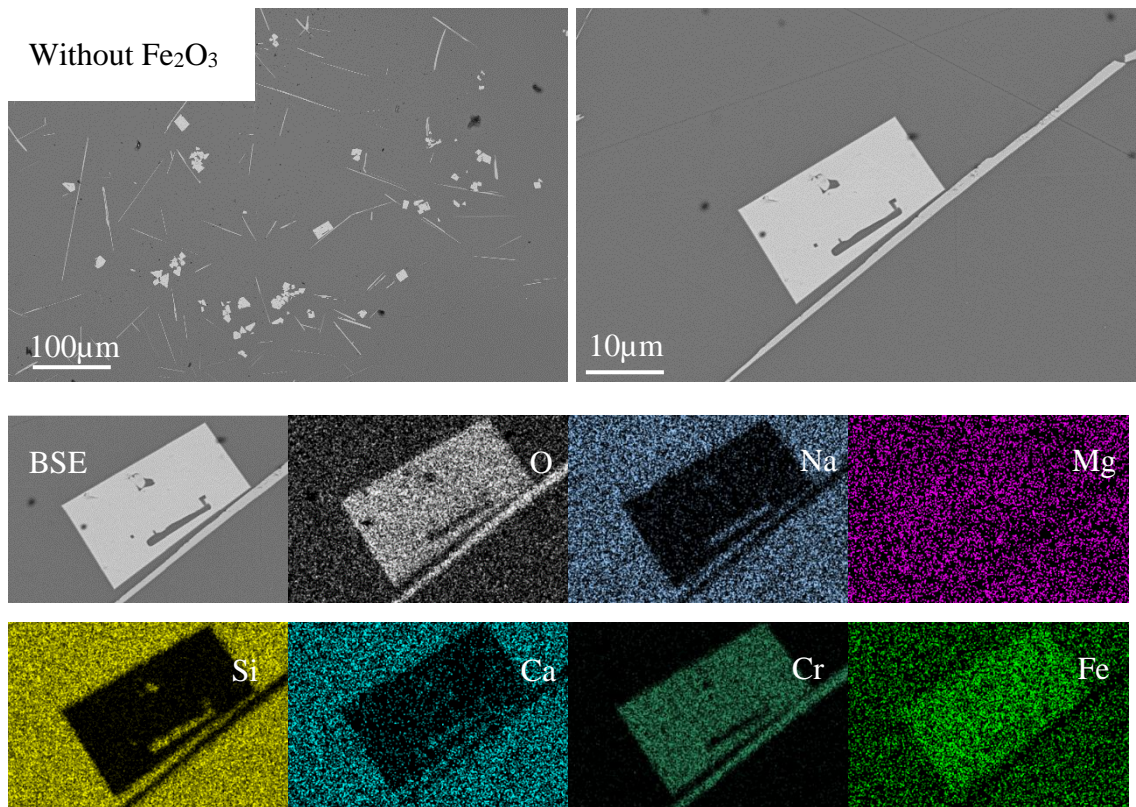
Figure 4.40 Microstructure of the PVC waste with no addition of Fe₂O₃. EDX maps show the distribution of key elements.

4.9.5 Mössbauer studies on the metal waste stream described in Section 4.9.1

Mössbauer studies were performed on the vitrified samples show in Figure 4.31, to determine the effect the addition of Fe_2O_3 had on the redox conditions of the melt. The metal waste was selected as this best represented the digestion of metal waste, as stated in the initial aims of this section of the thesis. Figure 4.41 shows the Mössbauer spectrum, with the associated fitting parameters shown in Table 4.10. The spectrum shows two sextet features which overlap, similar to the Mössbauer spectrum for the PVC waste shown in Figure 4.16. As previously stated, this is due to the ferrimagnetic properties of the identified magnetite phase within the vitrified product. As discussed previously magnetite can have a range of oxidation states dependent on the amount of structural Fe^{2+}, which can be reviewed quantitatively as the magnetite stoichiometry ($x = Fe^{2+}/Fe^{3+}$) . Using the same method as section 4.5 the relative areas of site A (tetragonal site, Fe^{3+})

and site B (octahedral site, Fe^{2+}, Fe^{3+}) can be obtained, using equation 1, to give the overall stoichiometry of the magnetite.
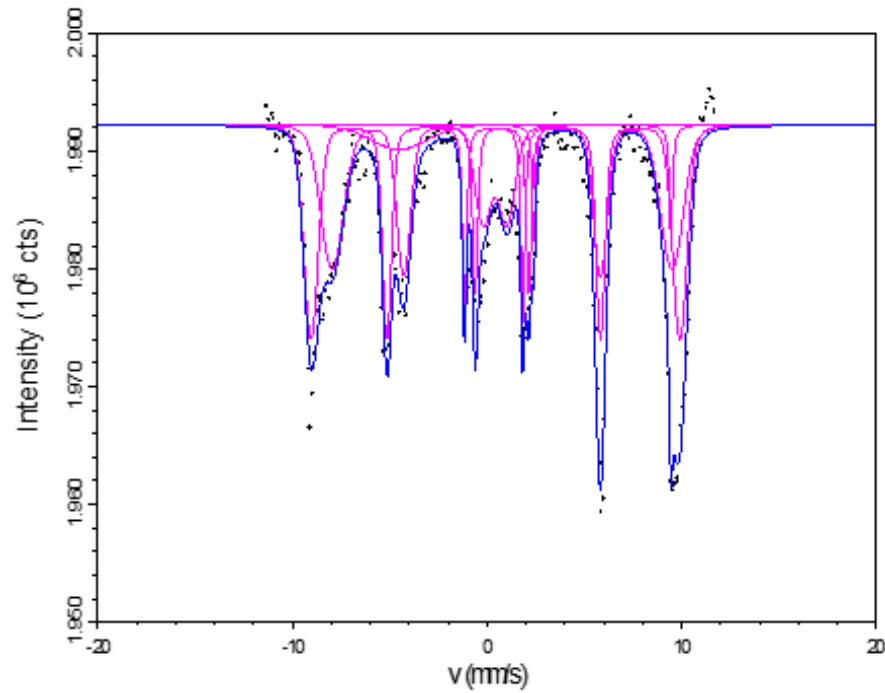
Figure 4.41 Mossbauer spectrum of fully vitrified product small scale metal waste with addition of the Fe₂O₃

Site	CS (mm/s)	QS (mm/s)	Assigned phase	Site	Area (±2%)	(Fe²⁺/ΣFe)
1	0.41	1.23	Fayalite	Fe^{2+}	7.5	
2	0.67	0.91	Chromite	Fe^{2+}	9.1	
3	1.92	3.04	Glass	Fe^{2+}	1.1	31.65 %
4	1.53	0.91	Glass	Fe^{3+}	2.1	
M1	0.38	0.04	Magnetite (M)	$^{T}Fe^{3+}$	39.6	
M2	0.77	0	Magnetite (M)	$^{O,T}Fe^{2+3+}$	40.5	

Table 4.10 Fitting parameters for the Mössbauer spectrum of the fully vitrified small scale melt (SSM) with Fe₂O₃ addition

Inserting the values obtained from the fitted Mössbauer spectrum, into eq (1), gives the following value;

$$\frac{\frac{1}{2} \times 40.50}{\frac{1}{2} \times 40.5 + 39.6} = 0.33$$

As discussed previously, magnetite can have a range of oxidation states dependent upon the amount of structural Fe^{2+}. For magnetite with an ideal Fe^{2+} content (assuming the Fe_3O_4) the mineral phase is known as stoichiometric magnetite (x = 0.50). This stoichmetric magnetite was present in the vitrified PVC waste, as shown in both the XRD trace (Figure 4.5) and the associated Mössbauer spectrum (Figure 4.16). As magnetite becomes oxidised, the Fe^{2+}/Fe^{3+} ratio decreases (x < 0.50). When the magnetite is completely oxidised (x = 0), the mineral is known as maghemite (γ-Fe_2O_3). For the Mössbauer spectrum shown in Figure 4.41, a value of x = 0.33 shows that the magnetite present in the vitrified product is nonstoichiometric or partially oxidized magnetite. For nonstoichiometric magnetite, the structure is often written as $Fe_{3-\delta}O_4$ (where δ ranges from 0 for stoichiometric magnetite to 1/3 for completely oxidised. Vandenberghe et al. (2000) states that the stoichiometry of the partially oxidised magnetite can be determined through the following relationship;

$$x = \frac{Fe^{2+}}{Fe^{3+}} = \frac{1 - 3\delta}{2 + 2\delta} \tag{2}$$

This gives the value for Fe^{2+} / Fe^{3+} ratio for partially oxidised magnetite as 0.3. Combined with the other Fe bearing mineral phases within the slag waste form, the overall $Fe^{2+}/\Sigma Fe$ ratio for the vitrified metal waste with the addition of the Fe_2O_3 is 31.65 %. This shows that there is a greater distribution of Fe^{3+} ions in the slag waste form with the addition of the Fe_2O_3 acting as an oxidising agent.

4.9.6 Effectiveness of oxidising the metallic fraction

The motivation for optimising the process in terms of oxidising the metal fraction, to provide a completely vitreous waste form, stems from the poor solubility of Pu in steels which can lead to the formation of distinct Pu bearing intermetallic phases (Booth et al. 2012). The results from this study suggest that Pu has a high affinity for the slag phases therefore efficient decontamination of the metal melt is technically feasible. As

mentioned previously, if clean separation of the metal and oxide phase can be achieved then substantial costs savings can be achieved by disposing the decontaminated steel as LLW. To achieve this the slag and metal phases would need to be tapped separately from the melter during processing or separated from the slag post processing which is undesirable. Therefore by optimising the system to oxidise the entire waste form, the risk of Pu bearing intermetallic phases settling can be avoided whilst ensuring a single process.

The results from this section of the project show some promising results with Figure 4.31 showing that with the addition of Fe_2O_3 the metallic fraction seen previously is now oxidised to give a completely vitreous waste form. The XRD trace in Figure 4.33 shows that Fe metal is oxidised to produce the major Fe bearing mineral phase of magnetite (Fe_3O_4) and fayalite (Fe_2SiO_4). The Mössbauer spectrum shown in Figure 4.41 confirms that the magnetite is in fact partially oxidised. It is known that chemical composition can have a large influence on the proportion of ferric and ferrous iron in silicate melts (Thornber et al. 1980; Gaillard et al. 2003). The results in this section show that the addition of the Fe_2O_3 results in a greater proportion of Fe^{3+} ions within the system.. The addition of Fe_2O_3 will increase the overall size of the waste form negating some of the benefits of the volume reduction seen in section 4.6 through thermal treatment. A potential option would be to sparge the melt with oxygen to aid oxidation of the melt (Sambasivam et al. 2007), however this does increase the risk of Pu carryover into the off-gas system.

Despite the addition of Fe_2O_3, the optimisation process still needed to be applicable to all waste streams to avoid any pre-handling of the PCM waste drums ensuring a single process was maintained throughout. In the case of waste streams where a metallic fraction was not expected (PVC and masonry waste) Fe_2O_3 was added at a 1:1 wt.% with the metal component from the mock up waste drum. This did not have a detrimental effect on the vitrified masonry waste, with an increase in crystallisation resulting from the addition of Fe_2O_3. Contrarily, the addition of Fe_2O_3 to the PVC waste resulted in a very poor waste form with large amounts of porosity and cracks, as shown in Figure 4.38. This is a concern in terms of waste processing as characterising the waste to determine the metal content prior to thermal treatment is undesirable. One option could be to weigh the waste container. It is known from Section 2.1.1 that the maximum weight of each drum is 100kg. However for drums containing large amounts of PVC and organic waste the space

occupied by the waste does not exceed 100kg. Therefore any waste drum which does not weigh 100 kg would be deemed unsuitable for additional Fe_2O_3 and would be treated with the addition of glass frit at a 1:1 wt. % ratio. This could potentially be a simple solution to avoid the poor waste form shown in Figure 4.39.

The results shown here display a certain level of success in enabling a fully oxidised system from high metallic waste streams providing a fully vitreous waste form. If clean separation of the metallic and oxide fraction can be achieved then, as shown by the calculated volume reductions and the associated cost saving, this would be the desirable treatment process. If this proves technically challenging, then this project has shown that with the addition of Fe_2O_3, the metallic fraction can be oxidised providing a stable waste form for disposal.

4.10 Conclusion and summary

The work contained within this Chapter has demonstrated the effectiveness of using SLS glass frit as a glass forming additive to aid with the vitrification of PCM waste. This provides an alternative to the economically unsuitable GGBS additive, producing a high performing vitrified waste form suitable for disposal within a GDF.

The main findings during the study were as follows:

- The necessity of using the clay/graphite crucible (plumbago) for the high metallic waste stream resulted in a reducing atmosphere during the melt. This produced a mixed slag/metal waste form with the slag fraction strongly depleted in Fe (Table 4.2).

- The remaining waste streams were processed within alumina crucibles producing a fully vitreous waste form for the PVC and masonry waste with the mix waste producing a small metallic fraction at the bottom of the crucible. The slag fraction was X-ray amorphous in the metal and masonry slag with a number of crystalline phases present for the PVC and mixed waste types.

- Ce was found to be homogenously distributed throughout all of the vitrified products. Ce was found to be more thermodynamically favourable to partition within the slag fraction.

- XANES studies determined Ce^{3+} to be dominant species within the glass. Trivalent species of Ce and Pu are known to have greater solubility in borosilicate

glass as opposed to tetravalent species. The concentration of Ce_2O_3 measured within the glass is far below the solubility limits therefore it is reasonable to expect that the slag waste forms developed here could incorporate Pu at the levels expected from the PCM waste.

- Mössbauer studies demonstrate the complexity of the interaction between a redox ion and the glass melt especially with a number of multivalent speices present, as present within the vitrified PCM waste samples.

- Large volume reductions were achieved through thermal treatment. PVC waste achieved the greatest volume reductions at 88.05%, due to the volatilisation of the large organic component. Volume reductions of 64.99% (masonry), 68.82% (metal), and 55.47% (mix) were achieved which is greater than the method of super compaction and cement encapsulation which has a best case scenario volume reduction of 58.35%.

- 112 day PCT dissolution tests were performed, the data suggests that the comparative durability of the four glasses, from the most to least durable is; MET > MAS > MIX > PVC. The dissolution results obtained in this study are similar to previous work considered potentially suitable for geological disposal (C. A. Utton et al. 2013).

- Analyses of the corrosion layer on the vitrified waste forms showed that Ca from solution had precipitated on the surface of the glass forming secondary phases in the form of C-S-H.

- Optimisation studies have shown the possibility of oxidising the metallic fraction from the high metallic waste streams with the addition of Fe_2O_3. This option provides a stable homogenous waste form if the metallic and slag fraction cannot be cleanly separated.

5 GLASS FORMULATIONS FOR THE IMMOBILISATION OF POND SCABBLINGS ILW.

5.1 Introduction

In the UK, most operational intermediate level waste (ILW) has been directly encapsulated in cement, however, there remains a large number of legacy intermediate level wastes, within the UK waste inventory, for which a decision on immobilisation has yet to be made. Concerns regarding the long term stability of the cementitious waste forms coupled with the large volume increase, has led to renewed interest in thermally treating the UK ILW inventory. Key drivers for the application of thermal treatment processes include the reduced volume, improved passive safety, and superior long term stability, of the vitrified waste form products. A number of waste streams have been identified as compatible with thermal treatment processes – including contaminated masonry waste.

A source of contaminated masonry waste is found in decommissioned silo ponds. Spent fuel requires cooling and storage to allow the short–life fission products to decay. The decay of fission products within the silo ponds leads to the contamination of the concrete lining. The contaminated concrete is removed in the form of scabblings.

This chapter investigates whether the contaminated concrete in the form of scabbled waste contain sufficient amounts of glass forming oxides to aid vitrification.

Section 3.4 explains the experimental setup and the materials used to simulate the contaminated masonry waste. The following chapter will concentrate on the results and the performance of the waste form.

5.2 Simulant Masonry Waste Characterisation

Representative scabbled pond waste was sourced from core drillings taken from the University of Sheffield (Figure 5.1). The core drillings were milled to a fine powder using

a TEMA mill. The composition of the core drillings were determined using XRF analysis is shown in Table 5.1. The major component of the core drilling was quartz (SiO_2), as confirmed by the strong intensity associated with Bragg reflections in the XRD pattern in Figure 5.2. Section 3.4 gives an overview of the experimental set-up. Using the sodium borosilicate phase diagram in Figure 3.7, five glass compositions were formulated. The melting temperature strongly indicates that the five compositions will vitrify at 1100°C, which is the temperature utilised in this body of work. The masonry waste from the core drilling, was used as the SiO_2 component with waste loadings ranging from 68 wt % to 72 wt %. The rationale behind the selected waste loadings and operating temperature are explained in Section 3.4.1.

Figure 5.1 Core drilling taken from the Hadfield building
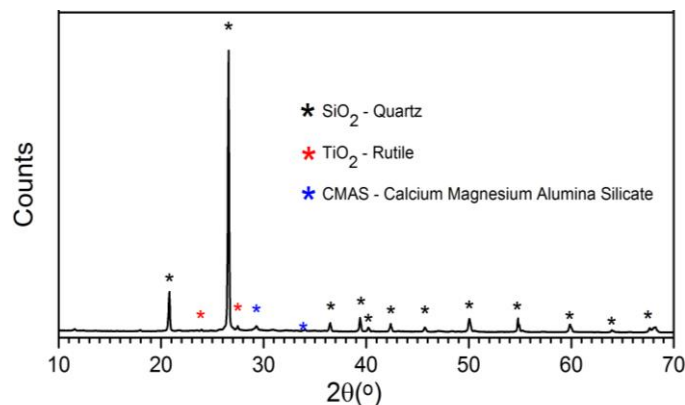
Figure 5.2 Powder X-ray diffraction patterns resulting from analysis of the simulant masonry waste showing identified reflections corresponding to quartz (SiO_2), rutile (TiO_2) and (CMAS) calcium magnesium alumina silicate.

152

Component	Wt%
SiO_2	77.05 ± 0.53
CaO	8.54 ± 0.18
Al_2O_3	3.46 ± 0.11
Fe_2O_3	1.22 ± 0.06
K_2O	1.08 ± 0.06
MgO	0.42 ± 0.05
TiO_2	0.21 ± 0.03
Na_2O	0.15 ± 0.03
P_2O_5	0.05 ± 0.02
Other	0.40 ± 0.05
LOI	7.42 ± 0.17

Table 5.1 XRF results showing composition of masonry waste

	Mass (g)
Crucible	6.3200
Masonry mass	1.0146
Total mass before heat treatment	7.3346
Total mass after heat treatment	7.2540
Mass loss	0.0806
Mass loss percentage	(0.0806/1.0146)* 100 = **7.8 wt% mass loss**

Table 5.2 mass loss of masonry waste after heat treatment at 1100°C for 6 hours

The mass loss can be attributed to the loss of water within the core drilling, associated with the cement binder. Kodur (2014) states that the mass of concrete at elevated temperatures is highly influenced by the type of aggregate, with siliceous aggregate

concrete, such as the core drilling used in this study, experiencing a much lower percentage of mass loss at high temperatures. As stated previously, the core drilling used in this study is assumed to be representative of the scabbled pond wastefound within the silo ponds. Therefore, it is possible the scabbled pond waste found within the silo ponds could have a different aggregate resulting in greater mass loss during thermal treatment.

5.2.1 Sodium borosilicate glass system

With the addition of Na_2O and B_2O_3 acting as glass forming agents, It was decided that the SiO_2 component within the masonry waste would form the SiO_2 component of a sodium borosilicate glass. The model proposed by Yun (1979), based on experimental ^{11}B NMR results, describes the mechanism of creation of non-bridging O atoms (NBOs) in a simplified ternary glass SiO_2-B_2O_3-Na_2O system. This model constitutes a valuable starting reference and gives a useful description of the structural evolution as alkali cations are added to the glass melt. This understanding will be particularly important for this study due to the varying ratio of sodium and boron concentrations within the different glass compositions. In this model, the ratio K = $[SiO_2]$/$[B_2O_3]$ and the ratio R=$[Na_2O]$/$[B_2O_3]$ (both in mol%) are the most important composition related structural parameters. It is common for the K and R ratios to be quoted in studies concerning the structure of sodium borosilicate glasses. One of the aims of this investigation is to understand the structure and properties of the vitrified product. Therefore, it is useful to determine the R value as it will be used extensively in the analysis of the vitrified glass samples. Table 5.3 gives the composition of the five batched compositions (Section 3.4) in molar % with the associated R and K ratio.

Composition number	SiO_2 (Mol%)	B_2O_3 (Mol%)	Na_2O (Mol%)	R ratio [Na_2O/B_2O_3]	K ratio [SiO_2/B_2O_3]
C1	70.0	16.0	14.0	0.88	4.38
C2	70.7	16.6	12.7	0.76	4.26
C3	72.6	14.6	12.7	0.85	4.97
C4	70.3	19.6	10.1	0.52	3.59
C5	72.3	19.0	8.7	0.46	3.81

Table 5.3 The targeted composition of the five vitrified waste forms in Mol % with the associated R and K values using the masonry waste as the SiO_2 component.

5.3 Results and Discussion

5.3.1 Analysis of phase assemblage

Table 5.4 shows the composition of the vitrified masonry waste for all five compositions (C1-C5) determined using XRF spectroscopy.
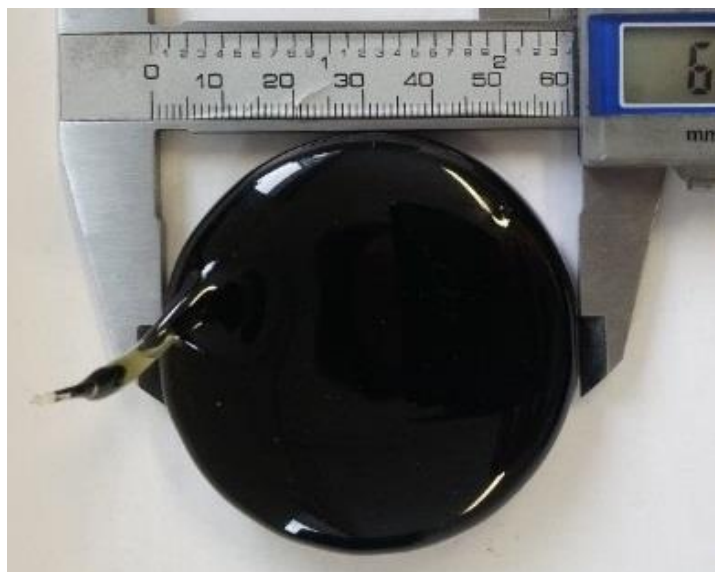
Figure 5.3: Vitrified masonry waste for C1

A noticeable melt line had formed within the crucible, resulting in increased amounts of Al_2O_3 within the glass, as shown in Table 5.4. Figure 5.3 shows a vitrified product M1 after heat treatment. Melting behaviour showed no violent reactions with no evidence of foaming within the crucible.

All glass compositions were successfully cast into a cylindrical mould. There were, however, noticeable differences in viscosity between the glass compositions. The glass compositions with lower amounts of SiO_2, including C1 and C4 at 68 wt. % SiO_2, resulted in molten glass with a lower viscosity at 1100 ºC.

The different compositions have varying levels of undissolved material within the glass matrix. Figure 5.4 shows optical images of C1, C3 and C5. The increased levels of undissolved material matches the increased intensity of the identified quartz mineral phase in the XRD trace as shown in Figure 5.5. C5 had a large amount of undissolved material contained within the glass matrix therefore displaying the strongest reflections

corresponding to quartz. The XRD pattern of C1 shows only diffuse scattering which confirms there is no undissolved material present within the glass matrix. C3 XRD pattern apparently shows the composition to be fully amorphous. However, the corresponding optical image in Figure 5.4 show low levels of undissolved material within the matrix, which are likely to be below the detection limits of the XRD. C5 and C3 have the same waste loading at 72 wt%, however, C5 clearly has greater amounts of undissolved material within the vitrified waste form. It known that the R ratio (Section 5.2.1) has a large influence in determining the structure of sodium borosilicate glasses.

(Wt %)	C1	M1	C2	M2	C3	M3	C4	M4	C5	M5
SiO_2	52.39	58.76 ±0.47	53.53	59.43 ±0.47	55.48	60.22 ±0.47	52.39	58.09 ±0.47	55.48	60.52 ±0.47
B_2O_3	18.00	11.37 ±0.20	18.7	11.88 ±0.20	15	10.26 ±0.20	22	14.68 ±0.23	19	12.73 ±0.21
Na_2O	14.1	15.56 ±0.23	12.68	12.77 ±0.21	13.1	13.07 ±0.21	10.1	12.16 ±0.21	9.1	11.25 ±0.21
Al_2O_3	2.35	3.98 ±0.11	2.4	3.92 ±0.11	2.49	4.02 ±0.12	2.35	3.72 ±0.11	2.49	3.36 ±0.11
K_2O	0.73	0.86 ±0.06	0.75	1.09 ±0.06	0.78	1.18 ±0.06	0.73	1.00 ±0.06	0.78	1.21 ±0.06
CaO	5.81	6.34 ±0.15	5.93	7.17 ±0.17	6.15	7.96 ±0.17	5.81	6.54 ±0.15	6.15	8.44 ±0.18
Fe_2O_3	0.83	0.89 ±0.06	0.75	0.91 ±0.06	0.88	1.13 ±0.06	0.83	1.03 ±0.06	0.88	1.29 ±0.06
SO_3	-	0.63 ±0.05	-	0.72 ±0.05	-	0.92 ±0.06	-	0.71 ±0.05	-	0.88 ±0.06
Other	5.79	2.06 ±0.09	5.16	2.63 ±0.09	6.12	1.94 ±0.08	5.79	2.55 ±0.09	5.67	0.99 ±0.06
Density (g/cm^3)	2.549 ± 0.040		2.536 ± 0.002		2.539 ± 0.002		2.492 ± 0.002		2.491 ± 0.030	

Table 5.4 Composition of vitrified core drilling. The table compares the premelt composition (M1-M5) and the actual post melting composition (C1-C5)
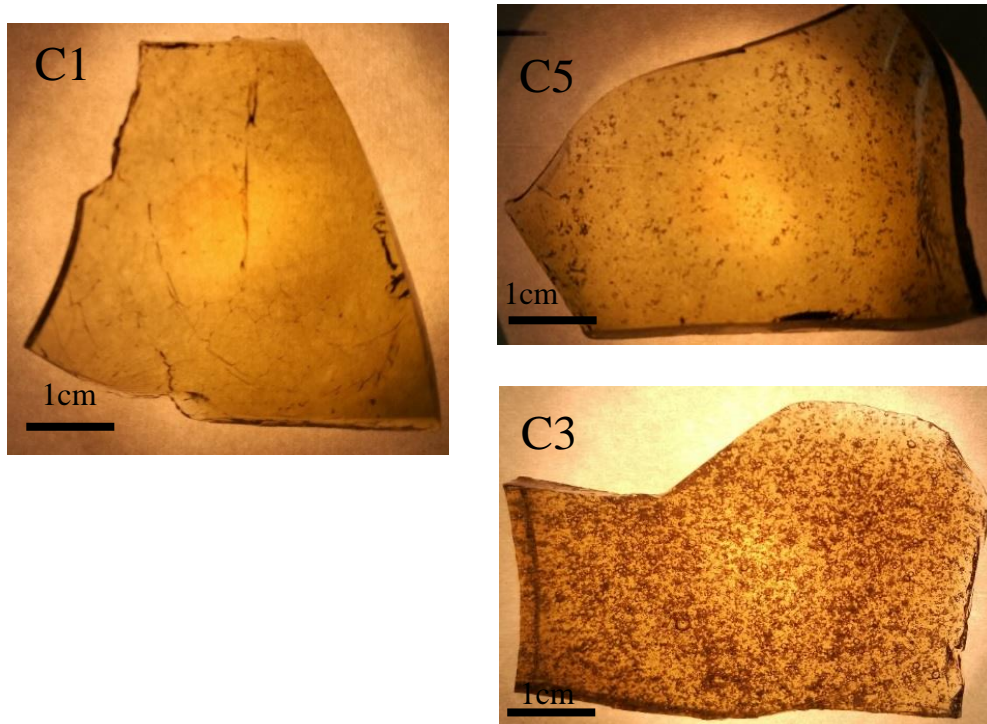
Figure 5.4 Images of Glass C1, C3 and C5 showing the varying levels of undissolved SiO_2 within the glass matrix

Additional Bragg reflections were identified in C5 with less intense reflections in C4. These reflections correspond to SiO_2. Figure 5.5 showed Bragg reflections, with low intensity, corresponding to cristobalite which suggests that some of the undissolved silica has undergone a phase transformation to cristobalite. The processing temperature of 1100ºC is low for this transformation to occur with Wahl et al. (1961) observing the transformation at 1400°C . However Palermo et al. (1998) study proved that sodium silicate promotes the conversion of quartz to cristobalite at temperatures close to 1050°C. Palermo et al. (1998) found that sodium silicate would become saturated with respect to silica, and cristobalite would crystallize. It is likely a similar mechanisms is occurring in this study, with the Na from the Na_2CO_3 fluxing agent stabilising the cristobalite at 1100°C. This is in agreement with the work performed by Ferrière et al. (2009).
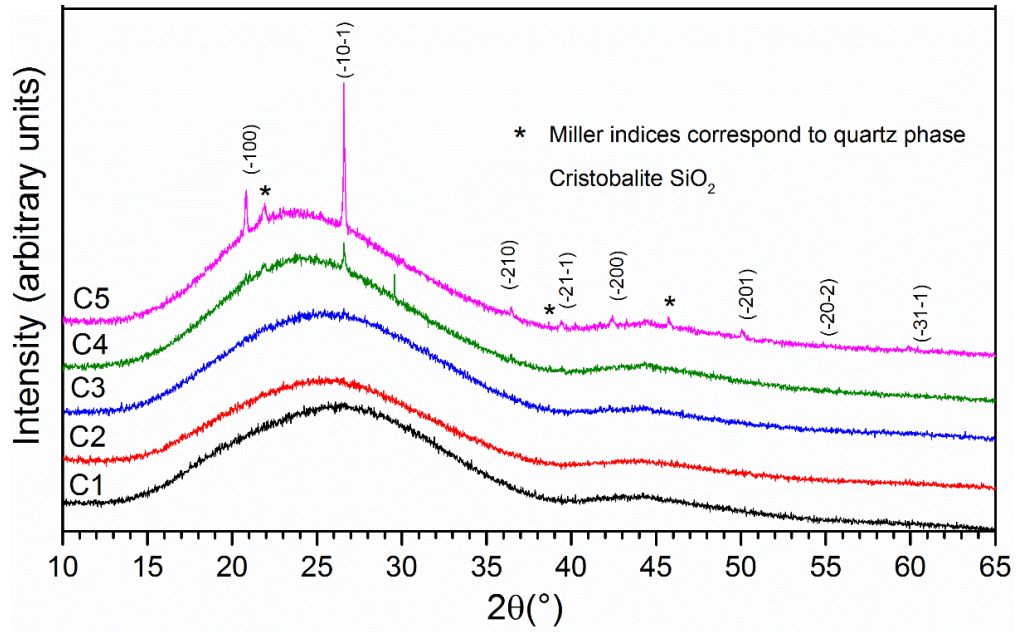
Figure 5.5 Powder X-ray diffraction patterns resulting from analysis of each of the vitrified simulant masonry waste glass compositions. Indexed reflections correspond to the quartz mineral phase (cristobalite) formed in glass composition C5. Miller indices shown are as (hkl).
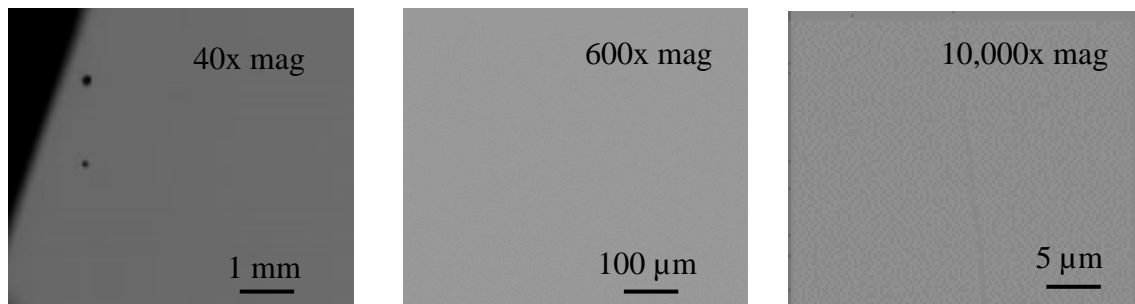
Figure 5.6 Optical micrograph image of C1 glass composition at various magnifications, showing no crystalline phases formed. The lack of image contrast suggests chemical homogeneity within the sample

5.3.2 Glass structure analysis – Raman spectroscopy analysis

An interesting feature of Figure 5.5 is that C5 and C3 have the same waste loading (72wt%) but C5 has Bragg indexed reflections corresponding to quartz, likely to be undissolved SiO_2 from the masonry waste (shown in Figure 5.4), whereas C3 has no apparent crystalline component, as evidenced by the diffuse scattering indicating an X-

ray amorphous material. A small volume fraction of crystallites cannot be ruled out, which would be below the detection limits of the XRD. TEM diffraction data would be required to achieve this which is outside the scope of this work. Figure 5.5 indicates that the ratio of sodium and boron (R value) clearly has an impact on the overall structure of the glass. In order to understand what effect the varying concentration of alkali cations are having within the glass network, in terms of structural evolution of the glass, a method of characterising the structure of amorphous materials is needed. Raman spectroscopy can be used for this purpose. Section 3.12 gives a general overview of the principles of Raman spectroscopy. The main question of interest in this study is the speciation of the silicate and borate structural units, and how these two types of glass formers are connected within the glass structure. The structure of the sodium borosilicate system has been studied extensively using Raman spectroscopy within the literature Furukawa (1981), Matson (1983), Yaday (2015), Kamitsos (1994), Koroleva (2010).

Figure 5.6 shows the Raman spectra of the five vitrified waste forms. Manara et al. (2009), investigated the behaviour of ternary SiO_2-Na_2O-B_2O_3 borosilicate glasses at high temperatures by Raman spectroscopy. Within this study Manara et al. (2009) showed different R ratio values and the effect the glass modifier has on the glass structure, which concluded that borosilicate glasses become more depolymerised with a high R ratio value. This section will use the approach of Manara et al. (2009) study, along with other relevant literature, to determine the effect the R value has on polymerisation of the glass structure.

Bell et al. (1969) states that the broad band at 460 cm^{-1} is due to bending of Si-O-Si bonds and that the change in the band shape and intensity are caused by incorporation of BO_4 units and BO_3 units into the silica network. The results shown in Figure 5.6 would agree with this finding, with an increase in boron content in C4 and C5 (22 wt.% and 19wt% respectively) leading to a Raman band at 460 cm^{-1} with a greater intensity as opposed to C1, C2 and C3. The increased boron content has promoted the formation of borate groups within the silica network.

The peak apparent at 620 cm^{-1} within the Raman spectra is used to investigate the effect of varying the R value on the glass structure. Manara et al. (2009) study has shown that the intensity of the peak at 620 cm^{-1} increases when the amount of Na_2O content within the glass is increased, and especially for R values greater than 0.8. The results shown in Figure 5.6 would agree with Manara's findings. From visual inspection it is clear that C1

has the largest intensity at peak $620cm^{-1}$ which corresponds to the largest R value of 0.88 whereas C5 with the lowest R value, 0.46, has the lowest intensity in that range.

The bands in the region of the spectra 800-1250 cm^{-1}, represent the extent of glass polymerisation and results from the Raman active silicon Q^n species. Figure 5.7 shows the deconvoluted region of the spectra 800-1250cm^{-1}. The bands are assigned to Si-O stretching vibrations, as already published in a variety of Raman studies of alkali and alkaline earth silicate glasses (Manara et al. 2009; Frantz 2005) as shown in Table 5.5.
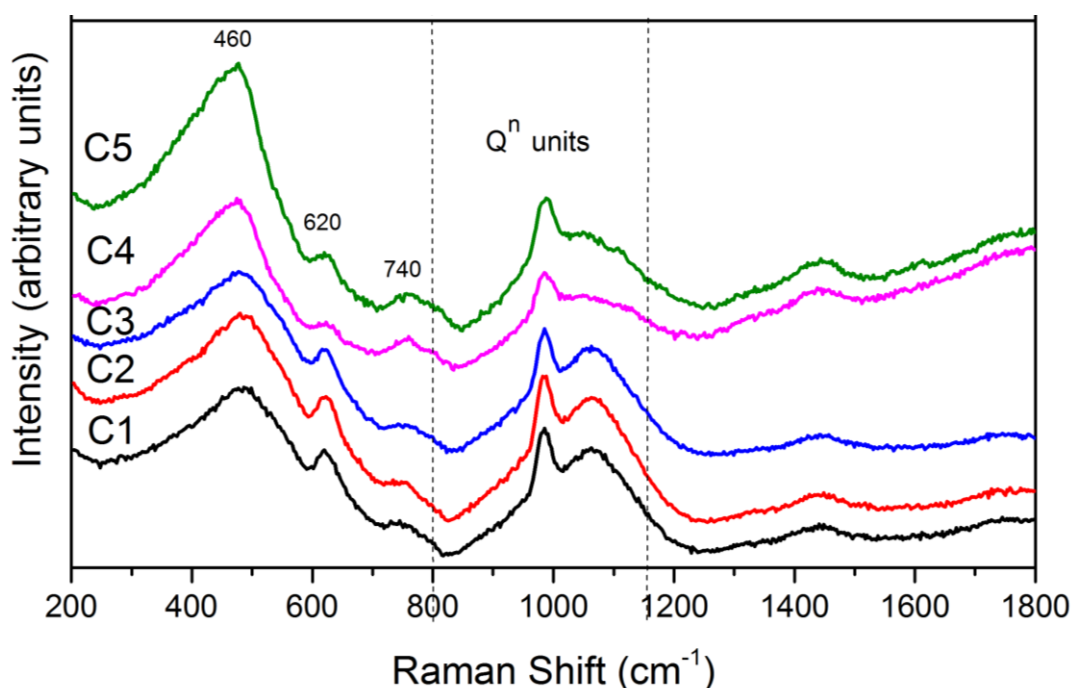
Figure 5.6 Raman Spectra for the vitrified masonry wasteforms in the region 200-1800 cm^{-1}. R ratio values of compositions C1=0.88, C2=0.76, C3=0.85, C4=0.52, C5=0.46

It is known that typical Portland cement contains between 1-3 wt % SO_3 (Taylor 1997). This is important to consider because many types of radioactive wastes that are destined to be incorporated in glass contain significant amounts of sulphur. Due to the low solubility of sulphate in silicate melts, sulphur can become the waste loading constituent during the vitrification of HLW. Vienna et al. (2014) states that when the sulphate capacity of the host glass exceeds 2 wt % (SO_3), an immiscible layer forms on top of the glass. This layer is problematic as it may include radioactive fission products which can hinder their incorporation into the glass matrix (Stefanovsky 1993). For this reason there

have been a number of studies, utilising Raman spectroscopy, to characterise sulphur environments in borosilicate glasses (Lenoir et al. 2008; Marion et al. 2009; McKeown et al. 2001). The peak evident at 988 cm^{-1} corresponds to the formation of tetrahedral SO_4^{2-} (sulphate) environments within the glass (McKeown et al. 2001). McKeown et al. (2001) showed that with the addition of SO_3, at 1.15wt.% within a borosilicate system, sharp peaks appear superimposed on the borosilicate bands near 990 and 630 cm^{-1}. Table 5.4 shows that the glass samples (C1 – C5) contain SO_3 ranging from 0.63 – 0.92 wt. %, therefore it is likely that the peaks shown in Figure 5.6 at 990 and 630 cm^{-1} are attributed to the SO_4^{2-} within the glass. Samples C4 and C5 have proportionally higher amounts of Q3 and Q4 species within the glass resulting in a broadening of the Raman bands plotted in Figure 5.7. Therefore this causes a slightly higher value for the Raman Shift for Samples C4 and C5 in the regions of Q3, Q3* and Q4.

Lenoir et al. (2008) was able to plot a linear relationship between an increase in SO_4^{2-} concentration within the host glass, with an increase in the Raman area relative to Gaussian band centred near 990cm^{-1}. There appears to be a linear relationship between the R values and the area relative to the Gaussian band centred near 990cm^{-1} presented in this study. Composition C5 has an R value of 0.46 with a corresponding area centred at 990cm^{-1} of 1.3%. Contrarily, composition C1 has an R value of 0.88 with a corresponding area centred at 990cm^{-1} of 6.4. This is consistent with previous studies by Manara et al. (2007) which investigated the behaviour of sulphur in silicate glasses as a function of alkali cation content. Other authors including Jantzen et al. (2004) report that sulphate solubility is improved by an increase of network modifier content thereby increasing network depolymerisation. The narrow peak observed at 990cm^{-1} is similar in frequency to symmetric S-O stretch vibrations of tetrahedral SO_4^{2-} ions found in sodium sulphate (McKeown et al. 2001). The peaks at 990cm^{-1} shown in Figure 5.7 are considerably broader than the peaks for the sodium sulphate due to an increase in the disorder of the sulphate tetrahedron in the glass compared with sulphate tetrahedron in crystals. The Na$^+$ act as charge compensating alkali ions in the glass bonding with the sulphate anions according to the reaction:

$$2(Si\text{-}O\text{-}Na)^+ + SO_4^{2-} \rightarrow 2(Si\text{-}O\text{-}Si) + Na_2SO_4 \qquad \text{(Manara et al. 2007)}$$
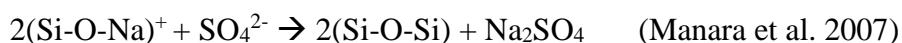
This explains the linear relationship between an increase in the area of the Raman band centred at 990cm^{-1} with an increase in the R value. Caution should be given with these

conclusions due to the relatively large error in determining the SO_4^{2-} composition and the small range of compositions studied in this thesis. In addition it should also be noted that the SO_4^{2-} was determined for the bulk of the sample and not exclusively from the glass phase. The Raman spectra however were taken only from the glass phase. The true SO_4^{2-} content could be lower than the bulk, if for example, Na_2SO_4 and $CaSO_4$ are present as separated phase. Despite these uncertainties, the results from this section are positive in terms of immobilising the SO_4^{2-} within the glass network. Vienna et al. (2014) states the solubility limit of sulphate in borosilicate glass is roughly 2 wt%. In this study the composition of SO_4^{2-} within the glass was below 2 wt%. For waste streams that have higher amounts of sulphate, this project has shown that sodium borosilicate glasses with a high R ratio can increase the solubility of sulphate within the glass.

Figure 5.5 shows that there remains undissolved SiO_2 within the glass matrix of M5. Sample M3 has lower levels of undissolved material as depicted by the X-ray amorphous diffraction pattern despite the same waste loading of 72 wt. % scabbled pond waste. This shows that the R value has an effect on the solubility of the scabbled pond waste in the glass. There have been a number of studies performed investigating the structure of borate and borosilicate glasses which can be used to assess the influence of the R ratio (Osipov et al. 2013; Koroleva et al. 2010; Matson et al. 1983; Yaday et al 2015; Manara et al. 2009). It is generally accepted in the literature that for low modifier oxide additions (R<0.5) triagonal BO_3^0 is converted to $B\emptyset_4$ ($\emptyset$ = bridging oxide) tetrahedral. For R > 0.5 a significant number of non-bridging oxygen atoms form, which prefer silicate over borate sites. C3 has an R value of 0.85 therefore the non-bridging oxygen atoms prefer silicate over borate sites which allows the SiO_2 to dissolve into the glass matrix. This shows that with an increase in Na_2O an increase in non-bridging oxygen atoms occurs, which essentially increases the degree of depolymerisation within the glass. This goes some way to explain why the scabbled pond waste is fully dissolved in C3 (R=0.85) as opposed to C5 (R=0.46) which shows inclusions within the glass structure. Osipov et al. (2013) showed that low alkaline borosilicate glasses (R<0.5), such as M5, contain a significant fraction of $Si-O-B_3$ bonds within the glass structure. The number of $Si-O-B_3$ bonds clearly outnumber the fraction for $Si-O-B_4$ bonds as expected from the low Na^+ fraction of these glasses.

Raman studies showed that the Na_2O/B_2O_3 ratio has a significant impact on the crystallisation behaviour of the glass sample with a lower R value promoting crystallisation within the structure.
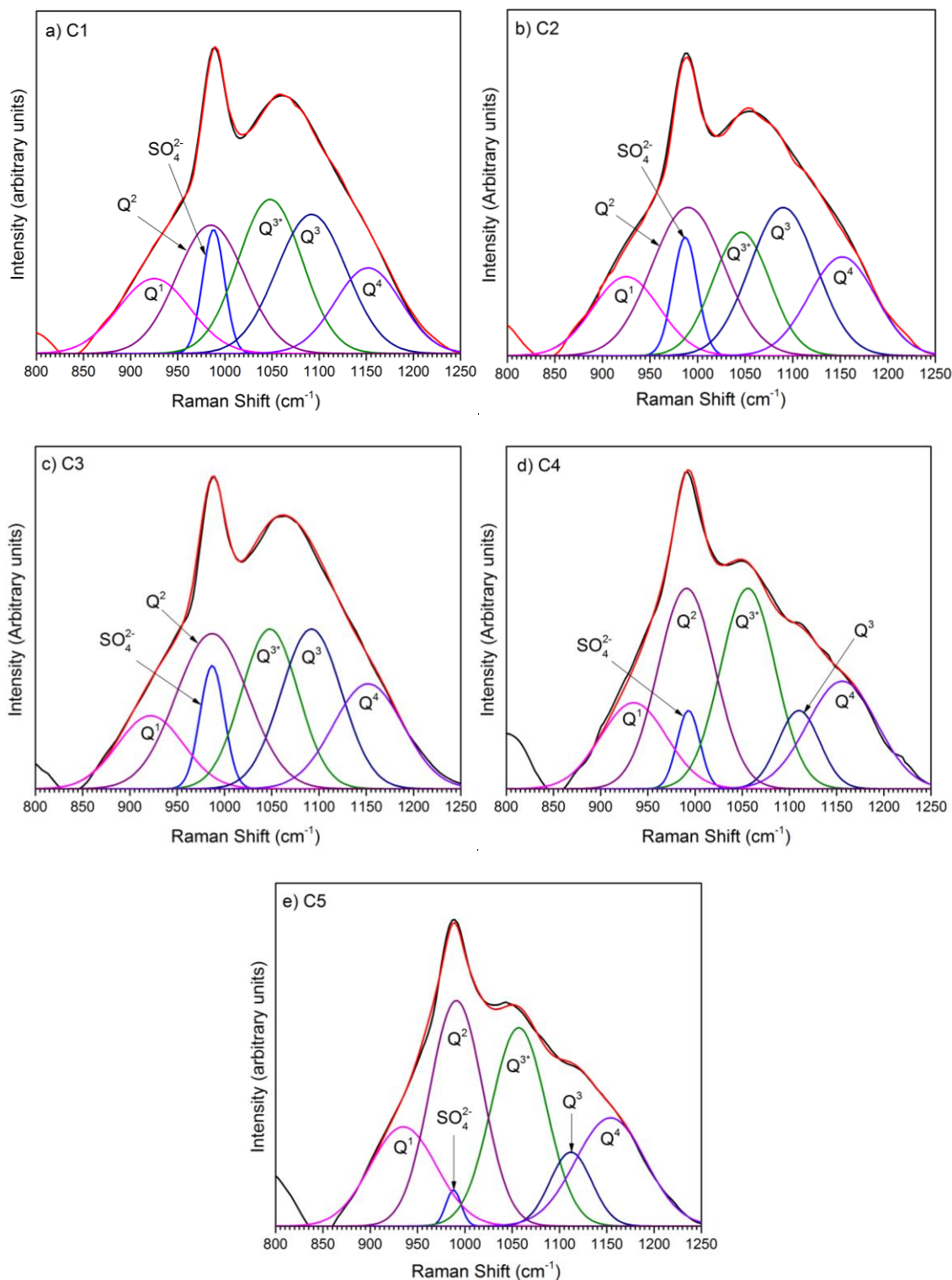
Figure 5.7 Gaussian peak-fit for the silicon Qn region of the Raman spectrum

	Raman Shift (±4cm^{-1})						Resolved Raman Fractional Area (± 2.0%)					
	Q^1	Q^2	SO_4^{2-}	Q^3	Q^{3*}	Q^4	Q^1	Q^2	SO_4^{2-}	Q^{3*}	Q^3	Q^4
C1	925	985	988	1048	1092	1152	12.6	20.6	6.4	23.5	23.3	13.6
C2	925	990	983	1046	1090	1152	12.2	25.1	6.8	16.7	23.4	15.8
C3	922	987	988	1048	1092	1152	10.6	24.6	6.6	20.1	21.6	16.5
C4	935	991	993	1056	1110	1156	13.8	27.8	4.3	27.1	8.1	18.8
C5	935	991	988	1057	1112	1154	16.0	29.2	1.3	26.9	7.7	18.9

Table 5.5 Peak assignments, positions and intensity relationships for bands in the region 800–1250 cm^{-1}, representative of the silicon Q_n region

5.3.3 Differential Thermal Analysis (DTA)

Figure 5.8 shows the endothermic and exothermic reactions as a function of temperature for the vitrified C5 sample when compared with a reference sample, in this case pure quartz. The endothermic and exothermic reactions correspond to specific thermal events in the glass (section 3.10), shown in Table 5.6. The endothermic event shown at 592°C corresponds to the glass transition temperature (T_g). It should be noted that the T_g occurs over a temperature range, therefore Figure 5.8 quotes the onset temperature of the T_g event along with the lowest endothermic point quoted as the T_g temperature, which is the widely regarded method of determining the T_g value. This value is comparable to typical sodium borosilicate values (Avramov 2005). The thermal event indicative of T_g occurs as the glass converts from a solid to a liquid in the glass transformation region (Kamitsos, E.I 1994). The physical properties change during the glass transformation region, the glass is essentially viscoelastic solid/liquid, the glass takes on a fixed but disordered arrangement (Ojovan 2008). The T_g will cause an increase in the thermal lag of the sample relative to the inert reference material resulting in an offset of the curve, as shown in Figure 5.8.
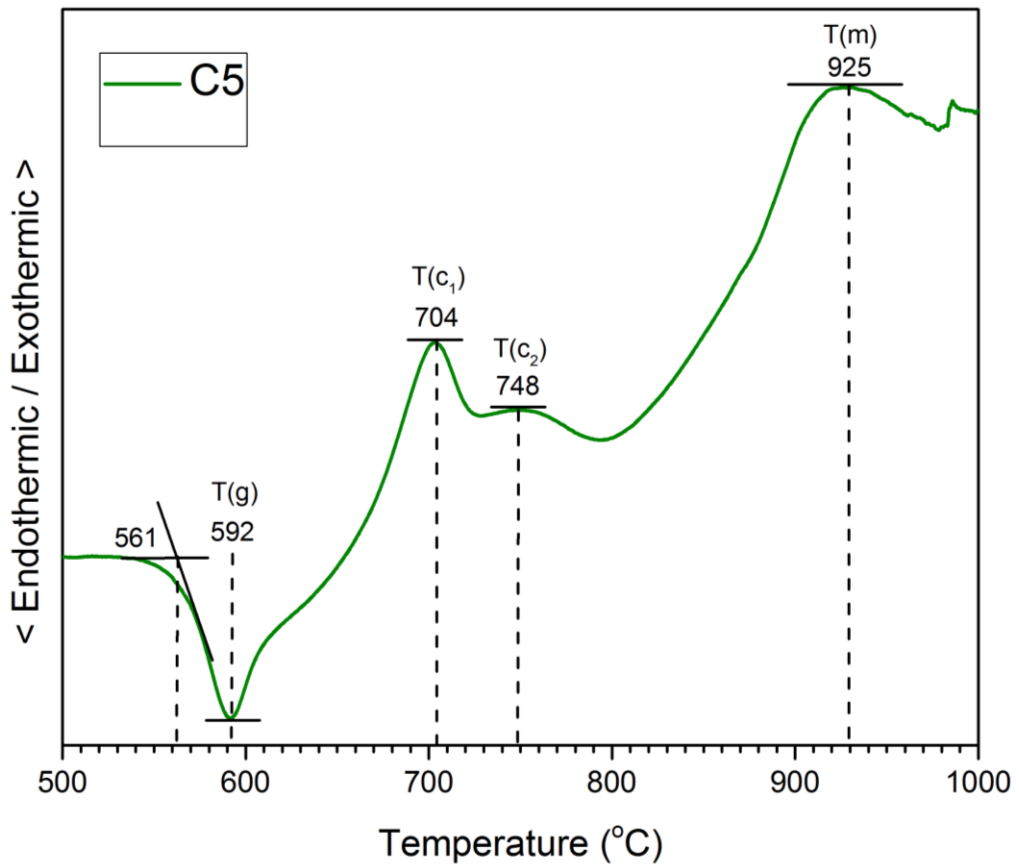
Figure 5.8 DTA trace for the C5 vitrified masonry waste. The samples were heated at 10°C per minute to 1100°C in an Argon atmosphere in platinum crucibles. All temperature values are shown in ºC.

Composition	T_g		T_C		T_m	Phase diagram T_m
	Onset	Peak	T_{C1}	T_{C2}		
C1	559 ºC	581 ºC	695 ºC	-	911 ºC	935 ºC
C2	562 ºC	585 ºC	698 ºC	-	918 ºC	940 ºC
C3	569 ºC	593 ºC	712 ºC	-	946 ºC	1035 ºC
C4	585 ºC	601 ºC	711 ºC	-	918 ºC	895 ºC
C5	561 ºC	592 ºC	704 ºC	748 ºC	925 ºC	950 ºC

Table 5.6 Thermal events in the vitrified masonry waste samples C1-C5. All temperature values are shown in ºC.

165

The exothermic event signalled by the peak at approximately 704°C, labelled T_{C1} in Figure 5.8 corresponds to the crystallisation temperature within the glass as the enthalpy of fusion is released from the sample. Compositions C1-C4 show only one crystallisation peak indicating a single phase is formed, C5 does show two crystallisation peaks indicating the formation of a secondary crystalline phase. This is confirmed in the XRD traces in Figure 5.5.

Table 5.6 also gives the expected T_m of the vitrified samples using the phase diagram shown in Figure 3.7. The measured T_m values are consistently lower compared to the expected phase diagram values. This is not surprising, as the composition of the glass is somewhat different to the composition shown in the phase diagram. When using the phase diagram to formulate potential glass compositions the representative scabbled pond waste was considered to be 100% SiO_2. However XRF studies show that the representative scabbled pond waste is composed of only 77.05 ± 0.53 wt. % SiO_2 (Table 5.1). Therefore the overall glass composition will have lower amounts of SiO_2, as shown in the XRF studies of the vitrified product (Table 5.4), which ultimately affects the temperature at which these raw materials initially form a eutectic melt for the SiO_2 to then dissolve into. The same general trends do still apply, with the C3 and C5 having the greatest T_m value (946 °C and 925 °C respectively) due to the increased amount of SiO_2 (72 wt. %).

It is agreed both in terms of waste vitrification (IAEA 2002) and general commercial glass technology (Rose et al. 2011) that the two most important criteria when considering melting technology is viscosity – temperature profile (η–T) and the liquidus temperature (T_{liq}). For melter technology that are designed to pour molten glass into waste containers, the liquidus temperature is vital. Bingham (2012) states that to avoid unwanted crystallisation during pouring, which could block the pouring nozzle or cause inhomogeneity in the glass, the molten glass must be maintained at temperatures sufficiently in excess of T_{Liq} until it has passed through the nozzle during pouring. The forming temperature, T_F, is the temperature at which the glass is formed or poured, and is usually cooler than the regions of the melter in which the melting and homogenisation takes place. To ensure problem free melting and pouring the value of (T_F–T_{Liq}) must have a substantial positive value. The glass samples formed in this report were cast at 1100˚C therefore T_F equals 1100˚C. Hrma et al. (1998) states that to avoid unwanted spinel formation, T_{Liq} must be at least 100°C below the lowest temperature in the melter. No spinel formation was detected within the vitrified samples in this Chapter, due to the

absence of metal fraction within the waste. However it is conceivable that steel, which provides structural support within the concrete walls of the silo ponds, could be present within the waste stream. Using this information, the glass composition must have a melting temperature below 1000°C to be compatible for pouring based on these requirements. Table 5.6 shows that all of the glass composition (C1-C5) have melting temperature below 1000°C, providing strong evidence that all of the glass compositions formulated here would be compatible with currently available technology platforms which pour molten glass.

5.3.4 Radionuclide retention and distribution within the glass network.

After the initial success of vitrifying glass composition C1-C5, subsequent melt C6 and C7 were doped with stable isotopes of Cs_2O (as Cs_2CO_3), CoO (as Co_3O_4), SrO (as Sr_2CO_3) and also U_3O_8, the composition of which can be found in Table 5.7. In this investigation, ^{90}Sr, ^{60}Co and ^{137}Cs can be safely simulated using their naturally occurring isotopes. The U_3O_8 and inactive simulants were milled together with the masonry waste with 1 part simulants to 9 parts masonry waste. This was then diluted down with further masonry waste; this approach minimised handling of the active materials. From the known initial glass batch, the retention rates of the elements within the glass can be calculated following thermal treatment, which is shown in Table 5.8.

The mass balance shown in Table 5.8 is encouraging, within the precision of the experiment. The small scale melts performed in this work result in an increase in Al_2O_3 content due to corrosion of the crucible. This is difficult to account for and results in all the oxides should read lower than expected. ^{137}Cs has been shown to be volatile at high temperatures, thus stabilization of this radioactive isotope in the glass matrix presents a challenge which must be met if the waste is to be successfully vitrified. Minimization of the amount of radioactive Cs emitted to the offgas stream reduces process hazard. The amount of Cs used in this study is at a concentration which would be considerably higher than expected in masonry waste classified as ILW. This conservative approach was chosen to ensure detection post processing. The retention rates for Cs in the glass (80%) are comparable with those found in previous studies (Cirero-Herman 1998) which showed Cs retention rates of 76.9% after processing similar borosilicate glasses at 1150°C.

(Wt %)	M1C	M2C
SiO_2	59.02 ± 0.47	59.18 ± 0.47
B_2O_3	11.45 ± 0.20	11.72 ± 0.20
Na_2O	15.61 ± 0.23	12.88 ± 0.21
Al_2O_3	3.88 ± 0.12	3.84 ± 0.11
K_2O	1.03 ± 0.06	1.23 ± 0.08
CaO	6.42 ± 0.15	7.31 ± 0.11
Fe_2O_3	1.04 ± 0.06	0.95 ± 0.06
MgO	0.19 ± 0.03	0.22 ± 0.03
SO_3	0.62 ± 0.05	0.69 ± 0.05
U_3O_8	0.06 ± 0.02	0.07 ± 0.02
CoO	0.06 ± 0.02	0.06 ± 0.02
Cs_2O	0.05 ± 0.02	0.04 ± 0.02
SrO	0.04 ± 0.02	0.06 ± 0.02
Other	0.62 ± 0.05	1.85 ± 0.09
Density	2.523 ± 0.014	2.529 ± 0.002

Table 5.7 XRF results of the C1 and C2 doped with inactive isotopes and U_3O_8 to give samples M1C and M2C

Information from BNFL ltd indicates that a caesium-containing gas evaporates from the melter at approximately 1000°C, and condenses on vents and outlets around the plants (Parkinson 2007) . Asano (1981) was unable to confirm the presence of $Cs_{(g)}$ or $CsO_{(g)}$ among the volatile species during the heating of a Cs containing sodium borosilicate glass at 1200ºC. Asano (1981) identified a number of volatile species containing Cs, Na and B including $CsBO_{2(g)}$. Caution must be given in comparison to this study due to the experimental conditions occurring under vacuum, while the samples were heated and

measured, which is unrealistic when considering a typical melter, which will be operated in air.

	Weight in glass C6 (g)	Wt% expected	Wt % measured	Retention (±10%)
Cs_2O	0.3287	0.22	0.18	80%
CoO	0.2525	0.17	0.15	90%
U_3O_8	0.3006	0.20	0.18	90%
SrO	0.1088	0.08	0.08	100%

Table 5.8 Retention rates of inactive isotopes and U_3O_8 within the vitrified glass waste form (C6), with associated errors

The sample volume and surface were both different in Asano (1981) which will also have an large influence on volatility of Cs. An investigation by the Japan Atomic Energy Research Institute confirmed that Cs vaporized as $CsBO_2$ which is consistent with Asano (1981) work. Therefore it can generally be accepted that Cs will volatilise as $CsBO_2$. Jantz (1980) has shown that $CsBO_2$ will condense and react with the steel chamber in the plenum, which indicates that gasoues alkali borate phases volatilize when borosilicate glasses are melted and then condense on colder substrates within the off-gas system. The results from this investigation show that up to 20 wt.% of Cs can volatilise, however these is significant uncertainty with error values of ±10 wt.%. The retention rates are certainly similar to that achieved in full scale melter systems, in which retention is typically higher than laboratory experiments due to lower SA/V ratio of the melt. The results from this section are encouraging to thermal treatment operators.

5.3.5 X-Ray absorption near edge spectroscopy (XANES)

X-ray absorption spectroscopy was used to determine the uranium speciation of the vitrified masonry waste in composition C6. Figure 5.9 shows the U L_3 edge X-ray Absorption Near Edge Structure (XANES) of the slag fractions, together with the data acquired for UTi_2O_6, $Y_{0.5}U_{0.5}Ti_2O_6$, $CaUO_4$ which were used as U^{4+}, U^{5+} and U^{6+} standards respectively. Previous work has shown that uranium can exist in the oxidation states U^{6+}, U^{5+} and U^{4+} in alkali borosilicate and silicate glasses (Farges et al. 1992; Connelly et al. 2013). Greaves et al. (1989) states that uranyl species bond to non-bridging oxygens within a silicate glass indicating an intermediate type role, with alkali ions acting

as charge compensators. The XANES spectra shown in Figure 5.9 provides straight forward determination of the uranium oxidation state in the glass. Using the position of the edge shift of sample C6 in comparison with the uranium standards, it is clear that U^{+5} is the dominant species, this is shown in Table 5.9. Uranium is a relatively mobile element in the near surface zone owing to the stability of U(VI) aqueous complexes. Therefore, during the vitrification of the representative scabbled pond waste oxidation to U^{+6} would not be preferred due to higher aqueous solubility. This section confirms oxidation to U^{+5} which is preferable.

Figure 5.10 is the first derivative of the $\mu(E)$ versus E curve and can be used to determine the exact position of the inflection point. The first maximum on the first derivative curve gives the position of the inflection point and hence the position of the absorption edge. This method confirms that the presence of U^{5+} as the dominant species within the vitrified masonry waste.
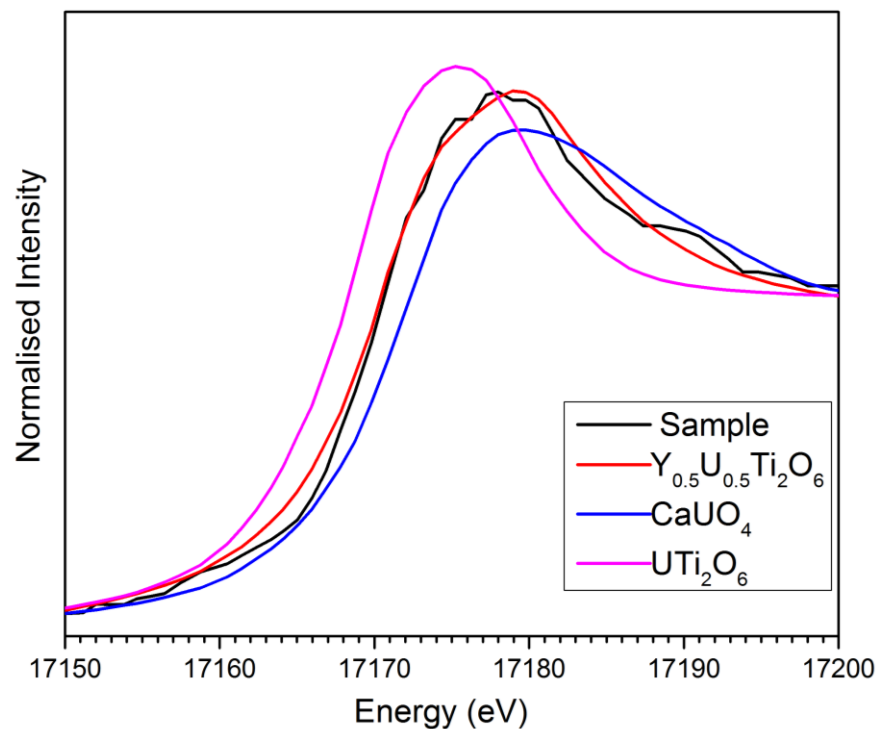
Figure 5.9 U L_3 edge XANES data from $Y_{0.5}U_{0.5}Ti_2$ (U^{5+} standard), $CaUO_4$ (U^{6+} standard), UTi_2O_6 (U^{4+} standard) and the vitrified masonry waste C6.

Sample	E_0(eV) ± 0.2	Oxidation State
Masonry C6	17167.2	+5
$Y_{0.5}U_{0.5}Ti_2O_6$	17166.3	+5
$CaUO_4$	17168.1	+6
UTi_2O_6	17164.3	+4

Table 5.9 U L$_3$ edge XANES data from UTi$_2$O$_6$ (U^{4+} standard), Y$_{0.5}$U$_{0.5}$Ti$_2$ (U^{5+} standard), CaUO$_4$ (U^{6+} standard) and vitrified masonry waste C6.
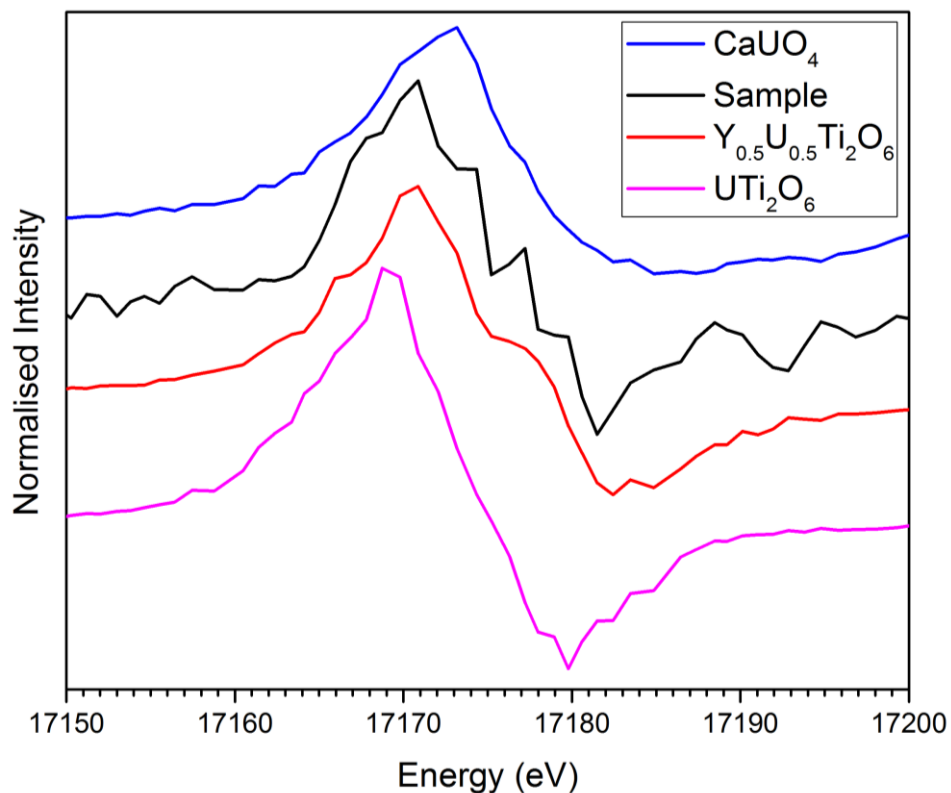
Figure 5.10 first derivative of the XANES data

5.3.6 Dissolution in simulated hyper alkaline conditions of a cementitious Geological Disposal Facility.

Dissolution experiments utilising the Product Consistency Test B (PCT-B) protocol were carried out on the vitrified representative scabbled pond waste C6. Section 3.5.2 describes the experimental set-up of the PCT-B test in greater detail. In summary, experiments were carried out for a period of 28 days in saturated $Ca(OH)_2$ solution, at a SA/V ratio of 1200 m^{-1}, at 50°C, and with sampling points at 1,3,7,14 and 28 days. ICP-OES analysis was used to determine the concentrations of all elements in solution. The concentration data was used to calculate normalised mass losses and mass loss rates. The glasses were leached in saturated $Ca(OH)_2$ solution, as this was taken to be a simplified representative for a solution that has come into contact with portland cement (PC) based mortar or concrete, which contain significant amounts of portlandite ($Ca(OH)_2$) and NRVB which will be used as the backfill material. The rationale for leaching the glass samples in high pH solution are explained in section 4.7. There have been a number of studies performed which investigate the chemical durability of UK vitrified wasteforms. These studies aim to inform the technical specification for the disposal facilities for these waste products and the treatment of their long-term behaviour in post-performance assessment (Utton et al. 2013; Utton et al. 2012; Corkhill et al. 2013; Backhouse 2016). These studies will be used to assess and analyse the chemical durability of the glass produced in this chapter.

Figure 5.11 shows the pH of the leachate for the vitrified masonry waste (C6) experiment. Generally, the leachate pH of the blanks remained consistent across the experiments. The pH does show a noticeable drop at the beginning of the experiment from ~ 12.7 to ~ 11.9 for the powder sample and ~ 12.8 to ~ 11.9 for the blank sample. These pH values are likely due to carbonation of the sample after removal from the anaerobic chamber rather than changes in the leachate chemistry during the experiments. The concentration of Ca remained relatively constant in the blank $Ca(OH)_2$ solution at 550 mg/L $\pm$ 60.5 as shown in Figure 5.12. This effectively constant Ca concentration in the blank solution is consistent with the exclusion of CO_2 under the anoxic conditions of the experiment. Contrarily, for the $Ca(OH)_2$ solution in contact with the glass powder (C6), the Ca concentration rapidly decreased from a value of ~500 mg/L ($\pm$ 45 mg/L) at 1 day to ~150 mg/L ($\pm$ 14 mg/L) at 28 days.
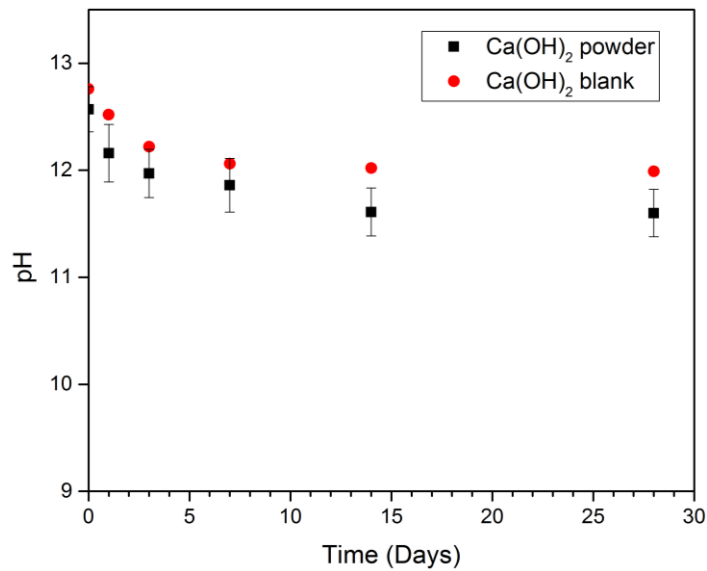
Figure 5.11 pH values for Ca(OH)$_2$ PCT-B experiments for the vitrified masonry waste form C6
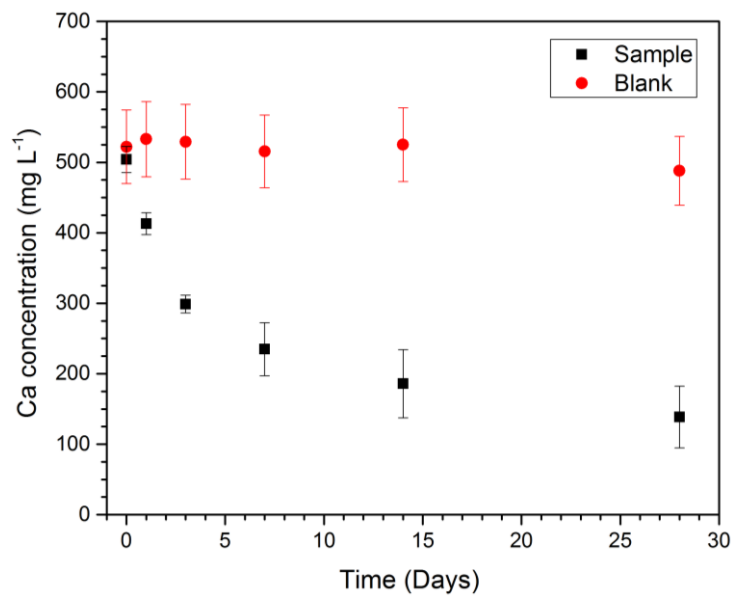
Figure 5.12 Solution concentration (mg/L) of dissolved Ca in blank (i.e. no glass) saturated Ca(OH)$_2$ solution and for vitrified masonry waste C6 glass.

The depletion of Ca from the glass sample solution, implies the precipitation of Ca bearing secondary phases at a rate which exceeds the diffusion of Ca into solution from the filter unit. Figure 5.13 shows SEM/EDX images of the glass particle post 28 days leaching in Ca(OH)$_2$. The BSE image shows an alteration layer has formed on the surface of the glass, as defined by the different contrast, corresponding to region 2 on the BSE image. Corkhill et al. (2013) aimed to gain a greater understanding of the formation of

alteration layers on UK HLW glass in saturated $Ca(OH)_2$. The results presented in this section are consistent with the general understanding of glass corrosion mechanisms in hyperalkaline $Ca(OH)_2$ solution (Corkhill et al. 2013). It is known that the parameters that control glass dissolution in the presence of Ca are; pH, surface to volume ratio and calcium concentration (Depierre et al. 2013). Garrault-Gauffinet (1999) study determined that Ca concentration is the most important parameter controlling the growth rate of C-S-H phase. Corkhill et al. (2013) proposes that the primary control on glass dissolution in saturated $Ca(OH)_2$ is equilibrium thermodynamics. (Berner 1992) states that in simplified CaO-SiO_2-H_2O systems the concentrations of Si and Ca in the aqueous phase are related to the precipitation of C-S-H phases by equilibrium thermodynamics. Corkhill (2013) states that the glass must dissolve to maintain these quasi-equilibrium conditions, resulting in the precipitation of C-S-H phases on the surface of the glass. The image of the glass particles post processing (Figure 5.15) and the rapid uptake of Ca from solution, as seen in the Corkhill (2013) study, indicates the glass synthesised in this chapter follows similar dissolution behaviour to that of the HLW glass studied by Corkhill (2013). The agglomeration of the particles during the experiment is also indicative of C-S-H phase, as this is the binding phase in cement chemistry.

The normalised mass loss for B and Na are shown in Figure 5.14 and the normalised mass loss Al, Fe, Si and U are shown in Figure 5.15 with the corresponding values of the normalized dissolution rate ($g/m^2/day$) given in Table 5.10.

The NL_i of network formers Si and B after 28 days is, (7.64 ± 0.858) x 10^{-3} and 0.489 ± 0.055 respectively, which is lower than that of the modifier cation Na with a NL_i of 0.817 ± 0.092 after 28 days.

The overall dissolution behaviour shown in Figure 5.14 is concurrent with generally accepted glass dissolution theory.
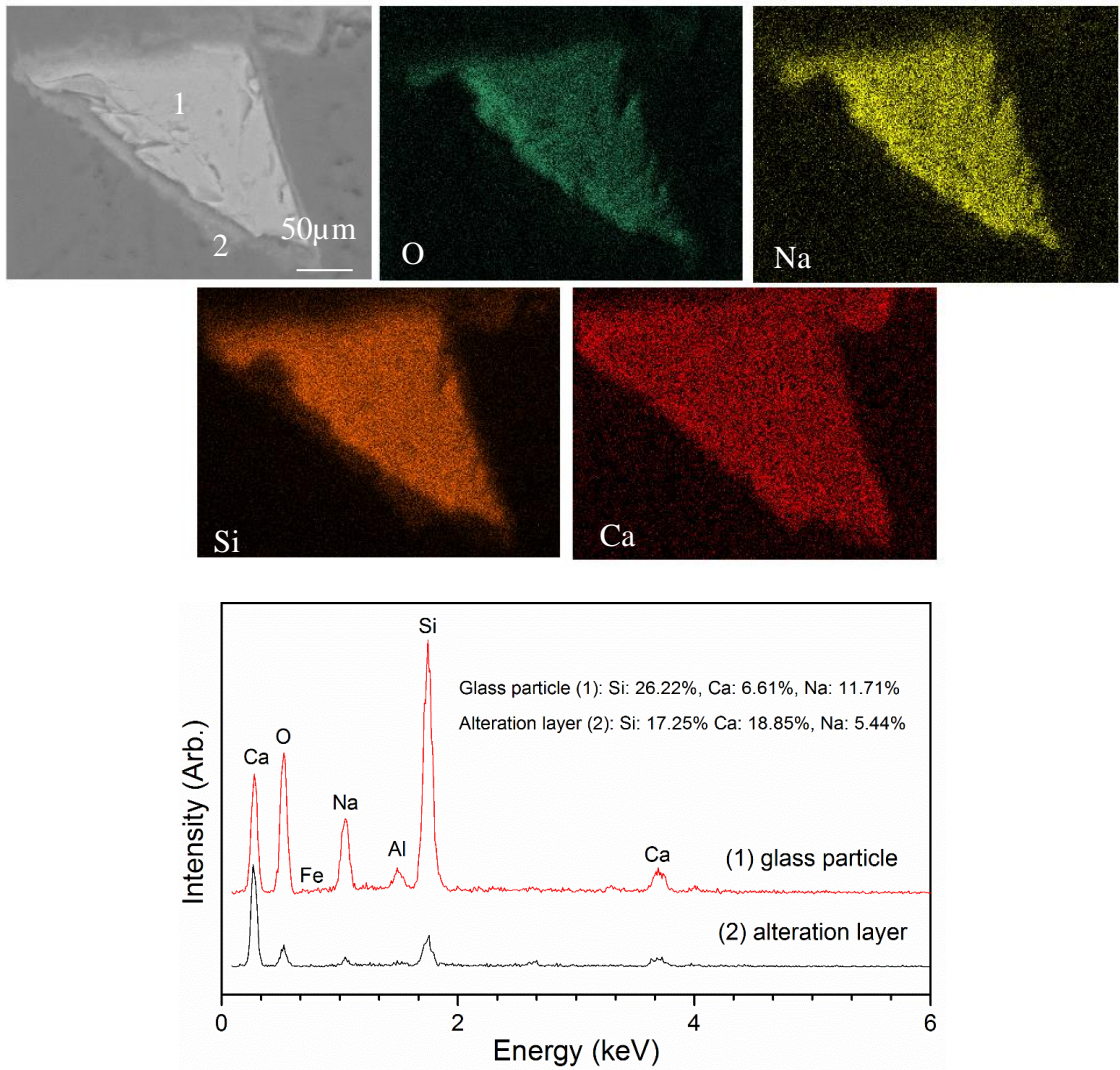
Figure 5.13 BSE micrograph and elemental maps of cross-sectioned C6 glass particle
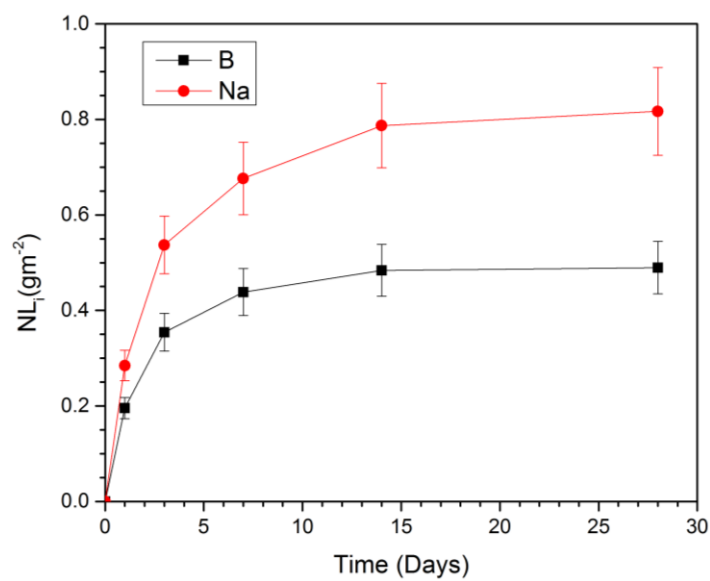
Figure 5.14 NL (B) and (Na) for vitrified masonry waste (C6) during 28 day PCT-B test
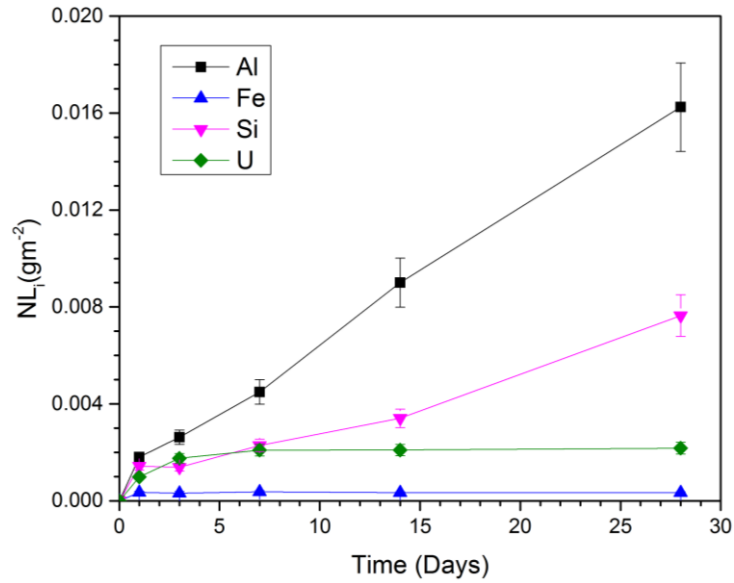
Figure 5.15 NL (Al), (Ce), (Fe), (Si) and (U) for vitrified masonry waste (C6) during 28 day PCT-B test.

Element	NL_i (g/m^{-2})		RL_i (g/m^2/d)	
	7 days	28 days	Initial (0-7 days)	Residual (14-28 days)
B	0.438 ± 0.049	0.489 ± 0.055	$(6.262 \pm 0.703) \times 10^{-2}$	$(1.749 \pm 0.196) \times 10^{-2}$
Na	0.676 ± 0.076	0.817 ± 0.092	$(9.663 \pm 1.084) \times 10^{-2}$	$(2.917 \pm 0.328) \times 10^{-2}$
Al	$(1.81 \pm 0.203) \times 10^{-3}$	$(1.625 \pm 0.182) \times 10^{-2}$	$(0.641 \pm 0.072) \times 10^{-3}$	$(0.758 \pm 0.085) \times 10^{-3}$
Fe	$(0.35 \pm 0.039) \times 10^{-3}$	$(0.33 \pm 0.037) \times 10^{-3}$	$(0.534 \pm 0.053) \times 10^{-4}$	$(0.120 \pm 0.013) \times 10^{-4}$
Si	$(1.43 \pm 0.161) \times 10^{-3}$	$(7.64 \pm 0.858) \times 10^{-3}$	$(0.327 \pm 0.036) \times 10^{-3}$	$(0.273 \pm 0.031) \times 10^{-3}$
U	$(0.99 \pm 0.113) \times 10^{-3}$	$(2.17 \pm 0.244) \times 10^{-3}$	$(0.299 \pm 0.034) \times 10^{-3}$	$(0.777 \pm 0.087) \times 10^{-4}$

Table 5.10 Normalized mass loss (g/m^{-2}) and normalized dissolution rates (g/m^2/day) of B, Na, Al, Fe, Si and U during the two main phases of dissolution in the first 28 days (initial and residual rate) in saturated Ca(OH)$_2$ solution for composition C6.

The general trend for the majority of elements is for the dissolution rate to drop and enter what is referred to as the residual rate. Figure 5.14 shows that after approximately 14 days the release rates for B and Na begin to level off (this occurs sooner for other elements), a characteristic of glass dissolution in closed systems, which is of particular importance as

this is representative of most geological disposal systems. As described in section 2.8 the dissolution rate will drop, because of either silica saturation in solution, or because of the protection from the reaction layers forming on the glass as alteration layers. The results in Table 5.10 show that the most likely mechanism in this case is the protection from alteration layers. During the residual rate shown in Figure 5.14 for both the B and Na (occurring at day 14), the NL_i of Si into solution increases from 0.0035 g/m^2 ($\pm$ 3.39 x 10^{-4} g/m^2) at day 14 to 0.0070 g/m^2 ($\pm$ 7.01 x 10^{-4} g/m^2) at day 28, therefore Si had not yet reached saturation within solution at day 14 when the residual rate occurs for B and Na. From this evidence it is assumed that the formation of alteration layers shown in Figure 5.13 is the dominant mechanism for the residual rate to occur.

Corkhill et al. (2013) describes the mechanisms of glass dissolution and the resultant formation of alteration layers of simulant HLW glass, during the first 28 days in both water and saturated calcium hydroxide. This study can be used as a useful comparison with the glass synthesised in this chapter. Interestingly, in Corkhill et al. (2013) study, the $NL_{(Al)}$ was observed to continuously increase in solution during the first 28 days. The $NL_{(Al)}$ in this work show the same trends, with the concentration of Al continuously increasing in the first 28 days, as shown in Figure 5.15. This confirms that it is not thermodynamically favourable to form C-A-S-H phases in the presence of Ca under these conditions, as suggested by Corkhill et al. (2013).

In terms of waste acceptance criteria for geological disposal, the result from this study are comparable to generally accepted HLW glasses (Harrison 2014; Gin et al. 2013; Curti et al. 2006). The results from this study show that the formation of an alteration layer, such as Figure 5.13, has a major impact on the mechanism of glass dissolution. Therefore, to determine durability of the glass waste form and allow comparison with other glass waste forms, elements need to be carefully selected as to represent maximum dissolution of the glass. ASTM C1285-02 (2002) states that elements that are not sequestered in precipitates that participate in surface alteration reactions, and are also not solubility limited, are good indicators of glass waste form durability. Boron is generally a good alteration tracer element (Scheetz 1984). However studies by Mercado-Dapierre (2013), which studied the effect of calcium on borosilicate glass alteration, showed that boron was retained within the alteration layer, deeming boron not a suitable tracer element for this investigation which uses similar experimental procedures. Na shows similar dissolution behaviour as B (Figure 5.14) and is not known to interact with the alteration

layer, therefore Na was used as the tracer element to determine the dissolution rate. The results in this study show an initial dissolution rate and a residual rate. Identifying and interpreting the final dissolution rates (residual rate in this study), is important as this will strongly affect the lifetime of the vitrified waste package (Harrison et al. 2009). The RL values in this study at 28 days for sodium are $((2.917 \pm 0.328) \times 10^{-2}$ g/m^2/d) which is comparable to generally acceptable vitrified packages including both the French R7T7 glass SON68 and MW, both of which are borosilicate glasses (Crovisier 2006).

The initial stage is when the most rapid dissolution rate occurs, therefore it is useful to compare the initial rates of the vitrified scabbled pond waste with other glasses potentially suitable for disposal within a GDF.

The initial RL_B and RL_{Na} are $6.262 \pm 0.703 \times 10^{-2}$ g/m^2/d and $9.663 \pm 1.084 \times 10^{-2}$ g/m^2/d respectively. Utton et al. (2013) performed similar glass dissolution experiments in saturated Ca(OH)$_2$ on laboratory simulant ILW glass. The initial RL_B and RL_{Na} at 50°C in this study were 0.023 ± 0.0013 g/m^2/d and 0.043 ± 0.0024 g/m^2/d respectively. This shows that the initial rate is much faster in the glasses synthesised in this Chapter. Additionally to this Utton et al. (2013) saw an incubation period where the elemental release rate into solution was much slower than would occur in the presence of water. Utton attributed this incubation period to the interactions between B in the glass and Ca in solution. Utton postulated that calcium borates form on the surface of the glass inhibiting dissolution. This incubation period was not seen in this study despite the B concentration in the glass being similar in both glass samples, 9.04 wt % (Utton) 11.04 wt% (C6 glass in current study). The results in this study would therefore disagree with Utton et al. (2013) interpretation of the incubation period being caused by the interactions between B in the glass and Ca in solution.

Backhouse (2016) also performed similar dissolution experiments on glasses with similar composition in saturated Ca(OH)$_2$. The RL_B and RL_{Na} from Backhouse (2016) are much closer with the values in this study than compared with Utton et al. (2013) study. The glass composition in Backhouse (2016) was $15Na_2O – 5CaO – 15B_2O_3 - 65SiO_2$ (given in Wt%), similar to composition M6 shown in Table 5.7.

The RL_B and RL_{Na} in Backhouse (2016) study was 0.048 ± 0.002 g/m^2/d and 0.097 ± 0.004 g/m^2/d respectively, which are very similar to the $R_{(0)}$ in this study shown in Table 5.10. Interestingly the incubation period noted in Utton et al. (2013) study was not seen

in Backhouse (2016). The glass studied in Backhouse (2016) work has similar CaO content (5 wt %) as the glass studied in this body of work (6.42 wt%). The glass in Utton et al. (2013) study had very low amount of CaO in the glass (0.39 wt%). Therefore the difference in the CaO may affect the occurrence of the incubation period noted by Utton et al (2013). The CaO, acting as a network modifier, would cause depolymerisation of the network forming Si and B atoms. Depolymerisation is associated with higher dissolution rates, therefore may restrict the ability of the calcium borate to inhibit dissolution.

In summary, it may be concluded that the vitrified scabbled pondwaste, is broadly comparable to other HLW glass products which share similar compositions, considered potentially suitable for geological disposal.

5.4 Conclusions and summary

The project has demonstrated the capability of using the glass forming oxides found within the scabbled pond waste originating from decommissioned silo ponds, to aid with vitrfication, to produce a homogenous high performing glass waste. The results from the dissolution experiment are shown to be similar to those glasses that are suitable for long term storage within a GDF.

The main findings of the study were;

- XRD studies showed all glass samples contained a large amorphous component within the structure with samples C4 and C5 containing Bragg indexed reflections corresponding to cristobalite.
- Sample C3 was found to have a completely amorphous structure, however sample C5, despite the same waste loading of 72 wt.%, had crystallisation within the structure in the form of cristobalite. Raman studies showed that the Na_2O/B_2O_3 ratio has a significant impact on the crystallisation behaviour of the glass sample with a lower R value promoting crystallisation within the structure.
- Thermal analysis showed typical T(g) values expected for a sodium borosilicate glass for all samples. A melting temperature of below 1000°C was identified for all the samples which, assuming an operating temperature of 1100°C for waste processing, provides good compatibility with currently available technology platforms.

- Volatilisation of radionuclides was shown to be comparable with generally acceptable waste practises with Cs retention rates of ~80% ± 10% showing particular promise. Importantly, to alleviate criticality concerns, the radionuclides were shown to be homogenously distributed within the glass matrix.

- XANES studies showed the average oxidation state of uranium within the glass was 5^+. This is advantageous in terms of waste packaging, as uranium oxide in the glass structure is considerably more stable than uranium metal.

- Dissolution results showed that the vitrified scabbled pond waste, is broadly comparable to other HLW glass products, considered potentially suitable for geological disposal.

6 NUCLEAR WASTE VITRIFICATION ON AN INDUSTRIAL SCALE.

6.1 Introduction

This Chapter highlights the work that was undertaken by the author as part of a secondment working with Kurion Inc. The placement involved the author assisting with a joint project between Kurion and the UK's National Nuclear Laboratory (NNL), to deploy a full-scale, active, incontainer vitrification (ICV) plant based on Kurion's GeoMelt technology, at NNL's Central Laboratory on the Sellafield site. The specific objectives for the three-month secondment were as follows;

1) Operational Support. Qualify as a Kurion GeoMelt operator and support commissioning of the system and provide shift support during melts.
2) Technical support. Work with Kurion and NNL staff to develop glass formulations for melt trials.
3) Analytical support. Utilize University of Sheffield facilities to analyse glass samples from melt trials.
4) Reporting. Support Kurion and NNL staff to report results for NDA soils trials.
5) Research plan. Provide a plan for future research utilizing the GeoMelt system at B-170.

Objectives 2 - 5 were met within the time frame of the secondment and will be reported on in this Chapter. Unfortunately, due to delays with the project, the system was not commissioned in time to allow radioactive melts within NNL's central laboratory, and thus objective 1 was not fully achieved. However, the student was able to acquire samples from the inactive melts performed at NNL's Workington site. This was performed on non – active soils.

In addition to this work the author attended a week long training course at the GeoMelt Test Facility located in Richland, Washington State. As part of this training course the author gained operational experience with the GeoMelt test rig, achieving the original objectives set out at the beginning of the secondment. This Chapter will describe the GeoMelt system and the glass formulations used to vitrify the two waste streams mentioned in Section 2.2, and the laboratory studies performed on the samples to characterise and determine the performance of the vitrified waste forms.

6.2 The GeoMelt system

The GeoMelt system relies on the principles of Joule heating to melt and homogenise the glass formulations, an overview of which can be found in section 2.5.1. The GeoMelt is categorised as a joule heated melter (JHM). Designing a melter for longevity is difficult due to the high temperatures associated with vitrification mainly due to issues with corrosion of the refractory material (Gan et al. 2002). The GeoMelt system avoids this problem by basing the design of the melter on an in-container vitrification system (ICV), this "one time use" is a major advantage of the GeoMelt system. A mullite based material is used for the refractory boxes used in the GeoMelt.
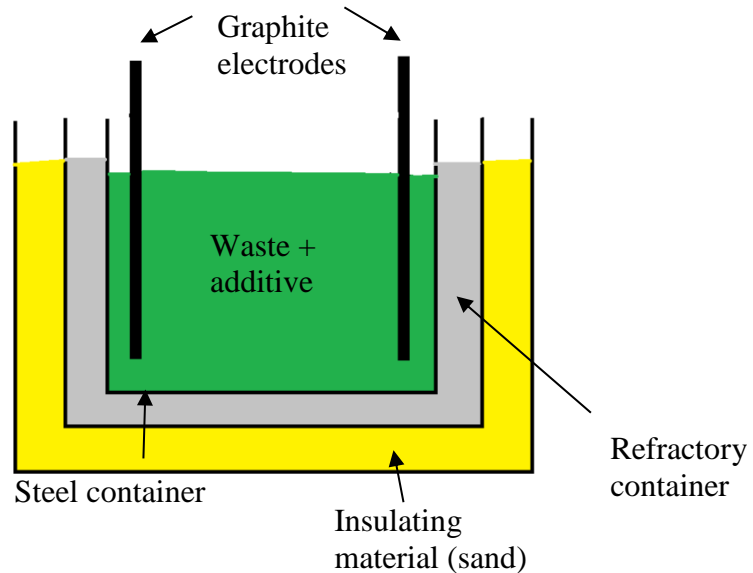
Figure 6.1 Basic schematic of the GeoMelt system

The GeoMelt system has two areas of engineering, the "hardware" and "software". The hardware includes the physical components in the melter, including the off gas system. The software includes the glass formulations to condition the waste. The facility

performance can be enhanced through improved glass formulations that are essentially transparent to the engineered facility. As shown in Figure 6.2 the joule heating effect within the melter is also a major advantage as it ensures the thermal energy is transferred and contained within the waste. This advantage ensures that the limiting factor for the size of the melter is the energy supplied to the system. The placement of the graphite electrodes needs careful consideration within large melters to ensure an efficient electrical circuit within the melter can be established.
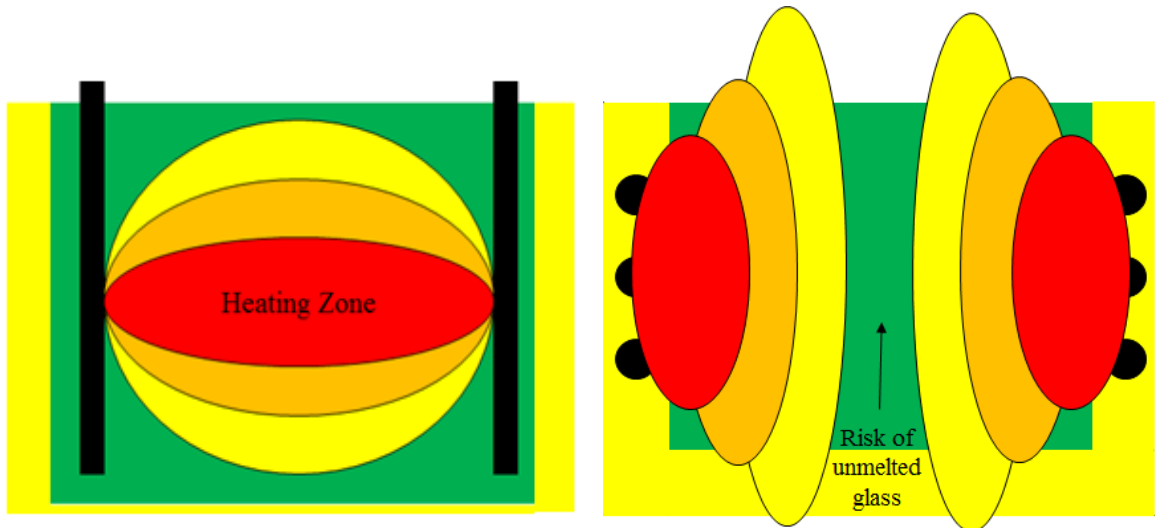
Figure 6.2 Temperature distribution within a typical induction furnace (Right). The size of the melter needs to be carefully considered to avoid unmelted glass within the centre of the furnace. (Left) The temperature distribution of the GeoMelt system, heat is generated from the waste itself.

Figure 6.2 (right) displays the heating profile of a typical induction melter. The obvious disadvantage compared with the joule heated melter, such as the GeoMelt, is that the heating elements essentially heat the walls of the melter. The energy is then dissipated from the walls of the melter into the waste. This limits the size of the melter as care needs to be taken to ensure that the thermal energy is transferred throughout, to ensure glass homogeneity and to avoid the risk of any unmelted glass in the centre of the melter. Figure 6.2 (left image) shows the heating profile of the GeoMelt system. The heat generated, through the joule heating effect of the electric current, is contained within the waste. Therefore, the heat is generated from the waste itself, and provided the electric current can be maintained, the limiting factor for the size of the melter is the electric supply to the system.

6.3 Joule Heating – Relationship with glass making

One of the objectives of the secondment was to provide operational support as a qualified GeoMelt operator. Due to limitations with access to the Sellafield site, the author was unable to experience any training on the GeoMelt within Sellafield. Fortunately, Kurion addressed this issue by inviting the author to Kurion's testing facility located at the Horn rapids test site, Richland, Washington state in the US. The author spent a week undergoing training on the GeoMelt test rig. This section will describe the operation of the GeoMelt and the relationship between Joule heating and glass making.
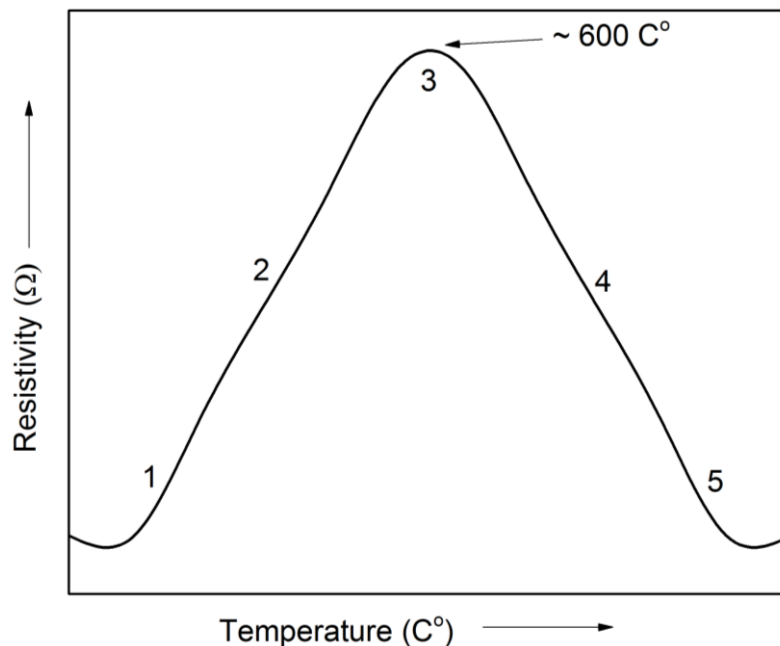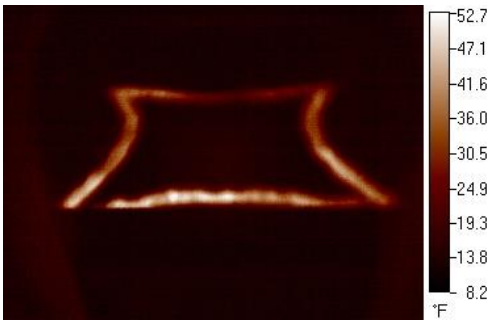
Figure 6.3 The relationship between resistivity as a function of temperature during the operation of the GeoMelt. The numbers (1-5) correspond to a particular time point during the glass making process.

Figure 6.3 is a plot of resistance as a function of temperature and is a useful concept when explaining the effect of Joule heating and the relationship this has on glass making. The annotated numbers (1-5) will be used with the corresponding images shown in Table 6.1 to explain the glass making process within the GeoMelt system.

Time point	Description	
1	The waste and the fluxing agents are not conductive therefore a conductive starter path must be set to ensure an electric current can pass through the waste material, in this case graphite flakes are used. To increase the amount of energy dissipated from the starter path in the form of heat, the resistance in the circuit needs to be increased. In order to increase the resistance, the voltage to the system needs to be increased. This is in accordance with Ohm's law (Section 2.5.1).	
2	The voltage is increased by using multiple voltage taps on the transformer. The voltage is increased in set phases. The resistance and the temperature follows this "step" relationship with the resistance increasing rapidly as the next Kw/phase is imposed, and the temperature then increases following this step change. The voltage taps not only reduce the risk of starter path burn up but also ensures the system is running at the highest power factor. The power factor is a measure of the efficiency of the system. It is an arbitrary value between -1 and +1 (+1 = 100% efficiency).	
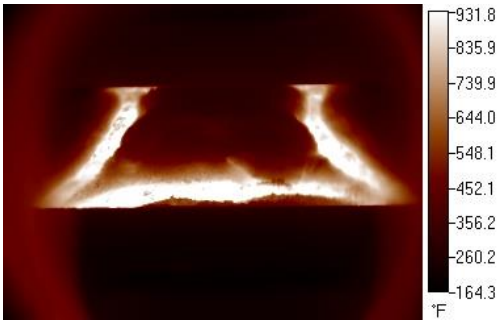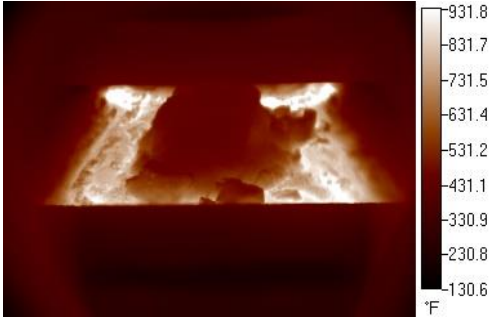
3	The resistance will continue to increase in the circuit until time point 3. At approximately 600°C the glass has the property of conducting current, therefore the resistance in the glass decreases with increasing temperature. This is due to the mobility of ions within the silica network. The material surrounding the starter path begins to become molten. Therefore, the molten glass becomes the path of least electrical resistance.	
4	As the temperature increases and the molten mass of glass grows in volume the electrical resistance decreases. Joule's law dictates that the dissipated energy in the form of heat will drop due to a decrease in electrical resistivity. To ensure the remaining material is heated the current in the circuit needs to be increased. Careful design of the electrodes must allow the required current to flow through the system.	
5	The entire batch is now molten glass. As the volume reduces inside the melter, more waste can be added, which will then dissolve into the molten glass. Convection currents in the molten glass will homogenise and ensure good mixing of the waste. After processing the system can be shut down. The glass will undergo a certain degree of annealing during this cooling period.	

Table 6.1 Summary of the Joule heating process during the GeoMelt process using the time points shown in figure 6.3

6.4 Vitrification of contaminated soils from the Sellafield site using the GeoMelt process

6.4.1 Introduction

Kurion Inc. has teamed with the UK's National Nuclear Laboratory (NNL) to install a GeoMelt In-container vitrification (ICV) system in the central laboratory at Sellafield. As part of the commissioning schedule two inactive melts were performed at NNL's Workington test facility, with the second melt serving as the first (inactive) soil melt for the NDA.

The primary objectives for the NDA testing are to:

1) Demonstrate that contaminated soils can be safely and effectively vitrified using the GeoMelt system;

2) Produce a durable and homogenous vitrified product that encapsulates key radionuclides of concern.

By utilizing the facilities within the ISL to analyse glass samples from melt trials, this section will determine the success of the project in terms of the above objectives.

Melt parameters including ICV temperatures, power usage, off gas flow and pressures and other key process data were recorded.

Deposits of soil near the Sellafield site were identified as representative of NDA contaminated soils. Table 6.2 shows the composition of the soil by XRF methods.

The high silica concentration of 82 wt. % requires additional fluxing minerals to lower the melting temperature of the soil from over 1700°C to approximately 1200°C. Although reducing the waste loading, the resulting lower melting temperature enables more efficient processing while optimizing retention of volatile radionuclides, such as ^{137}Cs, which has a volatilization temperature of approximately 1100°C. Based upon flux additions, Table 6.3 gives the target glass oxide composition of the vitrified soils. Table 6.4 gives the actual quantities of simulant materials.

Oxide Component	Sellafield Soil (wt%)
SiO_2	82.08 ± 0.56
Al_2O_3	7.94 ± 0.17
CaO	0.39 ± 0.05
TiO_2	0.37 ± 0.05
Fe_2O_3	2.99 ± 0.11
MgO	0.76 ± 0.05
K_2O	2.10 ± 0.09
Na_2O	1.08 ± 0.06
Other	1.31 ± 0.09
Total	99.02 ± 0.60

Table 6.2 XRF result of the Sellafield soil composition.

The initial batch of material, with composition shown in Table 6.3, was 203kg. An additional 267kg of feed material was added during processing resulting in a total of 470kg of material processed. This resulted in a total glass mass of 367 kg. The total operating period was 27 hours and 4 minutes. Figure 6.4 shows the final vitrified product within the refractory container. The white bubbling effect on the surface of the glass is a result of small air bubbles trapped in the glass during cooling and is likely due to the addition of boron as a fluxing agent.

Source	Oxide Component	Wt %
Soil	Al_2O_3	5.55 ± 0.14
	CaO	0.27 ± 0.03
	Fe_2O_3	2.09 ± 0.09
	TiO_2	0.26 ± 0.03
	MgO	0.53 ± 0.05
	Cr_2O_3	0.01 ± 0.01
	Na_2O	0.76 ± 0.05
	P_2O_5	0.07 ± 0.02
	Mn_3O_4	0.07 ± 0.02
	SiO_2	57.39 ± 0.47
	ZrO_2	0.02 ± 0.01
	BaO	0.03 ± 0.01
	SrO	0.01 ± 0.01
	K_2O	1.47 ± 0.08
	Sub Total	68.53 ± 0.50
Flux Additives	B_2O_3	10.49 ± 0.20
	CaO	8.40 ± 0.17
	Na_2O	12.59 ± 0.21
	Sub Total	31.47 ± 0.33
Total		100.00 ± 0.60

Table 6.3 The target glass oxide composition based upon XRF investigation of the Sellafield soils

Component	Mass (kg)
Soil	308
Borax ($Na_2B_4O_7 * 10 H_2O$)	123
Calcium Carbonate ($CaCO_3$)	68
Soda Ash (Na_2CO_3)	61

Table 6.4 Actual simulant mixture quantities.

Figure 6.4 Surface of the vitrified soils in the refractory container

6.4.2 Characterisation of the vitrified product

A large piece of the vitrified product shown in Figure 6.4 was analysed using the facilities within the ISL. XRD analyses, shown in Figure 6.5, confirms the glass is amorphous. The graphite inclusions are from the degradation of the graphite electrodes within the melt. Figure 6.6 displays SEM-BSE imaging of the vitrified soils. The lack of contrast confirms an X-ray amorphous structure and suggest chemical homogeneity within the glass sample. SrO was added to act as a tracer element to examine both retention and distribution of the inactive radionuclide simulant. The right image in Figure 6.6 shows that the Sr is homogenously distributed throughout the glass matrix with no evidence of any concentrated areas of Sr.
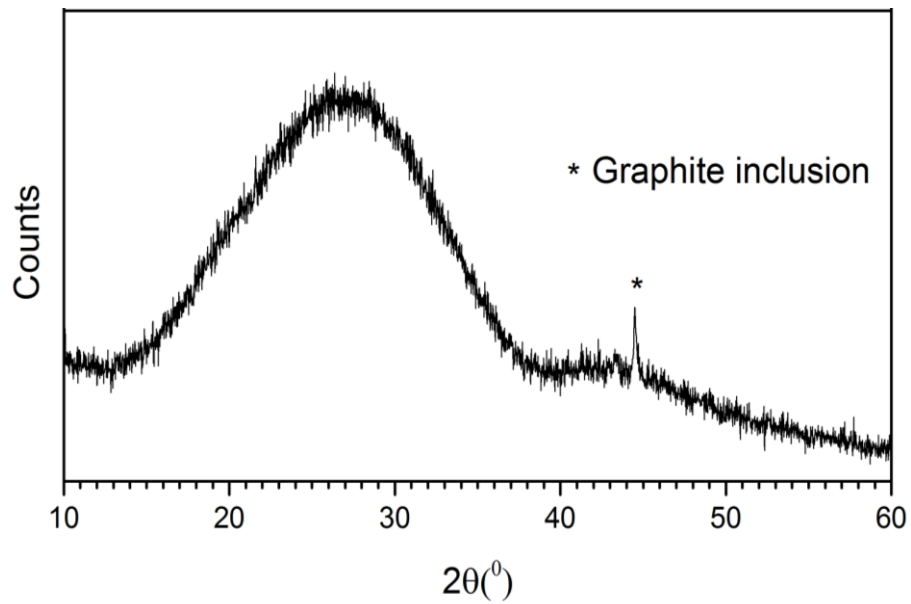
Figure 6.5 Powder X-ray diffraction patterns resulting from analysis of the vitrified product shown in figure 6.4. The diffuse scattering indicates an amorphous structure. The graphite inclusions are from burn up of the graphite electrodes.
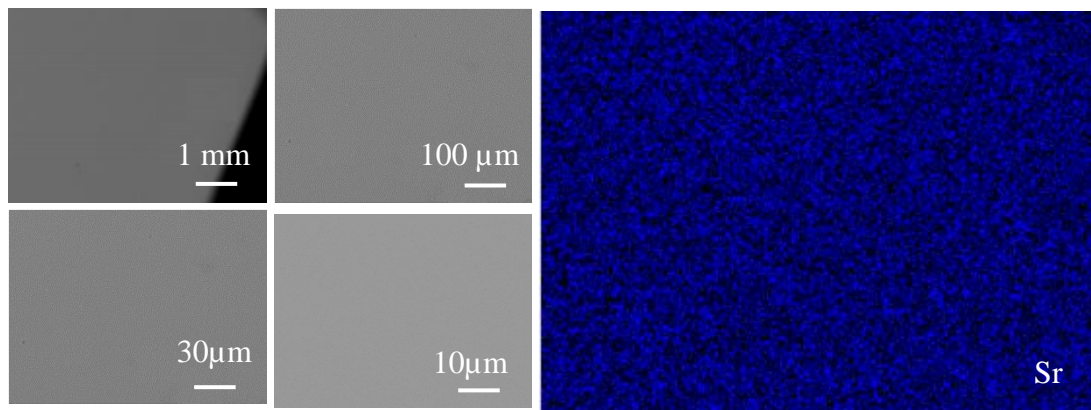
Figure 6.6 SEM-BSE images of the vitrified soils. (Left) Lack of contrast confirms an X-Ray amorphous structure and suggest chemical homogeneity within the glass sample. (Right) SrO was added as a trace element. EDX maps shows that the Sr is homogenously distributed throughout the glass matrix.

6.4.3 DTA investigation – Processability

Figure 6.7 shows the endothermic and exothermic reactions as a function of temperature of the vitrified soils when compared with a reference sample, in this case pure quartz. The endothermic event shown at approximately 570 °C corresponds to the glass transition point. This value is comparable to typical sodium borosilicate values. The exothermic

peak at 700°C corresponds to crystallisation within the glass. The melting temperature is less defined, but the graph seems to fall away at approximately 980°C indicating the onset of an endothermic reaction which would correspond to the melting temperature of the glass. Figure 6.8 shows the thermocouple data from various points within the melter during the vitrification process. The data shows that all regions of the melter reached the desired melting temperature of 1200°C. The lag in temperature of the upper thermocouple is due to the addition of waste as the volume of glass reduces, as described in Table 6.1. The upper thermocouple eventually reaches the target temperature when it comes into contact with the molten glass as the glass level rises within the container during feeding and processing of additional material. A target temperature of 1200°C was aimed for to ensure all of the material was processed and adequate convection mixing occurred.
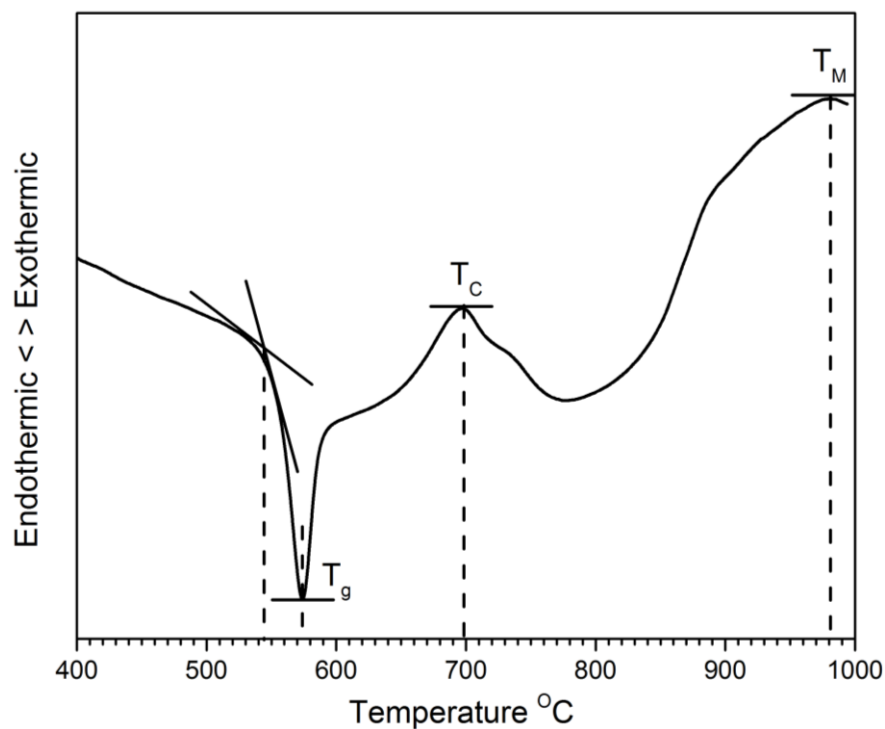
Figure 6.7 DTA measurement of the vitrified soils. The samples were heated at 10°C per minute to 1000°C in an argon atmosphere. The thermal events of the glass were measured as endothermic and exothermic reactions as a function of temperature.

Figure 6.7 shows that the melting point of the glass is approximately 980°C. Therefore it may be possible to lower the target temperature to 1100°C. Chapter 5 of this thesis has shown excellent levels of retention of Cs and U at 1100°C with glass compositions, similar to that used in this chapter. As mentioned, a benefit of a higher melting temperature is better mixing of the melt during to lower viscosity levels resulting in

stronger convection currents within the molten glass. The GeoMelt system is able to monitor the melting, a subsequent mixing of the glass via the IR camera situated within the melter. Hrma (1994) studied the property and composition relationship for Hanford high level waste glasses melting at 1150°C. Hrma (1994) determined the acceptable viscosity of the melt at 1150°C to be 2 – 10 Pa.s. If the viscosity is outside of this range then problems may be encountered in the melter. Glass with viscosity lower than 2 Pa.s tend to penetrate into the melter walls accelerating the corrosion of melter walls. Glass with viscosity higher than 10 Pa.s causes slow melting rate.
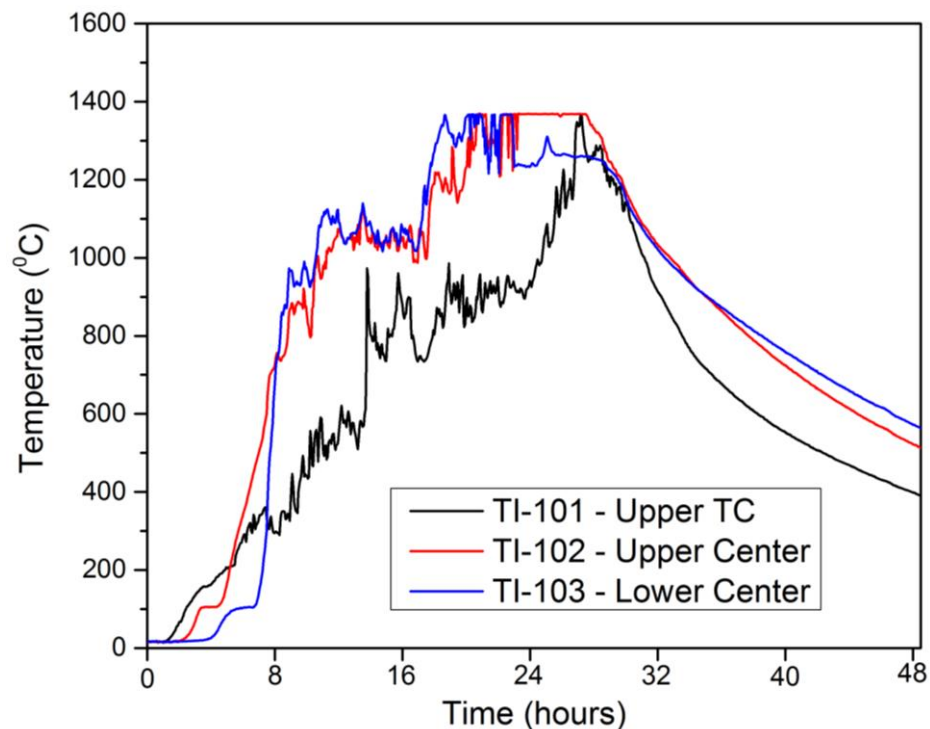
Figure 6.8 Thermocouple data showing the temperature of the melt. Graph adapted from internal Kurion report.

Unfortunately it was not possible to measure the viscosity of the glass processed during the Sellafield soil vitrification trials, however this would be useful data to the operators of the GeoMelt system. If the viscosity of the glass can be shown to be below 10 Pa.s (the acceptable viscosity as determined by Hrma (1994) at 1100°C, then a lower target temperature can bring the benefits of greater retention of radionuclides whilst producing a high performing vitreous waste form.

6.4.4 Determination of redox conditions within the Geomelt system

Mössbauer was used to determine the redox conditions within the Geomelt system. The same method was utilised in Chapter 4, the reader is referred to Section 4.5 for background information concerning the importance of redox conditions in the melter during radioactive waste vitrification. To briefly recap, the iron ratio provides important information in terms of processing and waste form considerations. For example, an Fe^{2+}/Fe^{3+} ratio value between 0.1 to 0.5 (as a measure of the redox state of the melt) should provide a sufficient level of safety against foaming or precipitations and should be the goal for processing nuclear waste glass (Goldman et al. 1985). Therefore it is useful to provide this information for the Geomelt operators. Figure 6.9 shows the Mössbauer spectrum for the vitrified Sellafield soils.
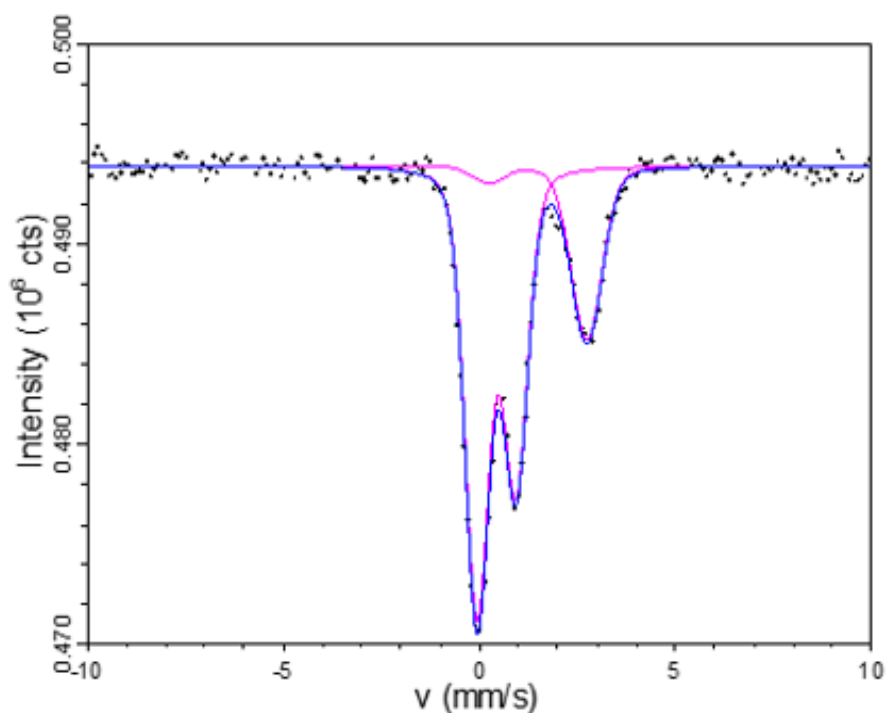
Figure 6.9 Mössbauer spectrum for vitrified Sellafield soils from the Geomelt. FeO content of 2.09 wt%. X axis = velocity (mm/s)

	CS (mm/s)	QS (mm/s)	Assigned phase	Site	Area (±2%)	($Fe^{2+}/\Sigma Fe$)
Soil Sample	1.49	2.5	Glass	Fe^{2+}	23.68	0.23
	0.44	0.99	Glass	Fe^{3+}	76.32	

Table 6.5 Fitting parameters for the Mössbauer spectrum shown in Figure 6.9.

Table 6.5 gives the fitting parameters for the Mössbauer spectrum. The Mössbauer spectrum shown in Figure 6.9 was fitted by using two Lorentzian doublets. Due to the amorphous structure shown in Figure 6.5 the two signals could be assigned to the Fe^{2+} and Fe^{3+} signal within the glass structure. This was achieved using the position of the centre shift (CS) and quadrupole splitting (QS) as described in Dyar et al. (2006) and Section 3.11. The Fe^{2+}/Fe^{3+} ratio is shown to be 0.23 (Table 6.5), this is between the values of 0.1 and 0.5 which Goldman et al. (1985) states should be aimed for.It is known that a value above 0.5 increases the risk of metal phases forming within the melter, which can short circuit the electrodes causing melt failure (Goldman et al. 1986). It should be noted that the Geomelt system uses a transformer which automatically regulates the flow of current throughout the melt, therefore a large drop in resistance through the circuit, caused by metal phases forming in the melt, would not cause the system to short. In the case of PCM waste vitrification, as investigated in Chapter 4, a reducing atmosphere (iron redox value of above 0.5) could be beneficial, as it would assist with the transfer of Fe into the metal fraction. From the results shown in Chapter 4, it is more favourable for the Pu to partition into the oxide fraction thereby decontaminating the metal fraction. Further volume reductions could be achieved if clean separation of the two phases could be separated allowing the disposal of metal waste as LLW. This would be challenging with the Geomelt one-time use processing method, as it limits the potential for in melt separation and attempting to separate the phases post-processing, especially in an active context is very difficult.

Jantzen (1990) states that when oxidising conditions are present ($Fe^{2+}/Fe^{3+} < 0.1$), oxygen forms causing excess foam to be produced. Figure 6.4 shows that the surface of vitrified waste form displays evidence of foaming. With a Fe^{2+}/Fe^{3+} ratio of 0.23 it shows that the Geomelt system oxidising conditions have caused some level of foaming. Foaming has been shown to block the flow of material into the melter (Jantzen 1990). The formation of the foam in this case however (Figure 6.4) has not affected the ability for material added to the melter to be incorporated and immobilised within the glass melt. This could prove problematic if the Fe^{2+}/Fe^{3+} ratio approaches 0.1. Higher glass viscosity has also shown to increase the occurrence of foaming (Cicutti et al. 2002).

In summary vitrification of the Sellafield soils were conducted within an oxidising environment with an Fe^{2+}/Fe^{3+} ratio of 0.23, deemed to be an acceptable value in terms of waste processing (Goldman et al. 1985).

6.4.5 Dissolution experiments – PCT-B

One of the specific aims of the melt trials was to produce a durable and homogenous vitrified product that encapsulates key radionuclides of concern. The PCT-B method can be used to determine the durability of the vitrified product. A 112 day variation of the PCT-B experiment was performed on the vitrified product shown in Figure 6.4, in $Ca(OH)_2$ solution to simulate the likely alkaline conditions which would be found within a GDF.

The Ca concentration in the blank solution remained constant at ~ 580 ppm over the 112 day testing period confirming the exclusion of CO_2 under anoxic conditions of the experiment. The Ca concentration showed a rapid decrease during the first 28 days (~580 to ~ 220 ppm) levelling out for the remainder of the test. The method of using the NL_B as a marker of glass dissolution has been shown to be controversial as there is evidence that boron is incorporated within the alteration layer (Mercado-Depierre et al. 2013). Therefore the normalised mass loss of Na, shown in Figure 6.10, can be used as a marker for glass dissolution. Table 6.6 shows the normalised mass loss (g/m^2) and the normalised dissolution rate $(g/m^2/day)$ for a number of elements including B, Na, K and Si. Measured values of NL_{Na} and NL_B were shown to increase rapidly over the first 14 days of the experiment corresponding to the rapid loss of Ca from solution, thereafter the NL_{Na} seems to be constant (28 days = 0.863 ± 0.1 to 112 days = 0.876 ± 0.1) whereas the NL_B increases at a slow rate (28 days = 0.848 ± 0.1 to 112 days = 0.997 ± 0.1). Figure 6.10 shows no evidence of resumed alteration within the 112 days of leach testing. The NL_{Na} for the vitrified soils at 28 days shown in Figure 6.10 (0.863 ± 0.1 g/m^2), is comparable to NL_{Na} of the vitrified masonry waste is section 5.3.6

The main area of interest is how the initial and residual dissolution rates, calculated above, compare with other studies concerning the durability of vitrified ILW, preferably from an industrial platform. Utton et al. (2013) study analyses the durability of a number of vitrified ILW streams, from full scale industrial platforms, in hyperalkaline conditions. The experimental set up from this study was similar to that used in this thesis, therefore provides an excellent basis for comparison. The initial rate of dissolution for the glass synthesised in Utton et al. (2013) report was 0.122 ± 0.015 (for $NL_{(B)}$), this matches closely with the initial $NL_{(B)}$ in this study at 0.152 ± 0.1. This is a promising result and shows the vitrified soils is comparable to other vitrified ILW streams.
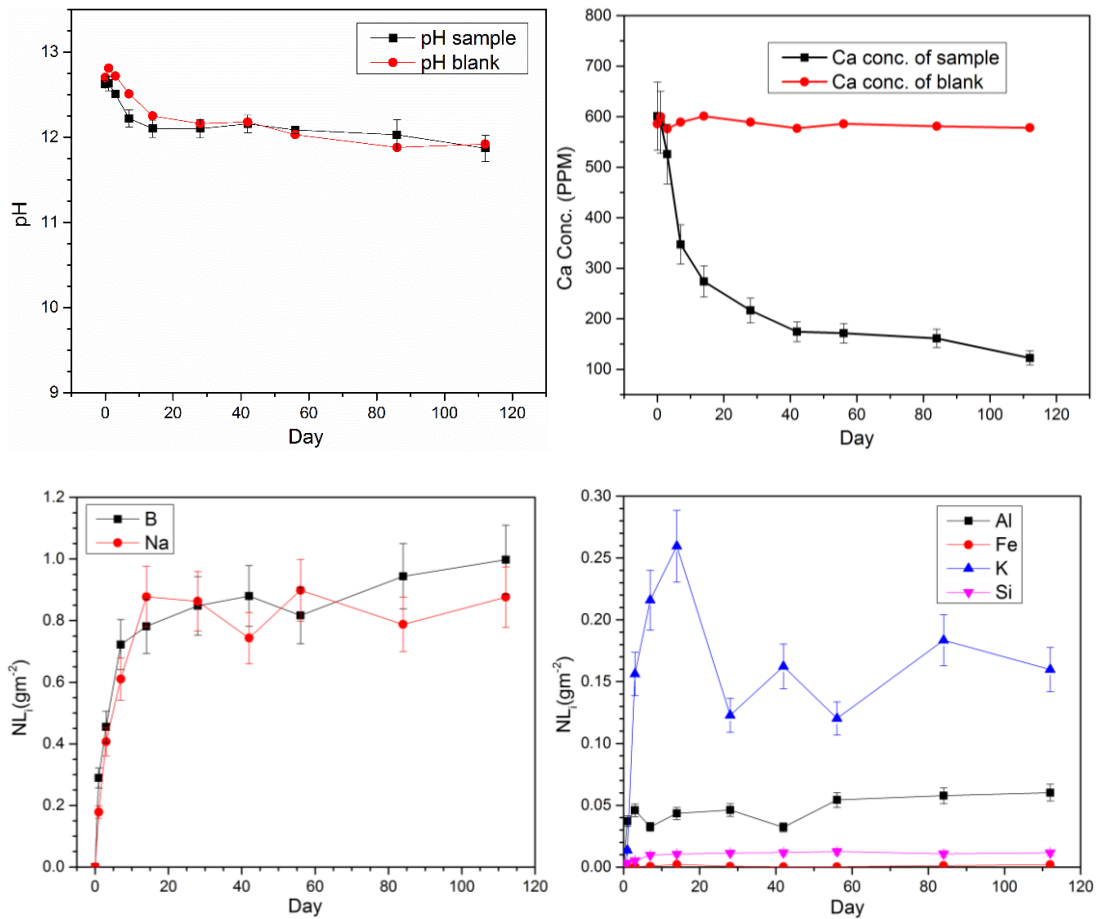
Figure 6.10 (Top left) pH values (Top right) Ca conc. (bottom left) $NL_{Na,B}$ (g/m²)

(bottom right) $NL_{Al,Fe,K,Si}$ (g/m²/day)

Day	NL_B (g/m²)	NL_{Na} (g/m²)	NL_K (g/m²)	NL_{Si} (g/m²)
Stage 1 (0-3)	0.455 ± 0.1	0.407 ± 0.1	0.156 ± 0.01	$(5.27 \pm 0.1) \times 10^{-3}$
Stage 2 (3-28)	0.848 ± 0.1	0.863 ± 0.1	0.122 ± 0.01	$(1.14 \pm 0.1) \times 10^{-2}$
Stage 3 (28-112)	0.997 ± 0.1	0.876 ± 0.1	0.16 ± 0.01	$(1.16 \pm 0.1) \times 10^{-2}$
	RL_B (g/m²/d)	RL_{Na} (g/m²/d)	RL_K (g/m²/d)	RL_{Si} (g/m²/d)
Stage 1 (0-3)	0.152 ± 0.02	0.136 ± 0.02	0.052 ± 0.01	$(1.86 \pm 0.1) \times 10^{-2}$
Stage 2 (3-28)	$(1.57 \pm 0.33) \times 10^{-2}$	$(1.82 \pm 0.35) \times 10^{-2}$	NA	$(3.49 \pm 0.46) \times 10^{-5}$
Stage 3 (28-112)	$(1.78 \pm 0.2) \times 10^{-3}$	$(1.6 \pm 0.16) \times 10^{-4}$	$(4.41 \pm 0.5) \times 10^{-4}$	$(1.43 \pm 0.16) \times 10^{-5}$

Table 6.6 NL (g/m²) and RL (g/m²/day) for B, Na ,K and Si during 112 day PCT-B
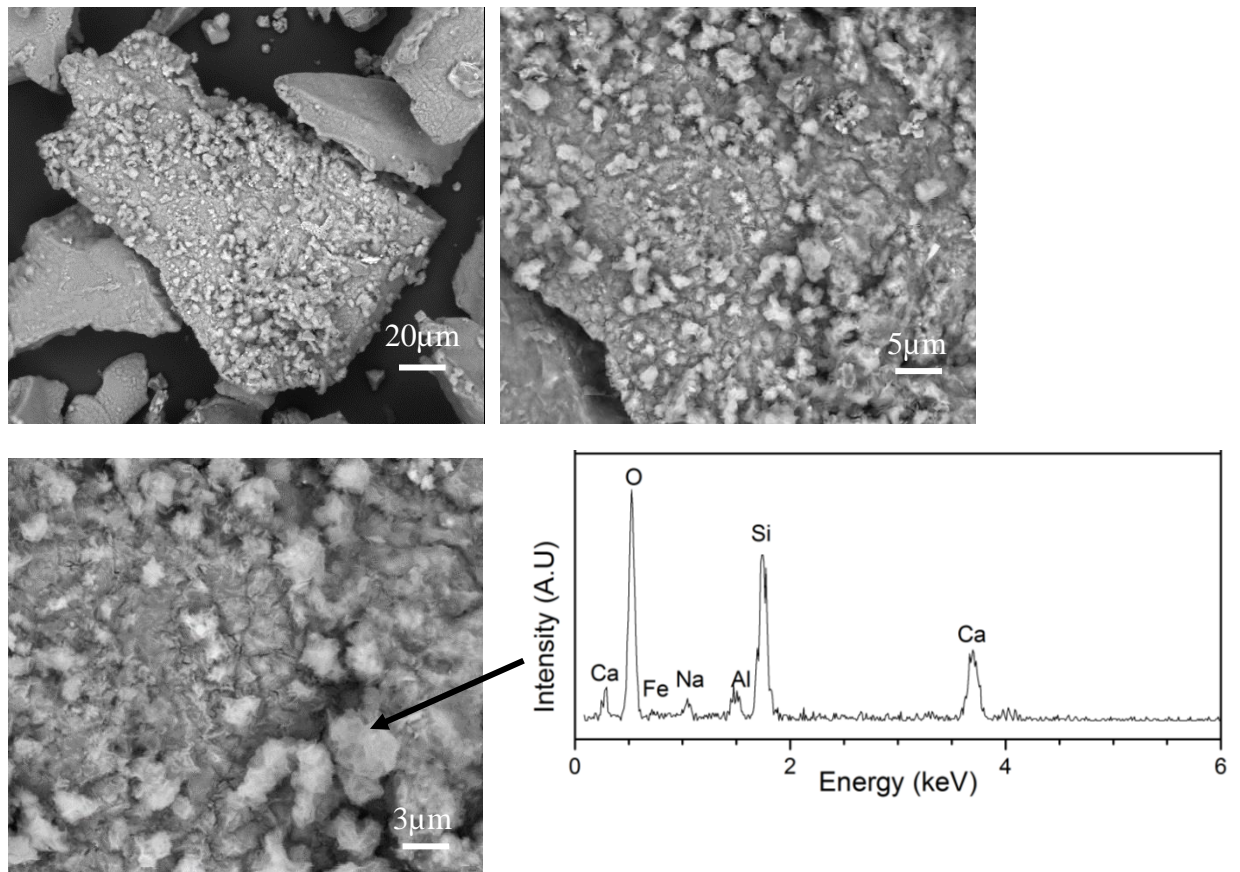
Figure 6.11 SEM micrographs of altered surface of a vitrified soils glass particle after 112 days in the high SA/V experiment showing surface of a particle and additional precipitates on its surface.

The glass powder subjected to high SA/V experiment, shown in Figure 6.11, exhibited significant agglomeration during testing. In addition a white layer had formed on the top surface of the agglomerated glass powder. The glass powders were dried and prepared for SEM investigation. The dehydration of the sample during preparation caused spalling and cracking of this agglomerated layer. Figure 6.11 shows a particle of glass covered in precipitates. The precipitates on the surface of the glass were identified using EDX (Figure 6.11). The precipitates primarily contained Ca and Si. This indicates that the white layer noted formed on the surface of the glass powders is a calcium silicate hydrate phase. The presence of Na suggests that it is substituting into this phase (Hong 1999; García Lodeiro et al. 2009). XRD studies were performed on the altered glass with the trace shown in Figure 6.12. It should be noted that XRD studies of the unreacted glass, shown in Figure 6.5, showed no crystalline peaks, only a diffuse scattering. Figure 6.12 shows

198

that the XRD trace for reacted bulk glass powder has peaks corresponding to calcite ($CaCO_3$) and peaks with less intensity corresponding to sodium silicate hydrate phase. This phase can have variable compositions, containing substituted ions and can be poorly crystalline, making positive XRD identification a challenge. $CaCO_3$ has formed on the surface of the glass because of carbonation the after sample has been removed from solution.
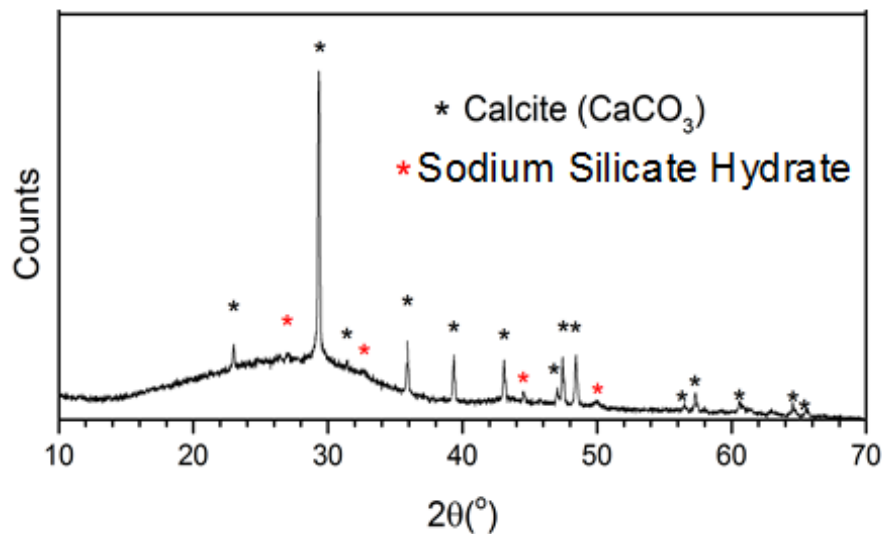
Figure 6.12 XRD pattern of altered powdered glass sample from the high SA/V experiment after 112 days leaching in Ca(OH)₂. Crystalline phases present in the form of calcite (CaCO₃) and calcium silicate hydrate (CSH) phase.

The incubation period noted by Utton (2013), as describe in section 5.3.6, was again not seen in the vitrified soils in this Chapter. The Ca concentration of the vitrified soils from the Geomelt is similar to that of the vitrified pond scabblings in Chapter 5. Therefore the presence of Ca in the glass seems to influence the presence of the incubation period seen by Utton (2013).

The presence of calcium in solution is effecting the dissolution of the vitrified soils from the Geomelt trials. The formation of protective precipitates on the surface of the glass, as shown in Figure 6.11, is believed to lower the overall rates of glass dissolution (Andriambololona 1992; Corkhill et al. 2013; Chave et al. 2011). It is reasonable to assume that under high pH conditions, the presence of calcium may be favourable for vitrified ILW durability

6.5 Conclusion

The overarching aim of this project is to provide the scientific understanding behind the thermal treatment process which will support a major investment in thermally treating a number of ILW streams. One such investment is from the recent partnership with Kurion Inc. and the NNL to install a full-scale, active, in container vitrification (ICV) plant based on Kurion's GeoMelt technology, at NNL's Central Laboratory on the Sellafield site. The student was able to work on the project during a three month secondment. This included acquiring a number of samples from various melt trials including soils from the Sellafield site and INL calcined waste. The key findings from the analyse were as follows;

- A vitreous monolith waste form was produced with 68.5 wt % waste loading, at 1200 ℃ with no porosity or obvious inclusions. XRD studies showed the glass was X-ray amorphous but with the presence of graphite from the burnup of the electrodes. Sr was added as a trace element, with EDX mapping showing homogenous distribution within the glass matrix.

- Thermal processing was investigated using DTA. The T_g of the vitrified soils was approximately 570 ℃ which is a typical value for sodium borosilicate glasses. Melting temperature was shown to occur at approximately 980 ℃. This shows the operating temperature could be lowered from 1200 ℃ to ensure maximum retention of radionuclides such as [137]Cs.

- Mössbauer results indicate that vitrification of the Sellafield soils was conducted within an oxidising environment with an Fe^{2+}/Fe^{3+} ratio of 0.23, deemed to be an acceptable value in terms of waste processing (Goldman et al. 1985).

- PCT-B experiments showed NL_{Na} at 28 days was comparable to the vitrified masonry waste investigated in section 5 which was shown to be acceptable in terms of disposal within a GDF.

- Due to the low amounts of volatiles within the soil any volume reductions gained from the densification of the soils is negated with the addition of the fluxing agents, to lower the melting temperature. Soils classified as LLW are not suitable for thermal treatment on economic grounds with disposal in LLW repository such as Drigg a more attractive option. However the melting trials presented in this body of work provides strong evidence that the contaminated soils could be used as the glass forming additives to be used to vitrify other ILW streams including sludge's and ion exchange resins.

7 UNDERSTANDING THE STABILITY OF THE VITRIFIED PCM WASTE PRODUCT USING ARCHAEOLOGICAL SLAG SAMPLES.

7.1 Introduction

There have been numerous studies using archaeological glass samples to better understand the long term behaviour of glasses (Brill 1961; Bianco et al. 2004; Michelin et al. 2013; Techer et al. 2000; Youngblood et al. 1978; Lombardo et al. 2013). In the case of nuclear waste vitrification this becomes a particularly useful tool when building a strong safety case for long term disposal of vitrified products. By studying the archaeological glass samples, a more accurate prediction of the long term behaviour of the vitrified wasteform product can be made by validating the outcome of short term, accelerated experiments.

This Chapter describes the methods used to study archaeological samples found within the town of Hayle, situated in west Cornwall. The history of the Copperhouse foundry, located in Hayle and first founded in 1754, means that the samples discovered are at least 250 years old. It may be possible to use the samples to predict the long term performance of the vitrified PCM waste products produced in Chapter 4. This method has been used previously by Michelin et al. (2013), who used vitreous archeological slag as analogues for vitrified nuclear waste. This Chapter describes the method of using the archaeological samples found at the Hayle site to determine and predict the long term stability of the vitrified PCM waste products. The main question of interest to be answered from this section, is can the archaeological glass samples found at the Hayle site be used as an historical analogue to predict the long term behaviour of vitrified PCM waste?

The town of Hayle has a relatively short history, unique to Cornwall, beginning in the first quarter of the 18th century. The Hayle estuary was chosen as the ideal location for the import of coal, timber and other sundries for the mining industry. The copper smelting industry was attracted to the area due to the easy availability of coal. From 1756 until 1820, the Cornish Copper Company (CCC), carried out copper smelting establishing the area of Hayle known as Copperhouse. Most of the slag produced from the site was used as aggregate but it is the slag that was cast into blocks that are of particular interest to this study. The blocks were used for the construction of revetments to bridge the many local streams and rivers in the area. 4000 – 6000 tons of ore were smelted annually until 1820 when the smelter ceased operation for economic reasons (Ferguson 1996).

7.2 Slag blocks and their composition

The only analyses known to have been performed on the slag blocks of Hayle were reported by Ferguson (1996) in which compositional analyses were performed using inductively coupled plasma (ICP) spectrometry. A sample taken from the revetment was analysed to measure the composition. The results for this are shown in Table 7.1.

When considering potential analogues to study the long term performance of radioactive waste glass, it is important to select an analogue which has been altered under relevant conditions. The geochemical environment can have a governing influence on how the glass alters over time (Bianco et al. 2004). It is expected that the vitrified PCM waste synthesised in Chapter 4 will be disposed within a GDF. The engineered barrier within the GDF will dictate the chemistry of the environment in contact with the glass, this is discussed in more detail in Section 2.1. In summary, due to groundwater flow through areas of high cement content both in terms of construction material used and other packaged cemented ILW streams, the glass will be subject to a high alkaline aqueous environment (Crossland 2001). Figure 7.1 shows the area where the samples were taken from. No sampling of the environment was taken, however research performed by Howland et al. (2000) measured the pH and total alkalinity of the Tweed Estuary (UK). Howland found that for rivers with low flow rates, the groundwater was rich in weathered bedrock ions. It is likely that these same conditions exist at the Hayle estuary. Therefore it is likely the slag samples were subjected to the high pH conditions similar to which might be relevant to the near field of a GDF environment.

Element	Wt %	Element	Wt %
SiO_2	52.12	K_2O	0.25
Al_2O_3	7.41	TiO_2	0.24
Fe_2O_3	26.47	MnO	0.24
MgO	0.80	CuO	0.32
CaO	7.50	ZnO	1.67
Na_2O	0.12	Total	97.14

Table 7.1 Composition of slag blocks from Ferguson (1996)

7.3 Copper slag samples used in this study

The samples that were investigated in this study were found near the bridge revetment as shown in Figure 7.1. From the literature (Hayes 1993) copper ore was smelted at 1200-1300°C. This temperature is slightly lower than the processing temperature of the simulant PCM waste shown in Chapter 4. However in both smelting procedures, all of the material present was molten, therefore the temperature difference is unlikely to lead to major differences in the resultant slag A number of samples were submerged in the stream itself. The samples were categorised by appearance, as shown in the Figure 7.2. No attempt was made to clean the samples.

Figure 7.1 The area where the samples were taken from
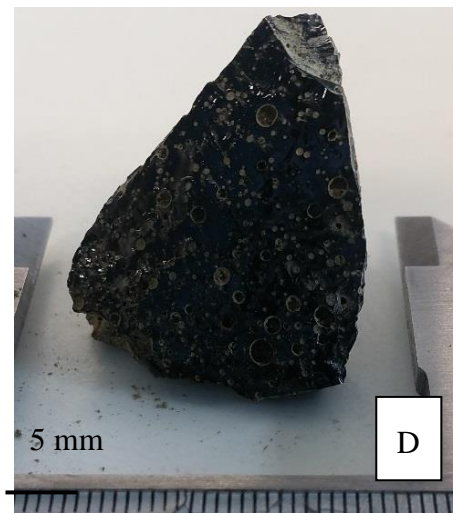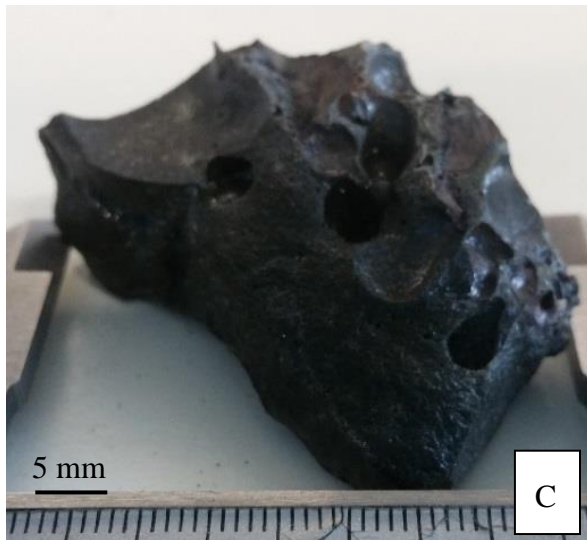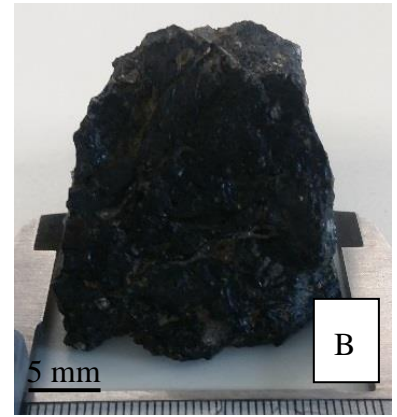
Figure 7.2 Samples (A-E) selected for analysis as potential PCM analogues for long term behaviour

7.4 Characterisation of Slag sample A-E

7.4.1 XRF studies

(Wt%)	A	B	C	D	E
SiO$_2$	41.11 ±0.38	38.26 ±0.38	23.94 ±0.30	32.95 ±0.35	34.98 ±0.24
MgO	0.93 ±0.06	0.10 ±0.02	0.39 ±0.03	0.32 ±0.03	0.17 ±0.03
Al$_2$O$_3$	20.47 ±0.26	3.18 ±0.11	27.45 ±0.21	4.97 ±0.12	3.42 ±0.12
CaO	5.28 ±0.14	5.42 ±0.14	15.42 ±0.23	18.34 ±0.17	7.06 ±0.11
Na$_2$O	0.19 ±0.03	0.04 ±0.02	0.23 ±0.03	0.04 ±0.02	0.03 ±0.02
Fe$_2$O$_3$	18.58 ±0.26	43.29 ±0.39	25.19 ±0.30	23.24 ±0.20	38.17 ±0.25
K$_2$O	7.61 ±0.17	0.12 ±0.02	0.28 ±0.03	1.19 ±0.06	0.22 ±0.03
CuO	0.16 ±0.03	2.03 0.09	0.09 ±0.02	0.01 ±0.01	4.99 ±0.14
SO$_3$	0.29 ±0.03	0.47 ±0.05	0.06 ±0.02	0.68 ±0.05	2.21 ±0.09
MnO	0.89 ±0.06	0.33 ±0.03	1.61 ±0.08	14.79 ±0.23	0.33 ±0.03
Other	3.39 ±0.11	2.11 ±0.09	5.26 ±0.14	2.10 ±0.09	4.89 ±0.14
Sum	99.80 ± 0.60	100.04 ± 0.60	99.77 ± 0.60	99.90 ± 0.60	99.93 ± 0.60

Table 7.2 XRF analysis show the compositions of the slag sample (A-F)

When choosing an appropriate analogue it is important that the sample has a similar composition to the radioactive waste glass. From the XRF results shown in Table 7.2, it was decided that samples A and B were most representative of the PCM slag samples synthesised in Chapter 4 because of the similar content of Si, Al, Ca and Fe. The low levels of Na in the Hayle samples compared to the PCM samples is disadvantageous, as it is know that an increase in Na content can lower the durability of glass samples (Chick et al. 1981). Table 7.3 shows the compositions of Hayle samples A and B compared with the composition of the vitrified PCM waste samples from Chapter 4.

Wt%	Sample A	Sample B	PVC	Masonry	Metal	Mixed
SiO_2	41.11	38.26	37.93	54.85	69.87	54.23
	±0.38	±0.38	±0.25	±0.44	±0.50	±0.44
MgO	0.93	0.10	0.85	0.86	1.17	0.93
	±0.06	±0.02	±0.06	±0.06	±0.06	±0.06
Al_2O_3	20.47	3.18	16.51	11.70	7.60	9.29
	±0.18	±0.11	±0.24	±0.20	±0.17	±0.18
CaO	5.28	5.42	5.46	7.07	7.43	6.90
	±0.14	±0.14	±0.14	±0.17	±0.17	±0.17
Na_2O	0.19	0.04	6.02	6.81	7.72	6.53
	±0.03	±0.02	±0.15	±0.15	±0.17	±0.15
FeO	18.58	43.29	30.38	17.65	0.82	18.13
	±0.26	±0.39	±0.33	±0.26	±0.06	±0.26
Sum	99.80	100.04	99.31	99.53	98.59	99.09
	±0.60	±0.60	±0.60	±0.60	±0.60	±0.60

Table 7.3 XRF results of sample A and B compared to composition of vitrified PCM waste simulants synthesised in Chapter 4

7.4.2 XRD with corresponding SEM/EDX maps

Figure 7.3 and Figure 7.4 show the XRD pattern for samples A and B respectively. The corresponding microstructure is shown in the SEM images with EDX analysis showing the distribution of key elements within the sample.
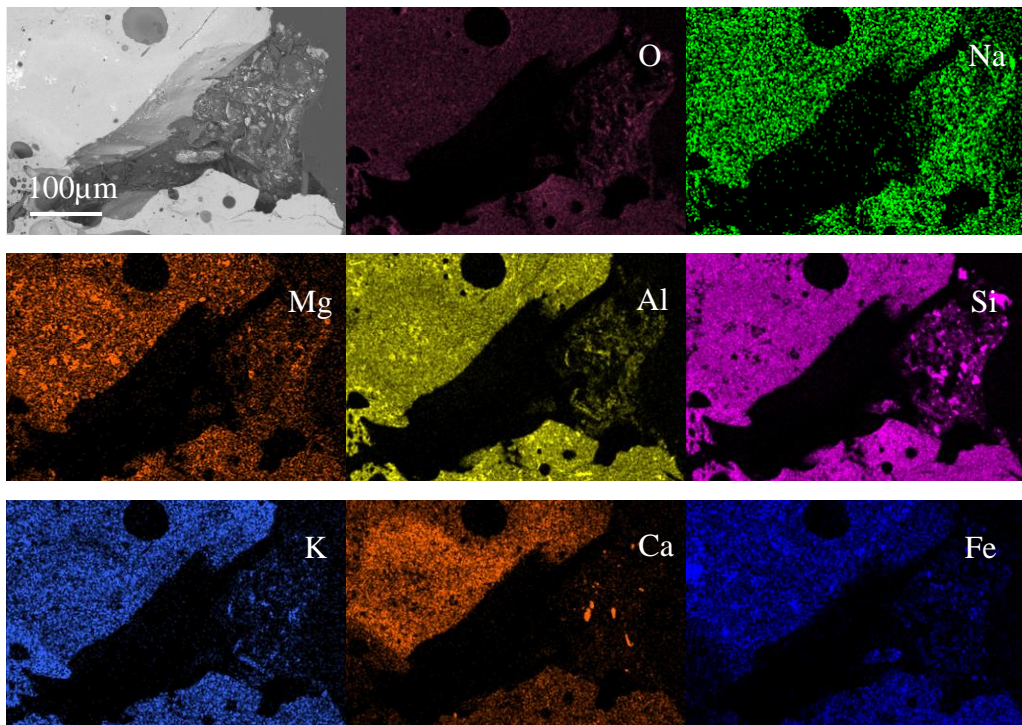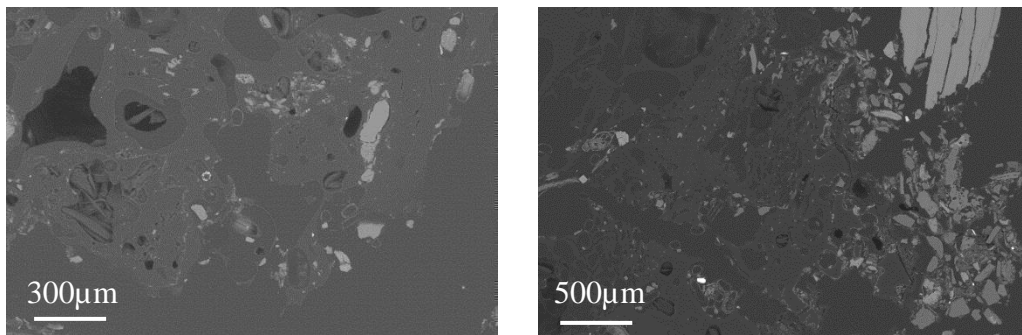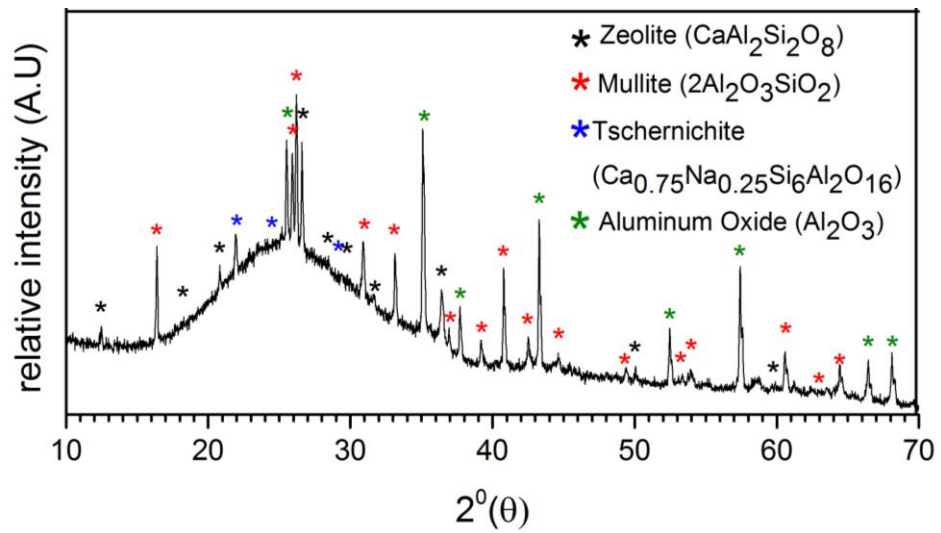
Figure 7.3 XRD trace and asscociated SEM/EDX mapping showing distribution of key elements within the Historical sample A from Figure 7.2.
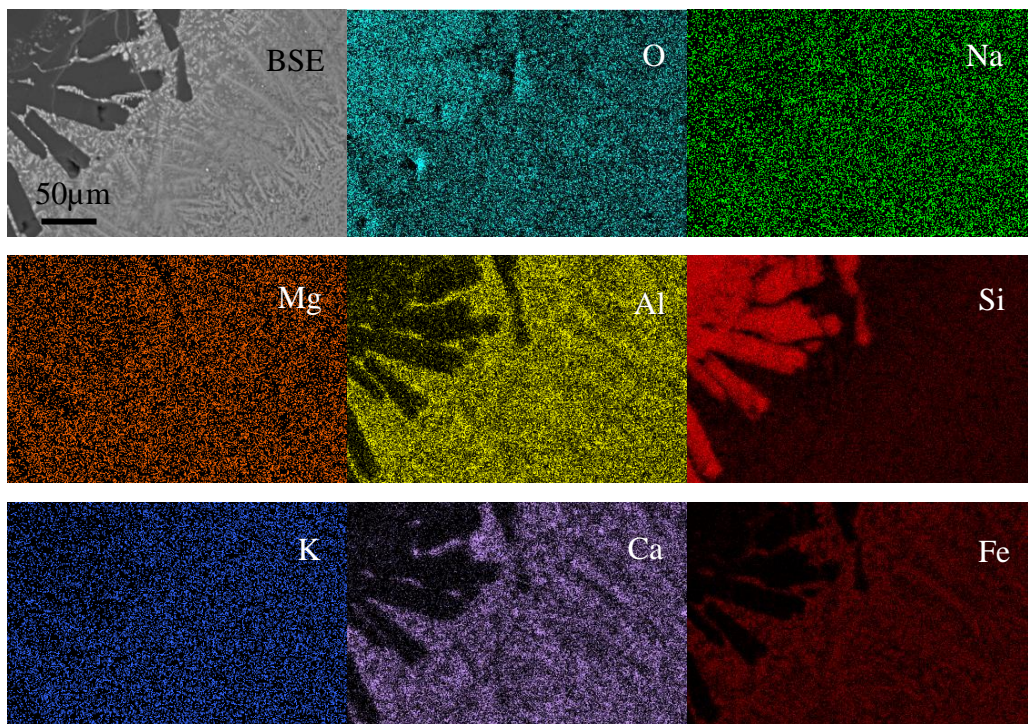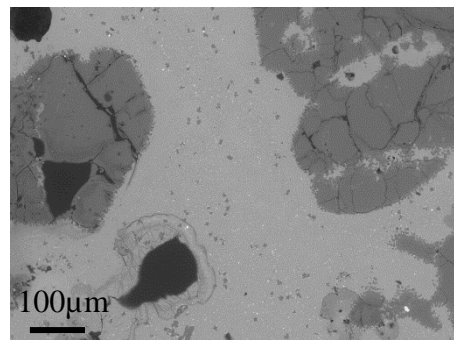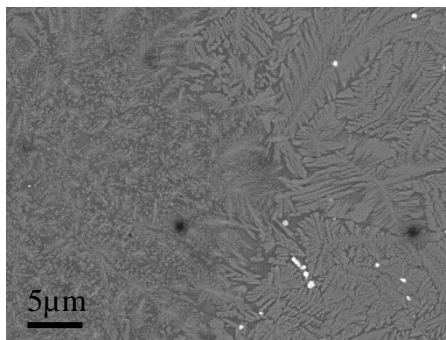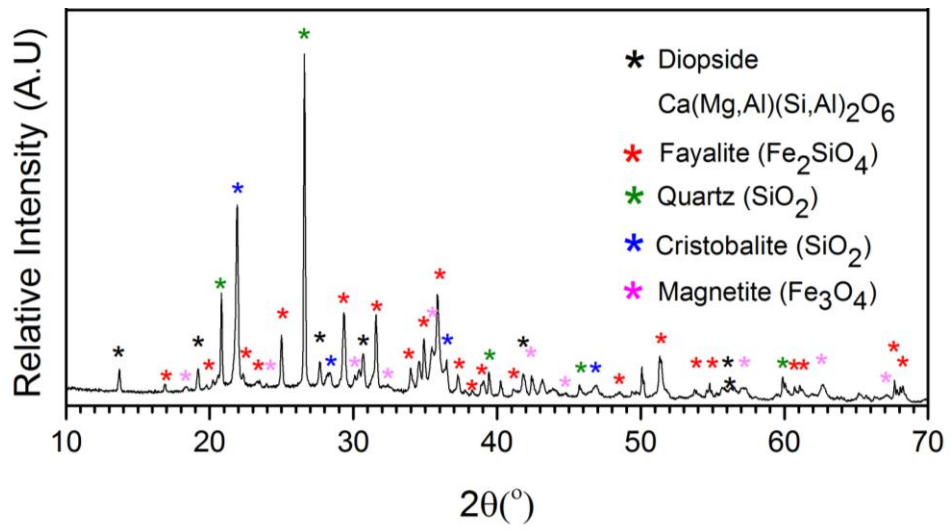
Figure 7.4 XRD trace and asscociated SEM/EDX mapping showing distribution of key elements within the Historical sample B from Figure 7.2

The XRD traces shown in Figure 7.3 exhibit diffuse scattering, indicating that sample A contains an amorphous component within the microstructure. From visual inspection (Figure 7.2) and the microstructure images (Figure 7.3) the sample is very porous. No alteration layers were apparent on the surface of the samples. This is likely due to the flow of water over the slag samples removing any alteration layers that would have formed on the surface of the samples and also due to unsaturated conditions. An attempt was made to study potential cracks in the slag samples, as shown in Figure 7.3. It was hoped that water would be stagnant within this area allowing the formation of alteration products, similar to that seen in Section 4.8. Figure 7.3 does show a higher concentration of Ca signal towards the edge of the samples within the cracked area. However this does not appear to be a secondary phase precipitated onto the surface of the glass, therefore unlikely to be a corrosion product. The XRD trace shown in Figure 7.3 shows the major phases contained within the sample. Unfortunately the phases identified were not those within the samples synthesized with Chapter 4, however the amorphous component of the sample identified does credit the use of an analogue for the long term behavior of glass.

The XRD trace shown in Figure 7.4 shows a number of crystalline phases that can be found in the vitrified in the PCM waste samples synthesised in Chapter 4, including diopside and magnetite. The microstructure shown in Figure 7.4 is very similar to that of the vitrified Mixed waste shown in Figure 4.11. The microstructure does contain large amounts of SiO_2 in the form of quartz which was not seen in the vitrified PCM waste samples. This could be undissolved SiO_2 which was known to be added to the copper smelting process as a fluxing agent (Davenport 2015). The most common ores used for copper production were rich in copper-iron-sulfur minerals. During the copper smelting process, the aim was to eliminate as much of the unwanted iron, sulfur and other minerals from the initial copper ore (Samans 1949). This was in part achieved by reacting iron sulfides with oxygen to produce magnetite, this is confirmed by the XRD trace shown in Figure 7.4. SiO_2 was added as a fluxing agent to lower the liquidus temperature and to ensure separation of the iron oxide and copper sulphide mix. This causes the following reactions which isolate the Cu from the other minerals (Moore 1990)

$$2CuS + 3O_2 \rightarrow 2CuO + 2SO_2$$

$$2FeO + SiO_2 \rightarrow Fe_2SiO_4$$
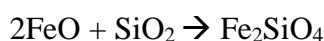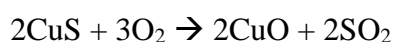
The reaction shown above produces the phase fayalite, which is identified within the XRD trace shown in Figure 7.4.

The phases identified in the XRD trace shown in Figure 7.4 for samples for B are consistent with what would be expected from the process of copper smelting. This is very promising as it provides strong evidence that sample B can be used as an effective analogue to model and predict the long term behavior of the slag samples synthesised in Chapter 4.

7.5 Mössbauer Spectroscopy

Mössbauer studies were performed on samples A and B to determine the Fe^{2+}/Fe^{3+} ratio. Mössbauer studies can also be used to determine the distribution of Fe throughout the multiple crystalline and amorphous components within the sample. From XRF studies shown in Table 7.2, sample A contains 18.58 wt% Fe_2O_3. XRD studies performed on sample A (Figure 7.3), show that sample A contains no Fe bearing mineral phases. Therefore the Fe signal must be from the large amorphous component within sample A. Two doublet features were fitted to the Mössbauer spectrum for sample A. Using the position of the CS and QS the two Fe signals can be assigned to the corresponding Fe^{2+} and Fe^{3+}, as described in Section 3.11. The results show that 69.8% of Fe ions in the amorphous component are Fe^{2+}. Figure 7.4 shows a number of Fe bearing mineral phases present within sample B. A sextet feature was fitted to the Mössbauer spectrum for sample B which corresponds to the identified magnetite phase due to its ferrimagnetic properties. The doublet feature fitted to the spectrum can be attributed to the identified fayalite mineral phase (Dyar et al. 2006).

It is important to try to determine the relationship between the results presented here and the long term performance of the vitrified PCM waste forms synthesised in Chapter 4. The vitrified waste forms will be present within a high pH environment, expected from a GDF. It is known that the chemical composition of the near field will be dominated by the dissolution of the soluble constituents of the cement and by the corrosion of the waste container (Crossland 2001).
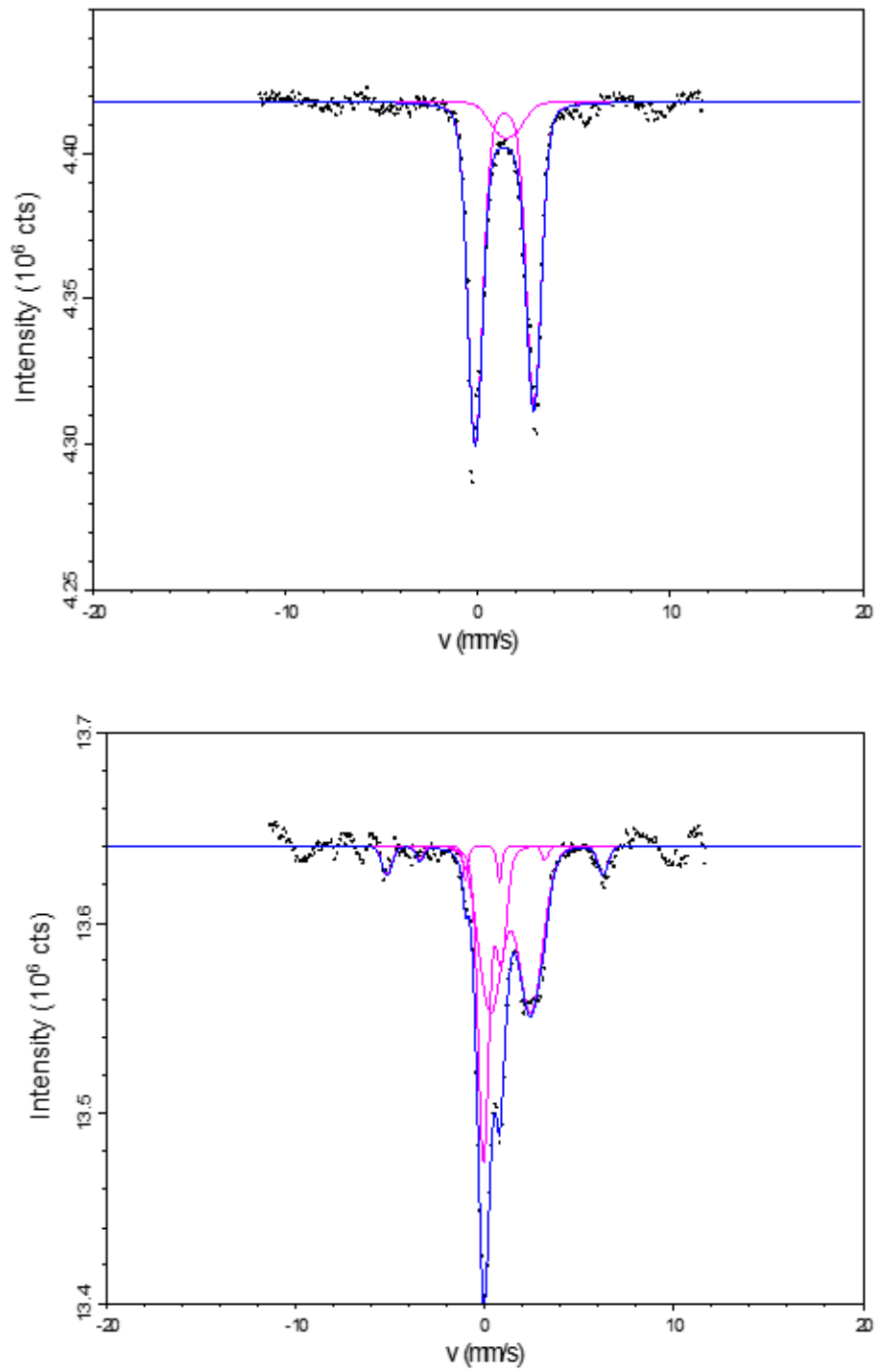
Figure 7.5 Mössbauer spectroscopy of Hayle samples A (Top) and B (Bottom).

	CS (mm/s)	QS (mm/s)	Assigned phase	Site	Area (±2%)	(Fe^{2+}/ΣFe)
Sample A	1.1	2.8	Glass	Fe^{2+}	69.8	69.8%
	0.8	0.1	Glass	Fe^{3+}	30.2	
Sample B	0.39	0.95	Glass	Fe^{3+}	34.6	65.5%
	1.35	2.13	Fayalite	Fe^{2+}	56.2	
	0.20	0.33	Magnetite	Fe^{2+}	9.2	

Table 7.4 Fitting parameters for the Mössbauer spectrum for sample A and B shown in figure 7.4.

This has been shown to cause the oxidation potential throughout the near field to become reducing approximately 100 years after saturation (Atkinson et al. 1988). The results shown in Table 7.4 show that both samples A and B have Fe^{2+} as the dominant Fe species within the slag (69.8 % and 65.5% respectively). This is in direct contrast with the Mössbauer results of the vitrified PCM waste streams in Chapter 4 (Table 4.5) which showed mainly Fe^{3+} due to the oxidative nature of the melts. The increased amounts of Fe^{2+} samples in this study are due to the reducing conditions with which the slag was fabricated.

7.6 28 day PCT-B experiment in high alkaline solution (Ca(OH)$_2$)

A 28 day PCT-B experiment was performed on samples A and B, following the standardized ASTM procedure as described in Section 3.5.2, meaning that the crushed slag samples were washed prior to dissolution testing. Figure 7.6 shows the NL$_i$ of a number of elements into solution for both dissolution experiments. The question from this part of the study is to determine how similar the mechanisms of corrosion are with the dissolution behavior of the vitrified PCM waste samples in Section 4.7 during the first 28 days. Sample A has a large release of Si in solution during the first 3 days (NL$_{Si}$ = 0.3 g/m^3), after which the concentration falls rapidly to very low levels, near the detection limits of the ICP. The release rate of the other elements (K, Al, Fe and Mg) follow the same behaviour. A possible reason for this is the rapid dissolution of corrosion products which would be present on the surface of the glass. It should also be noted that sample A

was found in contact with soils. No attempt was made to clean the soils prior to milling into a powder hence there could be a number of soluble minerals that could also influence the release rates of Si into solution. The vitrified PCM samples synthesised in Chapter 4 also saw a release of Si into solution during the first 3 days, however the NL_{Si} was two orders of magnitude lower at 0.003 gm^2. The dissolution behaviour of Sample A in $Ca(OH)_2$ is not concurrent with previous results contained within this thesis. The amount of $Ca(OH)_2$ in solution falls from ~680 ppm to 580ppm within the first 7 days. The $Ca(OH)_2$ levels off at ~580ppm for the remainder of the experiment. This suggests that $Ca(OH)_2$ is not forming secondary phases on the surface of the glass, as seen in previous chapters. This was seen from the SEM images of Sample A post dissolution, shown in Figure 7.6. The bulk of the glass showed little evidence of alteration products formed on the surface of the glass. However on close inspection there were glass particles showing evidence of secondary products as shown in the bottom image of Figure 7.6. EDX spectra showed the precipitates have increased amounts of Al and Mg when compared with the unaltered bulk glass. With the rapid rate drop shown in the $NL_{(Al)(Mg)}$ shown in Figure 7.5 after 3 days, this indicates that these elements are precipitating on the surface of the glass.

The dissolution behaviour of Sample B is similar to what would be expected from conventional glass dissolution, with an initial rate of dissolution within the first 7 days followed by a residual rate for the $NL_{(Si)}$. A promising result is that the $RL_{(Si)}$ seen in sample B is similar to that seen in the vitrified simulant PCM waste in Chapter 4. The initial $RL_{(Si)}$ for the Hayle slag sample B is $(8.80 \pm 0.3) \times 10^{-3}$ $g/m^2/d$ compared with $(6.16 \pm 0.2) \times 10^{-3}$ $g/m^2/d$ for the PVC waste streams.
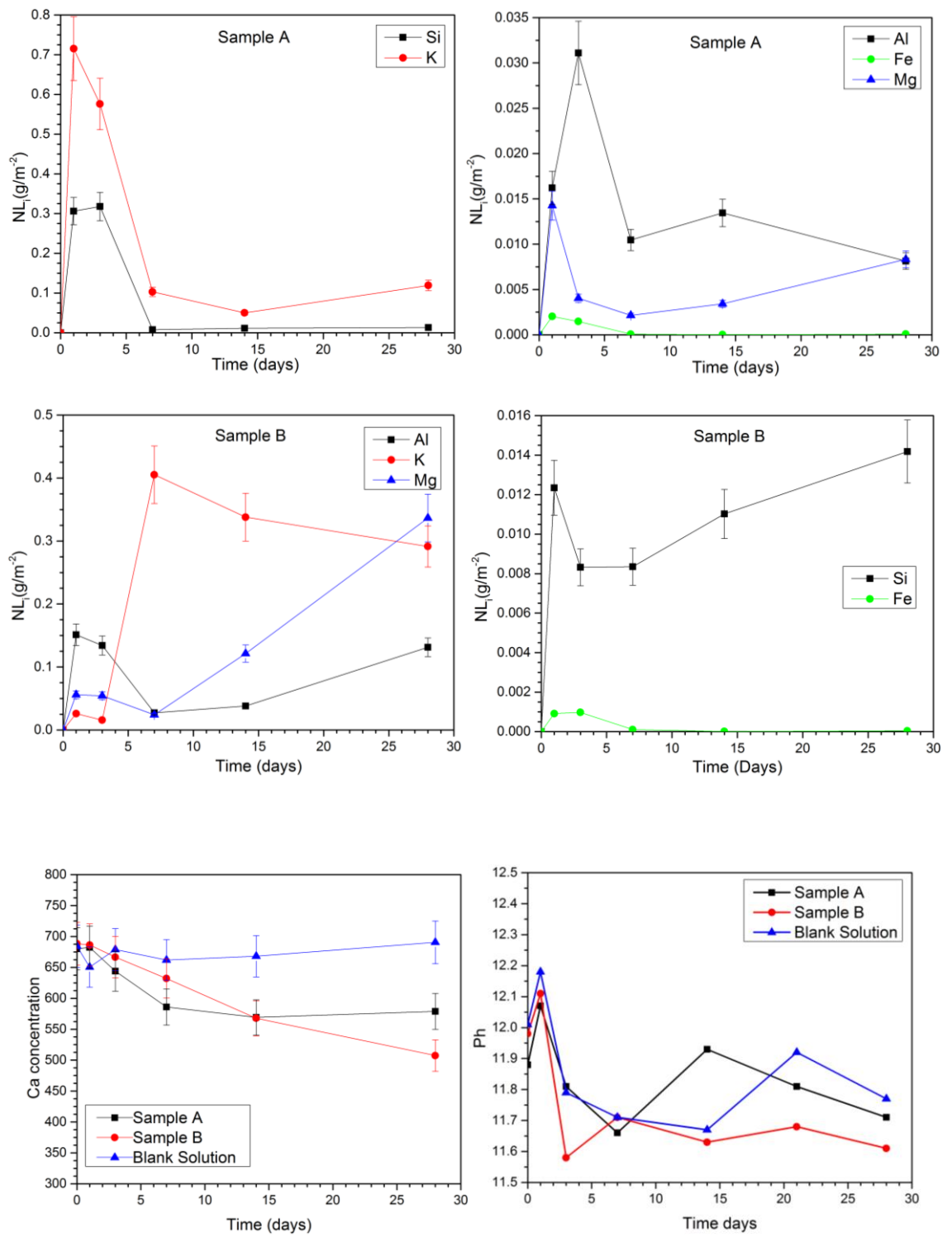
Figure 7.6 NL$_i$ of Si, Fe, Al, K, Mg and Ca concentration in saturated Ca(OH)$_2$
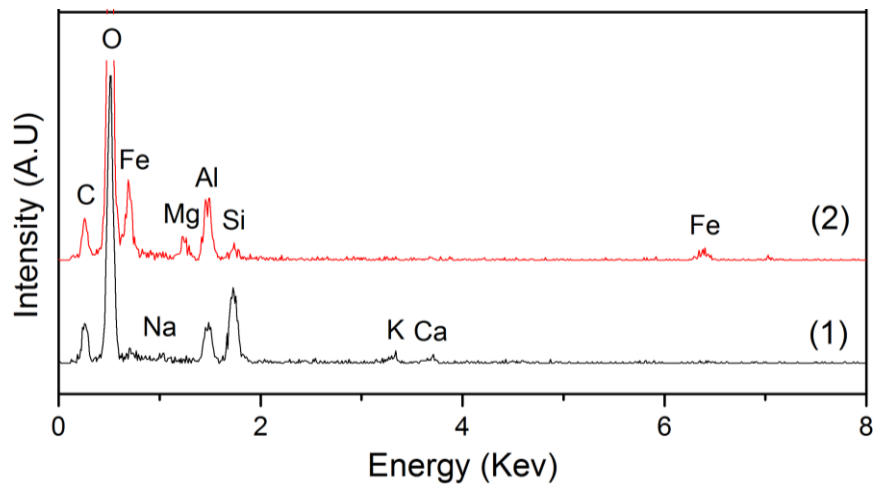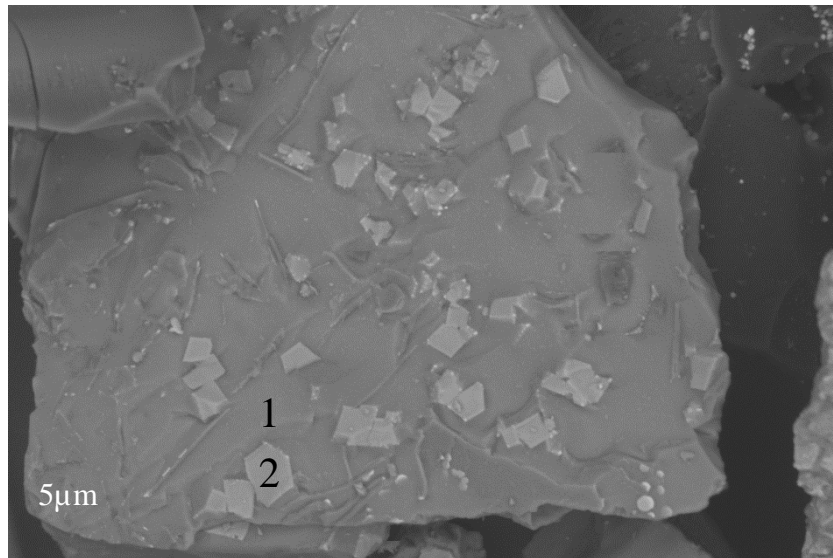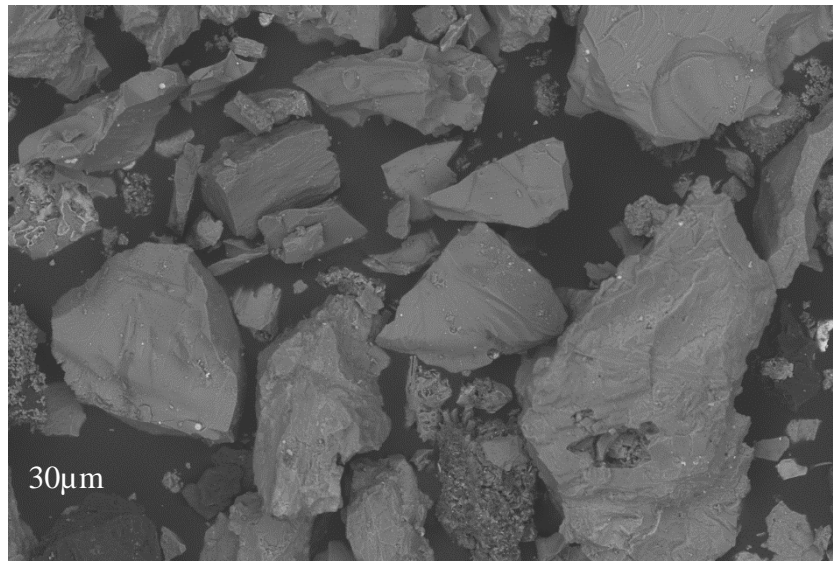
Figure 7.7 Glass sample A post 28 days dissolution test in saturated Ca(OH)₂. EDX scan shows composition of (1) bulk glass (2) precipitates.
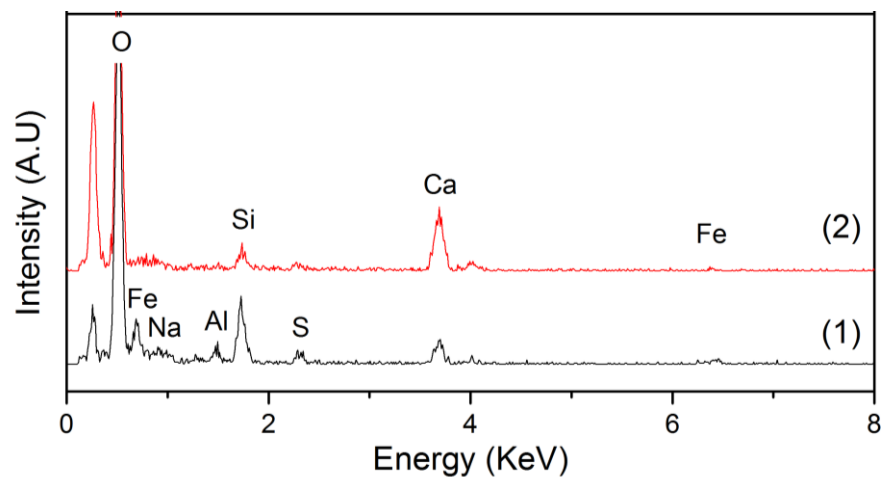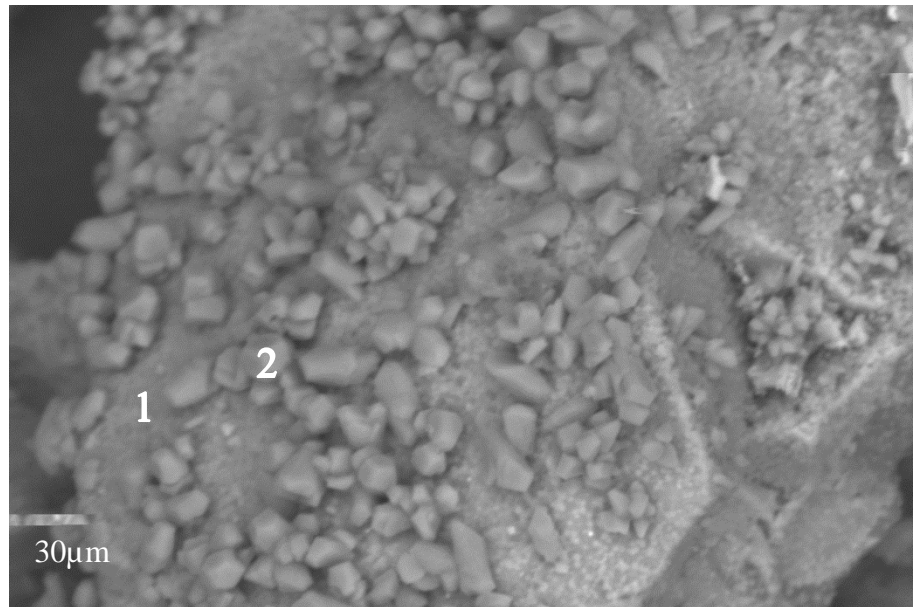
Figure 7.8 Glass sample B post 28 days dissolution test in saturated Ca(OH)₂. EDX scan shows composition of (1) bulk glass (2) precipitates.

The period where the $RL_{(Si)}$ declines, determined to be the residual rate between 7 and 28 days, was significantly higher in the Hayle sample B at $(2.85 \pm 0.3) \times 10^{-3}$ compared with $(1.13 \pm 0.1) \times 10^{-5}$. This could explain why the Ca concentration in solution is higher in the Hayle sample B after 28 days (~510 ppm) compared with the vitrified PCM simulant waste at ~160 ppm, ~240 ppm, ~200 ppm and ~180ppm for the PVC, Metal, Mixed and Masonry waste respectively. This indicates that, due to the higher $RL_{(Si)}$ seen in the Hayle slag sample B between 7 and 28 days, that Si saturation has not been reached. Therefore Ca precipitates on the surface of the Hayle slag B sample at a slower rate compared with the vitrified PCM glass samples as the Si from the glass has not reached saturation. Because the solution has not reached Si saturation the thermodynamic driving force for

C-S-H phases to form on the surface of the glass as postulated by Corkhill et al. (2013), is lower in the Hayle slag composition B.

7.7 Conclusion

The main question from this initial study is how effective are the slag samples found at the Hayle site for use as an alteration analogue for the vitrified simulant PCM waste performed in Chapter 4.

- This Chapter has shown that the composition of the analogue is similar to the nuclear waste glass. In particular the analogue samples have similar mass percentage of the baseline oxides within the glass, mainly Si, Al and CaO. Interestingly the analogue Sample B contains a similar microstructure, with common crystalline phases such as magnetite and diopside, to the vitrified Mixed waste in Chapter 4.

- It is likely that the analogue samples have been altered under similar conditions to a potential GDF environment. It is known that rivers which have low flows, rich in weathered bedrock ions have high pH and alkalinity values. These are the likely conditions to which the analogue samples have been subjected to for at least 250 years old.

- 28 day PCT durability test in saturated $Ca(OH)_2$ were performed on the analogue samples. Analogue Sample B showed similar behaviour to that of the vitrified simulant PCM waste samples in Chapter 4, with similar initial dissolution rates. Observations of the particles post dissolution showed evidence of Ca rich secondary products formed on the surface of the glass. It is promising that despite the age of the analogues, they still follow similar behaviour to the PCM samples in the presence of $Ca(OH)_2$.

This initial study has shown that the analogue samples found at the Hayle slags are relevant to studying the long term behaviour of the vitrified PCM waste simulants. This is based on the relatively similar composition of the samples and the environmental conditions the samples have been exposed to. This provides confidence that the samples are suitable to be used to help validate current glass models for vitrified PCM waste and should be the next aim for this study.

8 SUMMARY AND SUGGESTED FUTURE WORK

Note to reader: A more detailed summary of the results, showing key findings, can be found at the end of each individual result chapter. For the sake of brevity this will not be repeated here.

8.1 Summary

As plans for the GDF mature, volume reduction will be a critical component of waste form design leading to significant cost savings. Although cementation may have been seen as an effective solution to ILW disposal, large volume increase and concerns with the quality of the cementitious waste form derived from certain waste streams, make thermal treatment a very attractive prospect. As shown from this project thermal treatment produces a vitrified waste form with improved passive safety, superior long term stability whilst providing large volume reductions.

The overarching aim of this project was to contribute to accelerating the acquisition of knowledge and experience required to support the NDA in deploying thermal treatment technologies as a national asset for ILW treatment. The project has produced a clear set of results leading to greater understanding of the reactions leading to waste digestion in thermal treatment. Importantly, an understanding of product stability with respect to generic ILW disposal concepts, through accelerated dissolution experiments have been performed.

The project involved research away from the university, at a higher TRL, working with Kurion underpinning the scientific understanding behind the GeoMelt process. Using the facilities within the ISL, the performance of the vitrified product were analysed. The results show a capability of the GeoMelt to produce a high performing, durable waste form suitable for long term storage within a GDF. The author does recognise that no single waste form or process is suitable to economically handle the total clean-up of the

UK's nuclear legacy waste that the NDA faces. Utilizing alternative waste forms to suit the unique characteristics of these problematic waste can overcome the limitations of a baseline cementation method, creating significant opportunities to add flexibility, reduce risk, improve performance and ultimately lower the life cycle costs of the nuclear industry.

8.2 Future work

A major aim of the investigation, with regards to thermal treatment of PCM waste, was to understand the surrogate Pu partitioning between the glass and crystalline regions. EDS mapping was used to analyse the Ce partitioning between the amorphous and crystalline phases within the oxide fraction. It should be noted the volume interactions effects associated with the EDS measurements may lead to uncertainties with respect to the quantities analysed for different phases which are intimately associated in space. Future work could involve neutron activation to quantify partitioning of Ce between different phases and off gas. Possibilities are activating CeO_2 prior to melt and doing autoradiography or gamma spectroscopy on the products to look at partitioning; or activating the product to quantify small concentrations. This would provide a more accurate description in terms of Ce partitioning between the crystalline and glass phases. This is important because analysis of the alteration layer of the glass sample after 112 days of dissolution testing showed varying difference in the dissolution behaviour of the crystalline and glass phase, therefore depending where the Ce is concentrated, the leachability of Ce will depend on the properties of that phase.

A significant finding of this work was that with small variations in the ratio of Na_2O / B_2O_3, thereby changing the R value of the glass, caused the structure of the glass to significantly change, relating to the amount of dissolved masonry waste incorporated within the glass matrix. It would be interesting to note if changing the R value significantly affected other properties of the glass deemed essential for nuclear waste immobilisation such as durability, solubility and waste loadings. This is certainly an area of interest to glass scientist if relevant R values could be obtained to provide the maximum performance in the different criteria mentioned.

The continued partnership between Kurion Inc/ NNL and the ISL would be beneficial for both parties. There are a number of ILW streams that would be potentially viable for processing within the GeoMelt system. These include sludge (e.g. magnox sludge) and

spent organic ion exchange (IEX) resins. It has been shown from this body of work, that small variations in glass compositions can drastically effect waste form properties such as waste solubility and durability. Therefore laboratory scale glass melts are beneficial to optimise glass compositions before progressing to large scale melts. The use of ISL facilities means the performance of the vitrified products can be scientifically underpinned providing confidence to both the waste processing team and by building a strong safety case to meet the letter of compliance for permanent disposal within a GDF.

The Mössbauer investigation highlighted the complexity of redox measurement within a glass melt, especially with a number of multivalent species, such as the PCM melts. The results from the Mössbauer measurements indicate that the activity of the redox ion is determined by:

- The nature of the redox ion in terms of its size, charge and electronic configuration.
- The symmetry and coordination of the redox ion.
- The polarizability of the ligands associated with the redox ion.

The literature shows a number of gaps in terms of correlating the activity of redox ions in glass with the different factors determined above. This is certainly an area for development, and one which one further enhance the understanding redox conditions during vitrification.

The durability of the vitrified PCM waste samples in Chapter 4 shows that Fe has a large role to play in the durability of the samples. The micrographs also indicate that the crystalline phases may play a role in the dissolution of glass. This would suggest more durability studies need to be performed on glass-ceramic materials to determine what role the crystalline regions play in glass dissolution.

The dissolution behaviour of the archaeological samples shown in Chapter 7 show similarities with the dissolution behaviour of the PCM samples (Chapter 4). The study now needs to be taken further to understand the role Ca plays at the surface of the glass and what effect this has on the durability of the glass.

The study has shown the large effect multi-valent ions have on the solubility of a number of elements within the glass. This would be relevant for a number of waste streams, especially those that are poorly characterised. For examples the pond scabblings vitrified

in this project may have a coating of paint containing TiO_2. It would be useful to determine the effect any potential coatings, containing multivalent ions, would have on the solubility of the pond scabblings.

9 REFERENCES.

A.J.Connelly, P.A.Bingham, N.C.H. and R.J.H., 2010. *Thermal Treatment of Plutonium Contaminated Materials: Phase 1*,

Aboutaleb, D. & Safi, B., 2015. Structure and Properties of the Soda-Borate Glasses: Effect of Adding Fe2O3 Concentration. *Journal of Chemical Engineering & Process Technology*, 7(1), pp.2–5. Available at: https://www.omicsonline.org/open-access/structure-and-properties-of-the-sodaborate-glasses-effect-of-adding-fe2o3-concentration-2157-7048-1000268.php?aid=67801.

Andriambololona, Z., 1992. R7T7 Glass Alteration in the presence of mortar; effect of the cement grade. *Scientific Basis for Nuclear Waste Management XV, MRS Proc., vol. 257*, pp.151–158.

Applewhite-Ramsey, A. et al., 1995. High Temperature Vitrification of Surrogate Savannah River Site (SRS) Mixed Waste Materials (U). In *97th Annual Meeting of the American Ceramic Society*. p. 12.

ASTM C1285-02, 2002. Standard Test Methods for Determining Chemical Durability of Nuclear , Hazardous , and Mixed Waste Glasses and Multiphase Glass Ceramics : The Product Consistency Test (PCT) 1. *ASTM, Conshohocken, USA, 2002*, 15(Reapproved 2008), pp.1–26.

Atkins, M. & Glasser, F.P., 1992. Application of portland cement-based materials to radioactive waste immobilization. *Waste Management*, 12(2), pp.105–131. Available at: http://www.sciencedirect.com/science/article/pii/0956053X9290044J.

Atkinson, A., Everitt, N. & Guppy, R., 1989. Time dependence of pH in a cementitious repository. *Scientific basis for nuclear waste management XII*, 21(9).

Atkinson, A., Guppy, R.M. & UKAEA Atomic Energy Establishment. Materials Development Division., 1988. *Evolution of pH in a radwaste repository : Leaching of modified cements and reactions with groundwater.*, UKAEA Atomic Energy Establishment Materials Development Division. Available at:

https://inis.iaea.org/search/search.aspx?orig_q=RN:20080319 [Accessed August 22, 2017].

Atkinson, H. V & Davies, S., 2000. Fundamental aspects of hot isostatic pressing: An overview. *Metallurgical and Materials Transactions A*, 31(12), pp.2981–3000. Available at: http://dx.doi.org/10.1007/s11661-000-0078-2.

Avramov, I., 2005. The Glass Transition Temperature of Silicate and Borate Glasses. , (March).

BAAK, T. & HORNYAK, E.J., 1961. The Iron Oxygen Equilibrium in Glass: Effect of Platinum on the Fe2+/Fe3+ Equilibrium. *Journal of the American Ceramic Society*, 44(11), pp.541–544.

Backhouse, D.., 2016. *A Study of the Dissolution of Nuclear Waste Glasses in highly Alkaline Conditions*. The University of Sheffield.

Bell, R.J. et al., Spectra of glasses : the effect of disorder upon frequency spectra ?

Berner, U.R., 1992. Evolution of pore water chemistry during degradation of cement in a radioactive waste repository environment. *Waste Management*, 12(2–3), pp.201–219.

Bianco, B.. et al., 2004. Glasses on the seabed: Surface study of chemical corrosion in sunken Roman glasses. *Journal of Non-Crystalline Solids*, 343(1), pp.91–100.

Bickford, D.F. et al., 1988. Control of Radioactive Waste-Glass Melters: Glass Electrical Stability. *Advances in fusion of glass*.

Bingham, P.A. et al., 2008. The Use of Surrogates in Waste Immobilization Studies: A Case Study of Plutonium. *MRS Proceedings*, 1107, p.421. Available at: http://journals.cambridge.org/abstract_S1946427400093209 [Accessed May 3, 2017].

Bingham, P.A. & Hand, R.J., 2012. Vitrification of UK Intermediate Level Radioactive Wastes Arising from Site Decommissioning ... Vitrification of UK intermediate level radioactive wastes arising from site decommissioning : property modelling and selection of candidate host glass composit. , (February 2015).

Bingham, P. a., Hyatt, N.C. & Hand, R.J., 2012. Vitrification of UK intermediate level radioactive wastes arising from site decommissioning: property modelling and

selection of candidate host glass compositions. *European Journal of Glass Science and Technology*, 53(3), pp.83–100.

Booth, C.H. et al., 2012. Multiconfigurational nature of 5f orbitals in uranium and plutonium intermetallics. *Proceedings of the National Academy of Sciences*, 109(26), pp.10205–10209.

Brill, R.., 1961. The record of time in weathered glass. *Archaeology*, 14(1), pp.18–22.

Burger, E. et al., 2013. Impact of iron on nuclear glass alteration in geological repository conditions: A multiscale approach. *Applied Geochemistry*, 31.

Burns, R.. & Solberg, T.., 1990. 57Fe-Bearing Oxide, Silicate, and Aluminosilicate Minerals. *american chemical society*, 415, pp.262–283.

Cachia, J.N. et al., 2006. Enhancing cerium and plutonium solubility by reduction in borosilicate glass. *Journal of Nuclear Materials*, 352(1–3), pp.182–189.

Cailleteau, C. et al., 2008. Insight into silicate-glass corrosion mechanisms. *Nat Mater*, 7(12), pp.978–983. Available at: http://dx.doi.org/10.1038/nmat2301.

Caravaca, C. et al., 2008. Determination of the EpO2- stability diagram of plutonium in the molten LiCl-KCl eutectic at 450 C. *Journal of Nuclear Materials*, 377, pp.340–347.

Carstens, C., Meyer, W.C.M.H. & Hanley, T.L., 2014. Technical Support for Waste Management of Fission-Based Mo-99 Production. , (4).

Caurant, D. et al., 2009. *Glasses, glass-ceramics and ceramics for immbolisation of highly radioactive nuclear wastes*, Nova Science Publ.

Cerefice, G.., 1996. *Proliferation resistance of borosilicate glass as a host form for weapons - grade Pu.*

Chapman, C., Pope, J.M. & Barnes, S.M., 1986. Electric melting of nuclear waste glasses. *Journal of Non-Crystalline Solids*, 114(84), pp.226–240.

Chave, T. et al., 2011. Glass-water interphase reactivity with calcium rich solutions. *Geochimica et Cosmochimica Acta*, 75(15), pp.4125–4139. Available at: http://dx.doi.org/10.1016/j.gca.2011.05.005.

Chick, L.A. et al., 1981. Effects of composition on properties in an 11-component nuclear waste glass system. Available at:

https://inis.iaea.org/search/search.aspx?orig_q=RN:12642496 [Accessed August 6, 2017].

Cicutti, C. et al., 2002. Analysis of slag foaming during the operation of an industrial converter. *Latin American Applied Research*, 32(2804), pp.237–240.

Cirero-Herman, C.A; Workman, P; Erich, D.; Harden, J., 1998. *Commercial Ion exchange resin vitrification in borosilicate glass*, Available at: https://www.osti.gov/scitech/servlets/purl/676750.

Connelly, A.J. et al., 2013. The effect of uranium oxide additions on the structure of alkali borosilicate glasses. *Journal of Non-Crystalline Solids*, 378, pp.282–289. Available at: http://dx.doi.org/10.1016/j.jnoncrysol.2013.06.026.

Corkhill, C.L. et al., 2013. Dissolution of UK high-level waste glass under simulated hyperalkaline conditions of a colocated geological disposal facility. *International Journal of Applied Glass Science*, 4(4), pp.341–356.

Crossland, G., 2001. Nirex Report Why a cementitious repository ? , (June).

Crovisier, J.L., 2006. Long-term Corrosion of Two nuclear Waste Reference Glasses (MW and SON68): A Kinetic and Mineral Alteration Study. , (July).

Cummings, R., 2014. Waste Acceptance Criteria – Low Level Waste Disposal. , (March).

Curti, E. et al., 2006. Long-term corrosion of two nuclear waste reference glasses (MW and SON68): A kinetic and mineral alteration study. *Applied Geochemistry*, 21(7), pp.1152–1168.

Davenport, W.. & Partelpoeg, E.., 2015. *flash smelting: Analysis, control and optimization*, Elsevier.

Deegan, D. & Ismail, S., 2004. *Plasma meltig tests on surrogate PCM waste materials prepared for BNFL*,

Deegan, D. & Scales, C., 2007. The Role of Tetronics Plasma Vitrification Technology in the Management and Conditioning of Nuclear Waste. , (43390), pp.1179–1187. Available at: http://dx.doi.org/10.1115/ICEM2007-7271.

DEFRA, 2004. Managing Radioactive Waste Safely Proposals for developing a policy for managing solid radioactive waste in the UK. *Department for Environment, Food and Rural Affair*, p.91. Available at:

http://webarchive.nationalarchives.gov.uk/20031221042814/http:/www.defra.gov.uk/environment/consult/radwaste/pdf/radwaste.pdf.

Depierre, S. et al., 2013. Leaching of Nuclear Waste Glass in Cement Pore Water: Effect of Calcium in Solution. In F. Bart et al., eds. *Cement-Based Materials for Nuclear Waste Storage*. New York, NY: Springer New York, pp. 161–168. Available at: https://doi.org/10.1007/978-1-4614-3445-0_15.

Deschanels, X. et al., 2007. Plutonium solubility and self-irradiation effects in borosilicate glass. *Progress in Nuclear Energy*, 49(8), pp.623–634. Available at: http://linkinghub.elsevier.com/retrieve/pii/S0149197007000364 [Accessed May 3, 2017].

Donald, R., 2010. *Waste immobilization in glass and ceramic based hosts*, Wiley.

Doremus, R.H., 1975. Interdiffusion of hydrogen and alkali ions in a glass surface. *Journal of Non-Crystalline Solids*, 19, pp.137–144. Available at: http://www.sciencedirect.com/science/article/pii/0022309375900794.

Duffy, J.A. & Ingram, M.D., 1976. An interpretation of glass chemistry in terms of the optical basicity concept. *Journal of Non-Crystalline Solids*, 21(3), pp.373–410.

Duffy, J.A., Ingram, M.D. & Fong, S., 2000. Effect of basicity on chemical bonding of metal ions in glass and its relevance to their stability. *Physical Chemistry Chemical Physics*, 2(8), pp.1829–1833. Available at: http://dx.doi.org/10.1039/B000489H.

Durinck, D. et al., 2008. Borate distribution in stabilized stainless-steel slag. *Journal of the American Ceramic Society*, 91, pp.548–554.

Dyar, M.D. et al., 2006. Mössbauer Spectroscopy of Earth and Planetary Materials. *Annual Review of Earth and Planetary Sciences*, 34(1), pp.83–125. Available at: http://www.annualreviews.org/doi/10.1146/annurev.earth.34.031405.125049.

Ellison, A.J.G., Mazer, J.J. & Ebert, W.L., 1994. Effect of Glass Composition on Waste Form. , (November), p.142.

Ewing, R.C., 2005. Plutonium and "minor" actinides: safe sequestration. *Earth and Planetary Science Letters*, 229(3–4), pp.165–181. Available at: http://linkinghub.elsevier.com/retrieve/pii/S0012821X04006995 [Accessed May 3, 2017].

Farges, F. et al., 2007. Durability of silicate glasses: An historical approach. *AIP Conference Proceedings*, 882(November), pp.44–50.

Farges, F. et al., 1992. Structural environments of incompatible elements in silicate glass / melt systems : IV, V, VI. *Geochimica et Cosmochimica Acta*, 56, pp.4205–4220.

Ferguson, J., 1996. The Copper slag Blocks of Hayle, Cornwall: Remains of a late 18th Century Industry. *Mining History: The bulletin of the peak district mines historical society*, 13(2).

Ferrière, L., Koeberl, C. & Reimold, W.U., 2009. Characterisation of ballen quartz and cristobalite in impact breccias: new observations and constraints on ballen formation. *European Journal of Mineralogy*, 21(1), pp.203–217.

Flinn, J.. et al., 1980. *Characterisation of Iron-Enriched Synthetic Basalt for Transuranic Containment*,

Forsberg, C.., 1997. *Long - term Criticality Control in Radioactive Waste Disposal Facilities Using Depleted Uranium*,

Fournier, M., Gin, S. & Frugier, P., 2014. Resumption of nuclear glass alteration: State of the art. *Journal of Nuclear Materials*, 448(1–3).

Fox, K.. et al., 2008. Evaluation of Impurity Extremes in a Plutonium-loaded Borosilicate Glass. *Waste Management*.

Frantz, J.. & Mysen, B.O., 2005. *Silicate Glasses and Melts: Properties and structure* first., Elsevier B.V.

Freeman, C.., 1997. *Treatment Studies of Plutonium-Bearing INEEL Waste Surrogates in a Bench-Scale Arc Furnace*,

Frugier, P. et al., 2008. SON68 nuclear glass dissolution kinetics: Current state of knowledge and basis of the new GRAAL model. *Journal of Nuclear Materials*, 380, pp.8–21.

Furukawa, T. White, W.B., 1981. Raman spectroscopic investigation of sodium borosilicate glass structure. *Journal of Materials Science*, 16.

Gaillard, F., Pichavant, M. & Scaillet, B., 2003. Experimental determination of activities of FeO and Fe2O3 components in hydrous silicic melts under oxidizing conditions. *Geochimica et Cosmochimica Acta*, 67(22), pp.4389–4409.

Gan, H. et al., 2002. *Corrosion of Chromium-Rich Oxide Refractories in Molten Waste Glasses*,

García Lodeiro, I. et al., 2009. Effect of alkalis on fresh C-S-H gels. FTIR analysis. *Cement and Concrete Research*, 39(3), pp.147–153. Available at: http://dx.doi.org/10.1016/j.cemconres.2009.01.003.

Garrault-Gauffinet, S. & Nonat, A., 1999. Experimental investigation of calcium silicate hydrate (C-S-H) nucleation. *Journal of Crystal Growth*, 200(3), pp.565–574.

Gedikoǧlu, A., 1983. Mossbauer study of low temperature oxidation in natural magnetite. *Scripta Metallurgica*, 17(1), pp.45–48. Available at: http://www.sciencedirect.com/science/article/pii/0036974883900674.

Gin, S. et al., 2013. An international initiative on long-term behavior of high-level nuclear waste glass. *Materials Today*, 16(6).

Gin, S. et al., 2012. Effect of composition on the short-term and long-term dissolution rates of ten borosilicate glasses of increasing complexity from 3 to 30 oxides. *Journal of Non-Crystalline Solids*, 358(18), pp.2559–2570. Available at: http://www.sciencedirect.com/science/article/pii/S0022309312002748.

Gin, S. et al., 2013. New insight into the residual rate of borosilicate glasses: Effect of s/v and glass composition. *International Journal of Applied Glass Science*, 4(4).

Gin, S. et al., 2011. Nuclear glass durability: New insight into alteration layer properties. *Journal of Physical Chemistry C*, 115(38), pp.18696–18706.

Goldman, D.O.N.S. et al., 1985. Ferrous / Ferric Mossbauer Analysis of Simulated Nuclear Waste Glass with and without Computer Fitting. , 95, pp.691–695.

GOLDMAN, D.S., BRITE, D.W. & RICHEY, W.C., 1986. Investigation of Foaming in Liquid Fed Melting of Simulated Nuclear Waste Glass. *Journal of the American Ceramic Society*, 69(5), pp.413–417.

Gomez, E. et al., 2009. Thermal plasma technology for the treatment of wastes: A critical review. *Journal of Hazardous Materials*, 161(2–3), pp.614–626.

Gorski, C.A. & Scherer, M.M., 2010. Determination of nanoparticulate magnetite stoichiometry by Mossbauer spectroscopy, acidic dissolution, and powder X-ray diffraction: A critical review. *American Mineralogist*, 95(7), pp.1017–1026.

Grambow, B., 1992. Geochemical Approach to Glass Dissolution, in Corrosion of Glass, Ceramics and Ceramic Superconductors. *Noyes Publication*, (124–148).

De Grave, E. & Eeckhout, S.G., 2003. Mössbauer Studies of Some Magnetic Clinopyroxenes. *Hyperfine Interactions*, 148(1), pp.263–274. Available at: http://dx.doi.org/10.1023/B:HYPE.0000003788.80160.77.

De Grave, E. & Van Iseghem, P., 1986. Application of Iron-57 Mössbauer Spectroscopy to the Characterization of Silicate Glasses Used for High Temperature Incinerated Low-Level Radioactive Waste Products. In G. J. Long & J. G. Stevens, eds. *Industrial Applications of the M{ö}ssbauer Effect*. Boston, MA: Springer US, pp. 423–446. Available at: http://dx.doi.org/10.1007/978-1-4613-1827-9_22.

Greaves, G.N. et al., 1989. Glancing-angle x-ray absorption spectroscopy of corroded borosilicate glass surfaces containing uranium. *Journal of the American Chemical Society*, 111(12), pp.4313–4324. Available at: http://dx.doi.org/10.1021/ja00194a024.

Harrison, Mike T; Dunnet, B.F; Morgan, S; Scales, C.R, Small, J.S., 2009. *International research on vitrified HLW long-term behaviour: state of the art*, Available at: file:///C:/Users/Luke/Downloads/International-research-on-vitrified-HLW-long-term-behaviour-State-of-the-art.pdf.

Harrison, M.T., 2014. The effect of composition on short- and long-term durability of UK HLW glass. *Procedia Materials Science*, 7, pp.186–192. Available at: http://dx.doi.org/10.1016/j.mspro.2014.10.025.

Hayes, P.C. (Peter C.., 1993. *Process principles in minerals and materials production / by Peter C. Hayes ; with contributions from S.H. Algie ... [et al.]* S. H. Algie & P. C. (Peter C. . P. selection in extractive metallurgy Hayes, eds., Sherwood, Qld: Hayes Publishing.

Hewlett, P. & Liska, M., 1998. *Lea's chemistry of cement and concrete* 4th ed. P. Hewlett, ed., Elsevier Ltd.

Hong, S.-Y. & Glasser, F.P., 1999. Alkali binding in cement pastes. *Cement and Concrete Research*, 29(12), pp.1893–1903. Available at: http://linkinghub.elsevier.com/retrieve/pii/S0008884699001878.

Howland, R.J. et al., 2000. Distributions and seasonal variability of pH and alkalinity in

the Tweed Estuary, UK. *The Science of the total environment*, 251–252, pp.125–138.

Hrma, P.R. et al., Project Title : Modeling of Spinel Settling in Waste Glass Melter Lead Principal Investigator : Co Principal Investigators : Modeling of Spinel Settling in Waste Glass Melter Co-Principal Investigator.

Hrma, P.R., Nemec, L. & Schill, P., 1998. Modeling of Spinel Settling in Waste Glass Melter. *Project*, pp.423–424.

Hrma, P.R. & Piepel, G.F., 1994. *Property/Composition relationship for Hanford High-Level waste glasses melting at 1150C*,

Hutt, J.E.C. et al., 1999. Equiaxed solidification of Al–Si alloys. *Materials Science and Technology*, 15(5), pp.495–500. Available at: http://openurl.ingenta.com/content/xref?genre=article&issn=0267-0836&volume=15&issue=5&spage=495.

Hyatt, N.C. et al., 2006. Characterisation of Plasma Vitrified Simulant Plutonium Contaminated Material Waste. *MRS Proceedings*, 985. Available at: https://www.cambridge.org/core/article/div-class-title-characterisation-of-plasma-vitrified-simulant-plutonium-contaminated-material-waste-div/9EFDDA629728ED1D71002568BA3C789F.

Hyatt, N.C. et al., 2014. Thermal treatment of simulant plutonium contaminated materials from the Sellafield site by vitrification in a blast-furnace slag. *Journal of Nuclear Materials*, 444(1–3), pp.186–199. Available at: http://dx.doi.org/10.1016/j.jnucmat.2013.08.019.

Hyatt, N.C. et al., 2014. Thermal treatment of simulant plutonium contaminated materials from the Sellafield site by vitrification in a blast-furnace slag. *Journal of Nuclear Materials*, 444(1–3), pp.186–199. Available at: http://linkinghub.elsevier.com/retrieve/pii/S0022311513010313 [Accessed May 3, 2017].

IAEA, 2002. *Application of Ion Exchange processes for the treatment of radioactive waste and management of spent ion exchangers*,

IAEA, 2006. Application of Thermal Technologies for Processing of Radioactive Waste. , (December).

Inagaki, Y. et al., 1997. Effects of Water Redox Conditions and Presence of Magnetite on Leaching of Pu and Np From HLW Glass. *MRS Proceedings*, 506(January 1997), p.177. Available at: http://journals.cambridge.org/abstract_S1946427400248641.

Iyengar, S.J. et al., 2014. Magnetic, X-ray and Mössbauer studies on magnetite/maghemite core–shell nanostructures fabricated through an aqueous route. *RSC Adv.*, 4(110), pp.64919–64929. Available at: http://xlink.rsc.org/?DOI=C4RA11283K.

Jantzen, C, M., 1991. *Glass Melter Off-Gas System Pluggages: Cause, Significance, and Remediation*,

Jantzen, C, M., 1995. *Vitrification of Ion-Exchange (IEX) Resins: Advantages and Technical Challenges*,

Jantzen, C.., 1990. Determination of the Fe2_Fe3 Ratio in Simulated Nuclear Waste Glass by Ion Chromatography.pdf. , p.80.

Jantzen, C.M., Smith, M.E. & Peeler, D.K., DEPENDENCY OF SULFATE SOLUBILITY ON MELT COMPOSITION AND MELT POLYMERIZATION (U). , (865).

Johnston, W.., 1964. Oxidation - Reduction Equilibria in Iron-Containing Glasses. *J. Am. Ceram. Soc.*, 47(4), pp.198–201.

Kamitsos, E.I Kapoutsis, J.A Jain, H Hsieh, C.H., 1994. Vibrational study of the role of trivalent ions in sodium trisilicate glass. *Journal of Non-Crystalline Solids*, 171, pp.31–45.

Kemori, N., Shibata, Y. & Tomono, M., 1986. Measurements of oxygen pressure in a copper flash smelting furnace by an EMF method. *Metallurgical Transactions B*, 17(1), pp.111–117.

Kienzler, B. et al., 2003. Mobility and Criticality of Plutonium in a Repository. *Nuclear Technology*, 143(3), pp.309–321. Available at: http://www.tandfonline.com/doi/abs/10.13182/NT03-A3419.

Kinger, D.., Bowen, H.. & Uhlmann, D.., 1976. *Intorduction to Ceramics, 2nd Edition*, Wiley-interscience; 2 edition.

Kniess, C.T., Cardoso de Lima, J. & Prates, P.B., 2005. The quantification of crystalline

phases in materials: Applications of Rietveld method. *Sintering - Methods and Products*, pp.293–316.

Kodur, V., 2014. Properties of concrete at elevated temperatures. *ISRN Civil Engineering*.

Kuno, A. et al., 2000. Characterization of Natural Chromite Samples from Ophiolite Complexes in the Philippines by 57Fe M{ö}ssbauer Spectroscopy. *Journal of Radioanalytical and Nuclear Chemistry*, 246(1), pp.79–83. Available at: http://dx.doi.org/10.1023/A:1006724913427.

Leemann, A. et al., 2011. Alkali–Silica Reaction: the Influence of Calcium on Silica Dissolution and the Formation of Reaction Products. *Journal of the American Ceramic Society*, 94(4), pp.1243–1249. Available at: http://dx.doi.org/10.1111/j.1551-2916.2010.04202.x.

Lenoir, M. et al., 2008. Sulphate Incorporation in Borosilicate Glasses and Melts : a Kinetic Approach. , (September), pp.20–26.

Ledieu, A., Devreux, F. & Barboux, P., 2005. *The Role of Aluminium in the Durability of Alumino-borosilicate Glasses*,

Lin, J.-F. et al., 2016. High-Spin Fe 2+ and Fe 3+ in Single-Crystal Aluminous Bridgmanite in the Lower Mantle. *Geophysical Research Letters*, 43, p.doi:10.1002/2016GL069836. Available at: http://doi.wiley.com/10.1002/2016GL069836.

Lombardo, T. et al., 2013. Characterisation of complex alteration layers in medieval glasses. *Corrosion Science*, 72, pp.10–19. Available at: http://dx.doi.org/10.1016/j.corsci.2013.02.004.

Lopez, C. et al., 2003. Solubility of actinide surrogates in nuclear glasses. *Journal of Nuclear Materials*, 312(1), pp.76–80.

Mada, J. & Iida, S., 1977. Mössbauer Study of the Low Temperature Phase of Magnetite (Fe3O4). *Journal of the Physical Society of Japan*, 42(4), pp.1184–1189. Available at: http://dx.doi.org/10.1143/JPSJ.42.1184.

Maddrell, E., 2013. Hot isostatically pressed wasteforms for future nuclear fuel cycles. *Chemical Engineering Research and Design*, 91(4), pp.735–741. Available at: http://dx.doi.org/10.1016/j.cherd.2012.11.004.

Manara, D. et al., 2007. Sulfur Behavior in Silicate Glasses and Melts: Implications for

Sulfate Incorporation in Nuclear Waste Glasses as a function of alkali cation and V2O5 content. *Journal of Non-Crystalline Solids*, 353(March 2015), pp.12–23.

Manara, D., Grandjean, A. & Neuville, D.R., 2009. Advances in understanding the structure of borosilicate glasses: A raman spectroscopy study. *American Mineralogist*, 94(5–6), pp.777–784.

Mara, M.., 1977. Combustion of PVC. *Pure and Applied Chemistry*, 49(5), pp.649–660.

Marion, L. et al., 2009. Sulphate in liquid nuclear wastes : from production to containment. , (January).

Matson, D.W Sharma, S.K Philpotts, J.A., 1983. The structure of high-silica alkai silicate glasses: A raman spectroscopic investigation. *Journal of Non-Crystalline Solids*, 58, pp.323–352.

McCloy, J.S. et al., 2012. Rhenium Solubility in Borosilicate Nuclear Waste Glass: Implications for the Processing and Immobilization of Technetium-99. *Environmental Science & Technology*, 46(22), pp.12616–12622. Available at: http://dx.doi.org/10.1021/es302734y.

McKeown, D.A. et al., 2001. Raman studies of sulfur in borosilicate waste glasses: Sulfate environments. *Journal of Non-Crystalline Solids*, 288(1–3), pp.191–199.

Mercado-Depierre, S. et al., 2013. Antagonist effects of calcium on borosilicate glass alteration. *Journal of Nuclear Materials*, 441(1–3), pp.402–410.

Michael Egan, A.P. and G.T., 2008. Treatment of Plutonium Contaminated Material at Sellafield. , p.73. Available at: http://www.sellafieldsites.com/wp-content/uploads/2012/08/PCM-BPEO-Study-QRS-1372A-1-Version-2_0.pdf.

Michelin, A. et al., 2013. Effect of iron metal and siderite on the durability of simulated archeological glassy material. *Corrosion Science*, 76.

MILLER, B., TOOLEY, J. & THOMSON, G., 2006. Storage and Disposal of ILW and HLW in the UK: Implications for Copeland. , (December). Available at: http://www.copeland.gov.uk/sites/default/files/attachments/CIS/pdf/180107_nwg8a.pdf.

Miller, R.L. & Reimann, G.A., 1993. Id a ho N a tion a l Engineering Managed of Energy Thermodynamics of Gas-Metal-Slag Equilibria for Applications in in Situ and Ex

Situ Vitrification Melts IS. , (May).

Min, B.Y. et al., 2008. Partitioning ratio of depleted uranium during a melt decontamination by arc melting. *Nuclear Engineering and Technology*, 40(6), pp.497–504.

Moore, J.., 1990. *Chemical Metallurgy*, ELSEVIER.

Motz, H. & Geiseler, J., 2001. Products of steel slags an opportunity to save natural resources. *Waste Management*, 21, pp.285–293.

Moustakas, K. et al., 2005. Demonstration plasma gasification/vitrification system for effective hazardous waste treatment. *Journal of Hazardous Materials*, 123(1–3), pp.120–126.

Mysen, B.O. & Virgo, D., 1985. Iron-bearing silicate melts: Relations between pressure and redox equilibria. *Physics and Chemistry of Minerals*, 12(4), pp.191–200. Available at: http://dx.doi.org/10.1007/BF00311288.

NANBA, T., 2011. Characterization of glasses based on basicity. *Journal of the Ceramic Society of Japan*, 119(1394), pp.720–725. Available at: http://joi.jlc.jst.go.jp/JST.JSTAGE/jcersj2/119.720?from=CrossRef.

NDA, 2013. Packaging of Plutonium Contaminated Material at the Waste Treatment Complex. Available at: file:///C:/Users/Luke/Downloads/Summary-of-Assessment-Report-for-Plutonium-Contaminated-Material-at-the-Waste-Treatment-Complex-ext.-to-Final-and-Periodic-Review.pdf.

NDA, 2011. The 2010 UK Radioactive Waste Inventory (2011). Available at: https://ukinventory.nda.gov.uk/wp-content/uploads/sites/18/2014/02/2010-UK-Radioactive-Waste-Inventory-Main-Report.pdf ... (accessed 01/04/2017).

NDA/RWM, 2010. *Geological Disposal: System Technical Specification*, Available at: file:///C:/Users/Luke/Downloads/Geological-Disposal-Generic-Disposal-System-Technical-Specification-December-2010.pdf.

Nirex, 2004. Nirex Report A Review of International Literature on Immobilisation Matrices for Separated Stocks of Plutonium. , (September).

NuSAC, 2005. Plutonium Contaminated Material (PCM): A review of the status at Sellafield, Dounreay, Harwell and Aldermaston. , p.15. Available at:

http://www.hse.gov.uk/aboutus/meetings/iacs/nusac/131005/p15.pdf.

O.N, Koroleva, L.A Shabunina, Bykov, V.., 2010. Structure of borosilicate glass according to Raman spectroscopy data. *glass and ceramic*, 67, pp.11–12.

Ojovan, M.I., 2008. Viscosity and glass transition in amorphous oxides. , 2008. Available at: http://dx.doi.org/10.1155/2008/817829.

Ojovan, M.I. and W.E.L., 2005. *An Introduction To Nuclear Waste Immobilisation*, ELSEVIER.

Ojovan, M.I. & Lee, W.E., 2011. Glassy wasteforms for nuclear waste immobilization. *Metallurgical and Materials Transactions A: Physical Metallurgy and Materials Science*, 42(4), pp.837–851.

Orfeuil, M. & Robin, A., 1987. *Electric process heating : technologies, equipment, applications,* Columbus (Ohio) : Battelle press. Available at: http://lib.ugent.be/catalog/rug01:000764683.

Osipov, A.A., Osipova, L.M. & Eremyashev, V.E., 2013. Structure of alkali borosilicate glasses and melts according to Raman spectroscopy data. *Glass Physics and Chemistry*, 39(2), pp.105–112. Available at: http://dx.doi.org/10.1134/S1087659613020119.

Ozturtc, B. & Fruehan, R.J., DECONTAMINATION OF STEEL BY MELT REFINING A LITERATURE REVIEW.

Palermo, A. et al., 1998. Critical influence of the amorphous silica-to-cristobalite phase transition on the performance of Mn/Na2WO4/SiO2 catalysts for the oxidative coupling of methane. *Journal of Catalysis*, 177(2), pp.259–266. Available at: http://www.sciencedirect.com/science/article/pii/S0021951798921091.

Parkinson, B.G., 2007. Influence of Composition on Structure and Caesium Volatilisation from Glasses for HLW Confinement. , (November), p.207.

Paul, A., 1990. *Chemistry of Glasses*, Chapman and Hall.

Plodinec, M.., 1986. Vitrification Chemistry and Nuclear Waste. *Journal of Non-Crystalline Solids*, 84, pp.206–214.

Rajmohan, N., Frugier, P. & Gin, S., 2010. Composition effects on synthetic glass alteration mechanisms: Part 1. Experiments. *Chemical Geology*, 279(3), pp.106–

119. Available at: http://www.sciencedirect.com/science/article/pii/S0009254110003724.

Rechard, R.P. et al., 1996. Consideration of critically when directly disposing highly enriched spent nuclear fuel in unsaturated tuff: Bounding estimates. , (January 1996). Available at: http://www.osti.gov/servlets/purl/233337/.

Reid, D.P., Stennett, M.C. & Hyatt, N.C., 2012. The fluorite related modulated structures of the Gd2(Zr2−xCex)O7 solid solution: An analogue for Pu disposition. *Journal of Solid State Chemistry*, 191, pp.2–9. Available at: http://linkinghub.elsevier.com/retrieve/pii/S0022459611007092 [Accessed May 3, 2017].

Reimann, G.., 1991. *Technical Assessment of Processes to Enable Recycling of Low-Level Contaminated Metal Waste*,

Rose, P.B. et al., 2011. Crystallisation of a simulated borosilicate high-level waste glass produced on a full-scale vitrification line. *Journal of Non-Crystalline Solids*, 357(15), pp.2989–3001. Available at: http://dx.doi.org/10.1016/j.jnoncrysol.2011.04.003.

Rüssel, C. & Wiedenroth, A., 2004a. The effect of glass composition on the thermodynamics of the Fe2+/Fe3+ equilibrium and the iron diffusivity in Na2O/MgO/CaO/Al2O3/SiO2 melts. *Chemical Geology*, 213(1–3), pp.125–135.

Rüssel, C. & Wiedenroth, A., 2004b. *The Effect of Glass Composition on the Thermodynamics of the Fe2+/Fe3+ Equilibrium and the Iron Diffusivity in Na2O/MgO/CaO/Al2O3/SiO2 Melts*,

Samans, C.., 1949. *Engineering metals and their alloys*, Macmillian.

Sambasivam, R. et al., 2007. A new lance design for BOF steelmaking. *Metallurgical and Materials Transactions B: Process Metallurgy and Materials Processing Science*, 38(February), pp.45–53.

Schlienger, M.E., Buckentin, J.M. & Damkroger, B.K., 1997. Melt Processing of Radioactive Waste: a Technical Overview.

Schreiber, H.D. et al., 1987. Mutual interactions of redox couples via electron exchange in silicate melts - Models for geochemical melt systems. *Center for Glass Chemistry*

, *Virginia Military Institute, Lexington*, 92(2), pp.9233–9245.

Schreiber, H.D., 1980. Properties of redox ions in glasses: An interdisciplinary perspective. *Journal of Non-Crystalline Solids*, 42(1–3), pp.175–183.

Schreiber, H.D. & Hockman, A.L., 1987. Redox Chemistry in Candidate Glasses for Nuclear Waste Immobilization. *J. Am. Ceram. Soc.*, 70, pp.591–594.

Schumacher, R.F. et al., 1995. High-temperature vitrification of low-level radioactive and hazardous wastes.

Seitz, M.., Gerding, T.J. & Steindler, M.J., 1979. Decontamination of Metals Containing Plutonium and Americum.

Seitz, M.G., Gerding, T.J. & Steindler, M.J., DECONTAMINATION OF METALS CONTAINING PLUTONJUM AND AMERICIUM.

Senior, D., 2013. *Bradwell Care and Maintenance Sealing of the redundant Fuel Cooling Ponds*,

Shelby, J.., 2005. *Introduction to Glass Science and Technology*, The Royal Society of Chemistry.

Short, R.J. et al., 2005. Environment and oxidation state of molybdenum in simulated high level nuclear waste glass compositions. *Journal of Nuclear Materials*, 340(2–3), pp.179–186.

Siwadamrongpong, S., Koide, M. & Matusita, K., 2004. Prediction of chloride solubility in CaO-Al2O 3-SiO2 glass systems. *Journal of Non-Crystalline Solids*, 347, pp.114–120.

Snellings, R., 2013. Solution-controlled dissolution of supplementary cementitious material glasses at pH 13: The effect of solution composition on glass dissolution rates. *Journal of the American Ceramic Society*, 96(8), pp.2467–2475.

Soelberg, N.R. et al., 1995. Arc Melter Vitrification of Organic and Chloride Containing Materials.

Stefanovsky, S. V, 1993. Immobilising sulphate-bearing radioactive waste in glass. *Physical Chemistry*, 27(2), pp.157–167.

Strachan, D.., 2001. *Distribution and Solubility of Radionuclides and Neutron Absorbers in Waste Forms for Disposition of Plutonium Ash and Scraps, Excess Plutonium,*

and Miscellaneous Spent Nuclear Fuels, Available at: https://www.osti.gov/scitech/servlets/purl/799223/.

Sugilal, G., 2008. Cold Crucible Induction Melting Technology for Vitrification of High Level Waste: Development and Status in India.

Taylor, H.F.W., 1997. *Cement Chemistry* 2nd ed., Thomas Telford Ltd.

Techer, I. et al., 2000. Basaltic glass: Alteration mechanisms and analogy with nuclear waste glasses. *Journal of Nuclear Materials*, 282(1), pp.40–46.

Thiemsorn, W. et al., 2008. Influence of glass basicity on redox interactions of iron-manganese-copper ion pairs in soda-lime-silica glass. *Glass Physics and Chemistry*, 34(1), pp.19–29.

Thornber, C.R., Roeder, P.L. & Foster, J.R., 1980. The effect of composition on the ferric-ferrous ratio in basaltic liquids at atmospheric pressure. *Geochimica et Cosmochimica Acta*, 44(3), pp.525–532.

Topsoe, H., Dumesic, J.A. & Boudart, M., 1974. MOSSBAUER SPECTRA OF STOICHIOMETRIC AND NONSTOICHIOMETRIC Fe , 0 , MICROCRYSTALS. , (12), pp.411–413.

Trinidad, P., de León, C.P. & Walsh, F.C., 2008. The use of electrolyte redox potential to monitor the Ce(IV)/Ce(III) couple. *Journal of Environmental Management*, 88(4), pp.1417–1425.

Utton, C.A. et al., 2013. Dissolution of vitrified wastes in a high-pH calcium-rich solution. *Journal of Nuclear Materials*, 435(1–3), pp.112–122. Available at: http://linkinghub.elsevier.com/retrieve/pii/S0022311512006897.

Utton, C.A. et al., 2013. Formation of alteration products during dissolution of vitrified ILW in a high-pH calcium-rich solution. *Journal of Nuclear Materials*, 442(1–3).

Utton, C. a. et al., 2012. Chemical durability of vitrified wasteforms: effects of pH and solution composition. *Mineralogical Magazine*, 76(8), pp.2919–2930. Available at: http://openurl.ingenta.com/content/xref?genre=article&issn=0026-461X&volume=76&issue=8&spage=2919.

Vandenberghe, R.E. et al., 2000. Mössbauer characterization of iron oxides and (oxy)hydroxides: the present state of the art. *Hyperfine Interactions*, 126(1), pp.247–

259. Available at: http://dx.doi.org/10.1023/A:1012603603203.

Vienna, J.D. et al., 2013. Current understanding and remaining challenges in modeling long-term degradation of borosilicate nuclear waste glasses. *International Journal of Applied Glass Science*, 4(4).

Vienna, J.D. et al., 1996. Plutonium Dioxide Dissolution in Glass.

Vienna, J.D. et al., 2014. Toward understanding the effect of low-activity waste glass composition on sulfur solubility. *Journal of the American Ceramic Society*, 97(10), pp.3135–3142.

Volf, M.B., 1984. *Chemical approach to glass*, Elsevier.

Wahl, F.M., Grim, R.E. & Graf, R.B., 1961. Phase Transformations in Silica as Exmined by Continuous X-Ray Diffraction. *American Mineralogist*, 46, pp.196–208.

Warren, B.E., 1941. SUMMARY OF WORK ON ATOMIC ARRANGEMENT IN GLASS*. *Journal of the American Ceramic Society*, 24(8), pp.256–261. Available at: http://dx.doi.org/10.1111/j.1151-2916.1941.tb14858.x.

Wilson, P.., 1997. *The Nuclear Fuel Cycle: From Ore to Waste*, OUP Oxford.

Witwer, K., Dysland, E. & Ave, J., 2010. Thermal Treatment of UK Intermediate and Low Level Radioactive Waste : A Demonstration of the GeoMelt Process Towards Treatment of Sellafield Waste. *WM2010 Conference*.

Won, J. & Angell, C.., 1976. *Glass: Structure by Spectroscopy*, Marcel Dekker.

Worchester, S.. et al., *Decontamination of Metals by Melt Refining/Slagging*,

Yaday, A.K Singh, P., 2015. A review of the structures of oxide glasses by Raman spectroscopy. *RSC Adv.*, 5(67583).

Youngblood, E. et al., 1978. Celtic vitrified forts: Implications of a chemical-petrological study of glasses and source rocks. *Journal of Archaeological Science*, 5(2), pp.99–121.

Yun, Y.H. Feller,S.A. Bray, P.J., 1979. Correction and addendum to Nuclear magnetic resonance studies of the glasses in the system Na2O-B2O3-SiO2. *Journal of Non-Crystalline Solids*, 33, pp.273–277.

Zachariasen, W.H., 1932. The atomic arrangement in glass. *Journal of the American*

Chemical Society, 54(1), pp.3841–3851.

10 APPENDICES

APPENDIX 1: CLEANING GLASS SAMPLES AND VESSELS PRIOR TO DISSOLUTION EXPERIMENTS

The adhering fines were removed by the following steps:

- The glass was placed in a clean glass beaker which held approximately 2.5 times the sample volume.
- Cold isopropanol, which was held in the fridge overnight, was forcibly added to the glass from a squirt bottle. The volume of isopropanol added was about one and a half times the sample volume estimated by the height of the beaker.
- During the isopropanol addition, the squirt bottle was moved in a circular motion so that the waste stream agitated all the glass.
- The sample was allowed to settle for approximately 15s before the isopropanol was decanted off the glass.
- The above (three bullet points) process was repeated twice.
- Before decanting (after repeating twice) the beaker was placed in an ultrasonic cleaner, filled with water, for 3 minutes.
- This process was repeated until the supernatant no longer appeared cloudy.
- The beaker containing the washed glass was placed within a drying oven. After 1 hour the beaker was measures, this process was repeated until the combined weight of the beaker and the sample did not change between measurements.

1L HDPE bottles used in the experiments was cleaned by the following steps, to ensure no contamination during the dissolution experiment.

- Vessels were rinsed with DI water to remove any material
- The vessels and lids were soaked in 1% decon 90 solution (made with DI waste) for 16 hours (at room temperature)
- The vessels with DI water were rinsed out twice to remove bubbles and soaps.
- The vessels and lids were soaked in 1-3% HNO_3 (made with UHQ water) for 16 hours (at room temperature).
- The vessels were rinsed out with UHQ water 3 times.
- Each vessel was filled 80-90% with UHQ water and weighed to 2 d.p. The lids were closed and the bottles were left in an oven at 90°C for 16 hours.

- After cooling the bottles were weighed and if they were within 5% of the starting solution then the following steps were followed, if this wasn't the case the previous steps (bullet points) were repeated but with a different lid.
- The pH was then measured. If the pH was between 5 and 7 the vessel was qualified for use.

APPENDIX 2: UNCERTAINTIES OF XRF ANALYSIS.

Sample value	Allowed Tolerance	Uncertainty	Sample value	Allowed Tolerance	Uncertainty	Sample value	Allowed Tolerance	Uncertainty
0.05	0.01	0.02	6.50	0.10	0.15	44.00	0.27	0.41
0.06	0.01	0.02	7.00	0.11	0.17	46.00	0.27	0.41
0.07	0.01	0.02	7.50	0.11	0.17	48.00	0.28	0.42
0.08	0.01	0.02	8.00	0.11	0.17	50.00	0.28	0.42
0.09	0.01	0.02	8.50	0.12	0.18	52.00	0.29	0.44
0.10	0.01	0.02	9.00	0.12	0.18	54.00	0.29	0.44
0.11	0.01	0.02	9.50	0.12	0.18	56.00	0.30	0.45
0.12	0.01	0.02	10.00	0.13	0.20	58.00	0.30	0.47
0.13	0.01	0.02	11.00	0.13	0.20	60.00	0.31	0.47
0.15	0.02	0.03	12.00	0.14	0.21	62.00	0.31	0.48
0.20	0.02	0.03	13.00	0.14	0.21	64.00	0.32	0.48
0.30	0.02	0.03	14.00	0.15	0.23	66.00	0.32	0.50
0.40	0.03	0.05	15.00	0.15	0.23	68.00	0.33	0.50
0.50	0.03	0.05	16.00	0.16	0.24	70.00	0.33	0.51
0.60	0.03	0.05	17.00	0.17	0.26	72.00	0.34	0.51
0.70	0.03	0.05	18.00	0.17	0.26	74.00	0.34	0.53
0.80	0.04	0.06	19.00	0.18	0.26	76.00	0.35	0.53
0.90	0.04	0.06	20.00	0.19	0.28	78.00	0.35	0.54
1.00	0.04	0.06	22.00	0.19	0.29	80.00	0.36	0.54
1.50	0.05	0.08	24.00	0.20	0.30	82.00	0.36	0.56
2.00	0.06	0.09	26.00	0.20	0.30	84.00	0.37	0.56
2.50	0.06	0.09	28.00	0.21	0.32	86.00	0.37	0.57
3.00	0.07	0.11	30.00	0.22	0.33	88.00	0.38	0.57
3.50	0.07	0.11	32.00	0.23	0.35	90.00	0.38	0.57
4.00	0.08	0.12	34.00	0.23	0.35	92.00	0.38	0.59
4.50	0.08	0.12	36.00	0.24	0.36	94.00	0.39	0.59
5.00	0.09	0.14	38.00	0.25	0.38	96.00	0.39	0.59
5.50	0.09	0.14	40.00	0.25	0.38	98.00	0.40	0.60
6.00	0.10	0.15	42.00	0.26	0.39	100.00	0.40	0.60

APPENDIX 3: PRESENTATION OF WORK

The Author has produced the following publication from this body of work:

Boast, L., Stennett, M., & Hyatt, N. (2017). Thermal treatment of plutonium contaminated material (PCM) waste. *MRS Advances, 2*(13), 735-740. doi:10.1557/adv.2017.169

The work included in this thesis has also been disseminated at a number of conferences and meetings during this time which are listed below:

<u>Oral Presentation</u>

- NDA annual PhD bursary meeting – Manchester, January 2016
- DISTINCTIVE annual PhD meeting – Bristol, May 2016
- Meeting of the Materials Research Society – Boston, November 2016
- The American Ceramic Society – Kona, May 2017A

APPENDIX 4: PDF CARD NUMBERS FOR XRD TRACES

Magnetite PDF 33-664

Magnesioferrite PDF 36-398

Diopside PDF 19-239

Chromite PDF 34-140

Clinoferrosilite PDF 17-548

Fayalite PDF 31-633

Monticellite PDF 35-590

Rutile PDF 16-934

Calcite PDF 5-586

Tschernichite PDF 19-890

Aluminum Oxide PDF 43-1483